

Eddy currents from moving point sources of magnetic field in the Gravity Probe B experiment

A. S. Silberleit and M. G. Keiser

Gravity Probe B, HEPL, Stanford University, Stanford, CA 94305-4085, USA

(Submitted October 30, 1996)

Zh. Tekh. Fiz. **68**, 1–8 (February 1998)

Two boundary-value problems in plane geometry, modeling the field and current distribution produced by moving sources of magnetic field (fluxons) in surrounding normal metals, are solved analytically. In the first case a fluxon moves with a constant velocity in a superconducting plane separated by a vacuum gap from a half space filled with a metal having a low electrical conductivity. In the second case the half space is replaced by a thin metal layer of high conductivity. The problems are solved by perturbation techniques, the Fourier integral transform, and the Parseval identity. The latter is used to calculate the power dissipated in the metal. An estimate of the power dissipation is needed in order to calculate certain torques of magnetic origin in the Gravity Probe B project. © 1998 American Institute of Physics. [S1063-7842(98)00102-0]

INTRODUCTION

In the Gravity Probe B mission (GP-B) a rotating superconducting ball (superconducting gyro) will be orbiting the Earth in a circular polar orbit for over a year, and the drift of its axis resulting from two general-relativity effects will be measured (the details of the experiment are described in Refs. 1 and 2). According to theory, the drift is expected to be very small (0.042 arcsec/yr and 6.6 arcsec/yr in the east–west and north–south directions, respectively), so that the measurement accuracy must be very high, and the classical (nonrelativistic) torques causing the drift must be either eliminated or carefully accounted for.

In particular, there will be quantum-size sources of magnetic field (fluxons) on the surface of the superconducting rotor, which induce eddy currents and thus energy dissipation in the surrounding normal metals. Consequently, differential damping torques are produced and must be estimated.

In this paper we give such estimates by solving explicitly two corresponding model boundary-value problems in plane geometry (they may also be of interest for other applications). The complications associated with the spherical geometry of the GP-B experiment can be neglected, because the gap between the rotor surface and the surrounding normal metals is extremely small compared to the radius of the rotor (see Figs. 1 and 2).

The first problem treats a fluxon–antifluxon pair moving with a constant velocity in a superconducting plane (the rotor surface) separated by a gap from a half space having a finite electrical conductivity. For GP-B this problem models the influence of the so-called caging rod, which in reality hangs over only a relatively small portion of the ball's surface. However, the quantity of interest to us—the upper limit of the dissipated power—can obviously be found if one assumes that the metal covers the entire surface, which is modeled by a half space.

In the second problem the half space in the first problem

is replaced by a thin layer of high electrical conductivity. Under the conditions of GP-B the problem now models the influence of the six electrodes of the rotor's suspension system, which are made of a material having a high copper content. Again, the electrodes actually cover approximately 45% of the rotor's surface, but the most conservative estimate of the dissipated power and, hence, of the torques is obtained under the assumption that they cover the entire surface.

We conclude our paper with estimates of the spindown rate of the GP-B gyro due to eddy current energy dissipation.

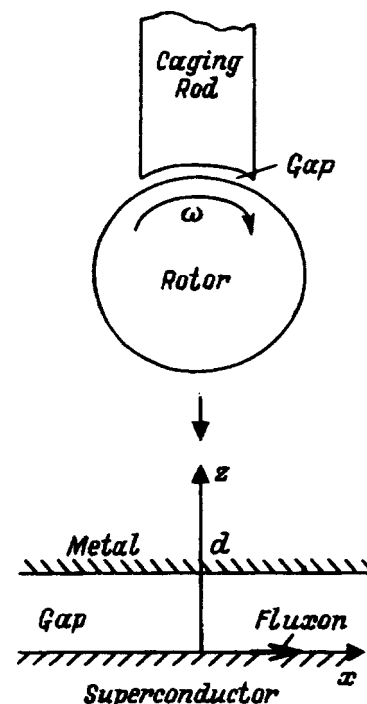


FIG. 1.

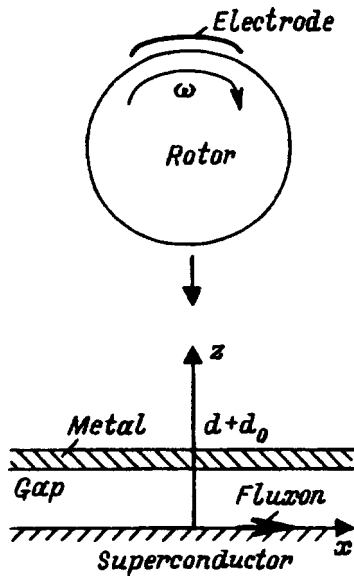


FIG. 2.

1. THE PROBLEM FOR A CONDUCTING HALF SPACE: STATEMENT OF THE PROBLEM AND REPRESENTATION OF THE SOLUTION

Let a metal having an electrical conductivity σ and a magnetic permeability $\mu = \mu_0$ occupy the half space $z' > d$ of a Cartesian coordinate system $\{x', y', z'\}$. The plane $z = 0$ is the surface of the superconductor, and a fluxon and an antifluxon move in it with a constant velocity $v \ll c$ along the x' axis; the layer $0 < z' < d$ is a dielectric gap (Fig. 1). The equations and boundary conditions for the magnetic induction \mathbf{B} and the eddy current density \mathbf{j} induced in the metal have the form (Ref. 3, Chap. 10): in the gap (medium 1)

$$\nabla' \cdot \mathbf{B} = 0, \quad \nabla' \times \mathbf{B} = 0; \quad 0 < z' < d, \quad |x'|, |y'| < \infty; \quad (1.1)$$

$$B_z|_{z'=0} = \Phi_0 [\delta(x' - x'_f(t)) \delta(y' - y'_f) - \delta(x' - x'_a(t)) \delta(y' - y'_a)];$$

$$\mathbf{B}|_{|x'|, |y'| \rightarrow \infty} \rightarrow 0; \quad (1.2)$$

in the conductor (medium 2)

$$\nabla' \cdot \mathbf{B} = 0, \quad \nabla' \times \mathbf{B} = \mu_0 \mathbf{j},$$

$$\nabla' \times \mathbf{j} = -\sigma \frac{\partial \mathbf{B}}{\partial t}; \quad z' > d, \quad |x'|, |y'| < \infty; \quad (1.3)$$

at the interface

$$\mathbf{B}|_{z'=d+0} = \mathbf{B}|_{z'=d-0}. \quad (1.4)$$

Here Φ_0 is the flux produced by a point source (in GP-B $\Phi_0 = h/2e$ is the magnetic flux quantum, h is Planck's constant, and e is the electron charge), δ is the Dirac delta function, and $x'_{f,a}(t) = x'_{f,a} + vt$, $y'_{f,a}$ are the coordinates of the fluxon and antifluxon, respectively; the prime attached to the symbol ∇ signifies differentiation with respect to the primed variables. Note that the current density \mathbf{j} can be eliminated from the last two equations in (1.3) to give one second-order equation for \mathbf{B} :

$$-\sigma \mu_0 \frac{\partial \mathbf{B}}{\partial t} = \nabla' \times \nabla' \times \mathbf{B} = -\nabla'^2 \mathbf{B},$$

$$z' > d, \quad |x'|, |y'| < \infty, \quad (1.5)$$

where the last equation is valid because \mathbf{B} is solenoidal.

We seek a quasistationary solution to (1.1)–(1.4); we introduce a dimensionless coordinate system comoving with the sources,

$$x = \frac{x' - x'_f(t)}{d} = \frac{x' - x'_f - vt}{d},$$

$$y' = \frac{y' - y'_f}{d}, \quad z' = \frac{z'}{d}. \quad (1.6)$$

In terms of these variables the above problem is rewritten as follows: for medium 1

$$\nabla \cdot \mathbf{B} = 0, \quad \nabla \times \mathbf{B} = 0; \quad 0 < z < 1, \quad |x|, |y| < \infty; \quad (1.7)$$

$$B_z|_{z=0} = \frac{\Phi_0}{d^2} [\delta(x) \delta(y) - \delta(x - x_0) \delta(y - y_0)]; \quad (1.8)$$

for medium 2

$$\nabla \cdot \mathbf{B} = 0, \quad \nabla^2 \mathbf{B} = -\kappa \frac{\partial \mathbf{B}}{\partial x}; \quad z > 1, \quad |x|, |y| < \infty; \quad (1.9)$$

at the interface

$$\mathbf{B}|_{z=1+0} = \mathbf{B}|_{z=1-0}. \quad (1.10)$$

Here we have omitted the obvious conditions at infinity and introduced the notation $x_0 = (x_a - x_f)/d$, $y_0 = (y_a - y_f)/d$; the only dimensionless parameter of the problem is

$$\kappa = \sigma \mu_0 v d. \quad (1.11)$$

Problem (1.7)–(1.10) can be solved by a more or less standard procedure using Fourier integral transforms in the variables x and y , but this approach leads to field and current distributions in the form of cumbersome double Fourier integrals, which impede further analytical calculations and obscure the physical meaning of the result. Instead we seek a perturbational solution in the form of a power series in the small parameter κ ($\kappa \ll 0.02$) under GP-B conditions):

$$\mathbf{B}(x, y, z) = \mathbf{B}^{(0)}(x, y, z) + \kappa \mathbf{B}^{(1)}(x, y, z) + \kappa^2 \mathbf{B}^{(2)}(x, y, z) + \dots, \quad (1.12)$$

where the functional coefficients $\mathbf{B}^{(k)}$, $k = 0, 1, 2, \dots$ must be evaluated from the following sequence of problems deduced from (1.7)–(1.10) and (1.12):

$$\nabla \cdot \mathbf{B}^{(k)} = 0, \quad \nabla \times \mathbf{B}^{(k)} = 0; \quad 0 < z < 1, \quad |x|, |y| < \infty;$$

$$B_z^{(k)}|_{z=0} = \frac{\Phi_0}{d^2} [\delta(x) \delta(y) - \delta(x - x_0) \delta(y - y_0)] \delta_{k0}; \quad (1.13)$$

$$\nabla \cdot \mathbf{B}^{(k)} = 0, \quad \nabla^2 \mathbf{B}^{(k)} = -(1 - \delta_{k0}) \frac{\partial \mathbf{B}^{(k-1)}}{\partial x};$$

$$z > 1, \quad |x|, |y| < \infty;$$

$$\mathbf{B}^{(k)}|_{z=1+0} = \mathbf{B}^{(k)}|_{z=1-0}, \quad (1.14)$$

where $k=0,1,2,\dots$, and $\delta_{00}=1$, $\delta_{k0}=0$, $k\geq 1$.

It follows from (1.12) and the second equation in (1.3) that the corresponding expansion for the current density in the conductor is

$$\mathbf{j} = \frac{1}{\mu_0 d} \nabla \times \mathbf{B} = (\varkappa \mathbf{j}^{(1)} + \varkappa^2 \mathbf{j}^{(2)} + \dots),$$

$$\mathbf{j}^{(k)} = \frac{1}{\mu_0 d} \nabla \times \mathbf{B}^{(k)}, \quad z > 1, \quad (1.15)$$

where we have taken into account the fact that $\nabla \times \mathbf{B}^{(0)} = 0$ in the entire half space $z > 0$. Accordingly, the current density is a first-order term in \varkappa , because without the conductor ($\varkappa=0$) there is no current at all.

Our goal is to determine $\mathbf{j}^{(1)}$, i.e., the principal term in the current distribution, and then to calculate the dissipated power to the first order. This can be done without any technical difficulties, and the result has a clear physical meaning.

2. THE PROBLEM FOR THE HALF SPACE: CURRENT DISTRIBUTION AND DISSIPATED POWER

We now turn to the sequence of problems (1.13), (1.14). The ‘‘unperturbed’’ solution $\mathbf{B}^{(0)}$, naturally, is the field of two point sources in the half space without the conductor. It satisfies the Laplace equation in the entire half space $z > 0$ with the boundary condition (1.13) and is therefore given by

$$\mathbf{B}^{(0)} = \nabla \psi^{(0)}, \quad z > 0,$$

$$\psi^{(0)}(x, y, z) = -\frac{\Phi_0}{2\pi d^2} \left(\frac{1}{R} - \frac{1}{R_0} \right), \quad (2.1)$$

where

$$R = \sqrt{x^2 + y^2 + z^2},$$

$$R_0 = \sqrt{(x-x_0)^2 + (y-y_0)^2 + (z-z_0)^2}$$

are the distances from the sources to an arbitrary point with coordinates (x, y, z) .

To find the principal term in the expansion of the current density (1.15), we need to know the field $\mathbf{B}^{(1)}$ satisfying problem (1.13), (1.14) with $k=1$, or rather the curl of this field in the conductor. Surprisingly, the latter may be determined without completely solving the corresponding boundary-value problem. Using (2.1), we write the field in the conductor in the form

$$\mathbf{B}^{(1)} = \mathbf{b}^{(1)} - \frac{x}{2} \mathbf{B}^{(0)} + \frac{1}{2} \psi^{(0)} \mathbf{e}_x = \mathbf{b}^{(1)} - \frac{x}{2} \nabla \psi^{(0)} + \frac{1}{2} \psi^{(0)} \mathbf{e}_x$$

$$= \mathbf{b}^{(1)} - \frac{1}{2} \nabla (x \psi^{(0)}) + \psi^{(0)} \mathbf{e}_x, \quad z > 1, \quad (2.2)$$

where $\mathbf{b}^{(1)}(x, y, z)$ is the new unknown field, and \mathbf{e}_x is the unit vector in the direction of the x axis.

Using (2.1), (2.2) and Eqs. (1.14) with $k=0$, one easily calculates

$$\nabla \cdot \mathbf{B}^{(1)} = \nabla \cdot \mathbf{b}^{(1)} - \frac{x}{2} \nabla \cdot \mathbf{B}^{(0)} - \frac{1}{2} \mathbf{B}^{(0)} + \frac{1}{2} \mathbf{B}^{(0)} = \nabla \cdot \mathbf{b}^{(1)},$$

$$\nabla^2 \mathbf{B}^{(1)} = \nabla^2 \mathbf{b}^{(1)} - \frac{x}{2} \nabla^2 \mathbf{B}^{(0)} - \frac{\partial \mathbf{B}^{(0)}}{\partial x} - \frac{1}{2} \nabla^2 \psi^{(0)} = \nabla^2 \mathbf{b}^{(1)}$$

$$- \frac{\partial \mathbf{B}^{(0)}}{\partial x}, \quad z > 1,$$

so that from equations (1.14) with $k=1$ we obtain

$$\nabla \cdot \mathbf{b}^{(1)} = 0, \quad \nabla^2 \mathbf{b}^{(1)} = 0, \quad z > 1. \quad (2.3)$$

Consequently, setting

$$\mathbf{b}^{(1)} = \nabla \psi^{(1)} + \nabla \times \mathbf{A}^{(1)}, \quad \nabla \cdot \mathbf{A}^{(1)} = 0, \quad z > 1, \quad (2.4)$$

we see that both unknown potentials $\psi^{(1)}$ and $\mathbf{A}^{(1)}$ are harmonic in the half space occupied by the conductor, and

$$\nabla^2 \psi^{(1)} = 0, \quad \nabla^2 \mathbf{A}^{(1)} = 0, \quad z > 1. \quad (2.5)$$

Introducing (2.4) into (2.2), we find that

$$\mathbf{B}^{(1)} = \nabla \left(\psi^{(1)} - \frac{x}{2} \psi^{(0)} \right) + \nabla \times \mathbf{A}^{(1)} + \psi^{(0)} \mathbf{e}_x, \quad z > 1. \quad (2.6)$$

According to (2.4), (2.5), the first two terms on the right side of (2.6) are irrotational; therefore

$$\nabla \times \mathbf{B}^{(1)} = \nabla \psi^{(0)} \times \mathbf{e}_x = \mathbf{B}^{(0)} \times \mathbf{e}_x, \quad z > 1. \quad (2.7)$$

On the basis of this equation Eqs. (1.15) and (1.11) can be used to determine the principal current-density term:

$$\mathbf{j} = \varkappa \mathbf{j}^{(1)} + O(\varkappa^2) = \sigma v \mathbf{B}^{(0)} \times \mathbf{e}_x + O(\varkappa^2), \quad z > 1. \quad (2.8)$$

The result (2.8) has a clear physical meaning. Indeed, when a conductor moves with the velocity $\mathbf{v}^{(0)}$ in an external magnetic field $\mathbf{B}^{(0)}$, the induced current density in it is known to be given by the Lorentz equation

$$\mathbf{j} = \sigma \mathbf{v}^{(0)} \times \mathbf{B}^{(0)}. \quad (2.9)$$

In our case, clearly, $\mathbf{v}^{(0)} = -v \mathbf{e}_x$, and as the conductivity is small, the induced magnetic field can be neglected in comparison with the external field $\mathbf{B}^{(0)}$; Eq. (2.9) goes over to (2.8) as a result.

We now calculate the power dissipated by a fluxon-antifluxon pair from the equation

$$P_{fa} = \frac{1}{\sigma} \int_{z' > d} j^2 dV' = \frac{d^3}{\sigma} \int_{z > 1} j^2 dV$$

$$\simeq \sigma v^2 d^3 \int_{z > 1} [(B_y^{(0)})^2 + (B_z^{(0)})^2] dV$$

(the approximate equality here and below indicates that the expression is calculated to the first nonvanishing order in \varkappa).

After substituting the expression (2.1) for $\mathbf{B}^{(0)}$ into the right side, we have only to compute the integrals for the final result, but the computation is found to be rather cumbersome, and its result depends on the relative position of the fluxon and the antifluxon.

Actually, however, we are interested in a universal upper bound for P_{fa} , which can be found in terms of the energy dissipation rate P_f of a single fluxon as defined by the equation

$$P_f = \frac{d^3}{\sigma} \int_{z>1} j_f^2 dV \approx \sigma v^2 d^3 \int_{z>1} [(B_{f,y}^{(0)})^2 + (B_{f,z}^{(0)})^2] dV. \tag{2.10}$$

We the magnetic field is naturally amenable to representation by the sum of the fluxon and antfluxon fields [see (2.1)], $\mathbf{B}^{(0)} = \mathbf{B}_f^{(0)} + \mathbf{B}_a^{(0)}$, $\mathbf{B}_f^{(0)} \sim \nabla(1/R)$, $\mathbf{B}_a^{(0)} \sim \nabla(1/R_0)$, with a corresponding decomposition of the current density from (2.9), $\mathbf{j} = \mathbf{j}_f + \mathbf{j}_a$. It is evident that $P_f = P_a$ and, hence,

$$P_{fa} = \frac{d^3}{\sigma} \int_{z>1} (\mathbf{j}_f + \mathbf{j}_a)^2 dV = \frac{d^3}{\sigma} \int_{z>1} (j_f^2 + j_a^2 + 2\mathbf{j}_f \cdot \mathbf{j}_a) dV \leq \frac{d^3}{\sigma} 2 \int_{z>1} (j_f^2 + j_a^2) dV = 2(P_f + P_a) = 4P_f. \tag{2.11}$$

Now, combining (2.11) with (2.10) and substituting the value of $\mathbf{B}_f^{(0)}$ from (2.1) into the integral for P_f , we find

$$P_{fa} \leq 4P_f \approx \sigma v^2 d^3 \frac{\Phi_0^2}{\pi^2 d^4} \int_{z>1} \left[\left(\frac{\partial}{\partial y} \frac{1}{R} \right)^2 + \left(\frac{\partial}{\partial z} \frac{1}{R} \right)^2 \right] dV = \frac{\sigma v^2 \Phi_0^2}{\pi^2 d} \int_{z=1}^{\infty} \int_{-\infty}^{\infty} \int_{-\infty}^{\infty} \frac{y^2 + z^2}{(x^2 + y^2 + z^2)^3} dx dy dz. \tag{2.12}$$

The integrals in (2.12) are readily computed, yielding the desired simple estimate:

$$P_{fa} \leq 4P_f = \frac{3}{4\pi} \frac{\sigma v^2 \Phi_0^2}{d}. \tag{2.13}$$

The value of P_{fa} is no more than half this upper bound.

3. THE PROBLEM FOR A HIGHLY CONDUCTING THIN LAYER: STATEMENT OF THE PROBLEM AND ASYMPTOTIC SIMPLIFICATION

We now turn to the second problem, in which the conducting half space is replaced by a conducting layer of thickness d_0 occupying the domain $d < z' < d + d_0$ (Fig. 2). The layer is assumed to be thin, $d_0 \ll d$, and its electrical conductivity to be high, so that the parameter κ is no longer small (under the conditions of GP-B $d_0 \sim 0.1d$, $\kappa \sim 30$).

Consequently, outside the layer in the half space $z > 0$ the magnetic field satisfies Eqs. (1.7) with the boundary condition (1.8) and vanishes at infinity, while in the layer $1 < z < 1 + d_0/d$ Eqs. (1.9) are valid; the appropriate matching conditions should be fulfilled at both surfaces of the layer [from here on we return to the dimensionless comoving coordinates (1.6)]. The solution to this problem is very complicated and difficult to analyze, necessitating an additional, physically meaningful simplification of the model. Obviously the most suitable approach is to replace the thin, highly conducting layer of finite thickness by an infinitely thin, conducting sheet with a surface current density $\mathbf{j}^s = \mathbf{j}^s(x, y)$ and to formulate corresponding matching conditions for the magnetic field at $z = 1$. The form of these conditions is well known (see Ref. 2, 7.21, and Ref. 3, Chap. 1, Sec. 2):

$$B_z|_{z=1+0} = B_z|_{z=1-0},$$

$$\mathbf{e}_z \times (\mathbf{B}|_{z=1+0} - \mathbf{B}|_{z=1-0}) = \mu_0 \mathbf{j}^s. \tag{3.1}$$

Consequently, all that is required to close the problem is to relate \mathbf{j}^s to the field \mathbf{B} . To do so, we introduce the vector potential \mathbf{A} :

$$\mathbf{B} = \nabla \times \mathbf{A}, \quad \nabla \cdot \mathbf{A} = 0, \tag{3.2}$$

and note that the last equation in (1.3) (the induction equation), which is valid in a real three-dimensional layer, gives

$$\mathbf{j} = \sigma v \frac{\partial \mathbf{A}}{\partial x}.$$

Hence, for the surface current density we can write

$$\mathbf{j}^s(x, y) = \sigma v d_0 \left. \frac{\partial \mathbf{A}}{\partial x} \right|_{z=1}. \tag{3.3}$$

Note that conditions (3.1) and (3.3) can be derived by a procedure, well known from the theory of ‘‘thin’’ bodies (plates and shells),⁴⁻⁹ for asymptotic integration of the complete three-dimensional problem.

Relations (3.1)–(3.3) enable us to formulate the entire boundary-value problem in terms of the vector potential. Using Eqs. (1.7) for $z > 0$, $z \neq 1$ and the boundary condition (1.8), we write

$$\nabla^2 \mathbf{A} = 0, \quad \nabla \cdot \mathbf{A} = 0, \quad z > 0, \quad z \neq 1;$$

$$\left. \frac{\partial A_y}{\partial x} - \frac{\partial A_x}{\partial y} \right|_{z=0} = \frac{\Phi_0}{d^2} [\delta(x) \delta(y) - \delta(x - x_0) \delta(y - y_0)];$$

$$\langle \mathbf{A} \rangle|_{z=1} = 0;$$

$$\left\langle \frac{\partial A_x}{\partial z} - \frac{\partial A_z}{\partial x} \right\rangle \Big|_{z=1} = -\kappa_0 \left. \frac{\partial A_x}{\partial x} \right|_{z=1},$$

$$\left\langle \frac{\partial A_z}{\partial y} - \frac{\partial A_y}{\partial z} \right\rangle \Big|_{z=1} = \kappa_0 \left. \frac{\partial A_y}{\partial x} \right|_{z=1}, \tag{3.4}$$

where

$$\kappa_0 = \kappa \frac{d_0}{d} = \sigma \mu_0 v d_0, \tag{3.5}$$

and the angle brackets signify a jump of the bracketed quantity:

$$\langle a \rangle|_{z=1} = (a|_{z=1+0} - a|_{z=1-0}).$$

The vector boundary-value problem (3.4)–(3.7) is still quite cumbersome and unappealing; fortunately, there is a natural way to reduce it to a simple scalar problem. Obviously, the surface current density has no z component, $j_z^s = 0$, so that (3.3) requires that $A_z = 0$ at least for $z = 1$. We therefore require that $A_z = 0$ everywhere and, accordingly, write

$$\mathbf{A} = A_x \mathbf{e}_x + A_y \mathbf{e}_y, \quad \nabla \cdot \mathbf{A} = \frac{\partial A_x}{\partial x} + \frac{\partial A_y}{\partial y} = 0, \quad z > 0. \tag{3.6}$$

To satisfy the zero-divergence condition (3.6), we set

$$A_x = -\frac{\partial \Pi}{\partial y}, \quad A_y = \frac{\partial \Pi}{\partial x}, \tag{3.7}$$

where $\Pi = \Pi(x, y, z)$ is the new function to be determined.

According to (3.3) and (3.7), the surface current density is expressed in terms of Π by the equations

$$j_x^s = -\sigma v d_0 \frac{\partial^2 \Pi}{\partial x \partial y} \Big|_{z=1}, \quad j_y^s = \sigma v d_0 \frac{\partial^2 \Pi}{\partial x^2} \Big|_{z=1}. \quad (3.8)$$

It is readily verified that the equation and boundary conditions (3.4) are valid if $\Pi(x, y, z)$ is a solution of the problem

$$\begin{aligned} \nabla^2 \Pi &= 0, \quad z > 0, \quad z \neq 1; \\ -\frac{\partial^2 \Pi}{\partial z^2} \Big|_{z=0} &= \frac{\Phi_0}{d^2} [\delta(x) \delta(y) - \delta(x-x_0) \delta(y-y_0)]; \\ \langle \Pi \rangle|_{z=1} &= 0; \quad \left\langle \frac{\partial \Pi}{\partial z} \right\rangle \Big|_{z=1} = -\alpha_0 \frac{\partial \Pi}{\partial x} \Big|_{z=1}. \end{aligned} \quad (3.9)$$

With the exception of the second derivative in the boundary condition (3.9) at $z=0$, this scalar problem is standard; its solution is given below.

4. THE PROBLEM FOR THE LAYER: SOLUTION AND CALCULATION OF THE DISSIPATED POWER

We solve problem (3.9) by means of the Fourier integral transform in the variables x and y ; for $z \geq 1$ this approach gives $\Pi(x, y, z)$ in the form

$$\begin{aligned} \Pi(x, y, z) &= \frac{1}{2\pi} \int_{-\infty}^{\infty} \int_{-\infty}^{\infty} \hat{\Pi}(\lambda, \nu, z) e^{i(\lambda x + \nu y)} d\lambda d\nu; \\ \hat{\Pi}(\lambda, \nu, z) &= D(\lambda, \nu) e^{-\gamma z}; \\ \gamma(\lambda, \nu) &= \sqrt{\lambda^2 + \nu^2} \geq 0, \\ D(\lambda, \nu) &= -\frac{\Phi_0}{d^2 \gamma} \frac{1 - e^{-i(\lambda x_0 + \nu y_0)}}{\gamma - i(\alpha_0/2)\lambda(1 - e^{-\gamma})}; \quad z \geq 1. \end{aligned} \quad (4.1)$$

In the domain $0 < z < 1$ the expression for $\hat{\Pi}(\lambda, \nu, z)$ differs slightly from (4.1), involving the exponentials of both $\pm \gamma z$, but we need only (4.1) for our purposes.

All the pertinent physical fields can be calculated from (4.1) using the equations of the previous section. In particular, for the surface current density, according to (3.8), we obtain

$$\begin{aligned} \mathbf{j}^s(x, y) &= \frac{1}{2\pi} \int_{-\infty}^{\infty} \int_{-\infty}^{\infty} \hat{\mathbf{j}}^s(\lambda, \nu) e^{i(\lambda x + \nu y)} d\lambda d\nu; \\ \frac{\hat{j}_x^s(\lambda, \nu)}{\sigma v d_0} &= \lambda \nu \hat{\Pi}(\lambda, \nu, 1) = \lambda \nu D(\lambda, \nu) e^{-\gamma}, \\ \frac{\hat{j}_y^s(\lambda, \nu)}{\sigma v d_0} &= -\lambda^2 \hat{\Pi}(\lambda, \nu, 1) = -\lambda^2 D(\lambda, \nu) e^{-\gamma}. \end{aligned} \quad (4.2)$$

To calculate the dissipation rate P_{fa} , we use the Parseval identity, which, given certain conditions on the function $f(x, y)$, has the form

$$\int_{-\infty}^{\infty} \int_{-\infty}^{\infty} |f(x, y)|^2 dx dy = \int_{-\infty}^{\infty} \int_{-\infty}^{\infty} |\hat{f}(\lambda, \nu)|^2 d\lambda d\nu,$$

where $\hat{f}(\lambda, \nu)$ is the Fourier transform of $f(x, y)$.

Consequently, on the basis of (4.2), (4.1) we can write the arrayed equations

$$\begin{aligned} P_{fa} &= \frac{d^2}{\sigma d_0} \int_{-\infty}^{\infty} \int_{-\infty}^{\infty} [(j_x^s(x, y))^2 + (j_y^s(x, y))^2] dx dy \\ &= \frac{d^2}{\sigma d_0} \int_{-\infty}^{\infty} \int_{-\infty}^{\infty} [(\hat{j}_x^s(\lambda, \nu))^2 + (\hat{j}_y^s(\lambda, \nu))^2] d\lambda d\nu \\ &= \sigma v^2 d_0 d^2 \int_{-\infty}^{\infty} \int_{-\infty}^{\infty} \lambda^2 \gamma^2 e^{-2\gamma} |D(\lambda, \nu)|^2 d\lambda d\nu \end{aligned}$$

or, substituting $D(\lambda, \nu)$ from (4.1),

$$P_{fa} = \frac{\sigma v^2 d_0 \Phi_0^2}{d^2} \int_{-\infty}^{\infty} \int_{-\infty}^{\infty} \left| \frac{1 - e^{-i(\lambda x_0 + \nu y_0)}}{\gamma - i(\alpha_0/2)\lambda(1 - e^{-\gamma})} \right|^2 d\lambda d\nu. \quad (4.3)$$

To further simplify the calculations and to obtain an upper bound that does not depend on the relative position of the fluxon and the antifluxon, we again estimate P_{fa} using the power P_f dissipated by a single fluxon; in this case the estimate is based on the obvious inequality for the factor in the integrand of (4.3)

$$|1 - e^{-i(\lambda x_0 + \nu y_0)}|^2 = 4 \sin^2 \frac{\lambda x_0 + \nu y_0}{2} \leq 4.$$

Equation (4.3) with this factor replaced by unity is obviously the sought-after P_f ; we therefore have

$$\begin{aligned} P_{fa} &\leq 4P_f = \frac{4\sigma v^2 d_0 \Phi_0^2}{d^2} C(\alpha_0); \\ C(\alpha_0) &= \int_{-\infty}^{\infty} \int_{-\infty}^{\infty} \frac{\lambda^2 e^{-2\gamma}}{\gamma^2 + (\alpha_0/2)^2 \lambda^2 (1 - e^{-2\gamma})^2} d\lambda d\nu, \\ \gamma(\lambda, \nu) &= \sqrt{\lambda^2 + \nu^2} \geq 0. \end{aligned} \quad (4.4)$$

The double integral representing the coefficient $C(\alpha_0)$ can be calculated explicitly, leading to the equation

$$\begin{aligned} C(\alpha_0) &= \frac{\pi}{2\alpha^2} \left[\ln \frac{\sqrt{1 + \alpha^2} + 1}{2} + \alpha \ln(\sqrt{1 + \alpha^2} + \alpha) \right. \\ &\quad \left. + \sqrt{1 + \alpha^2} \ln \frac{\sqrt{1 + \alpha^2} + 1}{2(1 + \alpha^2)} \right], \\ \alpha &= \frac{\alpha_0}{2} > 0. \end{aligned} \quad (4.5)$$

The derivation of this equation is given in the Appendix. An intermediate, single-integral representation arises in the course of the derivation:

$$\begin{aligned} C(\alpha_0) &= 2\pi \int_0^{\infty} \frac{\gamma e^{-2\gamma}}{\sqrt{1 + (\alpha_0/2)^2 p^2(\gamma)} [\sqrt{1 + (\alpha_0/2)^2 p^2(\gamma)} + 1]} d\gamma, \\ p(\gamma) &= 1 - e^{-2\gamma}, \end{aligned} \quad (4.6)$$

which provides a simple estimate for $C(\alpha_0)$:

$$C(\varkappa_0) < C(0) = \pi \int_0^\infty \gamma e^{-2\gamma} d\gamma = \frac{\pi}{4} \quad (4.7)$$

[in the limit $\alpha \rightarrow +0$, of course, Eq. (4.5) gives the same value for $C(0)$]. It is also clear from (4.6) that $C(\varkappa_0)$ is a monotonically decreasing function of \varkappa_0 , whose behavior for large values of the argument is given by

$$C(\varkappa_0) \sim \frac{2\pi}{\varkappa_0^2} (\ln \varkappa_0 + 0.75 - 3 \ln 2).$$

The combination of (4.4) and (4.7) leads to a simple upper bound for the dissipated power:

$$P_{fa} \leq 4P_f < \frac{\pi \sigma v^2 d_0 \Phi_0^2}{d^2}. \quad (4.8)$$

Note that the only difference of (4.8) from the corresponding bound (2.13) in the half-space problem, other than the numerical coefficient, is the factor d_0/d , i.e., the ratio of the thicknesses of the layer and the gap.

5. CONCLUSION

We conclude our paper with estimates pertinent to the Gravity Probe B experiment. In this case the fluxon–antifluxon pairs are situated on the surface of a gyroscope rotating with an angular frequency ω , so that their velocity is $v = \omega r_g$, where $r_g \approx 1.91$ cm is the radius of the rotor radius. Accordingly, the two upper bounds (2.13) and (4.8) for the maximum power P_{fa}^{\max} dissipated by a pair can be written as

$$P_{fa}^{\max} = K \frac{\sigma \omega^2 r_g^2 \Phi_0^2}{d}, \quad (5.1)$$

where $K = K_c = 3/4\pi \approx 0.24$ for the caging rod (modeled by a half space), and $K = K_e = \pi d_0/d \approx 0.31$ for the electrodes (modeled by a thin layer).

The only source of dissipated energy is the rotor kinetic energy $W = I\omega^2/2$, where $I \approx 91.9$ g·cm² is the moment of inertia of the rotor. An estimate of the kinetic energy loss during the time T is given by

$$\delta W = NTP_{fa}^{\max}, \quad (5.2)$$

where $N \sim 100$ is the number of fluxon–antifluxon pairs on the surface of the gyro.

The losses imply spindown of the gyro, expressed by a corresponding decrement $\delta\omega$ of the angular velocity; we wish to estimate this decrement. Since $\delta\omega$ and δW are small, both variations are related by

$$\delta W = \delta \left(\frac{I\omega^2}{2} \right) \approx I\omega \delta\omega,$$

so that

$$\frac{\delta\omega}{\omega} = \frac{1}{2} \frac{\delta W}{W}.$$

Substituting all the necessary expressions given above [see (5.1), (5.2)] in the latter equation, we obtain the desired estimate in the form

$$\frac{\delta\omega}{\omega} = NTK \frac{\sigma r_g^2 \Phi_0^2}{Id}. \quad (5.3)$$

For specific numerical estimates it is only required to know the flux quantum $\Phi_0 = 2 \times 10^{-15}$ Wb, the gap $d = 0.05$ cm, and the conductivity, which differs for the caging rod ($\sigma = \sigma_c \approx 2.4 \times 10^7$ ($\Omega \cdot \text{m}$)⁻¹) and the electrodes ($\sigma = \sigma_e \approx 6.5 \times 10^{10}$ ($\Omega \cdot \text{m}$)⁻¹); the latter values are given for titanium and copper at a temperature of approximately 2 K. For a characteristic mission duration $T = 1$ yr these data give $\delta\omega/\omega \sim 6.0 \times 10^{-10}$ and $\delta\omega/\omega \sim 1.2 \times 10^{-6}$ for the caging rod and the electrodes, respectively. These values are lower than, for instance, the differential damping induced by residual gas molecules, which is estimated as $\delta\omega/\omega \sim 3 \times 10^{-5}$ at a pressure of 10^{-11} torr (Ref. 1, p. 570). However, bearing in mind the most conservative assumptions adopted in our modeling, we can realistically expect values even one or two order of magnitude lower. The corresponding torques responsible for classical drift of the gyro spin axis are proportional to $\delta\omega/\omega$ and are also well below the danger level.

This work has been supported by NASA Grant NAS8-39225 for Gravity Probe B.

APPENDIX

Here we derive the explicit expression (4.5) for the coefficient $C(\varkappa_0)$ by calculating the double integral from its definition (4.4). The calculation is carried out in two main steps. First, exploiting the evenness of the integrand in (4.4) and using polar coordinates γ, φ in the λ, ν plane, $\lambda = \gamma \cos \varphi$, $\nu = \gamma \sin \varphi$, $\gamma = \sqrt{\lambda^2 + \nu^2}$, we write

$$\begin{aligned} C(\varkappa_0) &= 4 \int_0^\infty \int_0^\infty \frac{\lambda^2 e^{-2\gamma}}{\gamma^2 + (\varkappa_0/2)^2 \lambda^2 (1 - e^{-2\gamma})^2} d\lambda d\nu \\ &= 4 \int_0^\infty \gamma e^{-2\gamma} d\gamma \int_0^{\pi/2} \frac{\cos^2 \varphi}{1 + \alpha^2 p^2(\gamma) \cos^2 \varphi} d\varphi, \end{aligned}$$

$$\alpha = \frac{\varkappa_0}{2}, \quad p(\gamma) = 1 - e^{-2\gamma}.$$

The inner integral over φ reduces at once to a tabulated integral (see, e.g., Ref. 10, formula 446.00), giving the single-integral representation (4.6), which we now write in the form

$$\begin{aligned} C(\varkappa_0) &= \frac{2\pi}{\alpha^2} C_0(\alpha), \\ C_0(\alpha) &= \int_0^\infty \frac{\gamma e^{-2\gamma}}{p^2(\gamma)} \left[1 - \frac{1}{\sqrt{1 + \alpha^2 p^2(\gamma)}} \right] d\gamma \\ &= \int_0^1 \frac{\ln(1-p)}{p^2} \left[\frac{1}{\sqrt{1 + \alpha^2 p^2}} - 1 \right] dp. \end{aligned} \quad (A1)$$

Here we have introduced the new integration variable $p(\gamma) = 1 - e^{-2\gamma}$ in place of γ .

The second step is to calculate $C_0(\alpha)$; owing to the singularities at both the integration limits $p=0$ and $p=1$, it is more convenient to begin by calculating the indefinite integral

$$C_0(\alpha) = J(\alpha, p) \Big|_{p=0}^{p=1}, \tag{A2}$$

where

$$\begin{aligned} J(\alpha, p) &= \int \frac{\ln(1-p)}{p^2} \left[\frac{1}{\sqrt{1+\alpha^2 p^2}} - 1 \right] dp \\ &= [1 - \sqrt{1+\alpha^2 p^2}] \frac{\ln(1-p)}{p} \\ &\quad + \int \frac{1 - \sqrt{1+\alpha^2 p^2}}{p(1-p)} dp; \end{aligned} \tag{A3}$$

we have integrated by parts in (A.3). The last integral can obviously be split into a sum of several tabulated integrals, so that using, for example, formulas 241.01, 380.311, 380.001, and 380.111 from Ref. 10, after elementary but lengthy and tedious calculations, we arrive at the expression

$$\begin{aligned} J(\alpha, p) &= \left(\frac{1 - \sqrt{1+\alpha^2 p^2}}{p} - 1 + \sqrt{1+\alpha^2} \right) \frac{\ln(1-p)}{p} \\ &\quad + \ln(\sqrt{1+\alpha^2 p^2} + 1) - \ln(\sqrt{1+\alpha^2 p^2} - \alpha p) \\ &\quad - \sqrt{1+\alpha^2} \ln[\sqrt{1+\alpha^2 p^2}(\sqrt{1+\alpha^2 p^2} \\ &\quad + \sqrt{1+\alpha^2})], \quad \alpha > 0. \end{aligned}$$

Substituting this result into (A.2) and making use of the fact that the contribution of the entire first term containing $\ln(1-p)$ is zero, we obtain the expression

$$\begin{aligned} C_0(\alpha) &= \ln \frac{\sqrt{1+\alpha^2} + 1}{2} + \alpha \ln(\sqrt{1+\alpha^2} + \alpha) \\ &\quad + \sqrt{1+\alpha^2} \ln \frac{\sqrt{1+\alpha^2} + 1}{2(1+\alpha^2)}, \quad \alpha > 0. \end{aligned} \tag{A4}$$

Together with (A1) this equation gives exactly the expression (4.5) for $C(\kappa_0)$.

¹C. W. F. Everitt, *Report on a Program to Develop a Gyro Test of General Relativity in a Satellite and Associated Control Technology* (Stanford University, Stanford, 1980).

²J. P. Turneare *et al.*, *Adv. Space Res.* **9**, 29 (1989).

³W. R. Smythe, *Static and Dynamic Electricity*, 3rd ed. [McGraw-Hill, New York, 1989; IL, Moscow, 1954].

⁴R. Mittra and S. W. Lee, *Analytical Techniques in the Theory of Guided Waves*, Macmillan, New York (1971); Mir, Moscow, 1974.

⁵A. L. Gol'denveizer, *Izv. Akad. Nauk SSSR Mekh. Tverd. Tela*, No. 3, 5 (1992).

⁶E. V. Galaktionov and E. A. Tropp, *J. Cryst. Growth* **82**, 65 (1987).

⁷R. D. Gregory and F. Y. Wan, *Int. J. Solids Struct.* **21**, 1005 (1985).

⁸I. A. Zino and E. A. Tropp, *Asymptotic Methods for Problems in the Theory of Thermal Conductivity and Thermoelasticity* [in Russian] (Leningrad, 1978).

⁹S. A. Nazarov, *Algebra Anal.* **7**(5), 1 (1995).

¹⁰H. B. Dwight, *Tables of Integrals and Other Mathematical Data*, 4th ed. [Macmillan, New York, 1961; Nauka, Moscow, 1973].

Translated by James S. Wood

Energy loss of relativistic, multiply charged ions in an electron plasma

V. I. Matveev

Scientific-Research Institute of Applied Physics at Tashkent State University, 700005 Tashkent, Uzbekistan

S. G. Tolmanov

Thermal Physics Division of the Academy of Sciences of Uzbekistan, 700135 Tashkent, Uzbekistan

(Submitted August 4, 1995; resubmitted October 23, 1996)

Zh. Tekh. Fiz. **68**, 9–12 (February 1998)

A simple equation is derived for calculating the energy loss of a relativistic, multiply charged ion moving in an electron plasma in the region where the Born approximation fails. The contribution of the energy losses from collisions with solitary electrons is calculated using the exact Dirac equation for relativistic Coulomb scattering. © 1998 American Institute of Physics. [S1063-7842(98)00202-5]

The main factor responsible for slowing down fast charged particles moving in a plasma, as we know, is interaction with electrons. The polarization energy loss of an ion moving in an electron plasma can be calculated on the basis of the dielectric formalism. The equation for the energy loss per unit path length has the form¹

$$\frac{dE}{dx} = \frac{Z^2 e^2}{2\pi^2 iV} \int d^3k \times \left[\frac{\omega}{k^2 \epsilon_l(\mathbf{k}, \omega)} - \frac{\omega(V^2 - \omega^2/k^2)}{c^2(k^2 - \omega^2 \epsilon_{tr}(\mathbf{k}, \omega)/c^2)} \right]. \quad (1)$$

Here E is the energy of the ion, x is its coordinate, Ze is its charge, \mathbf{V} is its velocity, $\epsilon_l(\mathbf{k}, \omega)$ and $\epsilon_{tr}(\mathbf{k}, \omega)$ are the longitudinal and transverse permittivities of the gas, respectively, c is the speed of light, $\omega = \mathbf{k} \cdot \mathbf{V}$, and e is the electron charge. The standard computational scheme used to calculate the polarization energy loss of a fast (but nonrelativistic) ion from Eq. (1) is as follows: a) The second term in the brackets in Eq. (1) corresponds to Čerenkov radiation, which does not occur in the given situation, so that this term can be omitted; b) the integral of the first term, which corresponds to the excitation of longitudinal oscillations in the electron plasma, is computed up to certain maximum values of k_1 corresponding to the minimum impact parameters b_1 at which the electron plasma can begin to be treated as a collective system; the losses in a Maxwellian plasma due to collisions with the plasma as a collective system have been calculated previously,^{2,3} but for the case of nonrelativistic test-particle velocities; calculations of the stopping power of a degenerate electron gas have also been published (see, e.g., Refs. 4–8), where an expression has been obtained for the energy loss in the high-velocity limit independently of the degree of degeneracy:

$$\frac{dE}{dx} = - \frac{4\pi N(Ze^2)^2}{mV^2} \ln \frac{k_1 V}{\omega_p}, \quad (2)$$

where m is the electron mass, $\omega_p = 4\pi Ne^2/m$ is the plasma frequency, and N is the density of the electron plasma; c) for impact parameters smaller than b_1 the energy loss is attrib-

utable to collisions with solitary electrons and can be calculated from the Rutherford equation, which is well known as the exact solution for Coulomb scattering described by the nonrelativistic Schrödinger equation.

The following procedure must be used in calculating the energy loss of a relativistic, multiply charged ion: Steps a) and b) are unchanged, but step c) is modified, requiring that the Dirac equation be solved for relativistic collision velocities; the exact solution of this equation gives the Mott scattering cross section. But if the ion charge Ze is such that $Ze^2/\hbar V \ll 1$, the problem can be restricted to the first Born approximation.

In this article we assume that $Z \gg 1$ (e.g., $Z = 92$ for the bare uranium nucleus), so that $Ze^2/\hbar V \approx 1$ always (even, in particular, for $V \approx c$; i.e., the condition for validity of the Born approximation is violated despite the high velocity), and we take into account the region of solitary collisions by using the exact expression for the cross section.

CONTRIBUTION OF THE REGION OF SOLITARY COLLISIONS

We assume that the ion velocity is much higher than the average thermal speed of the plasma electrons; we can then consider an electron to be at rest before collision. The ion energy loss is expressed in terms of the cross section $\sigma(\epsilon)$ of energy transfer ϵ :

$$\frac{dE}{dx} = -N \int_{\epsilon_{\min}}^{\epsilon_{\max}} \epsilon \sigma(\epsilon) d\epsilon. \quad (3)$$

Next, following Akhiezer *et al.* (Ref. 9, Sec. 82: ‘‘Large momentum transfers’’), in relation to collisions with solitary electrons we regard the incident ion as an infinitely heavy particle, whose motion remains unchanged in collision. The cross section of scattering of an electron initially at rest by an ion moving with constant velocity can then be obtained by transforming to a frame in which the moving electron is scattered by a stationary ion. We denote the corresponding scattering angle by Θ . We can assume⁹ (excluding the range of very high energies) that the energy loss $\epsilon = \epsilon(\Theta)$, where

TABLE I.

Ion energy, MeV/nucleon	Ion charge					
	6	13	29	50	82	92
91.8	1.0311	1.0802	1.2256	1.4168	1.6366	1.6752
183.6	1.0340	1.1002	1.2943	1.6260	2.1293	2.2540
367.2	1.0530	1.1209	1.3678	1.8544	2.5596	3.2137
734.4	1.0575	1.1455	1.4306	2.0585	3.7396	4.4333
1285.2	1.0522	1.1505	1.4673	2.1815	4.3564	5.3506
1836	1.0689	1.1613	1.4846	2.2335	4.6402	5.8127
3672	1.0707	1.1638	1.5025	2.2953	4.9749	6.3560
7344	1.0714	1.1655	1.5064	2.3170	5.5868	6.5818
18360	1.0688	1.1696	1.5137	2.3266	5.1620	6.6521

$$\varepsilon(\Theta) = \frac{2mV^2}{(1-\beta^2)} \sin^2 \frac{\Theta}{2}, \quad \beta = V/c, \quad (4)$$

and the values ε_{\max} and ε_{\min} are attained at $\Theta = \pi$ and $\Theta = \Theta_{\min}$, respectively. As a result, Eq. (3) can be rewritten in the form¹⁰

$$\frac{dE}{dx} = -2N\pi \frac{(Ze^2)^2}{mV^2} \int_{\Theta_{\min}}^{\pi} \frac{\sigma(\Theta)}{\sigma_R(\Theta)} \cot \frac{\Theta}{2} d\Theta, \quad (5)$$

where $\sigma(\Theta)$ is the cross section of scattering of an electron by a stationary ion of charge Z for an arbitrary electron velocity V ; this cross section has been determined previously^{11,12} from the exact solution of the Coulomb scattering problem for the Dirac equation; $\sigma_R(\Theta)$ is the Rutherford cross section

$$\sigma_R = \frac{(Ze^2)^2(1-\beta^2)}{m^2c^4\beta^4(1-\cos \Theta)^2}. \quad (6)$$

According to Refs. 11 and 12, the ratio of the exact cross section to the Rutherford cross section $\sigma(\Theta)/\sigma_R(\Theta) \rightarrow 1$ in the limit $\Theta \rightarrow 0$, so that for small Θ_{\min} the integral (5) can be written in the form (cf. Ref. 10)

$$\frac{dE}{dx} = -4\pi \frac{N(Ze^2)^2}{mV^2} \ln \frac{2}{a(Z,V)\Theta_{\min}}. \quad (7)$$

The function $a(Z,V)$ takes into account the difference between the cross section of scattering of an electron by a multiply charged ion at relativistic velocities and the Ruth-

TABLE II.

Ion energy, MeV/nucleon	Ion charge					
	6	13	29	50	82	92
91.8	1.0300	1.0726	1.2118	1.4206	1.6399	1.6621
183.6	1.0431	1.1003	1.2942	1.6212	2.1082	2.2280
367.2	1.0562	1.1257	1.3746	1.8579	2.8311	3.1721
734.4	1.0658	1.1419	1.4322	2.0787	3.7137	4.4020
1285.2	1.0701	1.1477	1.4577	2.2099	4.3581	5.3392
1836	1.0717	1.1494	1.4666	2.2669	4.6712	5.8042
3672	1.0731	1.1505	1.4747	2.3291	5.0395	6.3584
7344	1.0736	1.1507	1.4773	2.3527	5.1865	6.5816
18360	1.0738	1.1508	1.4782	2.3612	5.2407	6.6643

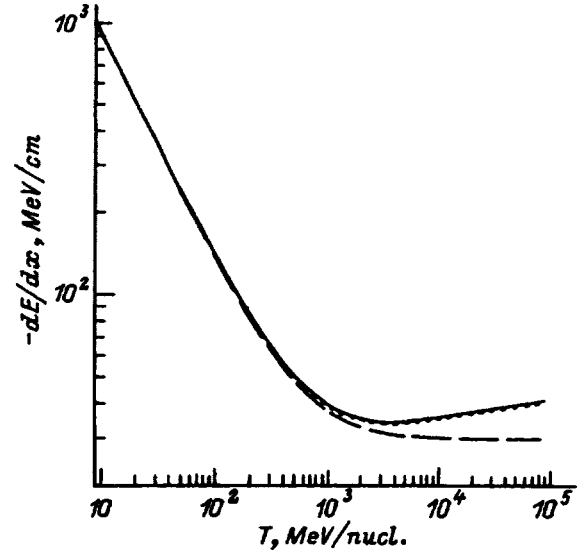


FIG. 1. $Z=6$.

erford cross section [i.e., $a(Z,V) \rightarrow 1$ as $\alpha = Z/c \rightarrow 0$ and $\beta \rightarrow 0$] and is determined from the following relation, taking into account the smallness of Θ_{\min} :

$$a(Z,V) = \lim_{\Theta_{\min} \rightarrow 0} \frac{2}{\Theta_{\min}} \times \exp \left\{ -\frac{1}{2} \int_{\Theta_{\min}}^{\pi} \frac{\sigma(\Theta)}{\sigma_R(\Theta)} \cot(\Theta/2) d\Theta \right\}, \quad (8)$$

which can be used in conjunction with data from Ref. 11 on the Mott cross section to find $a(Z,V)$ numerically. The relation between Θ_{\min} and k_1 is given by the equation

$$\Theta_{\min} = \frac{\hbar k_1}{p}, \quad p = \frac{mV}{\sqrt{1-\beta^2}}.$$

Consequently, the Coulomb logarithm in Eq. (7) has the form

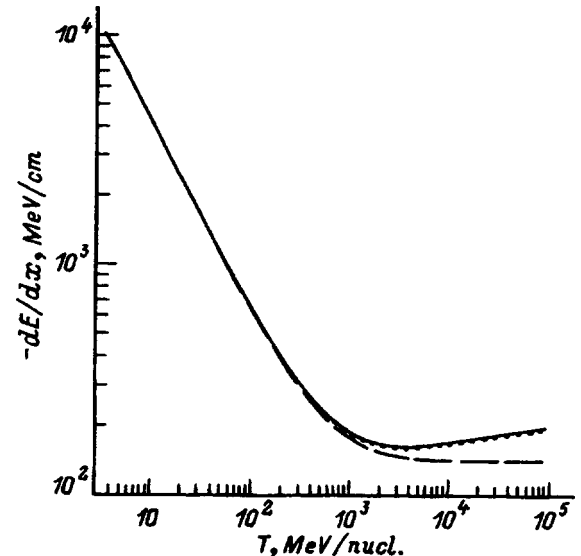


FIG. 2. $Z=13$.

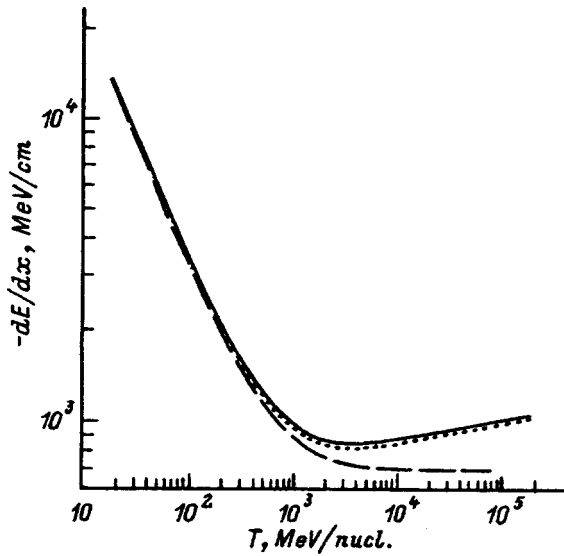


FIG. 3. Z=29.

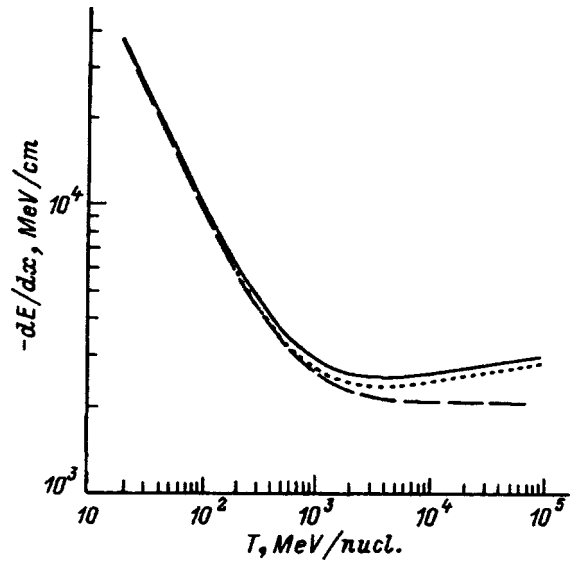


FIG. 4. Z=50.

$$\ln \Lambda = \ln \frac{2}{a(Z, V) \Theta_{\min}} = \ln \frac{2mV}{\hbar k_1 \sqrt{1 - \beta^2} a(Z, V)}$$

It is advantageous to introduce the function $f(Z, V)$, which is related to $a(Z, V)$ by the equation

$$f(Z, V) = \frac{1}{a(Z, V)} \exp \frac{\beta^2}{2} \tag{9}$$

Invoking the data of numerical calculations¹¹ for the ratio of the cross sections σ/σ_R , we can approximate $f(Z, V)$ as follows [the approximation for $a(Z, V)$ proposed in Ref. 10 yields less accurate values of $f(Z, V)$]:

$$f(Z, V) = 1 + [0.222592\beta - 0.042948\beta^2 + (0.6016 + 5.15289\beta - 3.73293\beta^2)\alpha - (0.52308 + 5.71287\beta - 8.11358\beta^2)\alpha^2]^2 \tag{10}$$

Consequently, the energy loss of a relativistic, multiply charged ion in collisions with solitary electrons is described by the equation

$$\frac{dE}{dx} = - \frac{4\pi N(Ze^2)^2}{mV^2} \left[\ln \frac{2mVf(Z, V)}{\hbar k_1 \sqrt{1 - \beta^2}} - \frac{\beta^2}{2} \right] \tag{11}$$

To test the validity of the approximation (10), the values of $f(Z, V)$ calculated numerically from the data of Ref. 11 are given in Tables I and II [Table I gives the values from Eqs. (8) and (9) and Table II gives the results of Eq. (10) for the same values of the ion charge and energy, where the first column gives the energy of a multiply charged ion in MeV/nucleon, and the remaining columns give the values of $f(Z, V)$ for ions with charges (in consecutive order) $Z=6, 13, 29, 50, 80,$ and 92]. It is evident from the tables that the proposed approximation (10) is good, at least within the limits of variation of Z and V for which the data of Ref. 11 are given.

Summing Eqs. (2) and (11), we obtain the total energy loss of a relativistic, multiply charged ion per unit length in motion through an equilibrium electron plasma:

$$\frac{dE}{dx} = - \frac{4\pi N(Ze^2)^2}{mV^2} \left[\ln \frac{2mV^2 f(Z, V)}{\hbar \sqrt{1 - \beta^2} \omega_p} - \frac{\beta^2}{2} \right] \tag{12}$$

Setting $f(Z, V) = 1$ in Eq. (12), we obtain an equation that corresponds to stopping theory and can be obtained from the standard computational scheme when the contribution of the region of solitary collisions is taken into account in the first Born approximation,

$$\frac{dE}{dx} = - \frac{4\pi N(Ze^2)^2}{mV^2} \left[\ln \frac{2mV^2}{\hbar \sqrt{1 - \beta^2} \omega_p} - \frac{\beta^2}{2} \right] \tag{13}$$

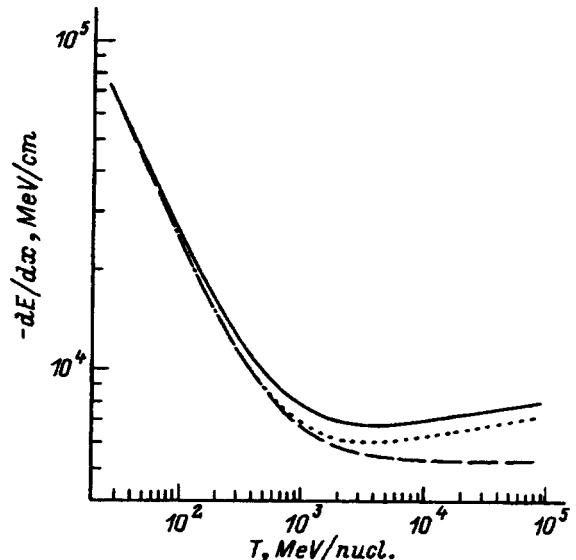


FIG. 5. Z=80.

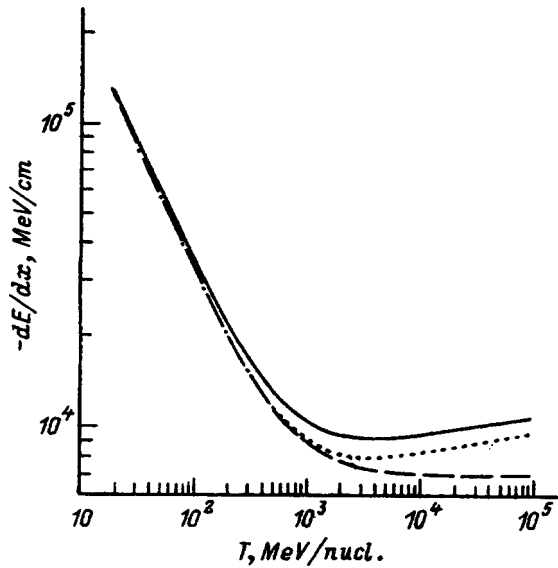


FIG. 6. $Z=92$.

We also give the nonrelativistic limit ($\beta \rightarrow 0, \alpha \rightarrow 0$) of Eq. (12) [which is derived with allowance for relation (9) and the fact that $a(Z, V) \rightarrow 1$ as $\beta \rightarrow 0$ and $\alpha \rightarrow 0$]:

$$\frac{dE}{dx} = - \frac{4\pi N(Ze^2)^2}{mV^2} \ln \frac{2mV^2}{\hbar\omega_p}. \quad (14)$$

It follows from a comparison of Eqs. (12) and (13) that our function $f(Z, V)$ introduced above describes the deviations (occurring for relativistic, high-charge ions) from stopping theory, which uses the first Born approximation. For low-charge ions the values of $f(Z, V)$ are close to unity, and allowing for the fact that the function f enters into Eq. (12) in the argument of the logarithm, our results for low Z do not deviate from the Born approximation, Eq. (13), whereas at high Z the deviations become appreciable; finally, in the nonrelativistic case Eq. (12) goes over to the well-known¹

result: Eq. (14). This behavior of Eq. (12) is illustrated in Figs. 1–6. Also shown in these figures is the dependence of the energy loss $|dE/dx|$ (MeV/cm) of relativistic ions for charges $Z=6, 13, 29, 50, 80, 92$ (it is assumed for illustration that $\omega_p=0.5$ a.u.=13.605 eV) on the ion energy T (MeV/nucleon). The solid curves represent the results of exact calculations from Eq. (12), the dashed curves represent the “Born approximation” (13), and the dotted curves represent the nonrelativistic limit (14). It is evident from the figures that the corrections for exact inclusion of the ion field increase as the ion charge increases, attaining (e.g.) approximately 15% for $Z=92$.

In summary, our Eq. (12) derived above can be used to calculate the energy losses of relativistic, high-charge ions in an electron plasma when the Born approximation is inapplicable. For fast, low-charge ions our results go over numerically to the Born approximation, and Eq. (12) goes over to the standard¹ nonrelativistic limit (14).

¹ *Plasma Electrodynamics*, edited by A. I. Akhiezer, I. A. Akhiezer, R. V. Polovin *et al.* [Pergamon Press, Oxford-New York, 1975; Nauka, Moscow, 1974].

² T. Hamada, *Aust. J. Phys.* **31**, 291 (1978).

³ R. M. May, *Aust. J. Phys.* **22**, 687 (1969).

⁴ E. Fermi and E. Teller, *Phys. Rev.* **72**, 399 (1947).

⁵ A. I. Larkin, *Zh. Éksp. Teor. Fiz.* **37**, 264 (1959) [*Sov. Phys. JETP* **10**, 186 (1959)].

⁶ R. H. Ritchie, *Phys. Rev.* **114**, 644 (1959).

⁷ Yu. N. Yavlinkii, *Zh. Éksp. Teor. Fiz.* **80**, 1623 (1981) [*Sov. Phys. JETP* **53**, 835 (1981)].

⁸ D. G. Yakovlev and S. S. Kotelnikov, *Zh. Éksp. Teor. Fiz.* **84**, 1348 (1983) [*Sov. Phys. JETP* **57**, 781 (1983)].

⁹ A. I. Akhiezer, E. M. Lifshitz, and L. P. Pitaevskii, *Quantum Electrodynamics*, 3rd ed., rev. (Nauka, Moscow, 1989).

¹⁰ V. I. Matveev and S. G. Tolmanov, *Zh. Éksp. Teor. Fiz.* **107**, 1780 (1995) [*JETP* **80**, 989 (1995)].

¹¹ J. A. Doggett and L. V. Spenser, *Phys. Rev.* **103**, 1597 (1956).

¹² A. I. Akhiezer and V. B. Berestetskii, *Quantum Electrodynamics* (Wiley, New York, 1965) [Russ. original, 3rd ed., Nauka, Moscow, 1969].

Translated by James S. Wood

Chemical ionization of hydrogen halide molecules in collision with metastable helium atoms

G. V. Klement'ev, V. A. Kartoshkin, and V. D. Mel'nikov

A. F. Ioffe Physicotechnical Institute, Russian Academy of Sciences, 194021 St. Petersburg, Russia

(Submitted January 30, 1997)

Zh. Tekh. Fiz. **68**, 13–15 (February 1998)

An anomaly of the temperature dependence of the cross section for chemical ionization of HBr molecules by metastable helium atoms $\text{He}^*(2^3S_1)$ is discovered. It is shown that the interaction anisotropy induced by rotation of the HBr molecule has a significant influence on the formation of the anomaly. © 1998 American Institute of Physics. [S1063-7842(98)00302-X]

We have previously¹ determined experimentally the temperature dependence of the cross section of chemical ionization of hydrogen chloride molecules by metastable triplet helium ions. In the interval 130 K–300 K we discovered a behavior not previously observed for any system: a sharp increase in the total chemical ionization cross section as the temperature was lowered [$\sigma(T) \sim T^{-1.4}$]. We hypothesized that anisotropy of the interaction plays a significant role, manifesting itself differently at different temperatures by virtue of the rotation of HCl molecules. It is only natural, therefore, to have an interest in continuing the investigation of the interaction of metastable helium atoms with such diatomic molecules, which have, first, a strong chemical bond and, second, a fairly high (of the order of 10 cm^{-1}) rotational constant R . In the present paper we have chosen HBr as the molecule of study. We determine the temperature dependence of the cross section of chemical ionization of this molecule by $\text{He}^*(2^3S_1)$ atoms in the temperature interval 220–300 K and offer an explanation of this dependence, taking into account the influence of rotation of the hydrogen halide molecule.

When a $\text{He}^*(2^3S_1)$ atom collides with a hydrogen bromide molecule, the principal role in the quenching of metastable excitation is played by Penning ionization, with the formation of a helium atom in the ground state, a HBr molecular ion, and an electron, and by associative ionization, with the formation of hydrogen or bromine atoms both directly, when H , Br^+ (or H^+ , Br), and an electron are formed, and also by way of restructuring, when HeBr^+ , H (or HeH^+ , Br), and an electron are formed.

In our experiment we have determined the total cross section of the inelastic process of chemical ionization. For this purpose a gas discharge was produced in an absorption chamber containing a He–HBr mixture, and the metastable triplet helium atoms were optically oriented in a longitudinal magnetic field with the use of circularly polarized radiation from a helium lamp. The widths of the magnetic resonance lines of the helium atoms in the metastable triplet state were determined, and the linewidth contribution due to the admixture of hydrogen bromide was identified by a procedure described in detail in Ref. 2. The absolute error of determination of the chemical ionization rate constant $C(T)$ did not

exceed 20%, and the relative error (with variation of the temperature) was at least a factor of two lower, because it is largely devoid of the error associated with inaccuracy in the determination of the partial pressure of hydrogen bromide. The discharge intensity was maintained as low as possible to minimize the difference of the rotational temperature from the temperature of the absorption chamber. A set of absorption chambers with HBr pressures of 5×10^{-4} torr and 7×10^{-4} torr (at 300 K) was used. The resulting experimental dependence is shown in Fig. 1. At $T=220$ K the rate constant has the value $C = 120 \times 10^{-11} \text{ cm}^3 \cdot \text{s}^{-1} \pm 20\%$, which gives the cross section $\sigma = 109 \text{ \AA}^2$ (or 390 a.u.). At $T=300$ K the rate constant drops to $85 \times 10^{-11} \text{ cm}^3 \cdot \text{s}^{-1} \pm 20\%$, which corresponds to $\sigma = 66 \text{ \AA}^2$ (or 240 a.u.). The second rate constant can be compared with the previously known value obtained in an experiment with a decaying plasma: $C = 100 \times 10^{-11} \text{ cm}^3 \cdot \text{s}^{-1} \pm 30\%$ (Ref. 3). Consequently, in the interval 220–300 K the cross section can be written in the form $\sigma(T) \sim T^{-1.5}$, i.e., as in the case of the system $\text{He}^*(2^3S_1)$ -HCl, the temperature dependence is very steep.

The following considerations must be borne in mind in the interpretation of the experimental results: First, the kinetic energy of the atomic particles in the gas discharge differs, following a Maxwellian distribution; second, rotational motion in the HBr molecule imparts anisotropy to the interaction of these molecules with metastable helium atoms, a feature that is especially prominent for a low rotational quantum number j .

Let the relative motion of two atomic particles depend on the spherically symmetric effective potential

$$U_{\text{eff}} = \frac{B}{r^n} - \frac{C}{r^6} + \frac{l(l+1)}{2\mu i^2}, \quad (1)$$

where the atomic system of units is used, r is the distance between the particles, μ is the reduced mass, n , B , and C are constants, and the quantum number l corresponds to the relative motion of the particles.

A detailed investigation of the behavior of the chemical-ionization cross section at low energies of relative motion for the potential (1) with $n=10$ is reported in Ref. 4. The characteristic decrease in the cross section as the energy is in-

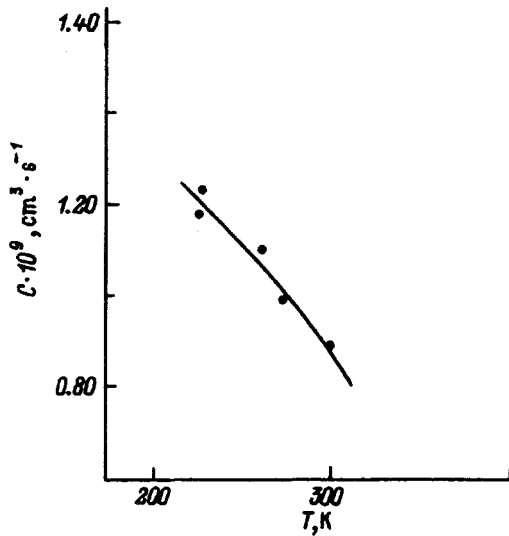


FIG. 1. Temperature dependence of the rate constant of chemical ionization of hydrogen bromide by metastable helium atoms.

creased [dependence of the type $\sigma(E) \sim E^{-5/6}$] takes place when the effective potential (1) has a distinct minimum (Fig. 2), as is clearly the case for the partial waves

$$\left(l + \frac{1}{2}\right) < \left(l + \frac{1}{2}\right)_{\text{lim}} = 0.74 \cdot C \left(\frac{\mu}{B}\right)^{1/2}, \quad (2)$$

where the height of the potential hump for the limiting wave is

$$U_{\text{max}}^{\text{lim}} = 0.056 \cdot C^{5/2} \cdot B^{-3/2}. \quad (3)$$

As long as condition (2) is satisfied, the position of the minimum depends very little on the mode number (index) of the partial wave:

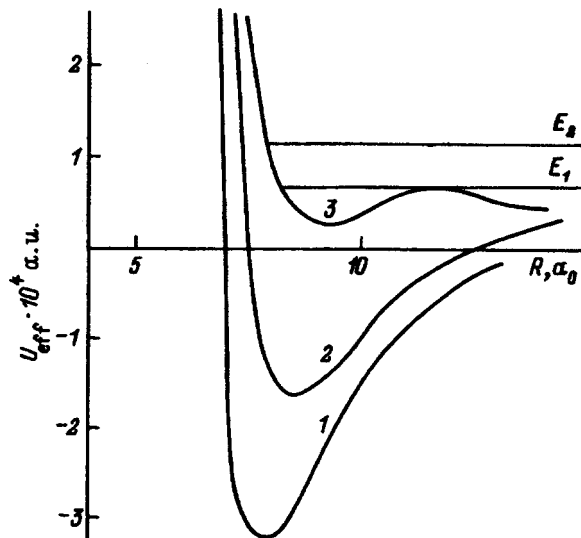


FIG. 2. Lennard-Jones potential with parameters $B = 1.4 \times 10^6$, $C = 7 \times 10^2$, and $\mu = 7 \times 10^3$ for three values of the quantum number l ($l_1 = 0$, $l_2 = 8$, and $l_3 = 20$). Here E_1 and E_2 are collision energies, with E_1 corresponding to the height of the potential barrier.

$$r_{\text{min}} = \left(\frac{5B}{3C}\right)^{1/4} \left(1 + \frac{y}{16}\right), \quad (4)$$

where

$$y = \frac{10B(l + (1/2))^2}{9\mu C^2}. \quad (5)$$

For a kinetic energy E of relative motion of the atomic particles the distance of closest approach of the particles (r_0) is given by the equation

$$r_0 = \left(\frac{B}{C}\right)^{1/4} \left[1 + \frac{B(l + (1/2))^2}{8\mu C^2}\right] \left(1 - 0.015 \frac{E}{U_{\text{max}}^{\text{lim}}}\right), \quad (6)$$

i.e., its variation is small for small values of E and values of l satisfying condition (2).

For the system $\text{He}^*(2^3S_1)\text{-HBr}$, based on the rules for averages and data from Refs. 5 and 6, the parameters of the spherically symmetric potential (1) have the values

$$B = 1.4 \times 10^6, \quad C = 720. \quad (7)$$

The limiting value of the quantum number l , according to (2), is then $l_{\text{lim}} = 36$, and $U_{\text{max}}^{\text{lim}} = 6.3 \times 10^{-4}$. At a given temperature T , therefore, for particles with energies lower than $U_{\text{max}}^{\text{lim}}$ the particles come quite close together, and an energy dependence with a power exponent close to $s = 5/6$ is established, while for higher-energy particles s is substantially lower. Consequently, to account for the significantly larger experimentally determined value $s = 1.5$, other attributes of the system must be taken into account, specifically those induced by rotation of the HBr molecule. Foremost is interaction anisotropy, which is manifested as a dependence of the parameters of the potential (1) and the autoionization width $\Gamma(R)$ on the angle θ between the axis of the molecule and the line joining the atomic particles. This dependence has comparatively little influence on the position and height of the maximum of the effective potential (1), but has a far stronger influence on the position and especially the depth of the minimum of this potential, and, finally, the position r_0 changes considerably (by 1–2 a.u.), so that the autoionization width $\Gamma(R)$ can increase severalfold if the exponential character of the dependence of this quantity on the distance is taken into account. However, interaction anisotropy appears only when the rotation of the molecule is fairly slow:

$$\frac{\alpha}{2R(j + 1/2)} > \frac{\Delta r}{v}, \quad (8)$$

where α is the admissible angle of rotation of the molecule during effective interaction (near the turning point for a variation of the distance Δr by 1 a.u.); for our example we set this angle equal to $\pi/4$; R is the rotational constant, j is the rotational quantum number, and v is the average relative velocity near the turning point.

Taking into account the value of the rotational constant R for HBr, we can assume that far more effective interaction (chemical ionization) due to the closer approach of the atomic particles takes place in the experimentally investigated temperature interval as long as the number j is not

higher than 3 or 4. Inasmuch as the fraction of such molecules decreases as the temperature increases, the end result will be an appreciable increase in s , consistent with the experimental results. Indeed, the fraction of such molecules

$$\beta = 1 - e^{-Rj(j+1)/kT} \quad (9)$$

is equal to 0.66 at $T=220$ K and has a considerably lower value of 0.55 at $T=300$ K; this difference is fully capable of providing an increase in the exponent by 0.6 in the presence of the steep dependence of the autoionization width on the distance. Of course, the possibility of a deviation of the rotational temperature from the temperature of the absorption chamber must be considered in explaining the experimental dependence.

In closing, it should be noted that the above-indicated attributes of the chemical ionization of hydrogen bromide will also produce major changes in the formation of polarized atoms during chemical ionization. For example, pro-

cesses leading to the formation of Br atoms are more likely to occur in the formation of atoms during chemical ionization.

This work has received support from the Russian Fund for Fundamental Research (Grant No. 95-02-04116-a).

¹V. A. Kartoshkin, G. V. Klement'ev, and V. D. Mel'nikov, *Opt. Spektrosk.* **71**, 929 (1991) [*Opt. Spectrosc. (USSR)* **71**, 535 (1991)].

²G. V. Klement'ev, V. D. Mel'nikov, and V. A. Kartoshkin, *Zh. Éksp. Teor. Fiz.* **77**, 52 (1979) [*Sov. Phys. JETP* **50**, 25 (1979)].

³J. A. Bush, M. McFarland, B. L. Albritton, and A. F. Schmeltekopf, *J. Chem. Phys.* **58**, 4020 (1973).

⁴V. G. Klement'ev and V. D. Mel'nikov, *Opt. Spektrosk.* **75**, 1177 (1993) [*Opt. Spectrosc. (Russia)* **75**, 692 (1993)].

⁵J. O. Hirschfelder, C. F. Curtiss, and R. B. Bird, *Molecular Theory of Gases and Liquids* (Wiley, New York, 1954).

⁶B. J. Garrison, W. H. Miller, and H. F. Schaefer, *J. Chem. Phys.* **59**, 3193 (1973).

Translated by James S. Wood

Possibility of the levitation of droplets in the atmosphere when they are charged by induction in an electric field under nonuniform evaporation conditions

V. A. Saranin

V. G. Korolenko *Glazov State Pedagogical Institute, 427600 Glazov, Russia*
 (Submitted May 28, 1996; resubmitted January 22, 1997)
Zh. Tekh. Fiz. **68**, 16–21 (February 1998)

The behavior of droplets in the atmosphere in an electric field has important bearing on the theory of thunderstorms. One of the possible mechanisms by which droplets become charged—the induction mechanism in the presence of nonuniform evaporation—is investigated in greater detail on the basis of recent experimental results (V. A. Saranin, *Zh. Tekh. Fiz.* **65**(6), 21 (1995) [*Tech. Phys.* **40**, 332 (1995)]). © 1998 American Institute of Physics. [S1063-7842(98)00402-4]

It has been established experimentally¹ that a nonuniformly evaporating water droplet in an electric field acquires an electric charge such that, on the one hand, the Coulomb force on the droplet is sufficient to overcome the force of gravity and, on the other, the droplets remain in equilibrium (in the sense that they preserve their shape). As a result, droplets for which these conditions are met simultaneously move upward. In the theoretical analysis of Vereshchagin *et al.*¹ the droplet charging mechanism is not precisely determined, and it is assumed that the charge on a droplet is independent of the field.

GENERAL PRINCIPLES AND STATEMENT OF THE PROBLEM

It is generally known that charge separation in a conductor in an applied external field and screening of the conductor take place in a time of the order of the relaxation time

$$\tau_1 = \frac{\epsilon_0 \epsilon}{\sigma},$$

where σ is the electrical conductivity of the medium, ϵ is its dielectric constant, and $\epsilon_0 = 8.85 \times 10^{-12}$ F/m.

The relaxation time for distilled water is $\tau_1 \approx 10^{-5}$ s. The charges are concentrated in a thin diffusion layer, whose thickness depends on the Debye–Hückel screening radius:

$$h_e = \sqrt{\frac{\epsilon_0 \epsilon_k T b_e}{e \sigma}},$$

where e is the ion charge, b_e is the ion mobility, and k is the Boltzmann constant.

Setting $T = 300$ K, $b_e = 10^{-7}$ m²/(s·V), and $e = 1.6 \times 10^{-19}$, for distilled water we obtain $h_e \sim 10^{-7}$ m. In spherical droplets of radius ~ 1 mm a spherical layer of thickness h_e can be regarded as plane, and the bulk density of charges in the liquid near the surface can be written in the form

$$\rho_e = \text{div}(\epsilon_0 \epsilon \mathbf{E}) \approx \frac{\epsilon_0 E_{1r} - \epsilon_0 \epsilon E_{2r}}{\Delta r} = \frac{\epsilon_0 E_r}{h_e}. \quad (1)$$

We assume that the droplet is conducting and that its interior is field-free, $E_{2r} = 0$. In this case, if a spherical droplet of radius R has a charge q and is situated in a homogeneous electric field of strength E_0 , then on its surface one has²

$$E_r = 3E_0 \cos \Theta + \frac{q}{4\pi \epsilon R^2}, \quad (2)$$

where Θ is the polar angle.

In the hierarchy of characteristic times, the relaxation time τ_1 is the shortest (indeed, as will be shown below, for example, the droplet charging times under various conditions are $\tau_2 \sim \tau_3 \sim 1$ s and $\tau_5 \sim 0.1$ s, and the characteristic relaxation time to steady-state convective diffusion is $\tau_4 \sim 10^{-2}$ s). In all transient processes, therefore, we assume steady-state charge and field distributions in the droplet. The longest time of the transient processes of interest here is of the order of a few seconds. This means that the variation of the mass of the droplet during its evaporation can be disregarded. In addition, we assume that it has a spherical shape, and we ignore all other droplet charging mechanisms except as a result of the evaporation of ions. If the liquid evaporates from the surface, the mass flow through unit surface is

$$j_m = \rho_l v_e. \quad (3)$$

In a reference frame attached to the surface we can assume that the liquid itself moves toward the surface with a velocity

$$v_e = j_m / \rho_l.$$

If the liquid is charged, the electric current density due to this liquid motion in the absence of appreciable slip of the ions relative to the neutral medium is

$$j_n = \rho_e v_e = \frac{\rho_e}{\rho_l} j_m = \frac{\epsilon_0 E_r j_m}{\rho_l h_e}. \quad (4)$$

The charge of the droplet then varies with time according to the law

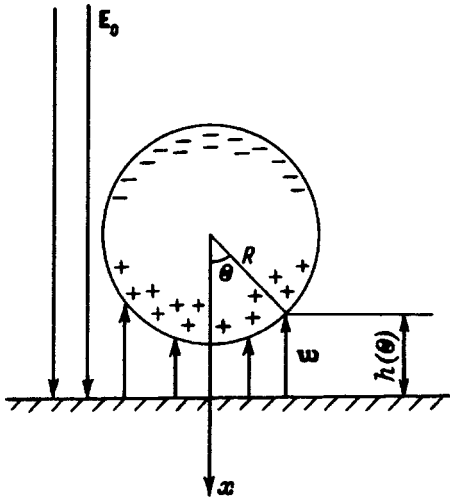


FIG. 1. Evaporating, electrically conducting, spherical droplet with a heat flux w directed onto it from below, in an electric field E_0 .

$$\frac{dq}{dt} = - \oint j_n dS = - \frac{\epsilon_0}{\rho_{nlc} h_e} \oint E_r j_m dS. \quad (5)$$

Obviously, for uniform evaporation from the entire surface we have $j_m = \text{const}$ and, hence,

$$\frac{dq}{dt} \sim q - q(t=0) = 0.$$

CHARGING OF A DROPLET DURING EVAPORATION IN FILM BOILING

Let us first consider the case of evaporation observed in the experiment of Ref. 1, viz., the evaporation of water droplets situated on a vapor cushion above a hot heat-transfer surface. The evaporation took place in a nearly homogeneous external electric field (Fig. 1). We assume that a uniform heat flux of density w is incident on the bottom surface of the droplet from the heat-transfer surface. The mass flux density (assuming that all the heat goes for evaporation) is then equal to

$$j_m = w_n / \kappa = w \cos \Theta / \kappa, \quad 0 \leq \Theta \leq \frac{\pi}{2};$$

$$j_m = 0, \quad \Theta > \frac{\pi}{2},$$

where κ is the specific heat of vaporization. If we assume that the principal heat-transfer mechanism is heat conduction, we have

$$w = \lambda \frac{\Delta T}{h(\Theta)} = \lambda \frac{\Delta T}{h_m + R(1 - \cos \Theta)}, \quad (6)$$

where λ is the thermal conductivity of water vapor, ΔT is the temperature difference between the surface of the droplet and the heat-transfer surface, and h_m is the shortest distance between the surfaces.

The substitution of Eq. (2) and j_m into (5) gives an equation for the charge Z :

$$\frac{dZ}{dt} = - \frac{\lambda \Delta T}{2 \rho_l h_e \kappa R} \int_0^{\pi/2} \frac{(\cos \Theta + Z) \cos \Theta \sin \Theta d\Theta}{r^{-1} + (1 - \cos \Theta)}. \quad (7)$$

Here Z and r are dimensionless quantities, defined as $Z = q/12\pi\epsilon_0 E_0 R^2$ and $r = R/h_m$. We denote the integral in Eq. (7) by J . It is readily calculated after a change of variables. We obtain

$$J = (Z + \gamma)(\gamma \ln(1+r) - 1) - 1/2, \quad \gamma = 1 + r^{-1}.$$

We then have the following equation in place of (7):

$$\frac{dZ}{dt} = - \frac{1}{\tau_2} (Z + Z_m). \quad (8)$$

Here

$$Z_m = \gamma - \frac{1}{2(\gamma \ln(1+r) - 1)},$$

$$\tau_2 = \frac{2 \rho_{nlc} h_e \kappa R}{\lambda \Delta T (\gamma \ln(1+r) - 1)}. \quad (9)$$

The solution of Eq. (8) has the form

$$Z = -Z_m(1 - \exp\{-t/\tau_2\}). \quad (10)$$

We see that Z_m has the meaning of the maximum charge acquired by the droplet, and τ_2 is the charging time. We now make some estimates. For $r \approx 1$ we have $Z_m \approx 0.71$, whereas for $r \gg 1$ we obtain $Z_m \approx 1$. We note, first of all, that a polarized particle in an electric field in an ionic medium acquires a maximum charge $q_m = 12\pi\epsilon_0 E_0 R^2$, which in dimensionless units corresponds exactly to $Z_m = 1$; second, the proportionality $q_m \propto E_0 R^2$ is entirely characteristic of induction charging mechanisms.^{4,5}

In estimating the charging time τ_2 , we choose the thermal conductivity of steam $\lambda = 2.4 \times 10^{-2}$ W/m·K and the temperature difference $\Delta T = 100$ K. Then from Eq. (9) for $r = 1$ mm and $R = 2$ mm we obtain $\tau_2 \approx 1$ s. This estimate agrees qualitatively with the experiments.¹ When a high voltage is suddenly applied, the droplets rise almost instantaneously to the upper electrode.

We now determine the field at which a droplet of radius 2 mm acquiring a maximum charge q_m can rise:

$$q_m E_0 \geq mg.$$

Accordingly, for water droplets we have

$$E_0 \geq \frac{1}{3} \sqrt{\frac{R \rho_l g}{\epsilon_0}} \approx 5 \times 10^5 \text{ V/m}.$$

This result is also consistent with the experimental work.¹

CHARGING OF DROPLETS DURING EVAPORATION IN CONVECTIVE DIFFUSION

The most interesting phenomenon is the occurrence of the investigated droplet charging mechanism in nature, i.e., the falling of droplets in the atmosphere. To analyze this problem, we first consider the opposite extreme case of evaporation, viz., the evaporation of a droplet moving at low velocities relative to air. The problem of the steady-state

convective diffusion of matter from the surface of a droplet falling in a different liquid at low Reynolds numbers has been solved previously.³ We therefore use the results of Ref. 3. For the mass flux density we then have

$$j_m = \rho_{\text{sat}}(1 - \varphi) \sqrt{\frac{3D\eta\nu}{2\pi R(\eta + \eta_1)}} \frac{(1 + \cos \Theta)}{\sqrt{2 + \cos \Theta}}. \quad (11)$$

Here ρ_{sat} is the saturated vapor density on the surface of the droplet, φ is the air humidity, d is the vapor diffusion coefficient, ν is the rate of descent of the droplet relative to the air, and η and η_1 are the viscosities of air and water, respectively. Equation (5) is now transformed as follows:

$$\frac{dZ}{dt} = -\frac{1}{\tau_3} \sqrt{\text{Re}}(1 - \varphi)J_1, \quad (12)$$

$$\tau_3 = \frac{4h_e\rho_l R}{\rho_{\text{sat}}} \sqrt{\frac{\pi(\eta + \eta_1)}{3D\nu\eta}},$$

where ν is the kinematic viscosity of air, and Re is the Reynolds number defined in terms of the droplet diameter; the integral J_1 in this case is equal to

$$J_1 = \int_0^\pi \frac{(1 + \cos \Theta)(\cos \Theta + Z)}{\sqrt{2 + \cos \Theta}} \sin \Theta d\theta$$

$$= \frac{4}{3}(Z + Z_m), \quad Z_m = \frac{6}{5} \left(\sqrt{3} - \frac{3}{2} \right) \approx 0.24. \quad (13)$$

Consequently, if the values of Re and φ are fixed in Eq. (12), the charge of the droplet is again given by an equation of the type (8), but with different values of the maximum charge Z_m and the relaxation (charging) time τ_3 . For $\text{Re}=1$, $\varphi=0.5$, $R=1$ mm, $\rho_{\text{sat}}=1.7 \times 10^{-2}$ kg/m³, $D=2.2 \times 10^{-5}$ m²/s, $\eta=1.8 \times 10^{-5}$ Pa·s, $\eta_1=10^{-3}$ Pa·s, and $\nu=1.5 \times 10^{-5}$ m²/s the value obtained for the charging time is $\tau_3=3.7$ s. The velocity of the droplet varies as it descends in the atmosphere, and evaporation is therefore a transient process. Let us estimate the relaxation time to steady-state convective diffusion τ_4 . The following relation has been derived³ for estimating this time:

$$\frac{\nu \tau_4}{R} \approx \left(\frac{\nu}{\pi D} \right)^{1/3}. \quad (14)$$

In the initial stages of descent we can assume that $\nu \approx g\tau_4$. For $R=1$ mm we then have

$$\tau_4 \approx \left(\frac{R}{g} \left(\frac{\nu}{\pi D} \right)^{1/3} \right)^{1/2} \approx 7.0 \times 10^{-3} \text{ s}.$$

Inasmuch as the characteristic relaxation times of the velocity are much longer than the above-estimated time, convective diffusion for a variable droplet velocity can be regarded as a quasisteady-state process, and the wind factor $\sqrt{\text{Re}}$ can be retained as a constant in the charge equation (12).

Studies of the evaporation of droplets in an airstream have shown that the wind factor $\sqrt{\text{Re}}$ remains invariant over a wide range of Reynolds numbers. For example, the Fresling equation often used for the rate of evaporation of a moving droplet has the form^{5,6}

$$\frac{dm}{dt} = \left(\frac{dm}{dt} \right)_0 + \left(\frac{dm}{dt} \right)_0 \beta \sqrt{\text{Re}} \text{Sc}^{1/3},$$

$$\left(\frac{dm}{dt} \right)_0 = -4\pi R D \rho_{\text{sat}}(1 - \varphi). \quad (15)$$

The Schmidt number $\text{Sc} = \nu/D$ for air can be taken equal to unity; β is the Fresling factor, which we set equal to $\beta=0.276$ (Ref. 6). The first term in Eq. (15) represents the mass variation associated with uniform evaporation, and the second term represents the same for nonuniform evaporation; consequently,

$$\frac{dq}{dt} \sim \left(\frac{dm}{dt} \right)_0 \beta \sqrt{\text{Re}} \sim \oint j_n dS.$$

Taking Eqs. (8), (12), and (13) into account as well, we can propose the following phenomenological equation for the charging of a droplet as it descends and evaporates non-uniformly in air in an electric field:

$$\frac{dZ}{dt} = -\frac{1}{\tau_5}(1 - \varphi)\sqrt{\text{Re}}(Z + Z_m), \quad \text{Re} = \frac{d2Rv}{\nu}, \quad (16)$$

where v is the droplet velocity in a reference frame attached to the air, and τ_5 has the significance of a characteristic droplet charging time.

Making use of the expression for τ_3 in (12) and the fact that $\text{Sc} \approx 1$, for $\text{Re} > 1$ we can set $Z_m = 1$ and, to within a constant,

$$\tau_5 = \frac{h_e \rho_l R}{4\pi D \rho_{\text{sat}} \beta}.$$

LEVITATION AND STABILITY; NUMERICAL SIMULATION OF A FALLING DROPLET

The equilibrium of a charged droplet in an electric field is known to be unstable against breakup of the droplet into small fragments. The equilibrium of a droplet in the zero-eccentricity approximation is stable if the following condition holds⁷:

$$\frac{q}{4\pi \epsilon_0 16\pi \alpha R^3} + b \frac{\epsilon_0 E_0^2 R}{4\alpha} < 1,$$

$$b = \frac{162}{35}. \quad (17)$$

On the other hand, the droplet can rise under the condition

$$qE_0 \geq mg = \frac{4}{3}\pi R^3 \rho_l g. \quad (18)$$

It has been shown¹ that when a droplet is charged as the result of several factors that do not depend directly on the external field, the simultaneous satisfaction of conditions (17) and (18) is possible only for relatively small droplet radii, such that

$$(R/a) = B < b^{1/4} = 0.682, \quad (19)$$

where $a = \sqrt{2\alpha/\rho_l g}$ is the capillary constant of the liquid, and B is the Bond number.

Unfortunately, there is an error in the derivation of Eq. (19) in Ref. 1, specifically the omission of a factor of 3, so that the correct result instead of (19) is

$$B < \sqrt{3} b^{1/4} = 1.18 = B_* \tag{20}$$

We now analyze the possibility of a droplet rising in the presence of inductive charging mechanisms, assuming that $Z/Z_m = n \leq 1$ in this case. We then set $q = n(12\pi\epsilon_0 E_0 R^2)$ in (17) and (18). Substituting this quantity into the latter equations, we readily obtain the droplet levitation condition

$$B < 3 \sqrt{\frac{2n}{9n^2 + b}} = f(n), \tag{21}$$

where f_n attains a maximum for $n = 0.717$.

The corresponding critical Bond number is also equal to (20):

$$B_* = 1.18.$$

When the droplet is charged to the maximum, $n = 1$, and expression (21) gives

$$B_* = 1.15.$$

This Bond number corresponds to the minimum field required for the equilibrium shape of a water droplet to become unstable:

$$E_{0m} = 7.2 \text{ kV/cm.}$$

We now write the equation of motion of a droplet as a whole in air, in projection onto the direction of motion:

$$m \frac{dv}{dt} = mg - F_c(v) - |q|E_0, \tag{22}$$

where $F_c(v)$ is the resistance of the medium, which we calculate for low numbers $Re \leq 30$ from Stokes' law

$$F_c(v) = 6\pi Rv\eta, \tag{23}$$

and for high $Re > 30$ from Newton's law of resistance

$$F_c(v) = \frac{\pi}{2} \rho v^2 R^2, \tag{24}$$

where ρ is the density of the air.

It follows from the experiment¹ and the above theory that in predominantly downward evaporation the electric force acting on the droplet is always directed upward and therefore enters Eq. (22) with a minus sign.

It is convenient to write Eq. (22) in dimensionless form, introducing the dimensionless radius (Bond number) $B = R/a$, the dimensionless field $w = (\epsilon_0 E_0^2 a / 4\alpha)^{1/2}$, the dimensionless velocity $u = 2av/v$, and the dimensionless charge $Q = ZB^2$, $Z = q / (12\pi\epsilon_0 E_0 R^2)$. Then in place of Eq. (22) we obtain

$$\frac{du}{dt} = \frac{1}{\tau} \left(1 - 18 \frac{|Q|w^2}{B^3} - F_2(u) \right),$$

$$F_2(u) = \begin{cases} 1.13 \times 10^{-6} u/B^2, & Re = uB \leq 30, \\ 4.71 \times 10^{-8} u^2/B, & Re = uB > 30. \end{cases} \tag{25}$$

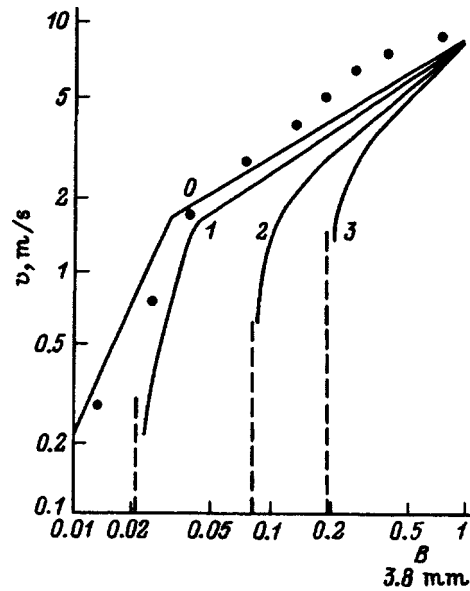


FIG. 2. Steady-state rate of descent of falling droplets versus their radius (in logarithmic scale). The values of E_0 (in kV/cm) are indicated alongside the curves.

The quantity τ has the units of time and is defined as $\tau = v/2ag$. The droplet charge equation (16) is now obtained in the form

$$\frac{dQ}{dt} = - \frac{B^{3/2}}{\tau_5} (1 - \varphi) \sqrt{u} \left(\frac{Q}{B^2} + Q_m \right). \tag{26}$$

Here $\tau_5 = 27.8$ s and $Q_m = 0.24$ for $Re \leq 1$, but if $Re > 1$, then $\tau_5 = 7.35$ s and $Q_m = 1$. The external parameters of problem (25), (26) are the relative humidity φ , the droplet radius $B(R)$, the external field $w(E_0)$, and the initial values of the charge and velocity of the droplet.

The system of equations (25), (26) is integrated numerically for the initial conditions $u(t=0) = Q(t=0) = 0$. The steady-state solution for Q and u are assumed to be known if the conditions $Q/Q_m \geq 0.95$ and $u/u_m \geq 0.95$ are satisfied. In this case, since u_m is unknown, the following condition is set in the numerical program to satisfy the second condition above:

$$|u_{i+1} - u_i| / u_{i+1} \leq 3/19i.$$

Here i is the number of integration steps. This condition corresponds to triple the relaxation time of the velocity, since $\exp(-3) \approx 0.05$. All the calculations are carried out for a relative humidity $\varphi = 0.8$.

We now discuss the integration results. Figure 2 shows graphs of the steady-state rate of fall of droplets as a function of their radius in fields $E_0 = 0, 1, 2, 3$ kV/cm ($w = 0, 0.0012, 0.0048, 0.0108$, respectively) in logarithmic scale. It is evident that for a given field only droplets having radii to the right of the vertical dashed lines continue to fall; all others levitate. The total spectrum of the droplets is limited above by their instability against breakup in the airstream; in all the calculations, therefore, it is assumed that $B \leq 1$. The points represent experimental data⁵ for $E_0 = 0$. Typical curves representing the time dependence of the rate of fall of the drop-

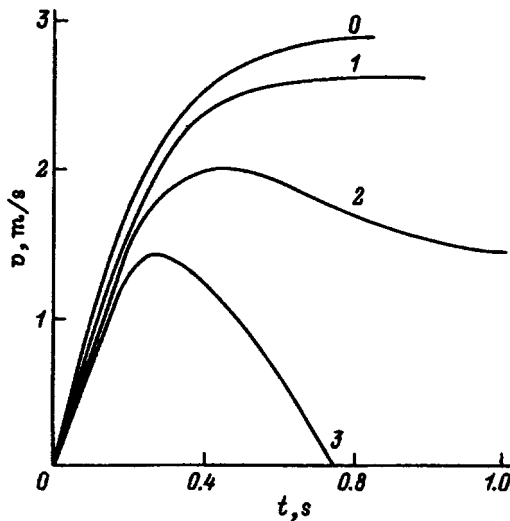


FIG. 3. Rate of descent of droplets versus time; $B=0.1$. The values of E_0 are the same as in Fig. 2.

lets for the same four field strengths and $B=0.1$ ($R=0.38$ mm for water) are shown in Fig. 3. In a field for which condition (18) begins to be satisfied, such droplets fall faster at first (the charge not yet reaching its maximum), and then their velocity decreases to zero, i.e., eventually they move together with the airstream or, if the air itself is stationary, they also remain stationary relative to the ground (levitate, Fig. 3). Figure 4 shows the relaxation time to steady-state descent of the droplets as a function of their radii (semilogarithmic scale). We see from the graphs in Figs. 3 and 4 that the relaxation time to levitation is substantially shorter than the characteristic relaxation times to steady-state descent [for $w(E_0)=\text{const}$]. Finally, Fig. 5 shows the distance traversed by the droplets to attain steady-state descent as a function of their radii.

The system (25), (26) has been solved numerically with other initial conditions. In one example the droplet velocity at the initial time is set equal to the steady-state rate of descent, and zero charge is assumed. At $t>0$ a droplet begins

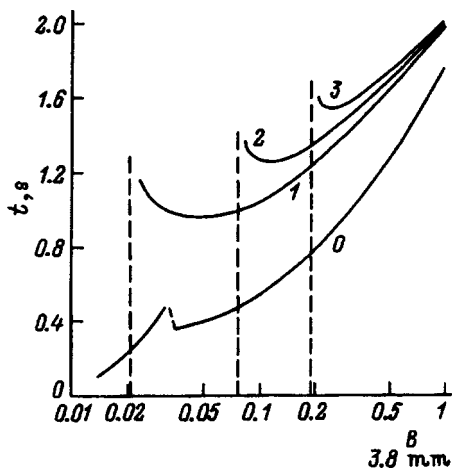


FIG. 4. Relaxation time to steady-state descent of droplets versus their radii. Semilogarithmic scale; the values of E_0 (in kV/cm) are indicated alongside the curves.

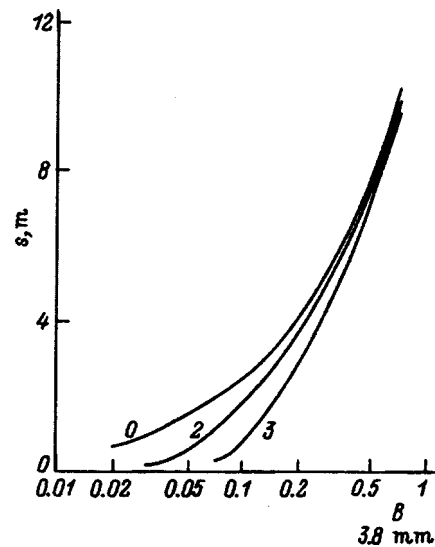


FIG. 5. Distance traversed by droplets up to the attainment of steady-state descent versus their radii. Semilogarithmic scale; the values of E_0 (in kV/cm) are indicated alongside the curves.

to move in an electric field and begins to build charge. The charge increases, and the velocity decreases. Finally, a descent regime characteristic of the initial conditions $u=0$, $Q=0$ is established. The time for the change in motion to take place in this case is of the order of seconds or a fraction of a second.

CONCLUSIONS

1. If nonuniform evaporation of an electrically conducting droplet takes place in an electric field, a discharging of the droplet can occur in a perfectly nonconducting medium.

2. If the maximum of the water-content spectrum of rain is assumed to occur at a droplet radius $R=0.8$ mm (Ref. 8), then in an electric field $\sim 2-3$ kV/cm the entire spectrum can become segregated into approximately equal flows: a flow of small droplets $B<0.1$ levitating or moving upward, and a flow of large droplets descending. The latter flow can be responsible for the so-called mirror effect observed by G. Simpson (see, e.g, Ref. 9), where the sign of the charge of the falling precipitation is opposite to that of the electric field (a positive field is assumed to be directed downward).

3. Owing to the instability of the equilibrium shapes of falling droplets in an airstream, their total spectrum is limited above by the Bond number $B=1$. The field required to levitate a water droplet for which $B=1$ is $E_0=6.8$ kV/cm, which is lower than the field required for the onset of instability, ~ 7.2 kV/cm. Consequently, the entire spectrum of droplets in the atmosphere is capable, in principle, of levitating in the presence of the appropriate electric field.

4. Inasmuch as the average electric fields in a thunderstorm and, moreover, in the absence of a thunderstorm are lower than 0.2 kV/cm, and as a field of 2-3 kV/cm is required for the phenomena described above to be appreciably manifested, the short time required for the droplets to become charged and the short distance traversed by them dur-

ing this time suggest that resonance versions of the indicated phenomena may be taking place.

¹V. A. Saranin, Zh. Tekh. Fiz. **65**(6), 21 (1995) [Tech. Phys. **40**, 332 (1995)].

²V. M. Muchnik and B. E. Fishman, *Electrification of Coarsely Disperse Aerosols in the Atmosphere* [in Russian] (Gidrometeoizdat, Leningrad, 1982).

³V. G. Levich, *Physicochemical Hydrodynamics* [in Russian] (Izd. AN SSSR, Moscow, 1952).

⁴I. P. Vereshchagin, V. I. Levitov, G. Z. Mirzabekyan, and M. M. Pashin, *Fundamentals of the Electrodynamics of Disperse Systems* [in Russian] (Énergiya, Moscow, 1974).

⁵S. L. Soo, *Fluid Dynamics of Multiphase Systems* [Blaisdell Publ. Co., Waltham, Mass., 1967; Mir, Moscow, 1971]; *Multiphase Fluid Dynamics* (Science Press, Beijing; Gower Technical, Brookfield, Vt. Aldershot, UK, 1990).

⁶N. A. Fuks, *Evaporation and Growth of Droplets in a Gaseous Medium* [in Russian] (Izd. AN SSSR, Moscow, 1958).

⁷S. O. Shiryayeva, "Breakup of droplets of conducting liquids in electric fields," Author's Abstract of Dissertation [in Russian] (Odessa, 1989).

⁸N. S. Shishkin, *Clouds, Precipitation, and Thunderstorm Electricity* [in Russian] (GITTL, Moscow, 1954).

⁹V. M. Muchnik, *Physics of Thunderstorms* [in Russian] (Gidrometeoizdat, Leningrad, 1974).

Translated by James S. Wood

Characteristics of the capillary motions of surfactant solutions with a charged free surface

S. O. Shiryayeva, D. F. Belonozhko, and A. I. Grigor'ev

Yaroslavl State University, 150000 Yaroslavl, Russia

(Submitted September 4, 1996)

Zh. Tekh. Fiz. **68**, 22–29 (February 1998)

A dispersion relation is derived and analyzed for the spectrum of capillary motions on the charged plane surface of a liquid in which a surfactant is dissolved. It is shown that two additional wave motions are generated in this kind of system by bulk diffusion and surface diffusion of the surfactant and are sensitive to the diffusion coefficients and elastic properties of the surfactant films and to the viscosity of the solution and the presence of a surface charge.

In solutions of inactive surfactants the growth rate of Tonks–Frenkel instability increases as the surfactant concentration increases. © 1998 American Institute of Physics.

[S1063-7842(98)00502-9]

The influence of surfactants on the laws exhibited by various types of liquid motion have been abundantly investigated in connection with a multitude of potential applications (see, e.g., Refs. 1–6). The possible influence of surfactants on the conditions underlying the onset of Tonks–Frenkel instability has also been studied.³ However, Ref. 3 is restricted to the special case of an insoluble surfactant, which forms on the free surface of a liquid a continuous elastic film in which the wave motions can be described by equations of the theory of elasticity (this is generally not obvious). Zelazo and Melcher⁴ have investigated the influence of a tangential electric field on the motion of a liquid under a monomolecular surfactant film.

In the present article we analyze the influence of surfactants on the relations underlying the development of instability of a charged liquid surface, proceeding as in Refs. 1 and 4–7 and working from the solution of the self-consistent problem, when the free-surface concentration of the surfactant dissolved in the liquid is governed by natural diffusion processes. We interpret the term *surfactant* in the twofold sense of either a substance that lowers the coefficient of surface tension or one that raises it (inactive surfactant), specifying one or the other as the need arises. It has been shown⁷ that these two types of surfactants influence the hydrodynamic stability of the free surface of a liquid differently. It has been determined⁸ that inactive surfactants have a destabilizing effect on the charged surface of a liquid.

1. We consider the problem of calculating the spectrum of capillary motions in a highly conducting liquid (for which the characteristic relaxation time of electric charge on the liquid surface is much shorter than the characteristic surfactant redistribution times and the characteristic hydrodynamic time scales) of infinite depth, with density ρ and viscosity ν , in which a certain surfactant is dissolved with concentration C . The entire system is immersed in the field of gravity \mathbf{g} and in an electrostatic field normal to the free surface. On account of diffusion the surfactant emerges to the surface and is distributed over it with an equilibrium surface concen-

tration Γ_0 . We assume that the surfactant is completely entrained by the motion of the liquid. Let σ be the coefficient of surface tension of the free surface in the presence of the surfactant, and let μ_n and μ_p be the chemical potentials of the bulk and surface phases of the surfactant. We assume that the relaxation time of the surfactant between the surface and the region of the bulk solution adjacent to the surface is small in comparison with the period $2\pi/\omega_0$ of the perturbation imparted to the equilibrium surface by a wave of frequency ω_0 . This means that the surface and bulk solutions are always in the equilibrium state. The electric field \mathbf{E} at the surface of the liquid depends on the interelectrode potential difference, i.e., between the lower electrode, which is the conducting liquid itself, maintained at a potential $\Phi_1=0$, $z \leq 0$, and the upper electrode, which is situated parallel to the unperturbed surface of the liquid at a distance b from it and has a potential $\Phi_2=V$.

We set up Cartesian coordinates with the z axis oriented vertically upward, $\mathbf{n}_z \parallel -\mathbf{g}$ (\mathbf{n}_z is the unit vector in the z direction) and with the x axis oriented along the direction of motion of a plane capillary wave $\sim \exp(st+ikx)$. We assume that the plane $z=0$ coincides with the unperturbed free surface of the liquid (s is the complex frequency, k is the wave number, t is the time, and i is imaginary unity). The function $\xi(x,t) = \xi_0 \exp(st+ikx)$ describes a small perturbation of the equilibrium plane surface of the liquid due to thermal capillary wave motion of very small amplitude $\xi_0 \sim (kT/\gamma)^{1/2}$, k_B is Boltzmann's constant, and T is the absolute temperature. We also assume that $\mathbf{U}(\mathbf{r},t)$ is the velocity field of the liquid due to the perturbation $\xi(x,t)$ and is of the same order as ξ_0 .

To simplify what follows, it is useful to reduce all quantities to dimensionless form, referring them to characteristic values and assuming that $g = \rho = \sigma = 1$, i.e., introducing the characteristic scales of the principal quantities

$$d_* = \left(\frac{\rho g}{\sigma} \right)^{-1/2}, \quad \nu_* = \left(\frac{\sigma^3}{\rho^3 g} \right)^{1/4}, \quad k_* = \left(\frac{\rho g}{\sigma} \right)^{1/2},$$

$$U_* = \frac{\rho\sigma}{g}, \quad s_* = \left(\frac{\rho g^3}{\sigma}\right)^{1/4}, \quad D_* = \left(\frac{\sigma^3}{\rho^3 g}\right)^{1/4},$$

$$\Gamma_* = \frac{\rho g}{\sigma}, \quad V_* = \left(\frac{\sigma^3}{\rho g}\right)^{1/4}, \quad C_* = \frac{\rho g}{\sigma}.$$

The linearized system of viscous hydrodynamic equations (the same notation is retained for all dimensionless quantities) describing the motion of the liquid in the analyzed system has the form

$$\frac{\partial \mathbf{U}}{\partial t} = -\nabla P(\mathbf{U}) + \nu \nabla^2 \mathbf{U} + \mathbf{n}, \quad (1)$$

$$\operatorname{div} \mathbf{U} = 0, \quad (2)$$

$$z \rightarrow \infty: \quad \mathbf{U} = 0, \quad (3)$$

$$z = 0: \quad -\frac{\partial \xi(x,t)}{\partial t} + U_z = 0, \quad (4)$$

$$z = 0: \quad \nu[\mathbf{n}(\boldsymbol{\tau} \cdot \nabla) \mathbf{U} + \boldsymbol{\tau}(\mathbf{n} \cdot \nabla) \mathbf{U}] + P_\tau(\xi) = 0, \quad (5)$$

$$z = 0: \quad -P(\mathbf{U}) + \xi + 2\nu \mathbf{n}(\mathbf{n} \cdot \nabla) \mathbf{U} - P_E(\xi) + P_\sigma(\xi) = 0, \quad (6)$$

$$\operatorname{div} \mathbf{E}_i = 0, \quad \mathbf{E}_i = -\nabla \Phi_i \quad (i=1,2), \quad (7)$$

$$z = 0: \quad \Phi_1 = 0, \quad (8)$$

$$z = b: \quad \Phi_2 = V, \quad (9)$$

$$z = 0: \quad \Phi_1 = \Phi_2, \quad (10)$$

$$\frac{\partial C}{\partial t} = D \left(\frac{\partial^2 C}{\partial x^2} + \frac{\partial^2 C}{\partial z^2} \right), \quad (11)$$

$$z = \xi: \quad \frac{\partial \Gamma}{\partial t} + \operatorname{div}(\Gamma \cdot \mathbf{u}_\tau) = D \left(\frac{\partial C}{\partial z} \right) + D_* \left(\frac{\partial^2 \Gamma}{\partial x^2} \right), \quad (12)$$

$$\mu_n(\Gamma) = \mu_p(C), \quad P_E(\xi) = W(1 + 2k\xi \coth(kb)),$$

$$W = \frac{\varepsilon E_0^2}{4\pi}, \quad E_0 = V/b,$$

$$P_\sigma(\xi) = \sigma(\Gamma_0) = \sigma(\Gamma_0)k^2\xi; \quad P_\tau \equiv \boldsymbol{\tau} \cdot \mathbf{n}_x \frac{\partial \sigma}{\partial \Gamma} \frac{\partial \Gamma_1}{\partial x},$$

$$\Gamma_1 = -\frac{\Gamma_0}{s + L\sqrt{D(s + Dk^2)}} \xi, \quad L = \left(\frac{\partial \mu_n}{\partial \Gamma_0} \right) / \left(\frac{\partial \mu_p}{\partial C_0} \right). \quad (13)$$

In these relations (in the electric part of the problem) the subscript 1 refers to the liquid, and the subscript 2 refers to the region between the upper electrode and the perturbed liquid surface; $P(\mathbf{U})$ is the internal pressure in the liquid, $P_\sigma(\xi)$ is the Laplace pressure under the plane surface distorted by wave motion, $P_E(\xi)$ is the electrostatic pressure (which is derived in Appendix A), $P_\tau(\xi)$ is the tangential force exerted on a unit area due to the variation of the coefficient of surface tension along the free surface in the presence of the surfactant (it is derived in Appendix B), \mathbf{n} and $\boldsymbol{\tau}$ are the unit vectors normal and tangential to the free surface of the liquid, and D_* is the surface diffusion coefficient of the surfactant.

2. The two-dimensionality of the problem [the perturbed surface profile $\xi(x,t)$ and the field $\mathbf{U}(\mathbf{r},t)$ are assumed to be independent of the coordinate y] enables us to scalarize the problem on the basis of the Helmholtz theorem, introducing the potential of the velocity field $\varphi(\mathbf{r},t)$ and the stream function $\psi(\mathbf{r},t)$ (Ref. 1):

$$\mathbf{U} = \hat{\mathbf{N}}_1 \varphi + \hat{\mathbf{N}}_2 \psi,$$

$$\hat{\mathbf{N}}_1 \equiv \nabla, \quad \hat{\mathbf{N}}_2 \equiv [\nabla, \mathbf{n}_y], \quad (14)$$

where \mathbf{n}_y is the unit vector in the y direction, and $\hat{\mathbf{N}}_1$ and $\hat{\mathbf{N}}_2$ are vector differential operators, which satisfy orthogonality relations and commutation conditions with the Laplacian; the Hermitian operator $\hat{\mathbf{N}}_1$ delineates the potential part of the motion, and the anti-Hermitian operator $\hat{\mathbf{N}}_2$ does the same for the rotational part.

The substitution of the expansion (14) into the vector equations (1) and (2), subject to the condition that the eigenvalues of the operators $\hat{\mathbf{N}}_1 \cdot \hat{\mathbf{N}}_2$ and $\hat{\mathbf{N}}_2 \cdot \hat{\mathbf{N}}_1$ are nonzero, yields the system of scalar equations

$$\frac{\partial \psi}{\partial t} - \nu \nabla^2 \psi = 0, \quad (15)$$

$$\nabla^2 \varphi = 0, \quad (16)$$

$$P(\mathbf{U}) = -\frac{\partial \varphi}{\partial t} - z. \quad (17)$$

Equation (14) can be used to transform the boundary conditions (3)–(6) for the vector velocity field $\mathbf{U}(\mathbf{r},t)$ into boundary conditions for the scalar functions $\varphi(\mathbf{r},t)$ and $\psi(\mathbf{r},t)$. Condition (3) is transformed to the relations

$$z \rightarrow -\infty: \quad \frac{\partial \varphi}{\partial x} - \frac{\partial \psi}{\partial z} = 0, \quad (18)$$

$$\frac{\partial \varphi}{\partial z} + \frac{\partial \psi}{\partial x} = 0. \quad (19)$$

Conditions (4)–(6) on the free surface of the liquid assume the form

$$z = 0: \quad \frac{\partial \xi}{\partial t} = \frac{\partial \varphi}{\partial z} + \frac{\partial \psi}{\partial x}, \quad (20)$$

$$\nu \left(2 \frac{\partial^2 \varphi}{\partial x \partial z} + \frac{\partial^2 \psi}{\partial x^2} - \frac{\partial^2 \psi}{\partial z^2} \right) = P_\tau, \quad (21)$$

$$\frac{\partial \varphi}{\partial t} + \xi + 2\nu \left\{ \frac{\partial^2 \varphi}{\partial z^2} - \frac{\partial^2 \psi}{\partial x \partial z} \right\} - P_E(\xi) + P_\sigma(\xi) = 0. \quad (22)$$

The system of equations (15)–(17) subject to the boundary conditions (18)–(22) represents the hydrodynamic part of the problem in scalar form. To satisfy the dynamical boundary condition for the normal and tangential components of the stress tensor (21), (22), we need to use the expression (A9) for $P_E(\xi)$ derived in Appendix A, along with the expression (B9) for the Laplacian pressure P_σ in the presence of the surfactant and the expression (B10) for the tangential force P_τ ; the latter two derived in Appendix B.

3. Solutions of the system (15), (16) that are bounded, periodic in x , and decaying in the limit $z \rightarrow -\infty$ must be sought in the form¹

$$\varphi = A_1 \exp(kz) \exp(st - ikx), \quad (23)$$

$$\psi = A_3 \exp[z\sqrt{k^2 + s/\nu}] \exp(st - ikx), \quad (24)$$

where A_1 , A_2 , and s are complex quantities.

The substitution of Eqs. (23) and (24) into the boundary conditions (20)–(22) yields a homogeneous system of algebraic equations in the constants A_1 , A_2 , and ξ_0 :

$$s\xi_0 = kA_1 - ikA_2, \quad (25)$$

$$\xi_0 \omega_0^2 + (ks + 2k\nu^3)A_1 - 2ik^2\sqrt{k^2 + s/\nu}A_2 = 0, \quad (26)$$

$$-i(2\nu sk^2 - k^3\chi)A_1 - [\nu sk^2 + \nu s(k^2 + s) - k^2\chi\sqrt{k^2 + s/\nu}]A_2 = 0,$$

$$\chi \equiv \frac{\chi_0}{1 + L\sqrt{D(s + Dk^2)}}, \quad \chi_0 = \frac{\partial\sigma}{\partial\Gamma}\Gamma_0,$$

$$\omega_0^2 \equiv k^3 + k - Wk^2 \coth(kb), \quad (27)$$

where $L \sim (\sigma D^2/\rho g^3)^{-1/4}$ has the significance of a characteristic reciprocal linear scale of variation of the bulk surfactant concentration near the surface, ω_0^2 has the physical meaning of the square of the dimensionless frequency of the wave motion of the surface of an inviscid, infinitely deep, conducting liquid in a normal electric field in the small-amplitude wave approximation, and W is the dimensionless energy density of the electric field near the unperturbed surface, i.e., it characterizes the pressure exerted by the electric field on the free surface of the liquid. The dimensionless parameter χ_0 , which is defined by Eq. (B10) in Appendix B, has the significance of an elastic constant of the surfactant film and varies from -1 to $+1$. Positive values of χ_0 correspond to inactive surfactants, which increase the surface tension of the free boundary, and negative values correspond to surfactants in the standard sense, i.e., those which reduce surface tension. Substituting Eq. (25) into (26), we obtain a system of two algebraic equations in the unknown constants A_1 and A_2 :

$$(s^2 + 2\nu k^2 s + \omega_0^2)A_1 - (\omega_0^2 + 2\nu ks\sqrt{k^2 + s/\nu})A_2 = 0, \quad (28)$$

$$i(-\chi k^3 + 2\nu k^2 s)A_1 + (s^2 + 2\nu k^2 s - \chi k^2\sqrt{k^2 + s/\nu})A_2 = 0. \quad (29)$$

The necessary and sufficient condition for the existence of a nontrivial solution of the homogeneous system of equations is that the determinant formed by the coefficients of the unknowns A_1 and A_2 be equal to zero:

$$\begin{vmatrix} s^2 + 2\nu k^2 s + \omega_0^2 & -i(\omega_0^2 + 2\nu ks\sqrt{k^2 + s/\nu}) \\ i(-\chi k^3 + 2\nu k^2 s) & s^2 + 2\nu k^2 s - \chi k^2\sqrt{k^2 + s/\nu} \end{vmatrix} = 0. \quad (30)$$

From this condition we obtain a dispersion relation for the spectrum of capillary motions of the liquid in the analyzed system:

$$-s^2(s + 2\nu k^2)^2 - \omega_0^2(\chi k^3 - \chi k^2\sqrt{k^2 + s/\nu} + s^2) + 4\nu^2 k^3 s^2 \sqrt{k^2 + s/\nu} + s^2 \chi k^2 \sqrt{k^2 + s/\nu} = 0. \quad (31)$$

For an inviscid liquid ($\nu=0$) without the surfactant ($\chi=0$) this equation reduces to the well-known dispersion relation for the spectrum of capillary waves in an ideal, infinitely deep liquid in a normal electric field, $s^2 = \omega_0^2$ (Ref. 9). The expression (B10) for χ can be used to rewrite Eq. (31) in the form

$$-s^2(s + 2\nu k^2)^2 \{s + D_* k^2 + L\sqrt{D(s + Dk^2)}\} + \omega_0^2 \{\chi_0 k^2 s(k - \sqrt{k^2 + s/\nu}) - s^2(s + D_* k^2 + L\sqrt{D(s + Dk^2)})\} + 4\nu^2 k^3 s^2 \{s + D_* k^2 + L\sqrt{D(s + Dk^2)}\} \times \sqrt{k^2 + s/\nu} - s^3 \chi_0 k^2 \sqrt{k^2 + s/\nu} = 0. \quad (32)$$

It follows from analytical calculations and from a numerical analysis of the dispersion relation (32) that the usual capillary liquid motions encountered in the absence of surfactants are supplemented in the given situation (in the presence of a surfactant) by two additional damped waves: one associated with wave motion in the elastic surfactant film on the free surface, and the other associated with the flow of the surfactant as it diffuses toward the surface from the bulk of the liquid.

The results of the numerical analysis of the dispersion relation (32) are shown in Figs. 1–6. Curves 1 describe the capillary wave motion, curves 2 describe the wave motion generated by the diffusion flow of surfactant in the bulk of the liquid, and curves 5 describe the wave motion associated with the surfactant diffusion surface.

It is readily discerned from Figs. 1 and 2 that when the parameter χ_0 (characterizing the elasticity of the surfactant film) passes through zero from the range $\chi_0 < 0$ into the range $\chi_0 > 0$ (into the inactive surfactant range), the wave process associated with diffusion of the surfactant in the bulk vanishes, and an aperiodic, unstable motion appears (curve 3). The corresponding instability is associated with the lowering of the coefficient of surface tension σ for inactive surfactants at the crests of the capillary waves (where the surfactant concentration is diminished). Since the oscillations of the coefficient σ as a function of the surfactant concentration does not exceed a few tenths of the average value of σ , the corresponding instability does not break up the surface of the liquid, it merely produces on the surface a wave relief whose amplitudes are commensurate with the wavelength (whereas the theory used in the calculations is valid only for waves of infinitely small amplitude¹). An increase in the surface charge density (increase in the parameter W) to the critical value $W \equiv W_* = 2$ produces the usual Tonks–Frenkel instability (Fig. 2), but with a growth rate that increases as χ_0 increases. The onset of this instability breaks up the surface of the liquid at once.

The curves 1 characterizing capillary wave motion in the presence of the surfactant (i.e., the influence of the surfactant on the decay rate and the frequency) are shown on a larger scale in Fig. 1b. It follows from the classical theory¹⁰ that the

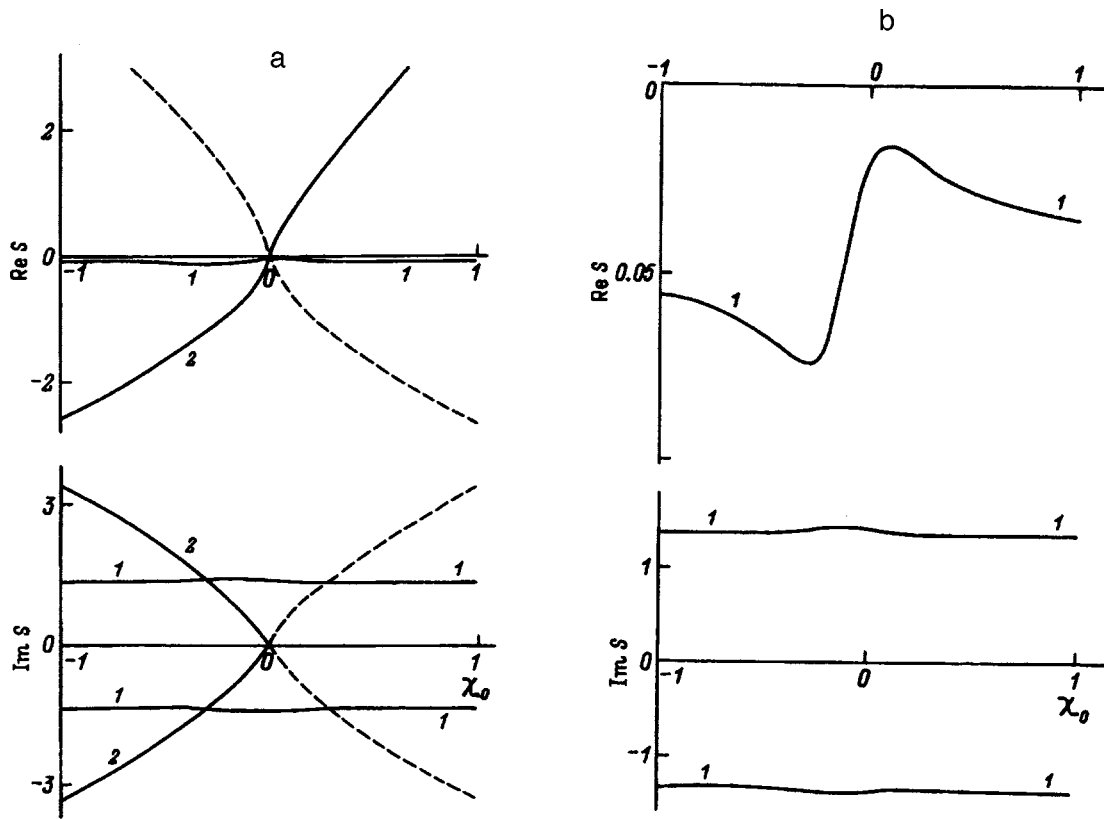


FIG. 1. Real and imaginary components of the frequency s of capillary motion of the liquid versus the parameter χ_0 , calculated for the uncharged liquid surface, $W=0, L=500, \nu=0.01, b=10, k=1, D=10^{-6}, D_*=10^{-6}$. The solid curves lie on the upper sheet of the Riemann surface (i.e., represent the dependences actually observed); the dashed curves (in cases where their presence can better depict the behavior of the observed curves) lie on the lower sheets.

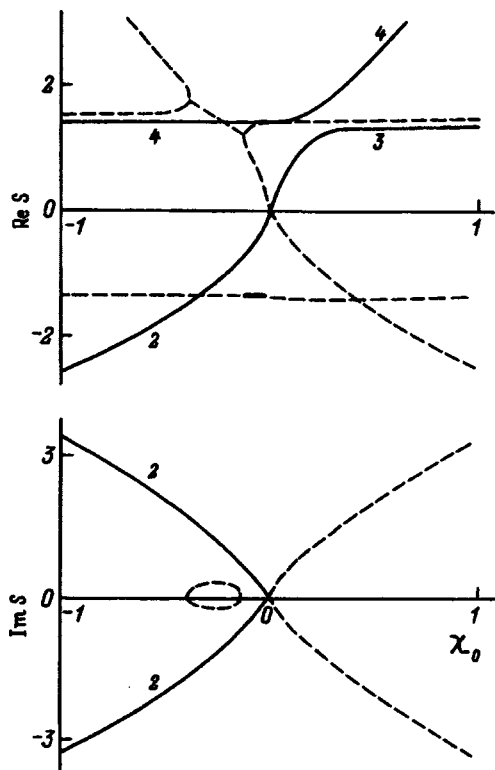


FIG. 2. The same as in Fig. 1, but calculated for a surface charge $W=4$ above the critical value for the onset of Tonks–Frenkel instability.

dependence of the decay rate on χ_0 exhibits nonmonotonic behavior in the range $\chi_0 \leq 0$. In the range $\chi_0 > 0$, on the other hand, the corresponding dependence is monotonic.

It is evident from Fig. 3 that as the bulk diffusion coefficient D increases, the growth rate of the wave motion 2 varies nonmonotonically, increasing at first and then, after attaining a certain value $D=D_0$, begins to decrease; however, the frequency of this motion decreases monotonically as D increases. The variation of D does not influence the wave motions 1 and 5.

Figure 4 shows the evolution of all three wave motions in the given system as the surface charge density W increases. Figures 5 and 6 show the variations of the evolving capillary motions of the liquid with the viscosity of the latter ν , both for the uncharged liquid surface (Fig. 5) and for a critical charge on the surface (Fig. 6). It is interesting to note the strong dependence on ν of the wave motion 2 associated with bulk diffusion of the surfactant.

In addition to the foregoing, the numerical calculations indicate a slight (tenths of one percent) increase in the growth rate of the instability of the charged liquid surface as the bulk diffusion coefficient D increases and as the parameter L increases (over the full ranges of their variation). The presence of the surfactant also affects the frequencies of the wave motion 1 on the charged liquid surface; this motion exists when the surfactant is present (it has very low frequencies and large decay rates) until the onset of Tonks–Frenkel instability at $W_*=2$, but without the surfactant the wave

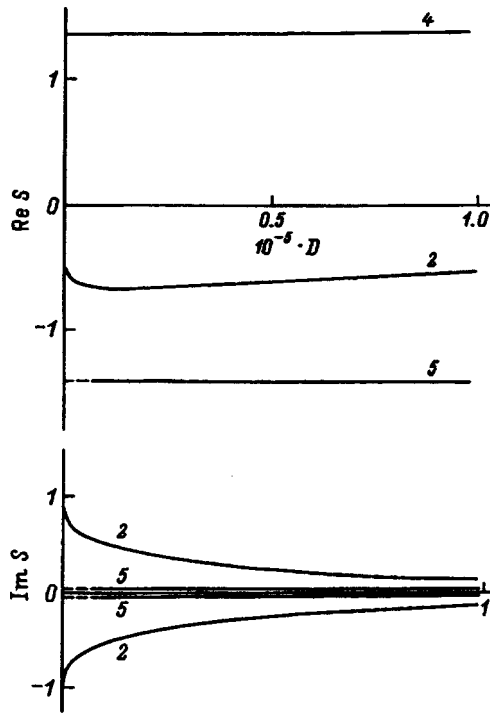


FIG. 3. Real and imaginary components of the frequency s versus the bulk diffusion coefficient of the surfactant D , $W=4$, $\chi_0=-0.1$, $L=500$, $\nu=0.01$, $b=10$, $k=1$, $D_* = 10^{-6}$.

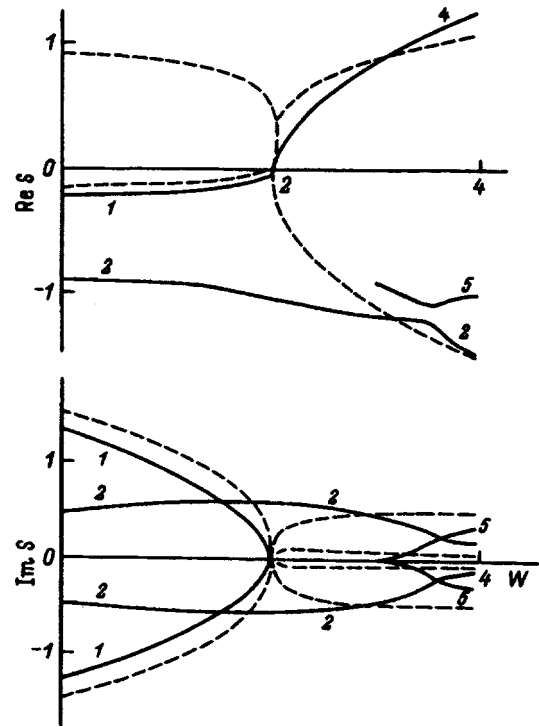


FIG. 4. Real and imaginary components of the frequency s of capillary motion of the liquid versus W , $\chi_0=-0.5$, $L=500$, $\nu=0.01$, $b=10$, $k=1$, $D=3 \times 10^{-6}$, $D_* = 3 \times 10^{-6}$.

motion I vanishes at some value $W \equiv W_0 < 2$.

APPENDIX A

Here we determine the pressure exerted by the electric field on the surface of the liquid layer in the above-described geometry. The mathematical formulation of the problem of calculating the interelectrode electric field has the form (7)–(10). The well-known occurrence of zero electric field in a conductor at once validates the assumption that the potential of the electric field in the liquid layer is $\Phi_1 = \text{const} = 0$. The stated problem therefore reduces to the simpler problem of determining the electric potential Φ_2 in the region between the perturbed surface of the liquid and the plane opposite electrode:

$$\nabla^2 \Phi_2 = 0, \tag{A1}$$

$$z = \xi: \quad \Phi_2 \equiv 0; \tag{A2}$$

$$z = b: \quad \Phi_2 \equiv V. \tag{A3}$$

It is natural to seek Φ_2 in the form

$$\Phi_2 = \Phi^{(0)} + \Phi^{(1)}, \tag{A4}$$

where $\Phi^{(0)}$ is the steady-state solution obtained for $\xi \equiv 0$, $\Phi^{(1)}$ is a small increment to $\Phi^{(0)}$ due to, and of the same order of smallness as, the deformation of the surface $\xi(x, t)$.

The expansion of the boundary condition (A2) in the vicinity of the unperturbed liquid surface $z=0$ in the linear approximation with respect to ξ and $\Phi^{(1)}$ gives

$$z=0: \quad \Phi^{(0)} + \Phi^{(1)} + \xi \frac{\partial \Phi^{(0)}}{\partial z} \equiv 0, \tag{A5}$$

The substitution of Eq. (A4) into (A1), (A3), and (A5) leads to the problems of finding the potentials of the zeroth approximation $\Phi^{(0)}$ and the first approximation $\Phi^{(1)}$:

$$\begin{aligned} \nabla^2 \Phi^{(0)} &\equiv 0, \\ z=0: \quad \Phi^{(0)} &\equiv 0, \\ z=b: \quad \Phi^{(0)} &\equiv V, \\ \nabla^2 \Phi^{(1)} &\equiv 0, \end{aligned} \tag{A6}$$

$$z=0: \quad \Phi^{(1)} \equiv -\xi \frac{\partial \Phi^{(0)}}{\partial z}, \tag{A7}$$

$$z=b: \quad \Phi^{(1)} \equiv 0. \tag{A8}$$

The solution of the problem in the zeroth approximation has the form

$$\Phi^{(0)} = -E_0 z, \quad E_0 = -V/b.$$

We seek a solution of the problem in the first approximation in the form

$$\Phi^{(1)}(x, z, t) = \Phi_*^{(1)}(x, z) \exp(mt),$$

which yields the following result upon substitution into Eqs. (A6)–(A8):

$$\Phi^{(1)} = -\frac{E_0 \xi}{\sinh(kb)} \sinh[k(z-b)].$$

The solution of problem (A1)–(A3) to within small first-order terms can be written in the final form

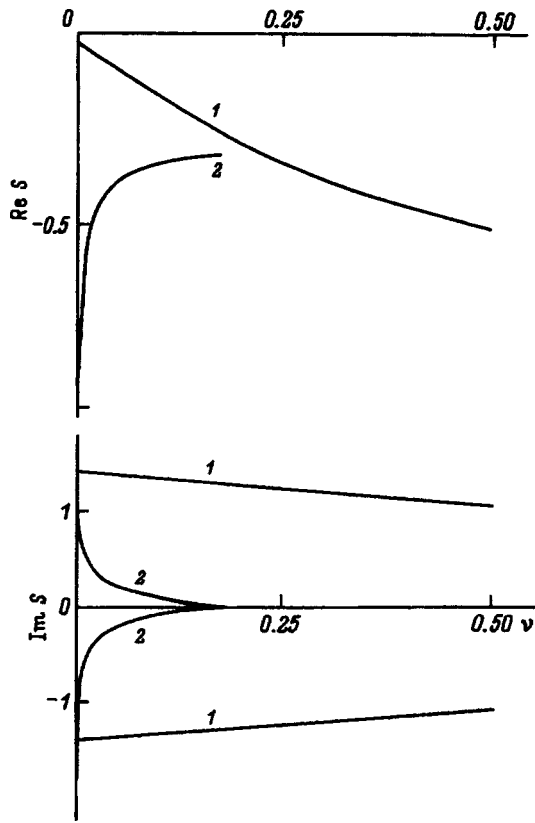


FIG. 5. Real and imaginary components of the frequency s of capillary motion of the liquid versus ν . $W=0$, $\chi_0=-0.1$, $L=500$, $\nu=0.01$, $b=10$, $k=1$, $D=10^{-6}$, $D_*=10^{-6}$.

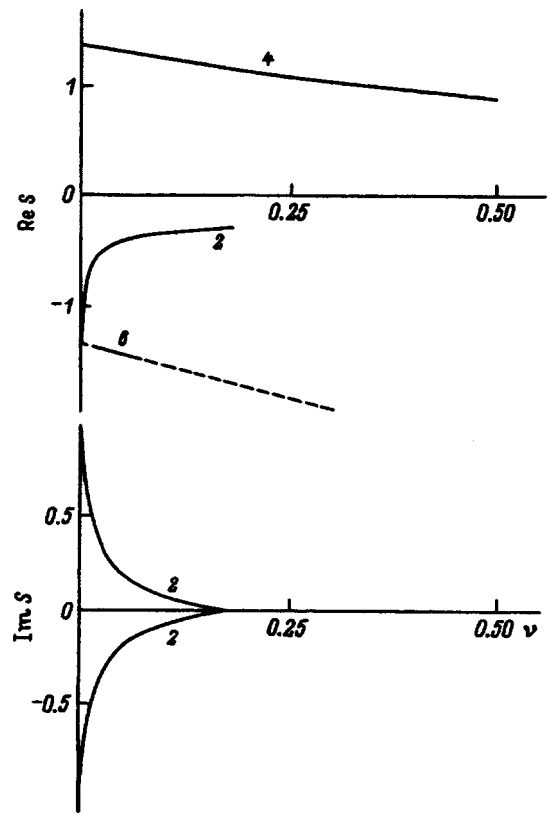


FIG. 6. The same as Fig. 5, but calculated for a surface charge $W=4$ above the critical value for the onset of Tonks–Frenkel instability.

$$\Phi = -E_0 z + \frac{E_0 \xi}{\sinh(kb)} \sinh[k(z-b)].$$

The projections of the electric field vector onto the coordinate axes are needed in order to write equations for the pressure of the electric field on the liquid surface and can be found with little difficulty:

$$E_x = -\frac{ikE_0 \xi}{\sinh(kb)} \sinh[k(z-b)],$$

$$E_z = E_0 + \frac{kE_0 \xi}{\sinh(kb)} \cosh[k(z-b)].$$

In the vicinity of the unperturbed liquid surface $z=0$ the components of the electric field vector can be written in the form

$$E_x = ikE_0 \xi,$$

$$E_z = E_0(1 + k\xi \coth(kb)).$$

These quantities determine the components of the Maxwell voltage tensor

$$\Pi_{ik} = \varepsilon E_i E_k - \frac{\varepsilon}{2} E^2 \delta_{ik}$$

on the perturbed liquid surface:

$$-\Pi_{zz} = \Pi_{xx} = -\frac{\varepsilon}{4\pi} \left(\frac{E_0^2}{2} + E_0^2 k \xi \coth(kb) \right),$$

$$\Pi_{ky} = \Pi_{yz} = \Pi_{yy} = 0; \quad \Pi_{xz} = \frac{\varepsilon}{4\pi} E_0^2 ik \xi.$$

Bearing in mind that the unit vector \mathbf{n} normal to the plane free liquid surface perturbed by wave motion is described in the linear approximation with respect to the small parameter ξ by the equation $\mathbf{n} = ik\xi \mathbf{n}_x + \mathbf{n}_z$ and retaining terms of zeroth-order and first-order smallness, we readily obtain an expression for the momentum flux density into the liquid (i.e., for the force on unit area of the surface):

$$\Pi_{ik} n_k = \frac{\varepsilon E_0^2}{8\pi} (ik\xi \mathbf{n}_x + (1 + 2k\xi \coth(kb)) \mathbf{n}_z).$$

The scalar multiplication of this vector by the normal vector \mathbf{n} in the linear approximation with respect to ξ yields an expression for the pressure of the electric field on the free surface of the liquid:

$$P_E(\xi) = W(1 + 2k\xi \coth(kb)). \tag{A9}$$

APPENDIX B

Equation (11) subject to the boundary conditions (12) and (13) is the mathematical formulation of the problem of calculating the surface concentration of the surfactant.

Inasmuch as the variations of Γ and C are induced by the surface perturbation ξ , it is natural to seek them in the form

$$\Gamma = \Gamma^0 + \Gamma_1, \quad C = C^0 + C_1,$$

where Γ^0 and C^0 are the surface and bulk concentrations of the surfactant for the unperturbed surface ($\Gamma^0 = \text{const}$, and C^0 can be a function of z), and the quantities Γ_1 and C_1 are of first-order smallness in ξ .

The series expansion of the boundary conditions (12) and (13) in the vicinity of $z=0$ enables us to write the differential equation (11) with the boundary conditions separately for quantities of zeroth-order and first-order smallness:

$$\frac{\partial^2 C^0}{\partial z^2} = 0,$$

$$z=0: \quad \mu_n(\Gamma^0) = \mu_p(C^0), \quad \frac{\partial C^0}{\partial z} = 0,$$

$$\frac{\partial C_1}{\partial t} = D \left(\frac{\partial^2 C_1}{\partial x^2} + \frac{\partial^2 C_1}{\partial z^2} \right), \tag{B1}$$

$$z=0: \quad \left(\frac{\partial \mu_n}{\partial \Gamma_0} \right) \Gamma_1 = \left(\frac{\partial \mu_p}{\partial C_0} \right) C_1, \tag{B2}$$

$$z=0: \quad \frac{\partial \Gamma_1}{\partial t} + \Gamma_0 \frac{\partial u_x}{\partial x} = D_* \left(\frac{\partial^2 \Gamma_1}{\partial x^2} \right) - D \left(\frac{\partial C_1}{\partial z} \right). \tag{B3}$$

The solution of the problem in the zeroth-approximation is obvious:

$$\Gamma^0 = C^0 = C_0 = \Gamma_0. \tag{B4}$$

It follows from Eqs. (B2) and (B4) that

$$\Gamma_1 = C_1/L, \quad L = \left(\frac{\partial \mu_n}{\partial \Gamma_0} \right) / \left(\frac{\partial \mu_p}{\partial C_0} \right), \tag{B5}$$

where L has the significance of a characteristic reciprocal linear scale of variation of the bulk surfactant concentration near the surface, i.e., $L \sim \sqrt{s/D} \sim (\sigma D^2/\rho g^3)^{-1/4}$; its characteristic scale is the capillary constant of the liquid.

Relation (14) can be used to express $\partial u_x/\partial x$ in terms of the partial derivatives of φ and ψ with respect to the coordinates:

$$\frac{\partial u_x}{\partial x} = \frac{\partial}{\partial x} \left(\frac{\partial \varphi}{\partial x} - \frac{\partial \psi}{\partial z} \right) = \frac{\partial^2 \varphi}{\partial x^2} - \frac{\partial^2 \psi}{\partial z \partial x}.$$

Invoking Eqs. (23) and (24), we can write

$$z=0: \quad \frac{\partial u_x}{\partial x} = (-A_1 k^2 + A_2 i k \sqrt{k^2 + s/\nu}) \exp(st - ikx).$$

Making use of this expression and taking (B5) into account, we transform condition (B3) as follows:

$$z=0: \quad \frac{1}{L} \frac{\partial C_1}{\partial t} = \frac{D_*}{L} \frac{\partial^2 C_1}{\partial x^2} - D \frac{\partial C_1}{\partial z} - \Gamma_0 \times (-A_1 k^2 + A_2 i k \sqrt{k^2 + s/\nu}) \exp(st - ikx). \tag{B6}$$

We seek a solution of the diffusion relation (B1) in the form $C_1 = f(z) \exp(st - ikx)$. The substitution of this expression into (B1) yields a differential equation in $f(z)$:

$$\frac{s}{D} = -k^2 + \frac{f''}{f},$$

whose solutions bounded in the limit $z \rightarrow -\infty$ are the functions

$$f(z) = B \exp \left[z \sqrt{\frac{s+k^2 D}{D}} \right],$$

which determine C_1 to within a constant factor B :

$$C_1 = B \exp \left[z \sqrt{\frac{s+k^2 D}{D}} \right] \exp(st - ikx). \tag{B7}$$

The factor B is determined by substituting Eq. (B7) into (B6)

$$B = - \frac{\Gamma_0 (-A_1 k^2 + A_2 i k \sqrt{k^2 + s/\nu}) \exp(st - ikx)}{s/L + k^2 D_* / L + \sqrt{D(s + Dk^2)}}.$$

The solution (B1) with the boundary conditions (B2) and (B3) is finally written in the form

$$C_1 = - \frac{\Gamma_0 G \exp \left[z \sqrt{\frac{s+k^2 D}{D}} \right] \exp(st - ikx)}{s/L + k^2 D_* / L + \sqrt{D(s + Dk^2)}},$$

$$G \equiv -A_1 k^2 + A_2 i k \sqrt{k^2 + s/\nu}.$$

The expression for the surface concentration is now rewritten

$$\Gamma_1 = - \frac{\Gamma_0 (-A_1 k^2 + A_2 i k \sqrt{k^2 + s/\nu})}{s + k^2 D_* + L \sqrt{D(s + Dk^2)}} \exp(st - ikx). \tag{B8}$$

Since $\sigma = \sigma(\Gamma)$, in the linear approximation for $P_\sigma(\xi)$ we obtain (1)

$$P_\sigma(\xi) \approx \sigma(\Gamma_0) k^2 \xi. \tag{B9}$$

To find the tangential force $P_\tau \equiv \tau \cdot \nabla \sigma$, we can use the equation

$$\nabla \sigma = \frac{\partial \sigma}{\partial \Gamma} \nabla \Gamma_1$$

and take advantage of the fact that in the assumed geometry the vector τ can be written in the form

$$\tau = \mathbf{n}_x + ikx \mathbf{n}_z.$$

Ultimately we have

$$P_\tau \equiv \tau \cdot \nabla \sigma \approx \frac{\partial \sigma}{\partial \Gamma} \frac{\partial \Gamma_1}{\partial x}.$$

By substituting relation (B8) into this equation, we can obtain an equation for P_τ in the first order of smallness:

$$P_\tau = -\frac{\chi}{s}(A_1 ik^2 + A_2 k^2 \sqrt{k^2 + s/\nu}) \exp(st - ikx),$$

$$\chi \equiv -\frac{s\chi_0}{s + k^2 D_* + \sqrt{D(s + Dk^2)}}, \quad \chi_0 \equiv \frac{\partial \sigma}{\partial \Gamma} \Gamma_0. \quad (\text{B10})$$

Here χ_0 has the significance of an elastic constant of the surfactant film and is rendered dimensionless by referring it to $\chi_{0*} = \sigma$.

¹V. G. Levich, *Physicochemical Hydrodynamics* [in Russian] (Fizmatgiz, Moscow, 1959).

²I. E. Nakhutin, P. P. Poluéktov, and Yu. G. Rubezhnyi, *Zh. Tekh. Fiz.* **55**, 415 (1985) [*Sov. Phys. Tech. Phys.* **30**, 246 (1985)].

³I. N. Aliev, *Magn. Gidrodin.* No. 1, 140 (1988).

⁴R. E. Zelazo and J. R. Melcher, *Phys. Fluids* **17**, 61 (1974).

⁵W. T. Tsai and D. K. P. Yue, *J. Fluid Mech.* **289**, 315 (1995).

⁶E. A. Ryabitskiĭ, *Izv. Ross. Akad. Nauk Mekh. Zhidk. Gaza*, No. 1, 3 (1996).

⁷L. M. Rabinovich, *Izv. Akad. Nauk SSSR Mekh. Zhidk. Gaza*, No. 6, 36 (1978).

⁸D. F. Belonozhko, S. O. Shiryayeva, and A. I. Grigor'ev, *Pis'ma Zh. Tekh. Fiz.* **22**(15), 60 (1996) [*Tech. Phys. Lett.* **22**, 626 (1996)].

⁹L. D. Landau and E. M. Lifshitz, *Electrodynamics of Continuous Media*, 2nd ed. (rev. and enl., with L. P. Pitaevskii), Pergamon, Press, Oxford New York (1984); Nauka, Moscow (1982).

¹⁰J. Lucassen, *Trans. Faraday Soc.* **64**, 2221 (1968).

Translated by James S. Wood

Turbulent cooling of the gas and dielectric recovery following a spark discharge

M. N. Shneider

High-Voltage Scientific-Research Center, 143500 Istra-2, Moscow District, Russia
(Submitted September 24, 1996)

Zh. Tekh. Fiz. **68**, 30–35 (February 1998)

A theoretical model is proposed for performing self-consistent calculations of the entire evolution of a spark discharge and the subsequent cooling of the postdischarge channel and dielectric recovery for a specified aperiodic discharge current pulse, taking into account the generation and dissipation of turbulent motion of the gas. The results are compared with the well-known experiments of E. P. Bel'kov, where it was discovered that the dielectric recovery rate depends on the characteristics of the discharge current pulse, which ultimately determine the intensity of the turbulent motion arising in the cooling channel. © 1998 American Institute of Physics. [S1063-7842(98)00602-3]

INTRODUCTION

It is a well-known fact that turbulent gas motion develops in a cooling postdischarge channel, creating far more rapid heat transfer than molecular heat conduction, so that the rates of cooling and expansion of the channel increase dramatically. This cooling regime occurs, in particular, after the termination of high-power spark discharges, pulsed arcs,^{1–4} and laser sparks.^{4,5} The cooling rate of the hot postdischarge channel is a problem of major practical importance, because the gas cooling time after passage of the current pulse determines the most important characteristic of gas-filled spark gaps: the rate at which the dielectric strength is restored (dielectric recovery rate). Conceivably the dynamics of decay of a natural lightning channel, like that of the long-arc laboratory spark used to simulate it, is also governed by the generation of turbulent motion in it.⁶

A simple theoretical model of the cooling of a postdischarge channel in a gas has been proposed,^{7,8} taking into account the generation of turbulence and its influence on the channel cooling and expansion process. However, because of the arbitrary specification of the initial conditions, the results of Refs. 7 and 8 can only be regarded as preliminary and qualitatively consistent with experiment. The validity of the model for practical calculations cannot be decided until its results have been compared with experiment. The paramount requirement in this endeavor is to know the characteristics of the state of the gas immediately prior to the onset of the experimentally observed turbulent cooling.

In the present article we discuss a model that can be used for a given discharge current pulse to carry out a self-consistent analysis of the entire process of the spark discharge and subsequent cooling of the postdischarge channel with allowance for the generation and dissipation of turbulent motion of the gas. The results are compared with the celebrated experiments of Bel'kov,^{1,2} where the dielectric recovery rate was found to depend on the characteristics of the discharge current pulse, which ultimately determine the intensity of the turbulent motion generated in the cooling channel.

MODEL OF THE EVOLUTION OF THE SPARK (PULSED ARC) CHANNEL

The results of the theory developed below are compared with experiment for a spark discharge in air at atmospheric pressure in a gap $d = 1$ cm and for subsequent discharge current pulses covering a broad range of parameters.^{1,2}

All the pulses listed in Table I have in common a comparatively rapid current rise in the first quarter period, $dI/dt > 10^9$ A/s. To date the evolution of such discharges has been studied in detail.^{9–13}

We use the approach proposed in Ref. 11 to obtain an approximate qualitative description of the channel expansion dynamics. Assuming that all the parameters in the channel are independent of the radius and disregarding the thickness of the envelope (whose rate of expansion in the energy-input stage essentially coincides with the shock velocity) and the influence of the self-magnetic field, we describe the evolution of a channel of unit length by the radially integrated equations of motion and energy

$$\frac{d}{dt} \left(\pi r^2 \rho_\infty \frac{dr}{dt} \right) = 2 \pi r (p - p_\infty), \quad (1)$$

$$\frac{d}{dt} \frac{\pi r^2 p}{\gamma - 1} + p \frac{d}{dt} \pi r^2 = W(t) - \Phi(p, T, t) \pi r^2, \quad (2)$$

where P_∞ and ρ_∞ are the pressure and density of the unperturbed gas, $W = I^2(t)/\pi r^2 \sigma(T)$ is the power of the electric current, $\sigma(T)$ is the conductivity of the plasma as defined by the Spitzer equation, and $\Phi(p, T, t)$ denotes the energy losses in radiation from unit volume (the form of the function Φ will be specified below).

Equations (1) and (2) are augmented with the equation of state of the gas in the channel

$$p = (\gamma - 1) \rho \varepsilon = \frac{\gamma - 1}{\gamma} \rho h, \quad \gamma(T) = c_p / c_v, \quad (3)$$

where ε and h are the energy and enthalpy per unit mass of the gas.

TABLE I. Characteristics of the current pulses for a spark discharge in air.

Pulse No.	I_m , kA	f , kHz	τ_a , 10^{-6} s	t_{pul} , 10^{-6} s
Pulse 1	60	200	0.926	15
Pulse 2	20	600	0.5	10
Pulse 3	4	1600	0.136	3

Note: Here I_m , f , and τ_a are the amplitude, frequency, and characteristic decay time of the current (the latter determined from the experimentally observed logarithmic decay rate); t_{pul} is the pulse duration.

To obtain a closed discharge model, we need one more equation for the density ρ or the internal energy ε (temperature T) of the plasma in the channel.

Detailed numerical calculations of the evolution of a pulsed arc have shown that for a current rise rate $\dot{I} \geq 10^9 - 10^{10}$ A/s the plasma temperature depends mainly on the equilibrium of the Joule heat release and the radiative energy loss with subsequent, essentially total absorption in the envelope;^{12,13} we therefore assume that the following relation holds in the first quarter period (i.e., at $t \leq t_1 = 1/4f$), as in the model of Ref. 13:

$$2\pi r \xi \sigma_r T^4 = I^2(t) / \pi r^2 \sigma(T), \quad (4)$$

where σ_r is the Stefan–Boltzmann constant, ξ is the gray-body emissivity factor of the plasma (for typical characteristics of the current rise stage $p/p_\infty \gg 1$ and $T > 2 \times 10^4$ K we have $\xi \approx 1$). In the energy balance equation (1) we can assume that $\Phi(p, T, t) = 0$ in this case. If the current and initial conditions are given, the system of equations (1)–(4) is completely defined. In our situation the density of the plasma is determined from the equation of state (3) as a function $\rho[p, \varepsilon(p, T)]$.

For typical discharge circuit parameters (which govern the decay rate of the current pulse) a large part of the electrical energy in the spark discharge evolves in the first quarter periods. The temperature and pressure in the channel then drop sharply, the envelope becomes partially transmissive to radiation, and the approximation (4) is no longer valid. However, since essentially all the discharge energy has been released at the time $t_1 = 1/4f$ and since the pressure and temperature of the gas in the channel satisfy the conditions $p(t_1) \gg p_\infty$ and $T(t_1) \gg T_\infty$, the subsequent expansion of the channel up to the onset of the isobaric stage can be regarded as a cylindrically symmetric explosion in a medium with counterpressure. It can be assumed here that all the electric current energy evolved in the discharge, $E = \int_0^{t_1} W(t) dt$, is imparted instantaneously to a thin cylinder [with radius $r_0 \ll r(t_1)$] of unperturbed cold gas of density ρ_∞ , drastically increasing the specific internal energy and, hence, the pressure of the gas.¹⁾ It is convenient to seek a solution in Lagrangian mass coordinates within the framework of standard one-dimensional gasdynamic equations. Problems of this kind have been solved by many authors (a comprehensive survey of the current status of the field is given in Korobeinikov's book¹⁴). We therefore omit the details of the numerical model.

The correct treatment of radiation during the explosion process poses a separate, rather complex problem. To ascer-

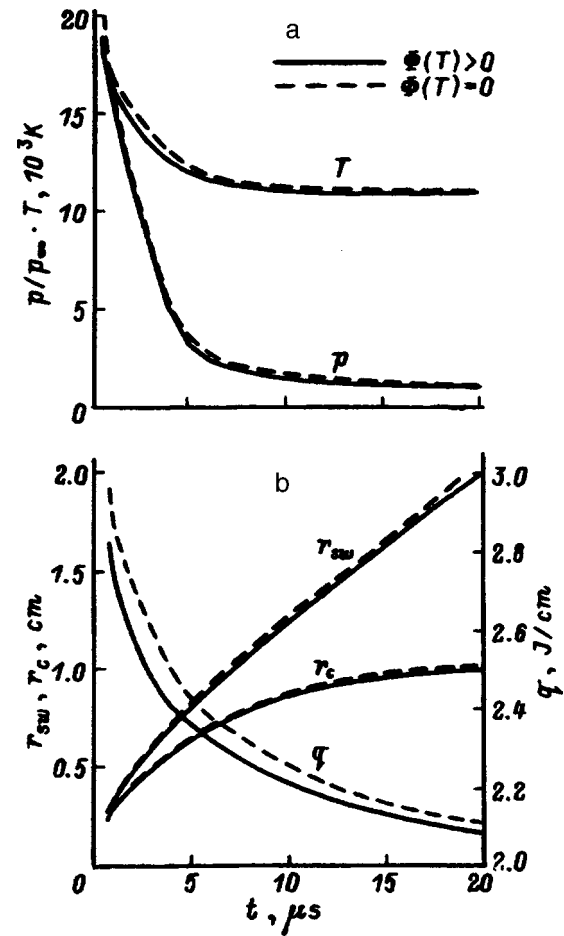


FIG. 1. Evolution of a pulsed arc in the cylindrical explosion model for pulse 1. The dashed curves correspond to nonradiative adiabatic expansion.

tain the degree to which radiation influences the channel parameters, we consider two models: 1) completely adiabatic expansion without radiation losses, i.e., $\Phi(p, T, t) = 0$; 2) the inclusion of radiative cooling (without absorption in the adjacent cold gas layers) with a specified rate of bulk energy loss from the hot air plasma,

$$\Phi(p, T) = \Phi(p_\infty, T)(p/p_\infty)^\alpha, \quad (5)$$

where $1 \leq \alpha < 2$; the values of $\Phi(p_\infty, T)$ are taken from Ref. 15.

In the calculations it is assumed that $\gamma = 1.2$; the conductivity of the plasma is approximated by the expression¹³ $\sigma(T) = \sigma_0 T^{0.4} = 1.725 T^{0.4}$ S/cm (T in K). A good means of determining $\varepsilon(p, T)$ in the channel is the interpolation formula for the specific internal energy of air¹⁶ $\varepsilon = 8.3(T_{[K]}/10^4/10^4)^{1.5}(\rho/\rho_\infty)^{0.12}$ eV/molecule $\approx 27.7 \cdot T_{[K]}^{1.5} \cdot (\rho/\rho_\infty)^{0.12}$ J/kg, which is valid at $T > 10^4$ K. As an example, Fig. 1 shows the results of calculations of the evolution of the parameters of a pulsed arc, labeled pulse 1 (for this case Eqs. (1)–(4) yield $E = 3.17$ J/cm). Figure 1a shows the temperature and pressure on the channel axis, and Fig. 1b shows the thermal energy per unit length q , the radius of the rarefied channel r_c , and the radius of the shock wave r_{sw} . The calculations show that the expansion of the

TABLE II. Results of calculations of the initial conditions for the isobaric stage.

Pulse No.	$t_p, 10^{-6}$ s	$T(t_p),$ K	$q(t_p),$ J/cm	$r_c(t_p),$ cm	$r_{sw}(t_p),$ cm	$\tilde{r}_c(t_p),$ cm
Pulse 1	~20	10800	2.1	1.1	2.1	1.27
Pulse 2	~10	11200	1.24	0.628	1.24	0.79
Pulse 3	~4.5	9700	0.08	0.23	0.415	0.25

postdischarge channel up to the onset of the isobaric stage can be regarded as an adiabatic process, i.e., the influence of radiation is slight.

At a later time the pressure and temperature of the gas in the channel decrease. We assume that the initial stage ends at the time $t = t_p$, when the pressure in the channel becomes equal to the ambient pressure, $p(t_p) = p_\infty$. The calculated main parameters of the onset of the isobaric stage are summarized in Table II.

The last column of Table II gives the approximate values of the initial radius of the isobaric stage, which are evaluated for the calculated quantities of heat $q(t_p) = \pi r^2 \rho \varepsilon$ from the equation^{7,8}

$$\tilde{r}_c(t_p) \approx \sqrt{q(\gamma - 1) / \pi \rho_\infty} \approx 0.25 \sqrt{q / p_\infty}. \quad (6)$$

The radial distributions of the temperature and density of the gas for pulses 1–3 up to the onset of the isobaric stage are shown in Fig. 2.

The subsequent cooling process accompanied by gas flow in the channel and the development of turbulent motion in it takes place at constant pressure.

ISOBARIC STAGE OF TURBULENT COOLING

We analyze the functional relations of turbulent cooling on the basis of the corrected and improved model of Refs. 7 and 8 using the following approximations: 1) Cooling takes place at constant pressure, i.e., $p = p_\infty = \text{const}$; 2) all macroscopic parameters are inhomogeneous in the channel and are equal to the cross-sectional averages; 3) the ideal-gas equation of state (3) holds at each value of the temperature T .

The pressure in the cooling channel becomes equal to the ambient pressure at an even higher temperature of the gas in it, $T \sim 10^4$ K. The subsequent drop in temperature occurs at almost constant pressure, accompanied by an increase in the density, which requires an influx of gas from the periphery of the channel. This radial flow is unstable, resulting in the development of turbulent motion of the gas in the channel. A possible mechanism of the experimentally observed hydrodynamic stability could be Rayleigh–Taylor instability in the high-density-gradient zone at the boundary of the predominantly radiation-cooled channel.^{17,18} The characteristic time τ_{inst} of evolution of this instability for typical parameters of the onset of the isobaric cooling stage in the postdischarge channel in air, $p = 1$ atm, $r \sim 1$ cm, and $T \sim (1.1 - 1.5) \times 10^4$ K, is $\tau_{\text{inst}} \sim 10^{-4}$ s, which agrees with experiment.¹⁻⁵

Since the cooling postdischarge channel is not bounded by walls, the turbulence generated in it closely resembles

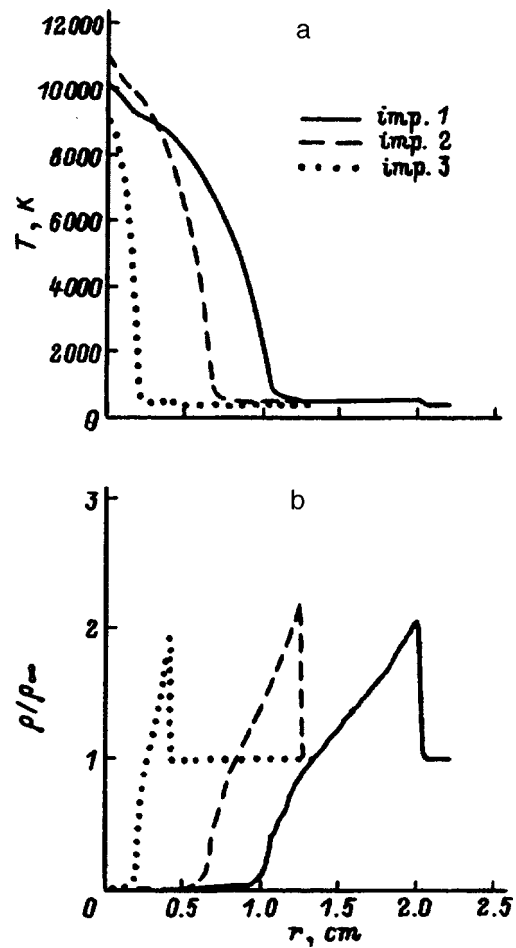


FIG. 2. Radial distributions of the temperature and the density of the gas up to the onset of the quasi-isobaric stage.

so-called free turbulence (e.g., a submerged turbulent jet, a turbulent wake, etc.), for which it has been established experimentally that the surface separating the turbulent region from the laminar region, on the average, moves into the undisturbed medium at a velocity of the order of the rms velocity of the turbulent fluctuations. Consequently, for the rate of expansion of the channel boundary it is assumed in Refs. 7 and 8 that $\dot{r} \approx \frac{1}{2} \sqrt{\langle u^2 \rangle} \approx \sqrt{K/2}$, where K is the kinetic energy of the turbulent fluctuations per unit mass of the gas. However, in the time interval $t_p < t \leq \tau_{\text{inst}}$ the expansion of the channel is controlled by slow molecular transport processes. Consequently, taking into account the delay of turbulence generation, we can write the channel expansion rate and the associated turbulent thermal diffusivity in the form

$$\dot{r} \approx \Theta(t - \tau_{\text{inst}}) \sqrt{K/2}, \quad (7)$$

$$\chi_r \approx \frac{1}{3} r \Theta(t - \tau_{\text{inst}}) \sqrt{2K}. \quad (8)$$

where $\Theta(t - \tau_{\text{inst}})$ is the Heaviside unit step function.

As for the kinetic energy K , its corresponding delay is insignificant, because the kinetic energy of radial flow of the gas toward the center of the channel is ultimately converted

into kinetic energy of turbulent fluctuations (except for a fraction of it that is converted into heat as a result of viscosity).

Allowing for the fact that thermal diffusion from the cooling channel takes place through the combined effect of molecular transport and the far more intense turbulent transport processes, we introduce the effective thermal diffusivity χ_{eff} and the effective thermal conductivity λ_{eff} :

$$\chi_{\text{eff}} = \chi_\lambda + \chi_t = \frac{\lambda}{c_p \rho} \left(1 + \frac{\chi_t \rho}{\lambda / c_p} \right) \equiv \frac{\lambda_{\text{eff}}}{c_p \rho},$$

$$\lambda_{\text{eff}}(T) \equiv \lambda(T) \left(1 + \frac{\chi_t \rho}{\lambda / c_p} \right), \quad (9)$$

where χ_λ and λ are the corresponding molecular transport coefficients.

The variation of the internal and kinetic energies of the gas, averaged over the channel cross section, is described by the following equations in the general case of variable volume and mass:^{7,8}

$$\begin{aligned} \dot{\varepsilon} \rho V + \varepsilon(\rho \dot{V} + \dot{\rho} V) + p \dot{V} \\ = \rho_\infty v_s h_\infty S - \lambda_{\text{eff}}(T - T_\infty) S / r - \Phi(T) V + \rho \Omega V, \end{aligned} \quad (10)$$

$$\dot{K} \rho V + K(\rho \dot{V} + \dot{\rho} V) = \rho_\infty v_s (v_g^2 / 2) S - \rho \Omega V. \quad (11)$$

Here V and S are the instantaneous volume and area of the lateral surface of the channel, Ω is a term that takes into account the viscosity-induced dissipation of kinetic energy into heat, $v_g = v_s - \dot{r}$ is the radial velocity of the cold gas entering the channel relative to a fixed axis (it determines the kinetic energy flux into the channel), and v_s is the flow velocity of the cold gas through the lateral surface (it determines the mass influx into the channel); from the equation of continuity we have $v_s = (\dot{\rho} V + \rho \dot{V}) / \rho_\infty S$. Consequently, for the turbulent motion in a cylindrical channel, taking (3) and (7) into account, from Eqs. (10) and (11) we obtain

$$\begin{aligned} \dot{\varepsilon} &= \varepsilon F, \\ \dot{K} &= -\Omega + (v_g^2 / 2 - K) [\Theta(t - \tau_{\text{inst}}) \sqrt{2K} / r - F], \\ F &= \{ \Omega + \Theta(t - \tau_{\text{inst}}) (h_\infty - h) \sqrt{2K} / r \\ &\quad - [\Phi + 2\lambda_{\text{eff}}(T - T_\infty) / r^2] / \rho \} / h_\infty, \\ v_g &= -\frac{1}{2} [rF\rho / \rho_\infty + \Theta(t - \tau_{\text{inst}}) (1 - \rho / \rho_\infty) \sqrt{2K}]. \end{aligned} \quad (13)$$

As mentioned, the turbulent motion generated in the cooling channel is more like free jet flow than pipe flow. But then jet flows are distinguished by significantly lower critical Reynolds numbers ($\text{Re} \sim 10$) than pipe flows. Consequently, even at the relatively low Reynolds numbers of the channel turbulence, $\text{Re} \sim 10^2$, fluctuations having the maximum scale ($\sim r$) and subsequent smaller scales can break up, transferring their kinetic energy along the spectrum without any appreciable decay, to smaller-scale fluctuations, where the effective viscous dissipation of kinetic energy into heat takes place (the phenomenon is actually a modification of the well-

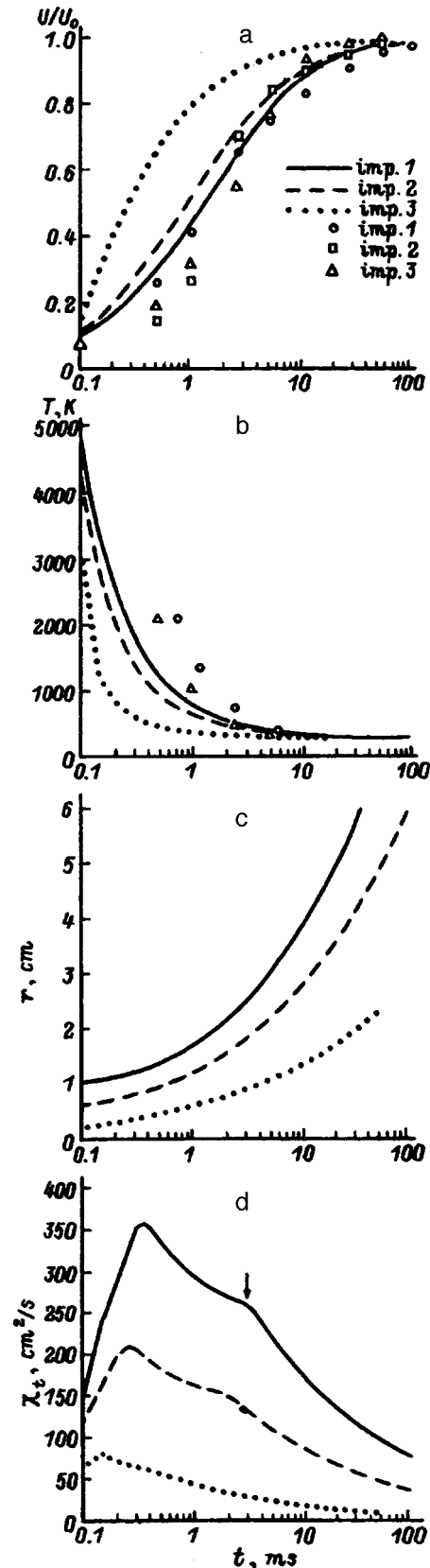


FIG. 3. Curves of dielectric recovery (a), the temperature of the gas in the channel (b), the channel radius (c), and the turbulent diffusion coefficient (d). The point symbols in graphs a and b represent experimental data.^{1,2}

known Richardson–Kolmogorov–Obukhov cascade process). To take the cascade dissipation mechanism (CDM)

TABLE III. Comparison of calculated and corresponding experimental values of the time τ_1 , 10^{-3} s.

Pulse No.	Theory	Experiment ^{1,2}
Pulse 1	25	13
Pulse 2	8.5	10
Pulse 3	3.4	2.8

into account, it is necessary to replace the single equation (13) for the turbulent fluctuations of K by deriving a system of analogous equations for the kinetic energy with the inclusion of various scales in the fluctuations, taking into account the spectral cascade of energy transfer. In the present article we investigate the CDM on the basis of the discrete spectral theory of isotropic turbulence in an incompressible fluid,¹⁹ as proposed in Refs. 7 and 8.

In our case the fluctuations of each scale decay not only as a result of the cascade transfer of kinetic energy and its viscous dissipation in the small-scale region as in the case of isotropic turbulence, but also as a result of an increase in the mass of the gas drawn into turbulent motion as the channel cools. As is the convention for all macroscopic parameters, we assume that the characteristics of all the scales are uniformly distributed in the channel and are equal to their cross-sectional averages, e.g., $u_i(t) \equiv \overline{u_i(r,t)}$. Here the total energy per unit mass of the turbulent fluctuations K and its rate of viscous dissipation into heat Ω are equal to

$$K = \frac{1}{2} \sum_{i=1}^n u_i^2 \quad \text{and} \quad \Omega = \nu \sum_{i=1}^n k_i^2 u_i^2,$$

respectively, where $\nu(T)$ is the kinematic viscosity, and n is the number of cascades included in the calculation. We assume that the kinetic energy of the gas flowing into the cooling channel is transferred by the maximum-scale fluctuations, and not until then is it spectrally transferred by the cascade mechanism. The inclusion of spectral cascade transfer reduces Eq. (13) to a system of n equations for i th-scale fluctuations.^{7,8}

The initial conditions for the given system (12), (13) are $r(t_p)$, $\varepsilon[T(t_p)]$, evaluated for a given current pulse, and $u_i(t_p) = 0$, $i = 1, \dots, n$, corresponding to the condition $K(t_p) = 0$.

Turbulent cooling calculations for a postdischarge channel have been carried out for pulses 1–3 with the initial conditions at $t = t_p$ in Table II. Since the characteristic time of evolution of instability satisfies the condition $\tau_{\text{inst}} \ll \tau_1$ (τ_1 is a characteristic dielectric recovery time), the same value $\tau_{\text{inst}} = 10^{-4}$ s is adopted for all cases in the calculations. The number n of cascades included in the process is chosen so that any further increase in n has no effect on the results. The upper limit $n \leq 15$ is sufficient for all the cases treated here. The temperature T is determined in the form of the function $T(\varepsilon)$ by the interpolation of tabulated data.²⁰ The dependence $\gamma(T)$ is also taken into account.

In Paschen’s theory the breakdown voltage depends only on the product pd for a given gas and a given electrode material. For $p \propto \rho T = \text{const}$ and $T \neq T_\infty$ the temperature de-

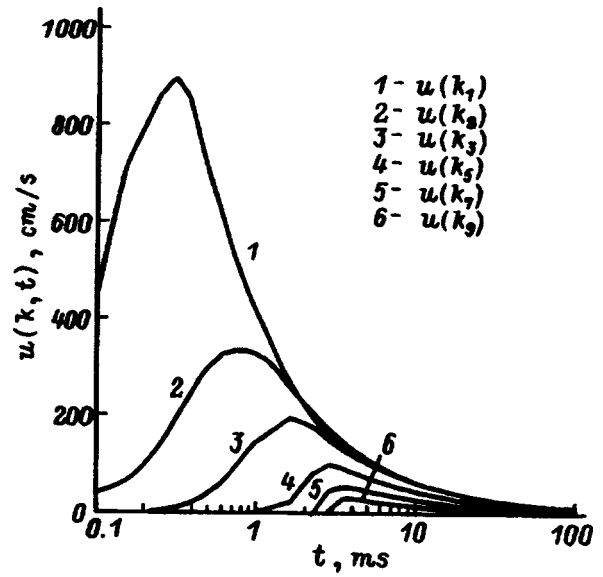


FIG. 4. Evolution of the turbulence spectrum in a postdischarge channel for pulse 1.

pendence of the breakdown criterion is taken into account essentially by changing the product pd to $p(T_\infty/T)d$. Consequently, for the gas temperature $T(t)$ obtained in our calculations the Paschen breakdown criterion²¹ can be used to plot the dielectric recovery curves

$$\frac{U}{U_0} = \frac{T_\infty}{T} \frac{\ln s_\infty}{\ln(s_\infty T_\infty/T)}, \quad s_\infty = \frac{Apd}{\ln(1 + 1/\tilde{\gamma})}, \quad (14)$$

where U_0 and $U(t)$ are the breakdown voltages of the given discharge gap for the cold and hot gases, respectively, A is a parameter, $A = 15 \text{ cm}^{-1} \text{ torr}^{-1}$ for air, and $\tilde{\gamma} \sim 10^{-3} - 10^{-1}$ is the secondary emission coefficient; for definiteness we assume that $\tilde{\gamma} = 0.01$.

Figure 3 shows the main results of the calculations of the cooling dynamics of the postdischarge channel and dielectric recovery for pulses 1–3. All the dielectric recovery curves agree with experiment^{1,2} within the measurement error limits. The theoretical and experimental values of the dielectric recovery time τ_1 corresponding to the time at which $U(t)/U_0 = 0.9$ are given in Table III.

A significant result is the abrupt drop of the turbulent diffusion coefficient χ_t (Fig. 3d), which characterizes the rate of cooling and expansion of the channel, in the final stage of cooling ($t \geq \tau^* \sim 1$ ms; the time τ^* for pulse 1 is indicated by an arrow). This behavior is associated one-to-one with the rapid decay of turbulence due to the formation of a well-developed spectrum of turbulent fluctuations at the time $t \sim \tau^*$ (Fig. 4) and the rapid viscous dissipation of kinetic energy in small-scale “harmonics.”

However, if the velocity of the resulting vortex motion is comparatively low in the cooling channel, during the entire characteristic cooling time (dielectric recovery time) the kinetic energy is concentrated in fluctuations having the maximum scale, of the order of the channel radius, for which viscosity is insignificant. Here the turbulence kinetic energy density decreases mainly as a result of an increase in the

mass of the gas drawn into the spatially confined vortex motion, i.e., a noncascade dissipation mechanism is operative.^{7,8} In this case the time derivative of the function $\chi_t(t)$ is continuous during the entire dielectric recovery time, as is indeed the result for the comparatively low-power pulse 3.

CONCLUSION

The qualitative and reasonably good quantitative agreement of the results with experiment indicate that the model discussed above correctly reflects the physical processes governing the rate of cooling and expansion of a postdischarge channel. It must be borne in mind, however, that the Paschen criterion used in the study contains constants that have been evaluated empirically in a study of breakdown in a cold gas of invariant chemical composition. It is impossible to mount a rigorous theory of dielectric recovery without a detailed analysis of the complex physicochemical kinetics in cooling air. Nonetheless, the results indicate the applicability of the proposed model for practical calculations of the cooling of spark channels in gases and the dielectric recovery time.

¹⁾The criterion underlying the choice of the radius r_0 is the requirement that the parameters of the droplet toward the end of the first quarter period, as determined by solving the system (1)–(4), be close to the corresponding parameters obtained in the explosion model at $t \sim t_1$.

¹E. P. Bel'kov, Zh. Tekh. Fiz. **41**, 1678 (1971) [Sov. Phys. Tech. Phys. **16**, 1321 (1972)].

²E. P. Bel'kov, Zh. Tekh. Fiz. **44**, 1946 (1974) [Sov. Phys. Tech. Phys. **19**, 1210 (1974)].

- ³J. M. Kulman and G. M. Molen, AIAA J. **24**, 1112 (1986).
⁴J. P. Greig, R. E. Pechacek, and M. Raleigh, Phys. Fluids **28**, 2357 (1985).
⁵S. N. Kabanov, L. I. Maslova, T. I. Tarkhova *et al.*, Zh. Tekh. Fiz. **60**(6), 37 (1990) [Sov. Phys. Tech. Phys. **35**, 655 (1990)].
⁶J. M. Picone, J. P. Boris, J. P. Greig *et al.*, J. Atmos. Sci. **38**, 2056 (1981).
⁷M. N. Shneider, Teplofiz. Vys. Temp. **31**, 365 (1993); Teplofiz. Vys. Temp. **32**, 56 (1994).
⁸M. N. Shneider, AIAA Paper 95-1994 (San Diego, 1995), 7 pp.
⁹S. I. Braginskii, Zh. Éksp. Teor. Fiz. **34**, 1548 (1957) [Sov. Phys. JETP **7**, 1068 (1958)].
¹⁰A. F. Aleksandrov, V. V. Zosimov, S. P. Kurdyumov *et al.*, Zh. Éksp. Teor. Fiz. **61**, 1841 (1971) [Sov. Phys. JETP **34**, 979 (1971)].
¹¹V. V. Korneev, A. N. Lobanov, and K. N. Ul'yanov, Élektrichestvo, No. 9, 25 (1984).
¹²Yu. K. Bobrov, V. V. Vikhrev, and I. N. Fedotov, Fiz. Plazmy **14**, 1222 (1988) [Sov. J. Plasma Phys. **14**, 715 (1988)].
¹³Yu. K. Bobrov, V. V. Vikhrev, and I. N. Fedotov, Tekh. Élektroin., No. 3, 3 (1988).
¹⁴V. P. Korobeinikov, *Problems in the Theory of Point Explosions* [in Russian] Nauka, Moscow, 1985.
¹⁵S. V. Dresvin, *Fundamentals of the Theory and Design of High-Frequency Plasmotrons* [in Russian] Énergoatomizdat, Leningrad, 1991.
¹⁶Ya. B. Zel'dovich and Yu. P. Raizer, *Physics of Shock Waves and High-Temperature Hydrodynamic Phenomena*, Vols. 1 and 2, transl. of 1st Russ. ed. [Academic Press, New York, 1966, 1967]; 2nd ed., Nauka, Moscow, 1966].
¹⁷Yu. Yu. Abramov, É. A. Azizov, and S. G. Solodovnikov, Fiz. Plazmy **15**, 1128 (1989) [Sov. J. Plasma Phys. **15**, 655 (1989)].
¹⁸M. N. Shneider, Pis'ma Zh. Tekh. Fiz. **21**(19), 10 (1995) [Tech. Phys. Lett. **21**, 771 (1995)].
¹⁹V. N. Desnyanskiĭ and E. A. Novikov, Prikl. Mat. Mekh. **38**, 507 (1974).
²⁰N. M. Kuznetsov, *Thermodynamic Functions and Shock Adiabats of Air at High Temperatures* [in Russian] Mashinostroenie, Moscow, 1965.
²¹Yu. P. Raizer, *Physics of the Gas Discharge* [in Russian] Nauka, Moscow, 1987.

Translated by James S. Wood

Experimental investigations of the formation of $\text{XeF}^*(B^2\Pi_{1/2})$ excimer molecules during the injection of SF_6 into a xenon plasma flow

A. A. Alekhin, V. A. Barinov, Yu. V. Geras'ko, O. F. Kostenko, F. N. Lyubchenko, and A. V. Tyukavkin

Central Scientific-Research Institute of Mechanical Engineering, 141070 Kaliningrad, Moscow District, Russia

(Submitted June 4, 1996; resubmitted August 21, 1997)

Zh. Tekh. Fiz. **68**, 36–42 (February 1998)

The luminescence of $\text{XeF}^*(B^2\Pi_{1/2})$ molecules from a zone formed in the injection of SF_6 gas into a freely flowing xenon plasma jet is investigated. The experiments show that both the energy characteristics of the luminescence and the geometrical dimensions of the plasma-chemical reaction zone can be controlled by varying the power input to the plasmatron and the mass flow rates of SF_6 and the xenon plasma. It is shown that the main contribution to the production of $\text{XeF}^*(B^2\Pi_{1/2})$ excimer molecules under the given experimental conditions is from two-particle ion-ion reactions involving Xe ions and SF_6^- and SF_5^- molecular ions. © 1998 American Institute of Physics. [S1063-7842(98)00702-8]

INTRODUCTION

Studies of the formation and luminescence of excimer molecules during the injection of halogen-containing substances into a plasma jet flowing freely into vacuum^{1–3} have demonstrated the highly efficient conversion of plasma flow energy into the narrowband emission of ultraviolet radiation from excimer molecules. The highest radiated output power is reported in Refs. 2 and 3 for the injection of halides of alkali metals into a xenon or krypton plasma jet. In the same papers it is assumed that the high efficiency of formation of excimer molecules in the experiments is attributable to the identical ground-level electronic structure of the alkali-metal halides and excimer molecules.

Consequently, it would be of utmost interest to investigate the processes of formation of excimer molecules using halogen carriers whose molecules have an electronic structure different from that of alkali-metal halides. The halogen carrier chosen for the present study is a dielectric gas (sulfur hexafluoride SF_6) widely used in excimer lasers.⁴

EXPERIMENT

The production of $\text{XeF}^*(B^2\Pi_{1/2})$ excimer molecules in the interaction of a supersonic xenon plasma flow with a subsonic dielectric gas (SF_6) jet injected into it was investigated on apparatus described in detail in Refs. 1 and 5. The plasma source was a magnetoplasma-dynamic accelerator with a plasma beam of diameter 60 mm at the orifice of the accelerator anode. The residual pressure in the vacuum chamber was ≈ 1 Pa. The xenon plasma ion temperature during the experiments varied in the interval $T_i = 2000$ –2500 K, and the electron temperature had values $T_e = 1$ –1.5 eV. The concentration of the xenon plasma at the SF_6 injection point was between 10^{14} and 5×10^{15} cm⁻³. The mass flow rate of SF_6 in the experiment varied in the interval $G[\text{SF}_6] = 0.5$ –2 g/s, and the flow rate of xenon through the plasmatron was $G[\text{Xe}_e] = 0.5$ –5 g/s. The plasma flow veloc-

ity varied between the limits 1000–2000 m/s and was minimum at high xenon mass flow rates and maximum at the minimum xenon mass flow rate.

The SF_6 was injected into the xenon plasma in a bilateral two-stream mixing configuration (Fig. 1) symmetrical about the axis of the plasma jet at a distance of 250 mm from the orifice of the plasmatron anode. The SF_6 injector consisted of two graphite tubes of length 230 mm, diameter 16 mm, and wall thickness 3 mm situated perpendicular to the axis of the plasma jet in such a way as to pass the plasma jet between them. The distance between the tubes was about 60 mm. Holes of diameter 0.7 mm pointing toward the axis of the plasma jet were drilled into the side of the walls at 5-mm intervals.

Over the entire range of plasma parameters and SF_6 mass flow rates used in the experiments a plasma-chemical reaction zone was formed within the mixing zone of the xenon plasma and SF_6 flows, the formation of $\text{XeF}^*(B^2\Pi_{1/2})$ molecules taking place in this reaction zone; a typical luminescence spectrum of these molecules is shown in Fig. 2.

The $\text{XeF}^*(B^2\Pi_{1/2})$ luminescence spectrum were recorded by the standard technique for the reported investigations.^{1–3} The recorded plasma luminescence spectra were normalized to the spectral sensitivity curve of the measurement system.

The spatial distribution of the luminescence intensity distribution of the $\text{XeF}^*(B^2\Pi_{1/2} \rightarrow X^2\Sigma)$ along the plasma jet (Fig. 3 had the same form as in experiments aimed at studying the luminescence of XeCl^* molecules during the injection of CCl_4 into a xenon plasma.¹ The luminescence intensity (concentration) distribution curves of XeF^* molecules along the axis of the plasma flow were typical in all the experimental series: Beginning at the orifice of the plasmatron anode, the background radiation level corresponding to continuous emission from the plasma was recorded (Fig. 3a). Farther downstream in the plasma, in line with the axis of

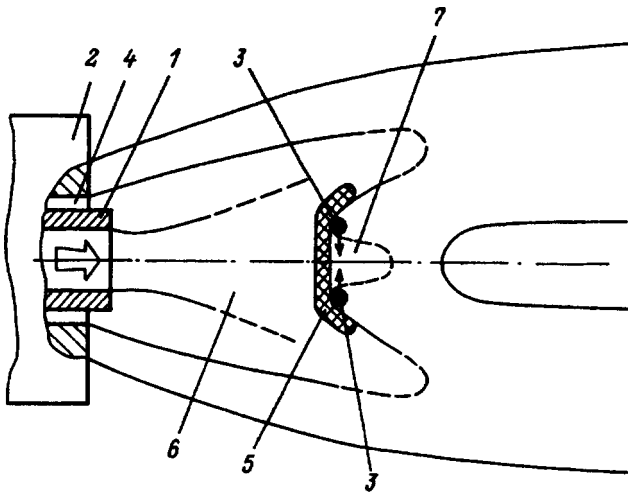


FIG. 1. Diagram of the bilateral two-stream injection of SF₆ into a xenon plasma. 1) Plasmatron anode; 2) magnetic coil of the plasmatron; 3) SF₆ injectors; 4) gap between the anode and the magnetic coil; 5) normal compression shock; 6) plasma jet; 7) plasma-chemical reaction zone.

observation of the optical measurement system, the luminescence intensity of the plasma at the wavelength $\lambda = 351$ nm ($B^2\Pi_{1/2} \rightarrow X^2\Sigma$ transition of the XeF* molecule) began to increase abruptly, corresponding to the initiation of plasma-chemical reactions in the mixing zone of the xenon plasma flow with the cold SF₆ gas. Farther downstream in the plasma the emission level in the $B^2\Pi_{1/2} \rightarrow X^2\Sigma$ band of the XeF* molecule reached its maximum, whereupon the luminescence intensity of the XeF* ($B^2\Pi_{1/2} \rightarrow X^2\Sigma$) molecular band began to fall off more or less gradually.

The length of the plasma-chemical reaction zone (Figs. 3b and 3c) where the XeF* ($B^2\Pi_{1/2}$) molecules were formed, measured along the half-maximum boundary of the XeF* ($B^2\Pi_{1/2}$) luminescence at the wavelength $\lambda = 351$ nm, varied along the plasma flow in the range $\Delta L_x = 20 - 60$ mm. The transverse width of the mixing zone was $\Delta L_y = 55 - 50$ mm in the injection cross section and decreased by 35–40% toward its downstream boundary in the plasma. In this case the length ΔL_x of the zone of luminescence of the XeF* ($B^2\Pi_{1/2}$) molecules increased as the power input to the plasmatron was increased. The length

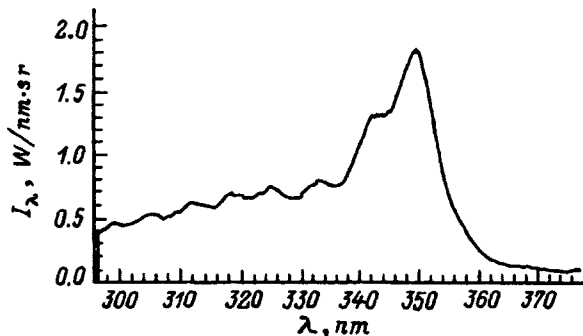


FIG. 2. Luminescence spectrum of XeF* molecules in the center of the plasma-chemical reaction zone during the mixing of a xenon plasma jet with a SF₆ gas flow injected perpendicularly into it, $N_i = 5 \times 10^{14}$ cm⁻³, $T_i = 2200$ K, $T_e = 1.4$ eV.

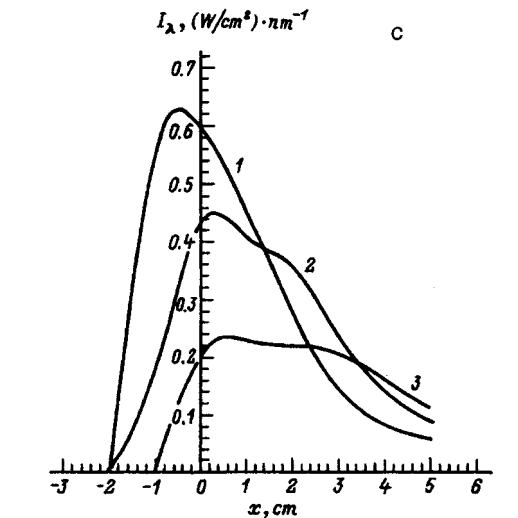
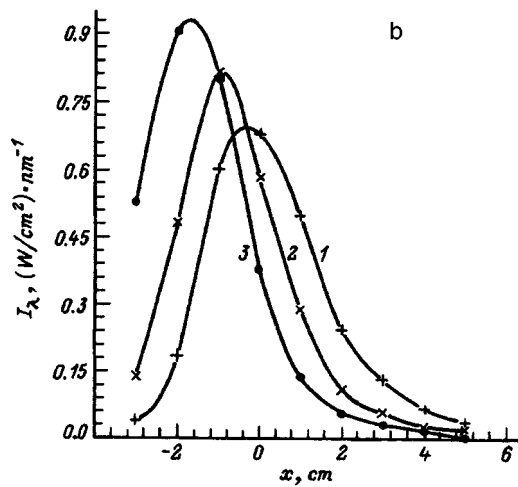
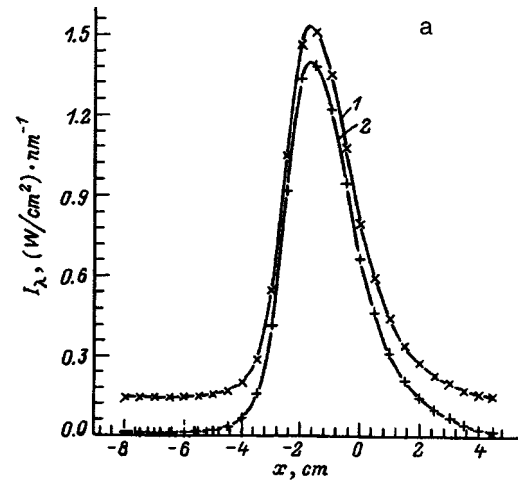


FIG. 3. Distribution of the luminescence intensity of XeF* molecules ($\lambda = 351$ nm) along the xenon plasma flow in the plasma-chemical reaction zone. a) The coordinates of the SF₆ injection point correspond to point 2 on the ordinate axis; $G[\text{SF}_6] = 2.0$ g/s, $G[\text{Xe}] = 1$ g/s, $N_{\text{Xe}} = 8 \times 10^{14}$ cm⁻³, $T_i = 2000$ K, $T_e = 1.2$ eV: 1) luminescence of the XeF* molecular band together with the continuous luminescence of the plasma; 2) luminescence of the XeF* molecular band; b) the coordinates of the SF₆ injection point correspond to point 1 on the ordinate axis, $G[\text{Xe}] = 0.5$ g/s, $I = 1000$ A, $N_{\text{Xe}} = 5 \times 10^{14}$ cm⁻³, $T_i = 2300$ K, $T_e = 1.4$ eV: 1) $G[\text{SF}_6] = 0.57$ g/s; 2) 1.0 g/s; 3) 2.0 g/s; c) the coordinates of the SF₆ injection point correspond to point 0 on the ordinate axis, $G[\text{Xe}] = 5$ g/s, $I = 1500$ A, $N_{\text{Xe}} = 5 \times 10^{15}$ cm⁻³, $T_i = 2000$ K, $T_e = 1.0$ eV: 1) $G[\text{SF}_6] = 2.0$ g/s; 2) 1.0 g/s; 3) 0.5 g/s.

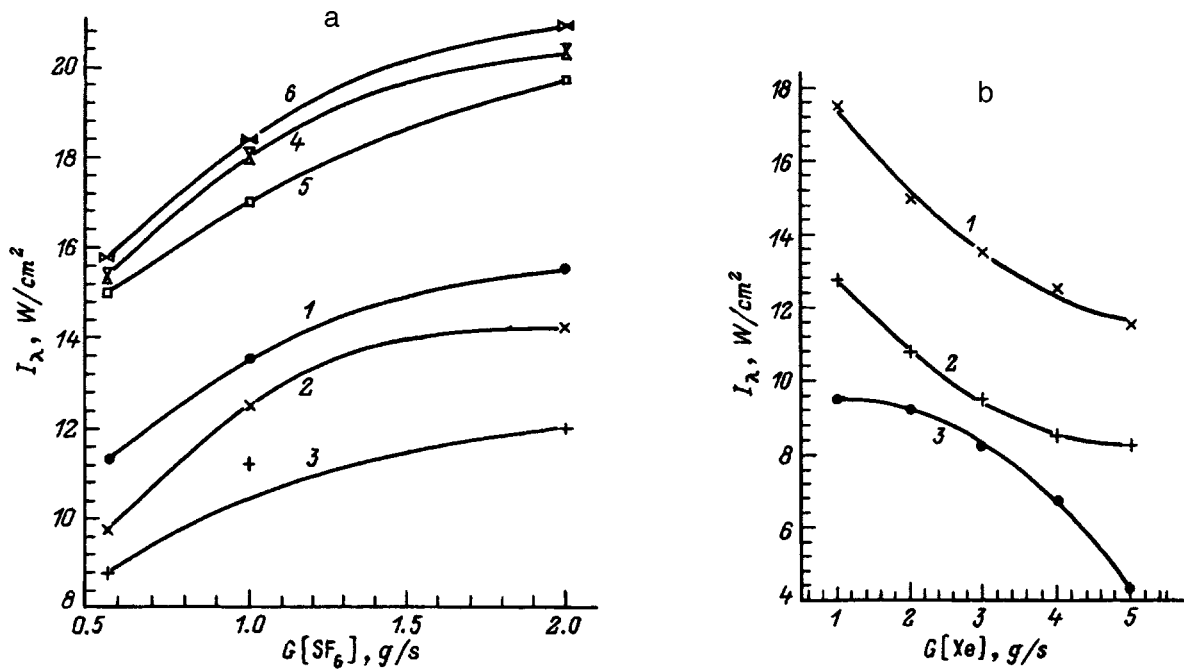


FIG. 4. Luminescence intensity of the XeF^* ($\lambda = 351$ nm) at the peak of the molecular band versus the mass flow rate of SF_6 (a) and versus the xenon plasma flow rate at $G[SF_6]=2$ g/s (b). a: 1,4) $W=32$ kW; 2,5) 42 kW; 3,6) 48 kW; 1-3) $G[Xe]=0.5$ g/s; 4-6) 1.0 g/s. b: 1) $W=32$ kW, $T_i=1800$ K, $T_e=0.8$ eV; 2) 48 kW, 2000 K, 1.0 eV; 3) 74 kW, 2300 K, 1.3 eV.

ΔL_x of the plasma-chemical reaction zone was influenced only slightly by variation of the xenon flow rate through the plasmatron, whereas ΔL_x decreased substantially when the mass flow rate of SF_6 injected into the plasma jet was reduced. This fact indicates that the length ΔL_x of the plasma-chemical reaction zone depends not only on the "burnout" of xenon ions in the reactions of formation of $XeF^*(B^2\Pi_{1/2})$ excimer molecules, but also quite strongly on the gase-dynamic mixing pattern of the supersonic xenon plasma flow with the SF_6 gas flow injected perpendicularly into it. The rate of decrease of the luminescence intensity of the $XeF^*(B^2\Pi_{1/2})$ molecules downstream in the plasma also differed, depending on the experimental conditions, and for xenon flow rates of 5 g/s and SF_6 flow rates of 0.5 g/s a plateau was recorded in the distribution of the luminescence intensity of the $B^2\Pi_{1/2} \rightarrow X^2\Sigma$ transition of the XeF^* molecule along the plasma flow (Fig. 3c).

The spatial position of the luminescence intensity maximum of the $XeF^*(B^2\Pi_{1/2})$ molecules in the flow mixing zone differed, depending mainly on the mass flow rate of the injected halogen carrier. For example, for high SF_6 flow rates ($G[SF_6] \geq 1$ g/s) the luminescence maximum shifted downstream along the plasma flow toward the plasmatron relative to the point of injection of the halogen carrier. The maximum shift encountered in the experiments was $\Delta l \approx 10$ mm at $G[SF_6]=2$ g/s. At medium flow rates of the halogen carrier ($G[SF_6]=1$ g/s) the position of the luminescence maximum of the $XeF^*(B^2\Pi_{1/2})$ molecules roughly coincided with the coordinates of the point of injection of the halogen carrier. With a further reduction in the SF_6 flow rate the luminescence maximum of the $XeF^*(B^2\Pi_{1/2})$ excimer molecules shifted along the xenon plasma flow below the halogen carrier injection point. Consequently, as in the injection of CCl_4

vapor,¹ at high SF_6 flow rates a gas target is formed in the injection zone, where the generation of a normal compression shock is accompanied by slowing of the incident plasma flow. Plasma-chemical reactions then take place behind the shock front as a result of diffusion of the xenon plasma into the SF_6 gas target under subsonic gas flow conditions. At low halogen-carrier flow rates the gas target is diffused by the incident plasma flow, and plasma-chemical reactions take place with diffusion of the subsonic SF_6 flow into the supersonic xenon plasma flow.⁶

The maximum brightness of the mixing zone in the $B^2\Pi_{1/2} \rightarrow X^2\Sigma$ band of the XeF^* molecule increased with the mass flow rate of the dielectric gas, irrespective of the power input to the plasma jet and the flow rate of the working medium through the plasmatron (Fig. 4a). For a fixed power input to the plasmatron and low xenon flow rates ($G[Xe] \leq 1$ g/s) the luminescence intensity of the plasma-chemical reaction zone increased with the xenon flow rate, attaining a maximum value $I_\lambda \approx 18$ W/cm^2 at $G[Xe]=1$ g/s ($G[SF_6]=2$ g/s). With a further increase in the xenon flow rate at $G[Xe] \geq 1$ g/s (Fig. 4b) the maximum luminescence intensity of the plasma-chemical reaction zone at $G[Xe]=5$ g/s for a power input to the plasmatron $W=74$ kW dropped to $I_\lambda \approx 4$ W/cm^2 .

Measurements of the power characteristics of the radiation from the $XeF^*(B^2\Pi_{1/2})$ molecules at the point in space corresponding to maximum luminescence of the excimer molecules showed that for high xenon flow rates through the plasmatron ($G[Xe]=2-5$ g/s) the output luminescence intensity increased almost linearly as the power input to the plasma was increased (Fig. 5a, curves 2 and 3). On the other hand, at a Xe flow rate $G[Xe]=1$ g/s and a power input to

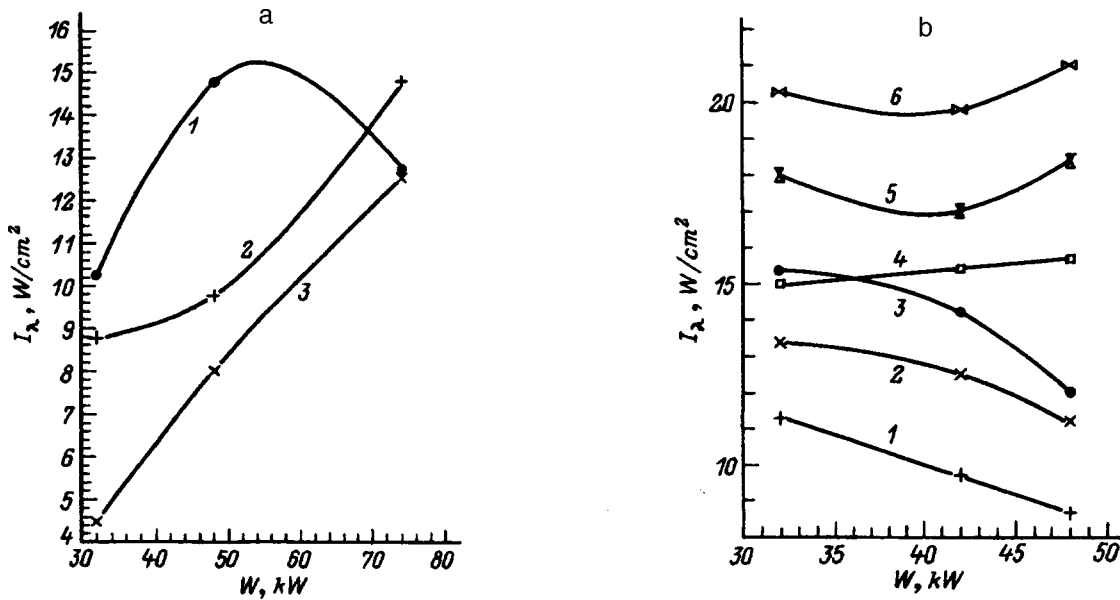


FIG. 5. Luminescence intensity of the XeF^* ($\lambda=351$ nm) at the peak of the molecular band versus power input to the plasmatron. a) $G[Sf_6]=2$ g/s: 1) $G[Xe]=1.0$ g/s; 2) 2.5 g/s; 3) 5.0 g/s. b: 1,4) $G[Sf_6]=0.57$ g/s; 2,5) 1.0 g/s; 3,6) 2.0 g/s; 1–3) $G[Xe]=0.5$ g/s; 4–6) 1.0 g/s.

the plasmatron >55 kW the luminescence intensity of the $XeF^*(B^2\Pi_{1/2})$ excimer molecules began to drop abruptly (curve 1 in Fig. 5a).

Experiments performed at low xenon flow rates $G[Xe]=0.5-1$ g/s showed that in the range of power inputs to the plasma $W=30-50$ kW and for $G[Xe]=0.5$ g/s a slight reduction in the brightness of $XeF^*(B^2\Pi_{1/2})$ was observed as the power input was increased, irrespective of the flow rates of the halogen carrier (curves 1–3 in Fig. 5b). At $G[Xe]=1$ g/s for each fixed value of the halogen-carrier flow rate (curves 4–6 in Fig. 5b), irrespective of the power input, the luminescence intensity of the $XeF^*(B^2\Pi_{1/2})$ molecules changed insignificantly, tending to increase very slightly. Allowing for the fact that the length of the plasma-chemical reaction zone increases as the power input to the plasmatron is increased, we can state that the total output energy increases only slightly with increasing power input at moderate xenon flow rates ($G[Xe]\approx 1$ g/s), definitely increases at high xenon flow rates ($G[Xe]\geq 2$ g/s), and decreases at low xenon flow rates ($G[Xe]\leq 1$ g/s) through the plasmatron.

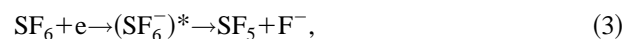
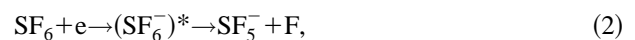
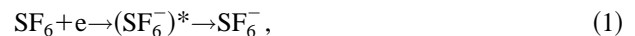
The maximum integrated luminescence power of the plasma-chemical reaction zone, equal to 270 W at a spectral luminescence intensity of $XeF^*(B^2\Pi_{1/2})$ molecules from the surface of the plasma-chemical reaction zone $I_\lambda \approx 21$ W/cm^2 , was attained for a power input to the plasmatron $W \approx 55$ kW, a xenon flow rate $G[Xe]=1$ g/s, and a halide flow rate $G[Sf_6]=2$ g/s.

DISCUSSION OF THE RESULTS

The above-described experiments have shown that both the brightness characteristics of the emitted radiation and the dimensions of the luminescence zone can be controlled by varying the mass flow rates of the components and the power input to the plasmatron. On the other hand, the integrated luminescence power of the plasma-chemical reaction zone in

the reported experiments is more than an order of magnitude lower than the parameters achieved in the injection of NaCl (Ref. 2). A qualitative analysis of the main processes involved in such a medium is carried out below to ascertain the causes of such a distinct difference.

The kinetics of the processes in the zone of injection of Sf_6 into the xenon plasma flow and the mechanism underlying the formation of excimer molecules differ significantly from the plasma-chemical processes in earlier studies.¹⁻³ Indeed, in the mixing zone of the Sf_6 with the xenon plasma flow, the first one or two collisions of an electron with a sulfur hexafluoride Sf_6 molecule as a result of the dissociative attachment reactions



which take place at $T_e=0.1-1$ eV with large cross sections,⁷ cause plasma electrons to bind to fluorine-containing components. The rate constant of electron attachment to a Sf_6 molecule with the production of an excited negative $(Sf_6^-)^*$ ion is high, $k_a=1.5 \times 10^{-6}-9 \times 10^{-8}$ cm^3/s at $T_e=0.1-1$ eV (Ref. 8). The attachment rate constant k_a depends weakly on the Sf_6 temperature T_x . The temperature T_x affects only the balance of Sf_6^- and Sf_5^- yields in the reactions (1) and (2). For example, the reaction (1) prevails for $T_x \approx 0.1$ eV, and the reaction (2) prevails for $T_x \approx 1$ eV (Ref. 8).

It is essential to note that the excited state of the negative molecular ion $(Sf_6^-)^*$ has a long lifetime, and the reaction (1) proceeds in two stages, i.e., the deactivation of the intermediate $(Sf_6^-)^*$ complex takes place predominantly as a result of collisions with a second particle:



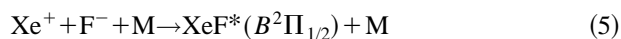
and the radiative deexcitation of the $(SF_6^-)^*$ complex is of minor status.⁷ Under the experimental conditions, therefore, there must be a large quantity of $(SF_6^-)^*$ in the zone of luminescence of the excimer molecules (the density of the medium $N \leq 10^{16} \text{ cm}^{-3}$).

The formation of free electrons in the zone of luminescence of the components due to the ionization of neutral components and negative plasma ions by electron impact can be ignored by virtue of the small cross section of such reactions and rapid cooling of the electrons in the excitation of vibrational states of the SF_6 molecules.

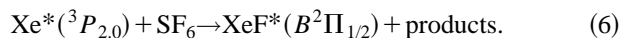
The variation of the component constituency of the luminescing regions on account of charge-transfer reactions of negative ions at neutral components of the plasma can also be disregarded in our case.^{9,10}

The mass flow rates of the xenon plasma and the SF_6 gas were close in our experiments, and SF_6 injection took place in a zone of area amounting to less than 20% of the cross section of the plasma flow at the injection point, so that the partial flow rate of free plasma electrons through the injection zone was always lower than the partial flow rate of SF_6 . Consequently, mainly the reactions (1) and (2) with the formation of negative molecular ions SF_6^- and SF_6^- and an excited negative $(SF_6^-)^*$ ion take place in the medium at the start of mixing, and these particles begin to interact with the plasma components Xe^+ and Xe , the halogen carrier SF_6 , and the neutral products of dissociation of SF_6 . It should be noted that the presence of a large number of negative molecular ions in the luminescing medium leads to the absorption the radiation from the excimer molecules in processes of photodissociation of the molecular ions.⁸ This is one of the factors that degrades the spectral characteristics of radiation from the plasma-chemical reaction zone.

We now consider possible channels of formation of excimer molecules in such a medium. The traditional assumption⁴ is that excimer molecules can be produced from two principal reactions: the three-particle reaction

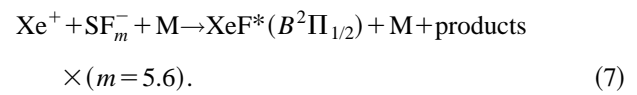


and the two-particle harpoon reaction



Under the conditions established in experiments with a degree of ionization $\alpha \approx 1$ the density of metastable $Xe^*(^3P_{2,0})$ atoms in the medium is low,⁶ the rate constant of the reaction (6) is also small,^{11,12} and the contribution of the reaction (6) to the production of excimer molecules is insignificant.

Bearing in mind that primarily negative molecular ions SF_6^- and SF_6^- and excited negative $(SF_6^-)^*$ ions are generated by the attachment reaction is (1)–(3), the F^- concentration in the mixing zone is low, and the reaction (5) is incapable of sustaining the experimentally observed luminescence intensity of the excimer molecules. It has therefore been assumed¹³ that the main contribution to the production of excimer molecules in the medium formed by the injection of SF_6 into an inert-gas plasma flow is from the three-particle ion–ion reactions



The stated assumption seems dubious. The reaction (7) unquestionably contributes to the integrated luminescence power of the flow mixing zone, but for the actual densities of the medium in our experiments, $N \leq 10^{16} \text{ cm}^{-3}$, and certainly under the experimental conditions reported in Ref. 13, where $N \leq 10^{14} \text{ cm}^{-3}$, binary collisions are prevalent in the medium, and three-particle reactions are impossible candidates for the production of $XeF^*(B^2\Pi_{1/2})$.

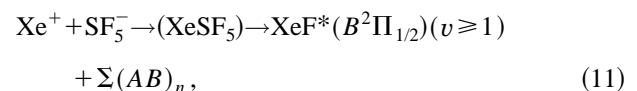
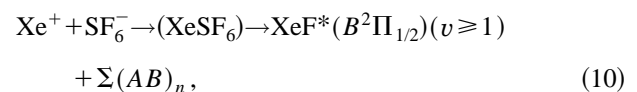
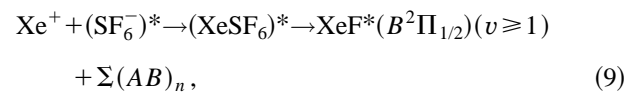
Moreover, the experimentally determined graphs of the luminescence intensity of $XeF^*(B^2\Pi_{1/2})$ show (Fig. 5b, curve 1) that for low xenon flow rates through the plasmatron the luminescence intensity of $XeF^*(B^2\Pi_{1/2})$ begins to decrease as the power input to the plasma increases, causing the degree of ionization and the ion and electron temperatures of the plasma flow to increase accordingly. This behavior completely contradicts the assumption of a three-particle mechanism underlying the production of $XeF^*(B^2\Pi_{1/2})$ in plasma-chemical reactions, because the rate constant of three-particle reactions increases with the temperature.

In contrast with Refs. 2 and 3, the ion–molecular reactions



where $(AB)_n$ denotes the reaction products, $n \geq 1$, $m \leq 6$, and $(XeSF_m)$ is an intermediate ion complex, do not take place in the medium, being ruled out by energy considerations.

The most probable channel of production of $XeF^*(B^2\Pi_{1/2})$ molecules in plasma-chemical reactions under the given experimental conditions could be the two-particle reactions



in which v is the vibrational quantum number, and the formation of $XeF^*(B^2\Pi_{1/2})$ ($v \geq 1$) takes place through the intermediate neutral complex $(XeSF_m)$, $m = 5, 6$.

The cross sections of the formation of intermediate complexes in the reactions (9)–(11) are determined on the basis of an ion–ion recombination model.¹⁴ The decay of the intermediate complexes by the channels (9)–(11) with the formation of an excited XeF^* molecule is estimated using a statistical model of two-particle reactions x , and the probability of such decay is $P_0 \approx 0.01$ (Ref. 15). The rate constant of the reactions (9)–(11) is calculated from the equation

$$k_0 = \frac{e^4}{4\pi\mu^{1/2}\epsilon_0^2} (3kT_i)^{-3/2}, \quad (12)$$

where ϵ_0 is the dielectric constant, and μ is the reduced mass of the ion-ion reaction; the values of the rate constant are $k_0 = 2 \times 10^{-9}$ cm³/s at $T_i = 0.1$ eV and $k_0 = 5 \times 10^{-9}$ cm³/s at $T_i = 1$ eV.

The results of estimates from Eq. (12) are close to the experimentally measured^{11,12} rate constants for reactions similar to (9)–(11).

The rate constants of the ion-ion reactions decrease as the temperature increases, consistent with the experimental results (Fig. 5b, curve 1). Moreover, the half-width of the luminescence band of the XeF* molecules is $\Delta\lambda \approx 15$ nm, and the molecular band has a long ($\Delta\lambda \approx 70$ nm tail on the short-wavelength side (Fig. 2). This profile implies that the production of XeF*($B^2\Pi_{1/2}$) molecules takes place in high vibrational states ($v \geq 1$), a condition that by and large conforms to two-particle reactions, where the energy deficit in the reaction is spent mainly in the excitation of vibrational states.

Consequently, the main contribution to the production of XeF*($B^2\Pi_{1/2}$) excimer molecules in the reported experiments is from the reactions (9)–(11), which takes place at rates close to those of gas-kinetic processes. The reaction rate constants are lower than for halides of alkali metals,³ and this fact together with the presence of a large number of negative molecular ions in the medium also leads to degradation of the radiation characteristics of the plasma-chemical reaction zone.

CONCLUSION

We have investigated the luminescence of XeF*($B^2\Pi_{1/2}$) molecules from a zone formed during the injection of SF₆ gas into a freely flowing xenon plasma jet. The maximum luminescence intensity of the XeF*($B^2\Pi_{1/2}$) molecules is 270 W for a spectral from the surface of the plasma-chemical reaction zone $P_\lambda \approx 21$ W/cm².

The reported series of experimental investigations has shown that both the energy characteristics of the luminescence and the geometrical dimensions of the plasma-chemical reaction zone can be controlled by varying the power input to the plasmatron and the mass flow rates of SF₆ and the xenon plasma.

We have shown that the main channel of production of XeF*($B^2\Pi_{1/2}$) excimer molecules under the given experimental conditions comprises two-particle ion-ion reactions involving Xe ions and molecular ions SF₆⁻ and SF₅⁻.

We have shown that the degradation of the integrated and spectral characteristics of luminescence from the Xe-plasma-SF₆ mixing zone in comparison with the injection of alkali-metal halides is attributable to the presence of a large number of negative ions of molecular gases in the medium and the lower rate constant for the production of excimer molecules.

¹A. A. Alekhin, V. A. Barinov, Yu. V. Geras'ko *et al.*, Zh. Tekh. Fiz. **63**(2), 65 (1993) [Tech. Phys. **38**, 91 (1993)].

²A. A. Alekhin, V. A. Barinov, Yu. V. Geras'ko *et al.*, Zh. Tekh. Fiz. **63**(2), 43 (1993) [Tech. Phys. **38**, 80 (1993)].

³A. A. Alekhin, V. A. Barinov, Yu. V. Geras'ko *et al.*, Zh. Tekh. Fiz. **65**(5), 9 (1995) [Tech. Phys. **40**, 409 (1995)].

⁴*Excimer Lasers*, edited by C. K. Rhodes [Springer-Verlag, New York, 1979; Mir, Moscow, 1981].

⁵V. V. Volchkov, A. G. Znak, V. F. Kuzovlev *et al.*, Kosmonavt. Raketost., No. 2, 86 (1994).

⁶O. F. Kostenko and A. V. Tyukavkin, *Theoretical and Experimental Studies of Problems in General Physics* [in Russian] (TsNIIMash, 1991), pp. 3–9.

⁷D. I. Slovetskii and A. A. Deryugin, in *Plasma Chemistry* [in Russian], edited by B. M. Smirnov, No. 13 (Energoatomizdat, Moscow, 1987), pp. 240–277.

⁸P. J. Chantry, in *Applied Atomic Collision Physics*, Vol. 3, edited by E. W. McDaniel and W. Nigan [Academic Press, New York, 1982; Mir, Moscow, 1986].

⁹Y. Wang, R. L. Champion, L. D. Doverspike *et al.*, J. Chem. Phys. **91**, 2254 (1989).

¹⁰Y. Wang, R. L. Champion, L. D. Doverspike *et al.*, J. Chem. Phys. **91**, 2254 (1989).

¹¹M. Tsuji, M. Furusawa, and Y. Nishimura, Chem. Phys. Lett. **166**, 363 (1990).

¹²M. Tsuji, M. Furusawa, and Y. Nishimura, J. Chem. Phys. **92**, 6502 (1990).

¹³V. S. Rogulich, V. P. Starodub, and V. S. Shevera, Opt. Spektrosk. **69**, 201 (1975) [Opt. Spectrosc. (USSR) **69**, 450 (1975)].

¹⁴B. M. Smirnov, *Atomic Collisions and Elementary Processes in a Plasma* [in Russian] Atomizdat, Moscow, 1968.

¹⁵V. N. Kondrat'ev, E. E. Nikitin, A. I. Reznikov, and S. Ya. Umanskiĭ, *Thermal Bimolecular Reactions in Gases* [in Russian] Nauka, Moscow, 1976.

Characteristics of the clustered structure of $\text{Pb}(\text{Li}, \text{La})(\text{Zr}_{1-y}\text{Ti}_y)\text{O}_3$ in the antiferroelectric–ferroelectric transition region

Z. A. Samoilenko, V. P. Pashchenko, V. M. Ishchuk, O. P. Cherenkov, and E. I. Pushenko

Donetsk Physicotechnical Institute, National Academy of Sciences of Ukraine, 340114 Donetsk, Ukraine
(Submitted August 20, 1996; resubmitted January 23, 1997)

Zh. Tekh. Fiz. **68**, 43–47 (February 1998)

Mesoscopic inhomogeneities and their influence on the behavior of the physical properties (optical reflectivity, dielectric constant, and Curie temperature) of a system of lead zirconate–titanate $\text{Pb}_{0.85}(\text{Li}_{1/2}\text{La}_{1/2})_{0.15}(\text{Zr}_{1-y}\text{Ti}_y)\text{O}_3$ solid solutions are investigated. It is established that the disruptions of long-range order have a mesoscopic scale and generate ion groups in the form of interlayers of elements of binary-oxide planes coherently embedded in the crystal structure of the host phase. It is shown that the clustering of the structure is manifested in nonlinearity of the physical properties of the lead zirconate–titanate solid solutions, where the most pronounced variations are characteristic of the coexistence region of the antiferroelectric and ferroelectric phases. © 1998 American Institute of Physics.
[S1063-7842(98)00802-2]

INTRODUCTION

One of the most timely problems in solid state physics is the study of inhomogeneities of real structures and their influence on the physical properties of matter. Of special interest in this regard are mesoscopic-scale inhomogeneities, which in recent times have been observed experimentally in metal-oxide magnets^{1,2} and in disordered amorphous alloys.³

Here we give the results of an investigation of mesoscopic inhomogeneities in a system of solid solutions based on lead zirconate–titanate $\text{Pb}_{0.85}(\text{Li}_{1/2}\text{La}_{1/2})_{0.15}(\text{Zr}_{1-y}\text{Ti}_y)\text{O}_3$ (we designate the composition of the solid solution by PLLZT 15/100– y/y), where y is the percent content of titanium. A composition–temperature (y – T) diagram of the phase states of this PLLZT series is shown in Fig. 1 (the results of a detailed investigation of the phase diagrams of the PLLZT system of solid solutions are given in Refs. 4–7). For a titanium content $y < 20\%$ the low-temperature state of the solid solutions is antiferroelectric (region AFE_T in Fig. 1), and for $y > 25\%$ it is ferroelectric (FE_R in Fig. 1). At temperatures below the phase transition point, solid solutions in the first interval of titanium compositions are characterized by tetragonal distortions of the unit cell, and those in the second interval are characterized by rhombohedral distortions.^{4–6,8}

Solid solutions in the intermediate range of titanium compositions ($20 < y < 25$, hatched region in Fig. 1) are characterized by a small energy difference between the ferroelectric and antiferroelectric states, and transitions between these states can be easily induced by external means: the application of an electric field or pressure. Coexistence of the ferroelectric and antiferroelectric phases is also characteristic of these solutions.

Our objective is to investigate mesoscopic inhomogeneities in solid solutions of the indicated composition and their influence on the behavior of certain physical properties: the

optical reflectivity r , the dielectric constant ε , and the Curie temperature T_c .

EXPERIMENTAL PROCEDURE

The mesoscopic structure was analyzed by an x-ray technique utilizing Debye-Scherrer powder-pattern photography in Cr-filtered $K\alpha$ radiation. An RKD x-ray diffraction camera was used. Thin sections were used for the photography; the diffraction patterns of each sample were recorded twice: once with the sample tilted at the angle $\psi_1 = 25^\circ$ and again at the angle $\psi_2 = 45^\circ$, focusing the diffraction orders in the intervals $\Theta_I = 20^\circ - 30^\circ$ and $\Theta_{II} = 40^\circ - 50^\circ$.

Each photograph was made with a 1-h exposure. The profiles and total intensities of the lines and diffuse bands were determined by microphotometry of the x-ray photographs. The x-ray photographs contain narrow Debye lines corresponding to the perovskite lattice of the investigated solid solutions, along with weaker diffuse bands (halos I and II) situated in the intervals of angles $\Theta_I = 25^\circ - 29^\circ$ and $\Theta_{II} = 45^\circ - 51^\circ$ after the (220) and (422) lines, respectively.

Adopting the volume of all coherently scattered centers of each of the indicated families of planes as 100%, we investigated the degree of disorder $\xi(\%)$ by estimating the volume fraction of clustered ions situated in the corresponding families of (220) and (422) planes and manifested by halos I and II, using the relations

$$\xi_I = \frac{N_{\text{Cl}}}{N}(220) = \frac{I_{\text{dif I}}}{I_{220} + I_{\text{dif I}}} 100\%$$

and, similarly,

$$\xi_{II} = \frac{N_{\text{Cl}}}{N}(422) = \frac{I_{\text{dif II}}}{I_{422} + I_{\text{dif II}}} 100\%.$$

The cluster dimensions m were calculated by the procedure of Ref. 9, using the most distinct diffuse maxima of

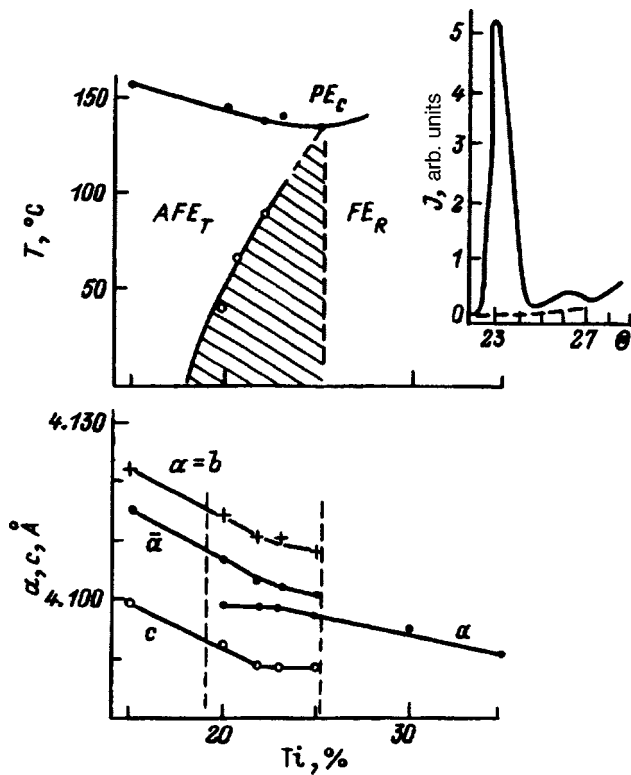


FIG. 1. Diagram of phase states of lead zirconate–titanate solid solutions.^{4,5}

halo I. For a focal spot of radius $r_0 = 1.5$ mm on the sample and a diameter of the x-ray camera $2R = 57$ mm we use the expression

$$\frac{B}{1.5} = \frac{\eta \cdot 19}{0.004 + 0.084 \cos \Theta} + 0.046 \cdot \Theta$$

(where $r_0 = 1.5$, $R/r_0 = 19$, B is the width of the diffuse maximum in millimeters, and Θ is its angular position) to calculate the dimensionless coefficient η , which relates the width B of the diffuse maximum to the cluster length m for the Cr $K\alpha$ radiation used here, through the formula $m = 0.182/\eta$ (Å).

An analysis of the fine structure of the diffuse bands in the angular intervals Θ_I and Θ_{II} for both halos according to the characteristic distribution of interplanar spacings corresponding to the positions Θ of the fluctuation maxima enabled us to trace the concentration redistribution of clustered groups of chemical elements in the domains of the crystal structure as the total composition of the solid solution $\text{Pb}_{0.85}(\text{Li}_{1/2}\text{La}_{1/2})_{0.15}(\text{Zr}_{1-y}\text{Ti}_y)\text{O}_3$ was varied in the interval $15 < y < 35$.

The optical reflectivity r was measured by means of an FOU photometer within error limits $\Delta r = \pm 1.5\%$. The dielectric constant ϵ and the Curie temperature T_c were estimated by standard procedures.^{3,4}

RESULTS AND DISCUSSION

A fragment of a typical diffraction pattern for the investigated pattern exhibiting the Debye–Scherrer line 220 and halo I is shown in Fig. 1. A qualitatively similar diffraction pattern is obtained in the interval of intermediate angles Θ ,

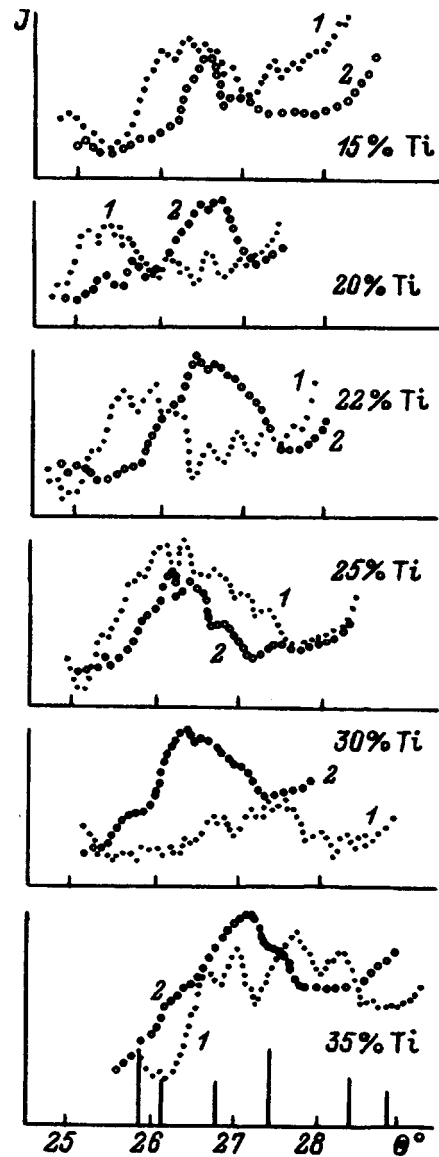


FIG. 2. Variations of the profile and position of the halos in the interval of angles $\Theta = 25^\circ - 29^\circ$. 1) Poled samples; 2) annealed samples. The bottom graph shows nomograms of characteristic structural reflections of ZrO_2 ($25^\circ - 27^\circ$) and TiO_2 ($27^\circ - 29^\circ$).

where the Debye–Scherrer line 422 occurs next to a diffuse scattering peak, which we call halo II. The lines and the halos are both the result of coherent x-ray scattering by scatterer ions with long-range positional order [the (220) and (422) planes] in the first case and with imperfect long-range order (clusters) in the second case.

To study the latter, we have performed a detailed analysis of the diffuse scattering for both halos. It is evident from Fig. 2 that the fine structure of the diffuse band in the interval of angles $\Theta_I = 25^\circ - 29^\circ$ changes significantly both in the profile and in the position of the maximum as the titanium concentration of the sample is increased and also when the sample is subjected to a depoling anneal (650°C , 1 h, cooling in the furnace). It must be borne in mind here that as the Ti concentration y is increased in the depoled samples, the halo shifts from the small-angle interval $\Theta = 25^\circ - 27^\circ$ for $y, 25$ to large-angle interval $\Theta = 27^\circ - 28^\circ$ for $y > 25$. The

ionic radius of Ti^{4+} (0.64 Å) is 21.95% smaller than that of Zr^{4+} (0.82 Å), i.e., by a factor much greater than the critical 15% required for the formation of a continuous series of solid solutions of ionic substitution. This means, first of all, that the shift of the halo toward larger angles Θ for $y > 25$ is evidence of an increase in the concentration fraction of titanium ions relative to zirconium in the corresponding clusters and, second, that these structural formations are influenced by high stresses as a result of local lattice distortions, all of which is conducive to the onset of relaxation processes, during annealing in particular, and is manifested in variations of the interplanar spacings d in the clusters.

The behavior just described is reflected in a decrease of the differences in the angular shifts of the halos of annealed samples, as is evident from the change in d from curves 1 and 2 in Fig. 3. Moreover, as new structural ion groupings evolve in the host solid solution, according to Ref. 10, processes of concentration and topological ordering of different-sized ions must take place with the imposition of new chemical bonds with altered crystallographic parameters in these local regions, which most likely have a quasiplanar geometry [since the radii of the Ti^{4+} , Zr^{4+} , and O^{2-} (1.36 Å) ions¹¹ differ by more than 2%; Ref. 12]. It is logical to assume that clusters of constitutionally simpler—binary—systems of the metal-oxygen type will take shape in these formations with ion packing in the form of a small family of planes of corresponding oxides, for which reflection nomograms are shown in Fig. 2. It can be assumed in light of these considerations that in poled samples, clusters with ion packing in the form of a group of planes specific to TiO_2 are predominant in the ferroelectric range ($y = 30 - 35$), and those with ion packing in the form of a group of planes specific to ZrO_2 are predominant in antiferroelectric samples ($y = 15 - 20$) (Fig. 2). In the ferroelectric–antiferroelectric transition region ($y = 20 - 25$) we encounter groups of planes of both oxides. A regrouping of bonds takes place during annealing, reversing the relative shares of the oxide planes; now the planes specific to ZrO_2 prevail in the ferroelectric range, and those associated with TiO_2 prevail in the antiferroelectric range.

This result underscores the mobile state of ionic order in the clustered planes of the crystal structure and bears witness to the absence of sharp boundaries between the disordered group of ions from the family of planes with broken long-range positional order (clusters) and host-lattice ions that preserve this order. The investigation of the linear dimensions m of the clusters forming halo I reveals that a sharp fragmentation—from 60 Å to 23–30 Å—of the clusters of poled and annealed samples (respectively) takes place in the interval of titanium concentrations $y = 20 - 25$ (Fig. 3).

Consequently, the diffraction pattern reveals regions of distorted crystal structure, spanning $m/d = 15 - 20$ interplanar spacings of the family of (220) planes. In the investigated samples the volume fraction of such regions ξ , which characterizes the degree of disorder in the family of corresponding crystallographic planes, according to our estimates, is 7–10% for halo I and 15–20% for halo II (Fig. 3). Here the dependence of ξ on the Ti concentration in the interval $20 < y < 25$ exhibits an extremal character with minima $\xi_I = 5$

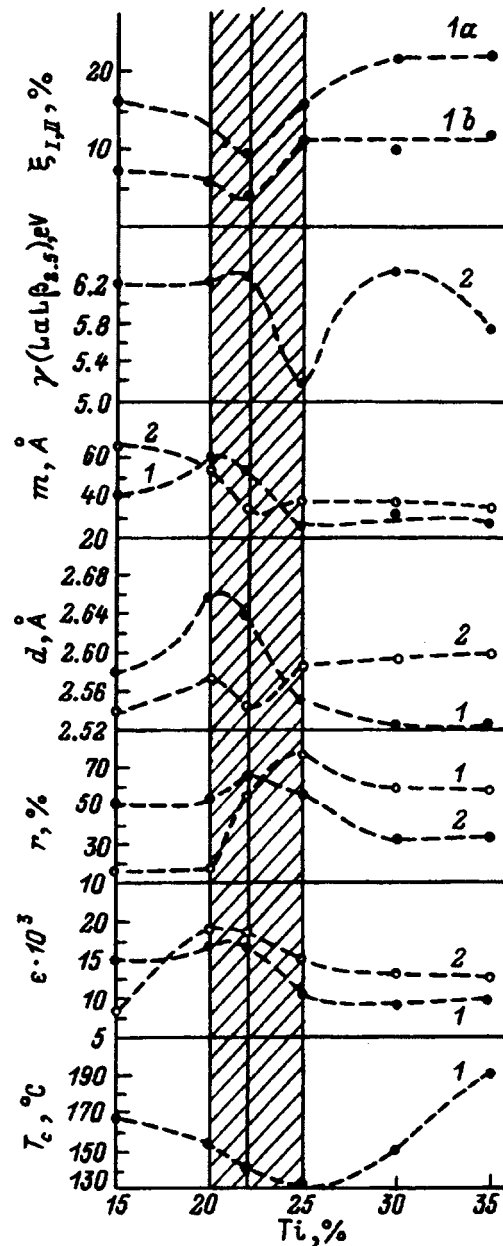


FIG. 3. Influence of the composition of $Pb_{0.85}(Li_{1/2}La_{1/2})_{0.15}(Zr_{1-y}Ti_y)O_3$ solid solutions on their physical parameters. The hatched area indicates the region of two-phase (FE+AFE) states. 1,2) The same as in Fig. 2.

and $\xi_{II} = 10$ at $y = 22$. The similarity of the functional dependences $\xi_I(y)$ and $\xi_{II}(y)$ indicates that they reflect the onset of the same $FE \rightleftharpoons AFE$ structural phase transition, and their numerical difference indicates the significantly greater crystallographic distortions of the long-range order structure in the family of (422) planes than in the (220) family, as reflected in the corresponding diffraction pattern fragments (the 220 line and halo I in contrast with the 422 line and halo II). Indeed, the more complex pattern of the fine structure of halo II relative to halo I (Figs. 2 and 4) requires that all possible groupings of the ions detectable in the experimental x-ray technique be brought into the analysis.

The several different intensity variations of the discrete fluctuation maxima (with normalization of the integrated intensities of the halos of each sample to unity) are illustrated

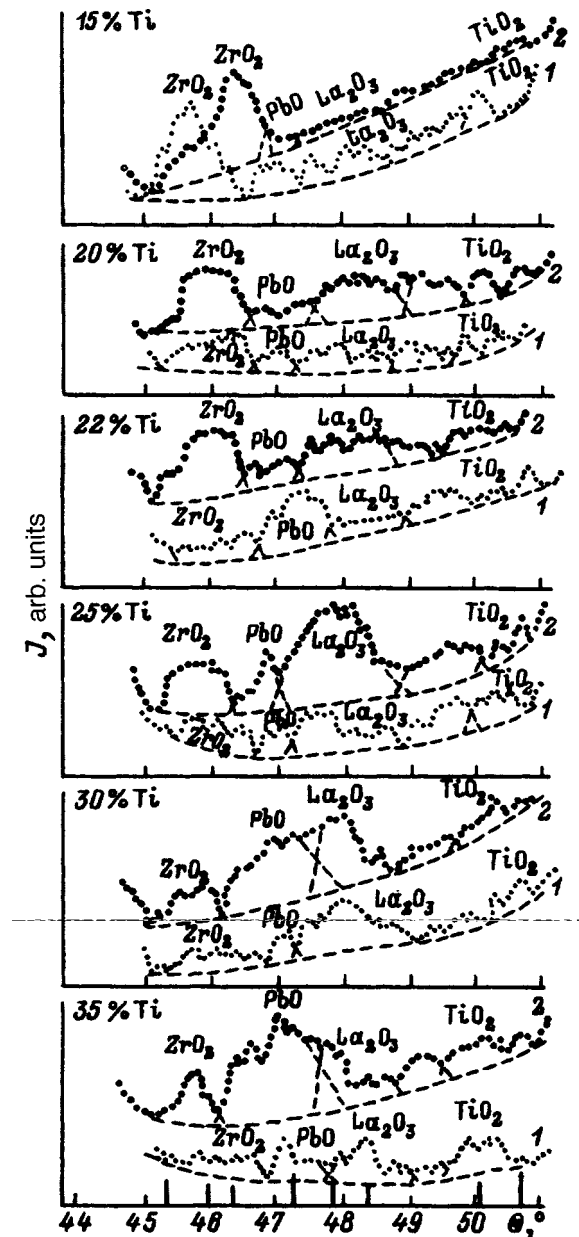


FIG. 4. Fine structure of diffuse x-ray scattering in the interval of angles $\theta = 45^\circ - 51^\circ$. The graphs show the fluctuation maxima of the intensity for postulated cluster groups. The bottom graph shows nomograms of characteristic structural reflections. 1, 2) The same as in Fig. 2.

in Fig. 5. It is noticeable that for both poled and annealed samples in the concentration range $15 \leq y \leq 20$ the Ti-containing and Zr-containing ion groups compete with each other, and in the concentration ranges $20 < y < 25$ and $25 \leq y \leq 35$ the same is true of Pb-containing and La-containing ions. The competition between Pb-containing and La-containing groups in the range $20 < y < 25$ exhibits an extremal character with extremum points corresponding to $y = 22$ for poled samples and $y = 25$ for annealed samples. The role of specific elements in the given structural states also changes. For example, in poled samples Pb clusters have the maximum intensity ($J_{\text{PbO}} = 0.5$), and La clusters have the minimum intensity in the extremal region of the two-phase state ($J_{\text{La}_2\text{O}_3} = 0.08$), whereas in annealed samples the situa-

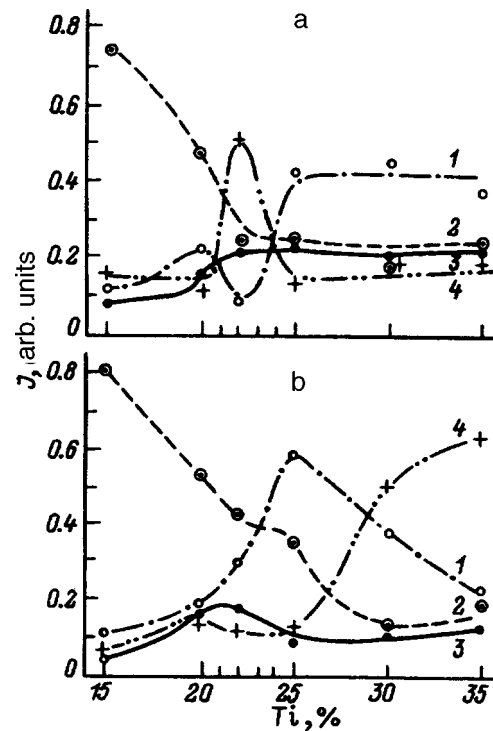


FIG. 5. Intensity distributions of diffuse-scattering fragments in the interval $45^\circ - 51^\circ$ for poled (a) and annealed (b) samples with respect to the proposed cluster groups of oxides. 1, \circ — La_2O_3 ; 2, \circ — ZrO_2 ; 3, - - - TiO_2 ; 4, + — PbO .

tion is reversed: $J_{\text{La}_2\text{O}_3} = 0.55$, and $J_{\text{PbO}} = 0.10$.

They continue to compete in the range of high concentrations. It must be inferred from the results shown in Figs. 4 and 5 that La and Pb, having sharply pronounced extrema, are the main contributors to the $\text{AFE} \rightleftharpoons \text{FE}$ structural phase transitions. To test this assumption we obtained and analyzed x-ray emission spectra of La $L\beta_{2,5}$, which are sensitive to the exchange interaction of lanthanum with its nearest neighbors in the solid solution. The extremal reduction of the width γ of the La $L\beta_{2,5}$ spectral band in an annealed sample of composition $y = 25$ (Fig. 3), which corresponds to the intensity maximum of La-containing groups (Fig. 5), confirms our assumption of the maximum chemical activity of lanthanum in the given structural state. According to Ref. 4, an increase in the concentration of La substituting for Pb at A sites of the perovskite cell within the limits of several lattice constants tends to lower the Curie temperature T_c and to increase the reflectivity r , in agreement with our results (Figs. 3 and 5).

Ions of the B sublattice (Ti^{4+} and Zr^{4+}), being situated at the center of an oxygen octahedron, are largely shielded, and their interaction with the environment is not as effective as for the Pb^{2+} and La^{3+} ions,⁴ so that the role of $\text{Ti} \rightleftharpoons \text{Zr}$ substitution in the crystal structure is most clearly manifested in the creation of mesoscopic stressed regions, whose formation and redistribution are reflected in prominent features of the curves representing the interplanar spacings $d(y)$ and the dielectric constant $\epsilon(y)$ (Fig. 3).

The data from the investigation provide a basis for the following pattern of local disruptions of the long-range order

structure in $\text{Pb}_{0.85}(\text{Li}_{1/2}\text{La}_{1/2})_{0.15}(\text{Zr}_{1-y}\text{Ti}_y)\text{O}_3$ solid solutions. The crystal structure exhibits two groups of families of planes with enhanced defect densities: (220) and (422).

In the family of (220) planes the most conspicuous regions are those having a linear dimension of 20–60 Å with a nonuniform distribution of titanium and zirconium ions, which create planar formations (clusters) with a new crystallographic order emerging in the form of a small group of planes of either predominantly Ti oxides or predominantly Zr oxides, which are coherently linked to the lattice structure of the host phase.

The family of (422) planes exhibits concentration nonuniformity in the distribution of all the chemical elements among the cationic sites of the perovskite lattice. Cluster formations of La and Pb oxides similar to those described above bear the greatest responsibility for the variations of the properties, manifesting an extremal dependence on composition.

The influence of size differences between the Ti^{4+} and Zr^{4+} cations in the *B* sublattice is dominant in the clustered structure. On the other hand, the influence of charge (donor–acceptor) differences between the La^{3+} and Pb^{2+} ions in the *A* sublattice of the perovskite structure is dominant in the clustered structure of the family of (422) planes.

CONCLUSIONS

The investigations of the defect state of the structure of lead zirconate–titanate solid solutions reveal in their structure two families of planes in which the positional long-range order of ions is the most disrupted. These planes are of the type (220) and (422). Disruptions of the statistical distribution of $\text{Ti} \rightleftharpoons \text{Zr}$ are predominant in the first case, and those of $\text{La} \rightleftharpoons \text{Pb}$ are predominant in the second case.

The clusters of the family of (422) planes promote diagonal distortions of the perovskite sublattice, and the clusters of the family of (220) planes are conducive to distortions along the edge *c*. Both types of clusters coexist in the anti-

ferroelectric and ferroelectric regions, but tetragonal distortions of the perovskite sublattice due to clusters of the family of (220) planes dominate in the antiferroelectric region, while distortions due to clusters of the family of (422) planes dominate in the ferroelectric region.

We have established that the disruptions of long-range order have a mesoscopic scale (15–20 interplanar spacings) and generate groups of ions organized into a new, incipient crystallographic order in the form of interlayers of elements of binary-oxide planes coherently embedded in the crystal lattice structure of the host phase.

We have shown that the clustering of the structure is manifested in nonlinearity of the physical properties of lead zirconate–titanate solid solutions as functions of the titanium concentration *y*.

¹V. P. Pashchenko, A. M. Nesterov, V. I. Arkharov *et al.*, Dokl. Akad. Nauk SSSR **318**, 371 (1991).

²V. I. Arkharov, Z. A. Samoilenko, V. P. Pashchenko *et al.*, Neorg. Mater. **29**, 827 (1993).

³Z. A. Samoilenko, *Cluster Materials* [in Russian], UrO RAN, Izhevsk, (1991), pp. 37–49.

⁴E. A. Zavadskii and V. M. Ishchuk, *Metastable States in Ferroelectrics* [in Russian] Naukova Dumka, Kiev, 1987.

⁵V. M. Ishchuk, N. I. Ivashkova, V. L. Sobolev *et al.*, Ferroelectrics **131**, 177 (1992).

⁶G. A. Smolenskiĭ, V. A. Bokov, V. A. Isupov *et al.*, *Ferroelectrics and Antiferroelectrics* [in Russian] Nauka, Leningrad, 1971.

⁷A. R. Shternberg, in *Electrooptical Ferroelectric Ceramics* in [Russian] Latv. Univ., Riga, (1977), pp. 5–104.

⁸V. M. Ishchuk, V. P. Pashchenko, Z. A. Samoilenko, and O. P. Cherenkov, Ferroelectrics **21**, 161 (1996).

⁹L. I. Kitaigorodskii, *X-Ray Structural Analysis of Fine-Crystalline and Amorphous Solids* [in Russian] (GITTL, Moscow-Leningrad, 1952).

¹⁰M. A. Krivoglaz (Naukova Dumka, Kiev, 1988), pp. 3–39.

¹¹I. I. Kornikov, N. M. Matveeva, L. I. Pryakhina *et al.*, *Metallochemical Properties of Elements of the Periodic Table. Supplement* [in Russian] Nauka, Moscow, 1966.

¹²K. Meĕer, *Physicochemical Crystallization* [in Russian] Metallurgiya, Moscow, 1972.

Translated by James S. Wood

Macrostructure of high-temperature superconducting YBaCuO thin films grown by laser ablation

K. N. Yugaĭ, G. M. Seropyan, A. A. Skutin, K. K. Yugaĭ, and A. B. Murav'ev

Omsk State University, 644077 Omsk, Russia

(Submitted September 10, 1996; resubmitted June 16, 1997)

Zh. Tekh. Fiz. **68**, 48–51 (February 1998)

The superconducting parameters and macrostructure of YBaCuO thin films grown by laser ablation on SrTiO₃ substrates are influenced by the substrate temperature during growth. In a study of this influence it is found that the macrostructure has significant bearing on the superconducting parameters of the films and on the critical current, in particular. For $J_c \leq 10^5$ A/cm² the films have a distinctly pronounced granular structure, while for $J_c > 10^5$ A/cm² the films do not have any kind of block structure. © 1998 American Institute of Physics. [S1063-7842(98)00902-7]

INTRODUCTION

The application of high-temperature (high- T_c) superconducting thin films in the construction of superconducting electronics elements (sensors, SQUIDs, flux transformers) has prompted investigations of the interaction of macrostructural elements with the superconducting parameters of thin films. At this point we have a fairly clear picture of the macrogranular structure of high- T_c superconducting ceramics, which accounts for their low current-carrying capacity, whereas the temperature T_c at which the superconducting transition begins and the width ΔT of the superconducting transition can be extremely high both for ceramics and for thin films. This consideration suggests that the critical current density J_c must depend directly on macrostructural elements of the superconductor (intergranular boundaries, intercrystallite layers, twinning boundaries, dislocation networks, etc.). In other words, the macrostructure of a superconductor, of a superconducting thin film in particular, determines the form of the weak links and the types of Josephson junctions in them: SIS, SNS, SS'S, etc. The properties of the intergranular boundaries have been investigated in several papers.^{1–5} Experiments on the growth of high- T_c superconducting thin films by laser ablation demonstrate a considerable spread of critical current densities J_c , from 10^3 A/cm² to 10^7 A/cm² (for ceramic samples $1–10^3$ A/cm²).

Numerous studies of the structure of yttrium barium cuprate (YBaCuO) ceramics have revealed a certain macrostructure hierarchy: grains-subgrains-crystallites-twin structure.⁶ In the present article we hypothesize that the large spread of J_c is also attributable to salient features of their macrostructure, where a macrostructure hierarchy similar to that in ceramic samples is possible in films with low critical current densities $J_c \leq 10^5$ A/cm² (low- J_c films), whereas epitaxial films with high critical current densities $J_c > 10^5$ A/cm² (high- J_c films) approaching the maximum possible for high- T_c superconductors have a low-defect, single-crystalline macrostructure. The experimental results obtained in the study show that, all other conditions being equal, the substrate temperature T during deposition has a

significant influence on the growth of low- J_c and high- J_c films.

EXPERIMENT

Thin films of YBa₂Cu₃O_{7- δ} were grown by laser ablation.⁷ An LTI-403 pulsed solid-state YAG-rod laser with a wavelength $\lambda = 1.06$ μ m, pulse duration $\tau = 20$ ns, and a pulse repetition rate of 14 Hz was used to deposit the films. The substrates were SrTiO₃ (100) single crystals with dimensions $7 \times 7 \times 1$ mm. The films were deposited *in situ* at an air pressure ~ 1 torr in the chamber of a VUP-4 vacuum station. The YBa₂Cu₃O_{7- δ} target was mounted directly in the laser beam at a 30–40° angle. The target–substrate spacing was $l = 3$ cm, and the deposition time was $t = 3$ min. Upon completion of the deposition process, the pressure in the chamber was raised to 1 atm, and the film was cooled to room temperature over a 30-min period. The substrate temperature T was varied from 700 °C to 900 °C.

The superconducting parameters of the films (T_c , ΔT , and J_c) were measured by the standard four-probe technique. The value of J_c corresponded to a 1 μ V output voltage. Superconducting bridges having widths from 20 μ m to 50 μ m were cut by laser scribing. The film thicknesses were measured on an MII-4-0 interference microscope and were ~ 100 nm.

RESULTS AND DISCUSSION

The formation of the structure of YBaCuO thin films is known to depend significantly on the substrate temperature during deposition. Consequently, with a view toward obtaining films with different structures and with different values of the superconducting parameters, the substrate temperature was varied ($T = 700–900$ °C), while all the other deposition parameters were held constant. The experimental results are summarized in Table I.

The lower limit of T , when the film goes over completely to the superconducting state at a temperature of 77 K (i.e., when an orthorhombic structure is formed), corresponds to 730 °C. The upper limit, or highest substrate temperature

TABLE I.

$T, ^\circ\text{C}$	$R'_{300}\Omega$	Type of conductivity	T_c, K	$\Delta T, \text{K}$	$J_c, \text{A/cm}^2$
700	3400	semiconductor	-	-	-
720	500	metal	84.2	>7.2	*
730	200	metal	84.0	4.2	$3.4 \cdot 10^3$
740	90	metal	89.0	3.8	$6.0 \cdot 10^5$
760	80	metal	89.0	2.2	$2.8 \cdot 10^6$
780	80	metal	90.0	1.8	$2.7 \cdot 10^6$
800	60	metal	89.6	1.8	$3.0 \cdot 10^6$
800	40	metal	89.0	2.4	$1.5 \cdot 10^6$
820	80	metal	90.2	1.8	$4.9 \cdot 10^6$
820	90	metal	89.0	2.2	$3.3 \cdot 10^6$
840	200	metal	90.6	1.8	$1.5 \cdot 10^6$
860	260	metal	90.4	2.8	$7.0 \cdot 10^5$
880	290	metal	89.6	2.8	$7.0 \cdot 10^5$
890	300	metal	88.2	5.6	$3.9 \cdot 10^3$
900	400	metal	85.0	>8	*

Note: The values of J_c for these films are not determined by the four-probe technique; R_{300} denotes the resistance at room temperature; the type of conductivity also pertains to room temperature.

at which films with good superconducting parameters can still be obtained, corresponds to $\sim 880^\circ\text{C}$. At higher temperatures T considerable broadening of the superconducting transition is observed, along with a sharp drop in J_c relative to the optimum deposition temperature ($T \sim 820^\circ\text{C}$). An unexpected result was the insignificant variation of the superconducting parameters over a rather broad temperature interval ($700\text{--}840^\circ\text{C}$). Graphs of $J_c(T)$, $T_c(T)$, and $\Delta T(T)$ are shown in Figs. 1–3, respectively. It is evident that the critical temperature, unlike J_c and ΔT , remains high over a broad temperature interval ($740\text{--}890^\circ\text{C}$). Obviously, the orthorhombic phase is highly prevalent in films at substrate temperatures from 760°C to 840°C . At temperatures below 740°C the fraction of tetragonal phase begins to increase, and at temperatures above 890°C not only does the fraction of orthorhombic phase decrease, but the substrate material begins to react with the YBaCuO, so that oxygen is lost.

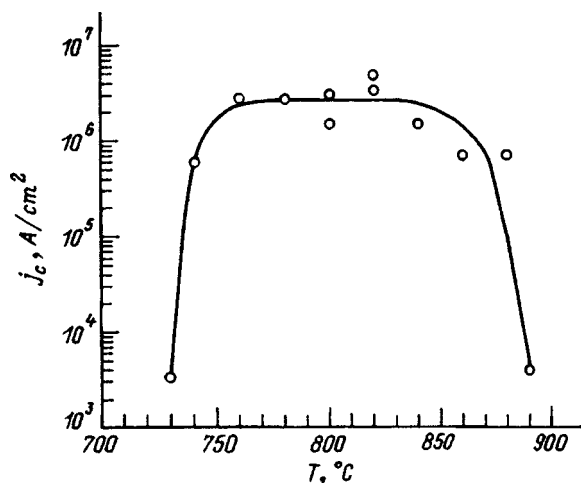


FIG. 1. Critical current density J_c versus substrate temperature.

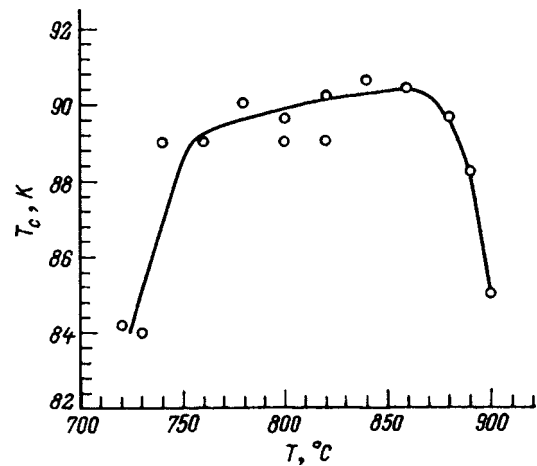


FIG. 2. Critical temperature J_c versus substrate temperature.

It follows from these considerations that the influence of the characteristic oxygen deficiency associated with the tetragonal structure primarily affects the intermediate layer between the elements of the film structure. We know from abundant published data (e.g., Refs. 8 and 9) that as δ is varied from 0 to 1, the $\text{YBa}_2\text{Cu}_3\text{O}_{7-\delta}$ film undergoes a series of major changes. In the interval $0 < \delta \leq 0.4$ YBaCuO is a superconductor with an orthorhombic phase. The coexistence of tetragonal and orthorhombic phases is observed for $0.4 \leq \delta < 0.9$. When $\delta \geq 0.9$, the main volume of the film has a tetragonal structure.

Films exhibiting a large spread of superconducting parameters were selected for the investigation of YBaCuO thin films in a Neophot-2 optical microscope. The surfaces of the films were etched to reveal their macrostructure. A granular structure with grain diameters $\sim 2\text{--}3 \mu\text{m}$ is clearly discerned on a film with $J_c = 3.4 \times 10^3 \text{ A/cm}^2$ (Fig. 4), the grains in this case consisting of finer subgrains with dimensions smaller than $1 \mu\text{m}$. No order of any kind is observed in the grains. A slight variation of the grain packing density from 10^7 cm^2 to $1.5 \times 10^7 \text{ cm}^2$ takes place over the entire area of the film.

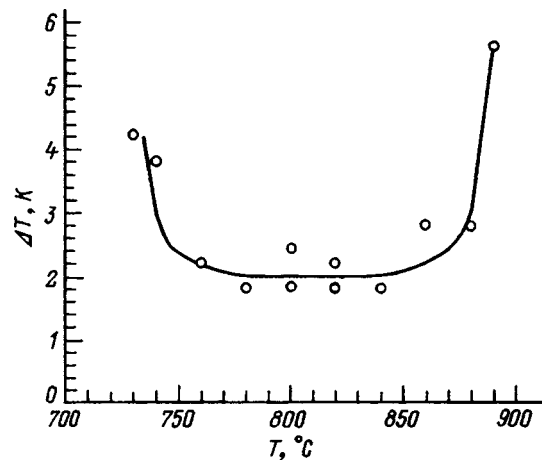


FIG. 3. Width of the superconducting transition ΔT versus substrate temperature.

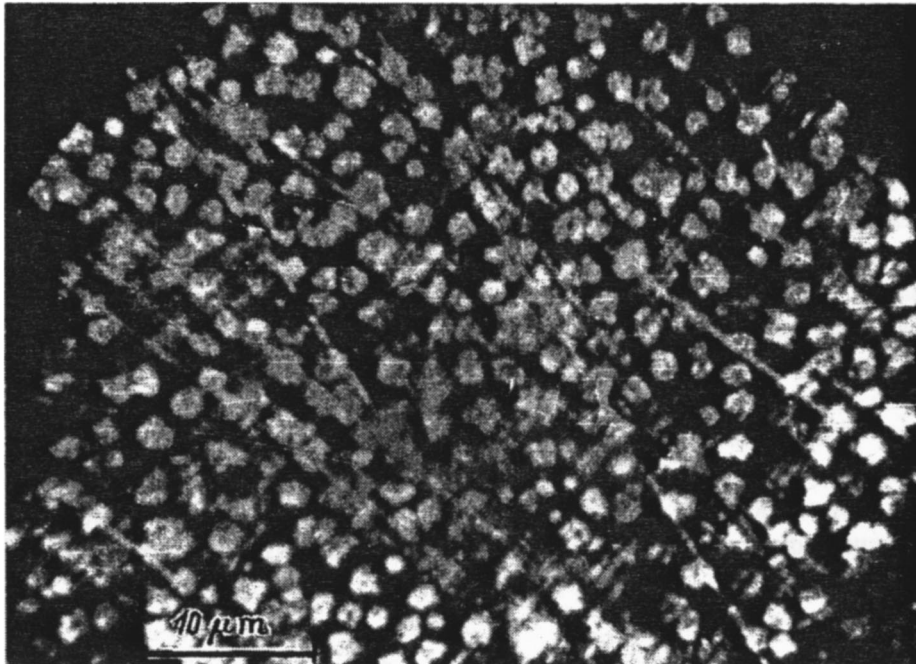


FIG. 4. Photomicrograph of the surface of a film with $J_c = 3.4 \times 10^3$ A/cm².

Neither grains nor crystallites are observed for films with $J_c = 7.0 \times 10^5$ A/cm² and $J_c = 1.5 \times 10^6$ A/cm² (Fig. 5). The surface is smooth except for sparse droplets comprising solidified blobs of the molten target material. Unfortunately, the resolving power of the microscope was not good enough to investigate macrostructural defects at the level of twinning boundaries. It is obvious, however, that the high critical current densities of high- J_c films ($J_c > 10^5$ A/cm²) are associated with the low count of macrostructural defects or, in other words, with the closeness to a single-crystalline macrostructure throughout the entire volume of the film.

The following scheme of macrostructure evolution can be inferred from the results of the investigations, progressing from low- J_c to high- J_c films: emergence of islands of orthorhombic phase → growth of the ortho-phase islands → bridging of the islands and the formation of a granular structure with channels for the passage of supercurrent (despite the greatly diminished current-carrying capacity of the films as a result of the relatively thick interlayers between grains) → coalescence of grains, so that higher-quality and thinner intercrystallite layers begin to act as the weak link (the small angles of misorientation of the adjacent crys-

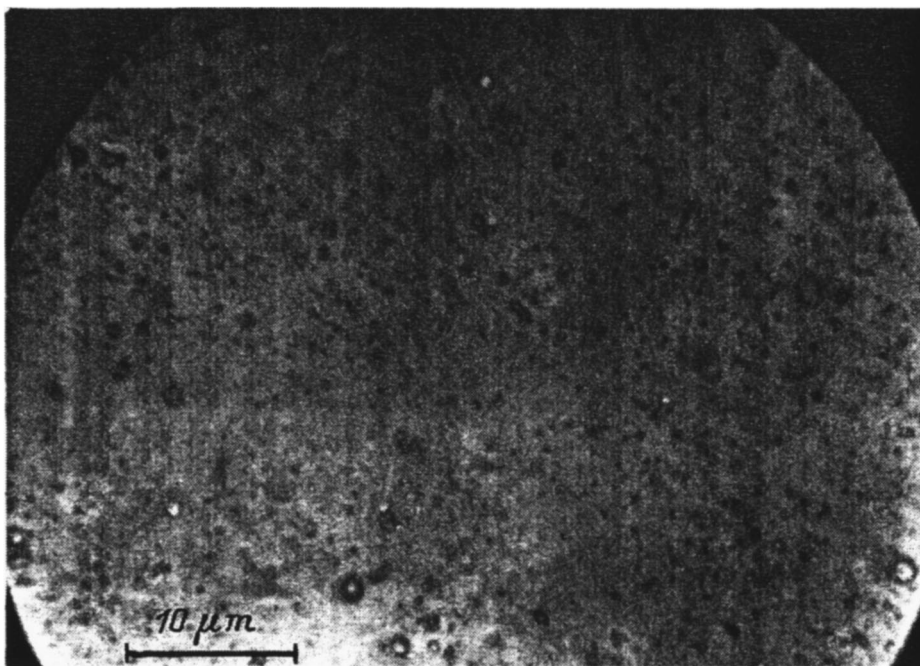


FIG. 5. Photomicrograph of the surface of a film with $J_c = 1.5 \times 10^6$ A/cm².

tallites also enhance the current-carrying capacity)→formation of twin-free regions, where the critical current density J_c acquires the maximum possible values ($\sim 10^7$ A/cm²).

CONCLUSION

The results of the reported investigations lead to the conclusion that the macrostructure of YBaCuO thin films grown by laser ablation determines the values of the critical current density J_c . For $J_c \leq 10^5$ A/cm² the macrostructure of the film is determined by defects in the form of grains, crystallites, and twinning regions. For $J_c > 10^5$ A/cm² the film has a low-defect, single-crystalline structure.

The authors are deeply grateful to T. K. Panova for collaboration in obtaining the photomicrographs of the film surfaces.

¹D. Dimos, P. Chaudhari, J. Mannhart, and F. K. LeGoues, Phys. Rev. Lett. **61**, 219 (1988).

²S. E. Babcock and D. C. Larbalestier, J. Mater. Res. **5**, 919 (1990).

³Y. Zhu, H. Zhang, H. Wang, and M. Suenaga, "Grain boundary studies by the coincidence site lattice model and electron energy loss spectroscopy of the oxygen K-edge in YBa₂Cu₃O_{7- δ} ," Preprint (1992).

⁴H. W. Zandbergen, R. Gronsky, and G. Thomas, J. Microsc. Spectrosc. Electron. **13**, 307 (1988).

⁵H. W. Zandbergen, R. Gronsky, and G. van Tendeloo, J. Supercond. **2**, 337 (1989).

⁶E. Z. Meřlikhov, Usp. Fiz. Nauk **163**(3), 27 (1993) [Phys. Usp. **36**, 129 (1993)].

⁷K. N. Yugaï, A. A. Skutin, G. M. Seropyan *et al.*, Sverkhprovodimost' (KIAE) **7**, 1026 (1994).

⁸P. K. Gallagher *et al.*, Mater. Res. Bull. **22**, 995 (1987).

⁹W. Qinag *et al.*, Phys. Lett. A **158**, 75 (1988).

Ion bombardment of amorphous silicon films during plasma-enhanced chemical vapor deposition in an rf discharge

A. S. Abramov, A. Ya. Vinogradov, A. I. Kosarev, and M. V. Shutov

A. F. Ioffe Physicotechnical Institute, Russian Academy of Sciences, 194021 St. Petersburg, Russia

A. S. Smirnov and K. E. Orlov

St. Petersburg State Technical University, 195251 St. Petersburg, Russia

(Submitted October 9, 1996)

Zh. Tekh. Fiz. **68**, 52–59 (February 1998)

The characteristics of ion and electron fluxes to the surface of a growing silicon film are investigated in various rf discharge regimes in silane at frequencies of 13.56 MHz and 58 MHz in plasma-enhanced chemical vapor-deposition (PECVD) apparatus. The energy spectra of the ions and electrons bombarding the growing film are measured. The electronic properties of films grown under various degrees of ion bombardment are studied. The correlation of these properties with the ion parameters in the rf discharge plasma during film growth is discussed.

© 1998 American Institute of Physics. [S1063-7842(98)01002-2]

INTRODUCTION

The growth mechanism, structure, and properties of films grown by plasma-enhanced chemical vapor deposition (PECVD) are determined by the temperature regime and parameters of the gas-discharge plasma. The composition and properties of the vapor-phase particles and the bombardment of the film surface with ions and electrons play important roles in the process of film growth. The influence of ion bombardment on the growth and properties of hydrogenated amorphous silicon films has been observed, for example, in Refs. 1–4. The application of a constant negative bias $25 \text{ V} < U_b < 75 \text{ V}$ to the substrate has been found to lower the density of defects in silicon films.² This fact has been attributed to an increase in the energy of the ions bombarding the growing film. However, the cited paper does not give any quantitative data on the energy and flux of the ions, nor is it known what fraction of the applied bias is dedicated to accelerating the ions bombarding the film. The observed^{5–7} increase in the growth rate and improvement in the quality of films when the frequency of the applied field is raised are most likely also associated with changes in the ion bombardment parameters,⁸ but there is no direct experimental corroboration to that effect.

Information about the nature of the electron and ion fluxes to the substrate in a radio-frequency discharge used to grow silicon films and their influence on the properties of the films is given in Ref. 4, but only for a 13.56-MHz discharge.

The comparison of results from different studies is hampered by the complex dependence of the ion fluxes, like the dependence of the film properties, on external hardware parameters such as the reactor geometry and the power input to the discharge (i.e., the rate of energy deposition), as well as the gas mixtures used and the external parameters of the discharge (pressure, flow rate, etc.).

Here we give the results of measurements of the energy spectra of ions and electrons in an industrial PECVD appa-

ratus at frequencies of 13.56 MHz and 58 MHz in various regimes used for the deposition of hydrogenated amorphous silicon layers. We also give the results of an investigation of the electronic properties of amorphous silicon films grown under various ion bombardment conditions and discuss the correlation of these properties with the characteristics of the ions.

EXPERIMENTAL APPARATUS AND PROCEDURE

The reactor used in the study is shown schematically in Fig. 1. The characteristics of the ions and electrons in the rf discharge were measured by means of a flat, four-grid retarding-field energy analyzer. The analyzer was placed in line with the substrate on the grounded electrode. The powered electrode, with a diameter of 220 mm, was positioned at a distance of 25 mm from the 230×230 -mm grounded electrode, whose central area (of diameter 75 mm) was occupied by the substrate. The construction of the energy analyzer and the fine points of the measurement procedure have been described earlier.^{9,10} The input aperture of the energy analyzer had a diameter of 5 mm. All parts of the energy analyzer, except the stainless steel casing, were made of nickel. The grids had a 140×140 - μm mesh size and 80% transmission. The first grid of the analyzer was grounded. For measurements of the ion parameters the potential of the second, electron-retarding grid was maintained at $U_2 = -100 \text{ V}$, the potential of the third grid was varied over the range $U_3 = 0$ to $+300 \text{ V}$ for ion energy analysis, and the potential of the fourth grid was set high enough to suppress the secondary-electron current from the collector: $U_4 = -18 \text{ V}$ (Ref. 11); the collector had zero potential, $U_k = 0$. The following potentials were supplied for measurement of the electron parameters: $U_2 = +300 \text{ V}$, $U_3 = 0$ to -100 V , $U_4 = 0$, $U_k = +18 \text{ V}$. The energy scanning time was approximately 5 s.

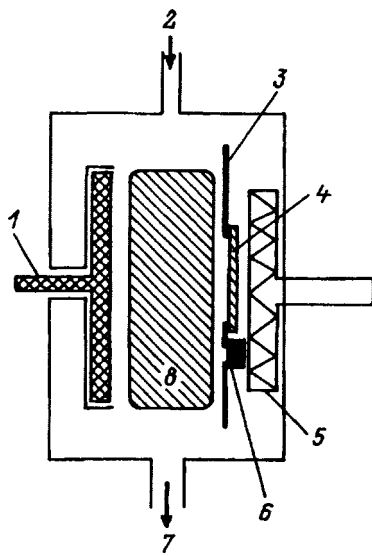


FIG. 1. Diagram of the experimental reactor. 1) Powered electrode; 2) vapor; 3) grounded electrode; 4) substrate; 5) heater; 6) energy analyzer; 7) evacuation; 8) plasma.

The ion and electron characteristics were measured in the following regimes: 1) with the powered electrode dc-shorted to ground [direct-current short-circuit (dcSC) regime]; 2) with the powered electrode insulated from ground [direct-current open-circuit (dcOC) regime]; 3) with a constant bias applied to the powered electrode.

The difference between these regimes¹²⁻¹⁴ is illustrated in Fig. 2, which shows the position of the plasma-layer interface in an asymmetric discharge. In the dcOC regime no direct current flows between the electrodes, so that the electron and ion fluxes to each electrode must be equal. Only when the plasma comes into contact with an electrode does an electron current flow to the electrode, so that the plasma-layer interface must touch an electrode in the dcOC regime. Since the grounded electrode has greater area, the current density and, accordingly, the thickness of the layer next to it are smaller. As a result, the constant potential difference between the grounded electrode and the plasma is lower than between the plasma and the powered electrode. Consequently, a self-bias voltage U_{sb} is generated. In the dcSC regime the constant electrode potentials are equal, so that the potential differences in the layers must also be equal. As a result, the boundary of the plasma does not reach the grounded electrode, and only ion current flows to the latter. If the thicknesses of the layers and the power released in them are small, the transition from dcOC to dcSC should not significantly alter the parameters of the positive column and the layer next to the powered electrode. In this case the ion flux to the electrodes remains constant, and the energy of ions bombarding the grounded electrode increases by the amount of the self-bias voltage. The ion energy can be gradually increased relative to the dcOC regime by applying various voltages to the powered electrode. A reduction in the ion energy or a change in the ion flux is possible only when the parameters of the positive column of the plasma change.

The measurements were carried out for discharges in argon, hydrogen, and silane at two frequencies f

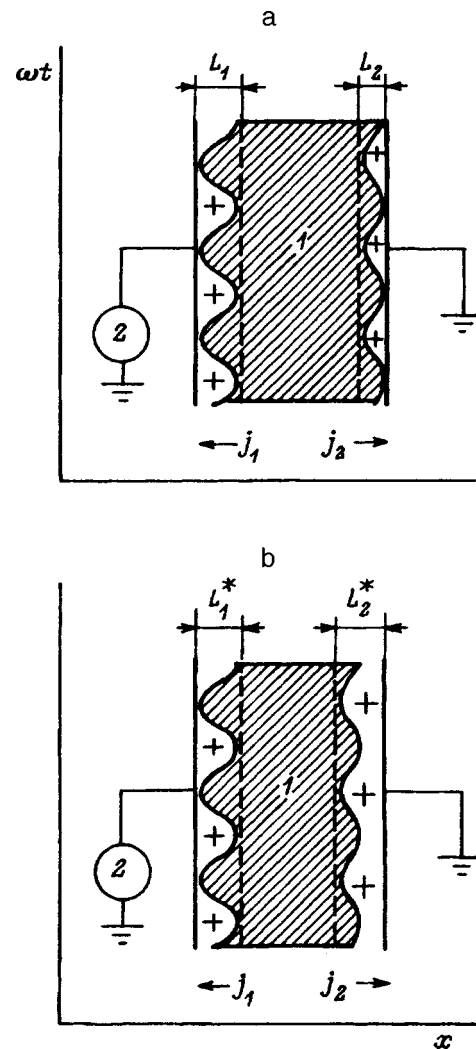


FIG. 2. Schematic diagram of an rf discharge with different electrode areas in the dc open-circuit (a) and dc short-circuit (b) regimes. 1) Plasma; 2) powered electrode.

= 13.56 MHz (hf) and 58 MHz (vhf). The discharge burning conditions in the silane were the chosen the same as for the film deposition: substrate temperature $T_s = 250^\circ\text{C}$, silane flux $Q = 28$ sccm, pressure $P = 0.17$ torr at $f = 13.56$ MHz and $P = 0.056$ Torr at $f = 58$ MHz. The rf (vhf) power W was varied from 5 W to 30 W. The primary concern was to measure the ion and electron characteristics as functions of the rf power and the voltage applied to the powered electrode.

Films of hydrogenated amorphous silicon were deposited on silicon, quartz, and glass-ceramic substrates in a single pass. The configuration of the electrodes in the form of strips with a 2-mm gap between them made it possible to measure the electrical conductivity, the photoconductivity, and the carrier diffusion length by the dynamic interference grating method.¹⁵ The following procedure was used to characterize the electronic properties of the films: 1) measurement of the temperature dependence of the electrical conductivity $\sigma(T)$; 2) measurement of the optical absorption due to transitions from localized states in the mobility gap into the conduction band by the constant photocurrent method

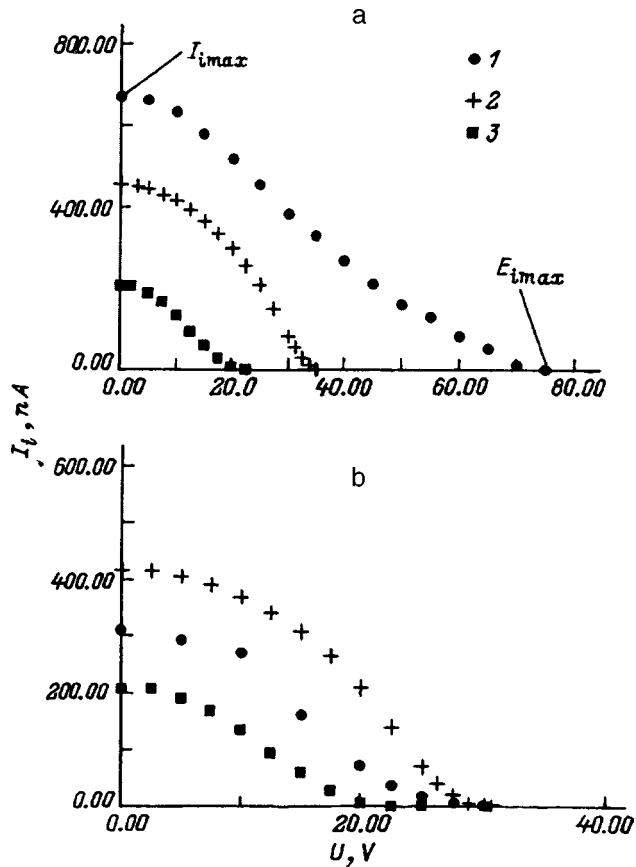


FIG. 3. Collection current I_i versus retarding voltage U in the dcSC (a) and dcOC (b) regimes. 1) Ar, $f=13.56$ MHz, $P=0.12$ torr, $W=14$ W; 2) SiH_4 , $f=58$ MHz, $P=0.056$ torr, $W=17$ W; 3) H_2 , $f=58$ MHz, $P=0.36$ Torr, $W=10$ W.

(CPM); 3) measurement of the diffusion lengths of electrons L_e and holes L_h by the dynamic interference grating method; 4) optical measurements, including laser interferometry during growth of the films, measurement of the Raman spectra, and infrared spectroscopy.

Processing of the measurement results yielded the room-temperature electrical conductivity σ_{π} , the preexponential factor σ_0 , the conductivity activation energy $E_a = (E_c - E_f)|_{T=0}$ (E_c is the edge of the conduction band, and E_f is the position of the Fermi level), and the coefficient γ characterizing the temperature shift of the Fermi level. The results of the CPM optical absorption measurements were used to calculate¹⁶ the density of defect states in the bandgap N_d , the characteristic energy of exponential decay of the density of states near the valence band E_{vt} , the Urbach energy E_U , and the position of the peak of the defect states, E_d .

PARAMETERS OF THE PLASMA AND FLUX OF CHARGED PARTICLES TO THE SUBSTRATE

Figure 3 shows the ion retardation curves, i.e., the collector ion current in the energy analyzer as a function of the voltage on the third grid U for discharges in argon, hydrogen, and silane, obtained in the dcOC and dcSC regimes for close values of the power input. Clearly, the changeover to the dcSC regime has the effect of raising the maximum ion

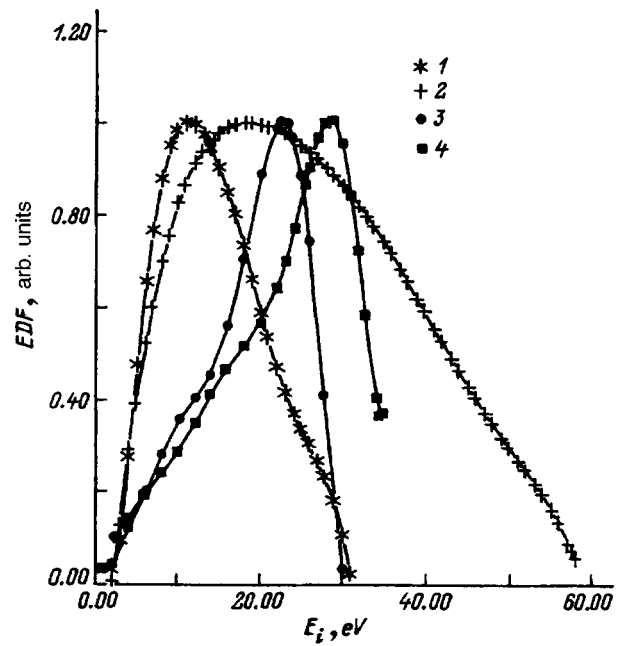


FIG. 4. Ion energy distribution function for a discharge in silane, $W=15$ W. 1) $f=13.56$ MHz, dcOC regime; 2) $f=13.56$ MHz, dcSC regime; 3) $f=58$ MHz, dcOC regime; 4) $f=58$ MHz, dcSC regime.

energy. In an argon discharge the transition to the dcSC regime produces a substantial reduction in the ion flux, whereas in silane and hydrogen it remains essentially constant.

Figure 4 shows the ion energy distribution functions obtained by differentiation of the retardation curves (Fig. 3) for a discharge in silane at two frequencies in the dcSC and dcOC regimes. In comparing these curves, it must be borne in mind that the hf discharge at 13.56 MHz burned at a higher pressure than the vhf discharge at 58 MHz. In the 58-MHz discharge the majority of the ions have near-maximum energy. This result indicates that the ions are generated in the positive column and are accelerated by the total voltage across the layer with almost no collision losses. The small number of collisions in the layer causes a broadening of the spectrum of the ions on the low-energy side. Upon transition to 13.56 MHz the thickness of the layer increases, with a simultaneous increase in the number of ion-atom collisions as a result of the increase in pressure. As a result, the majority of the ions undergo collisions in the layer and do not gain energy until the final mean free path. The result is a broad ion spectrum with a maximum at medium energies.

If we assume that the parameters of the layer at the powered electrode and the positive column do not change upon transition to the dcSC regime, as is probably true for discharges in silane and hydrogen, we can estimate the power input W_i to the ions in the electrode sheaths. In fact, the ion current in the layer is equal to the short-circuit current, and the constant voltage drop is equal to the maximum ion energy in the dcSC regime. Accordingly, $W_i = I_{sc}(E_{i \max}/e)$, where $E_{i \max}$ is the maximum ion energy, and e is the electron charge. This estimate of W_i as a function of the total power for argon and silane discharges at various frequencies is shown in Fig. 5. Also shown here is the calculated $W_i(W)$

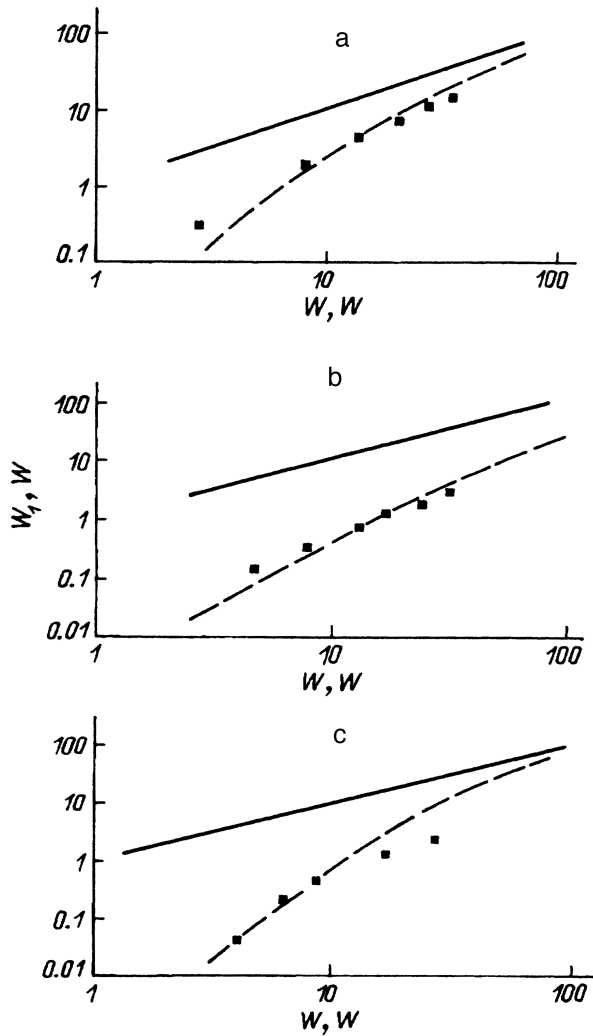


FIG. 5. Ion power input W_i versus total power input W to the discharge. a) Argon at a frequency $f=13.56$ MHz; b) silane $f=13.56$ MHz; c) silane at $f=58$ MHz.

curve obtained on the assumption of a constant ion density in the layer.¹¹ It is evident from the figure that for silane the experimental values of W_i are close to the calculated values in order of magnitude. In silane W_i is a small fraction of the total power, whereas in argon at 13.56 MHz it is close to W . The power input to the ions increases by an order of magnitude itself upon transition to the dcSC regime, because it is augmented by the losses in the layer next to the grounded electrode; it follows, therefore, that the discharge regime in argon must undergo a significant change. This conjecture is supported by the fact that the ion flux to the grounded electrode increases upon transition to the dcSC regime (Fig. 3). It also follows from the calculations that the discharge regimes in the three cases represented in Fig. 5 are different. In silane at 13.56 MHz, owing to the large fraction of the electron energy lost in the excitation of molecular vibrational levels, the energy relaxation length λ_e is smaller than the dimensions of the layer. In this regime we observe an α -discharge, in which the ionization depends on the local value of the electric field and takes place in the layer.¹⁷ At a frequency of 58 MHz, because of the decrease in the pressure and the

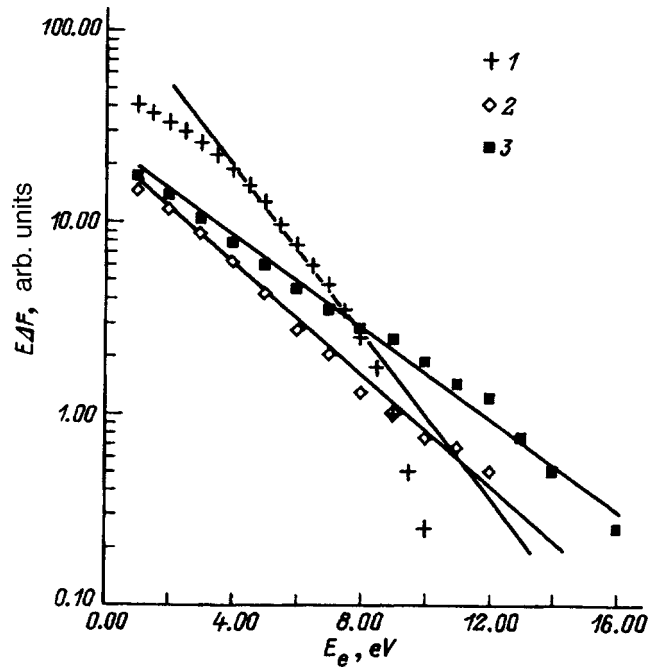


FIG. 6. Electron retardation curves for a silane discharge, $f=13.56$ MHz, $P=0.17$ Torr. 1) $W=8$ W; 2) 13 W; 3) 24 W.

layer thickness, λ_e becomes shorter than L . In this case the heating of electrons and ionization depend on the electric field in the layer, even though they take place in the body of the plasma.¹¹ In argon, on the other hand, stochastic heating associated with collisions of electrons with the moving plasma-layer interface must be taken into account in calculating the ionization.¹⁸

Figure 6 shows the electron retardation curves in semi-log scale. It is evident that in the first approximation the electron distribution function can be approximated by a Maxwellian distribution with temperature T_e . It must be borne in mind that the energy spectrum of the electrons can be recorded only in the dcOC regime. The dependence of T_e on the power input is shown in Fig. 7. The electron temperature $T_e \approx 3.25 \pm 1.0$ eV at $f=13.56$ MHz, and $T_e \approx 2.5 \pm 0.5$ eV at $f=58$ MHz.

We have chosen the maximum energy $E_{i \max}$ and the total ion current $I_{i \max}$ to characterize ion bombardment. Figure 8 shows $E_{i \max}$ and $I_{i \max}$ as functions of the rf power at a frequency of 13.56 MHz. It is readily perceived that $E_{i \max}$ increases with the rf power in both regimes, the difference between $E_{i \max}$ in the dcSC and dcOC regimes increasing as the rf power is increased. At low rf power levels $E_{i \max}$ is identical for both regimes, but the difference in $E_{i \max}$ becomes substantial at higher power levels. This result can be attributed to the fact that the discharge does not go beyond the boundaries of the grounded electrode at low rf power, and we therefore have a situation where the electrode areas are equal, and there is no difference between the dcSC and dcOC regimes. In the dcSC regime $I_{i \max}$ also increases more rapidly with the power than in the dcOC regime.

Graphs of $E_{i \max}$ and $I_{i \max}$ as functions of the rf power at a frequency of 58 MHz are shown in Fig. 9. It is evident from a comparison of Figs. 8 and 9 that in the same power

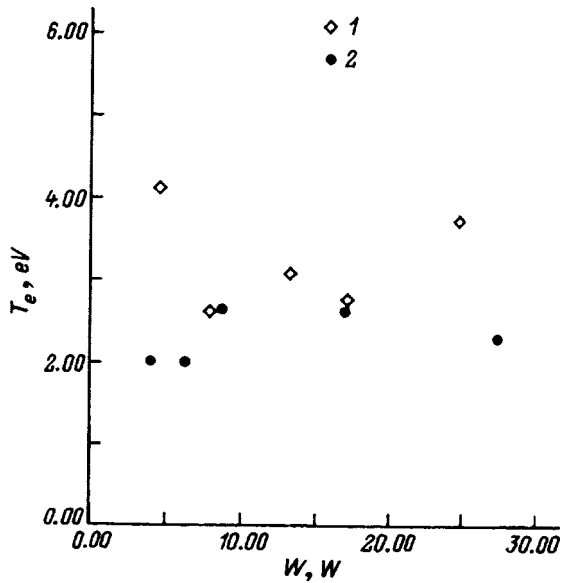


FIG. 7. Electron temperature T_e versus rf power. 1) $f=13.56$ MHz; 2) $f=58$ MHz.

range the maximum ion energy at the higher frequency is lower, and the ion flux is higher; when the rf power is varied identically from 0 to 30 W at 58 MHz and at 13.56 MHz, the ion energy and current change differently: the difference between $E_{i \max}$ in the dcSC and dcOC regimes is not as pronounced at $f=58$ MHz; $I_{i \max}$ is identical in the two regimes

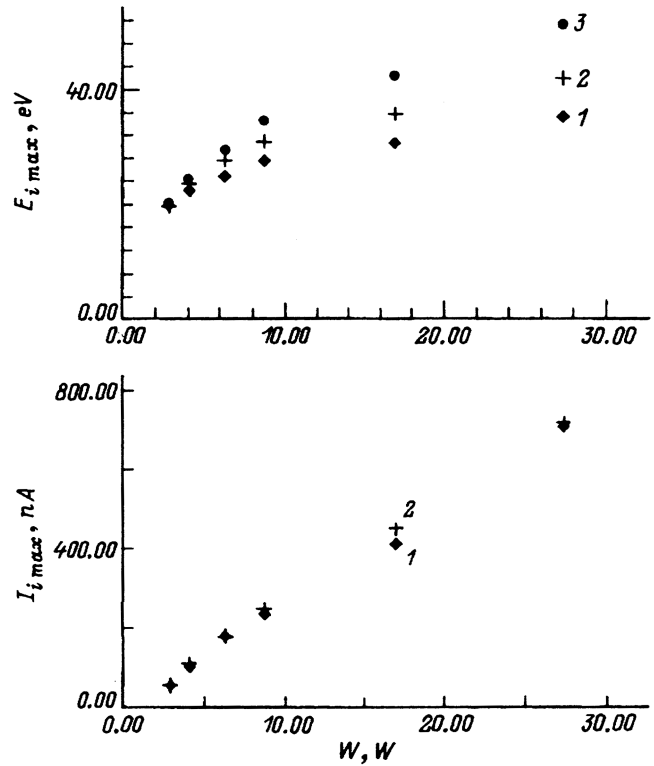


FIG. 9. The same as Fig. 8, at $f=58$ MHz.

at $f=58$ MHz, but at $f=13.56$ MHz the difference between the ion currents in the dcSC and dcOC regimes increases as the power is increased.

FILM GROWTH UNDER DIFFERENT ION BOMBARDMENTS

A practical way to determine the influence of the ion energy and flux on the growth and characteristics of the film is to vary $E_{i \max}$ and $I_{i \max}$ independently. Figures 8 and 9 show $E_{i \max}$ and $I_{i \max}$ as functions of the power input. The ion energy can be increased with little change in their flux by varying the potential of the powered electrode. The ion flux increases as the power is increased. On this basis films were deposited for comparison under the following conditions: three samples (136-01, 136-02, and 136-03) were deposited at $f=58$ MHz at low power with identical ion fluxes, three different biases and, hence, three different values of $E_{i \max}$. For the next sample (136-04) the power was increased until $E_{i \max}$ attained the values of $E_{i \max}$ encountered for low-power, positive-bias discharges (136-01). The ion flux increased in this case. Sample 136-05 was prepared at high power with negative bias to lower $E_{i \max}$. Samples of the 137 series were prepared analogously at $f=13.56$ MHz. We have thus investigated samples obtained for various energies $E_{i \max}$ and $I_i \approx \text{const}$ and other samples obtained for various fluxes I_i and $E_i \approx \text{const}$. The parameters of the sample growth processes are summarized in Table I. It is evident from this table that the rate of growth of hydrogenated amorphous silicon films prepared at $f=58$ MHz is 2–5 times the rate of deposition at 13.56 MHz. As the power is raised (without the application of additional bias U_b), the film growth rate increases from 1.2 Å/s to 2.4 Å/s at

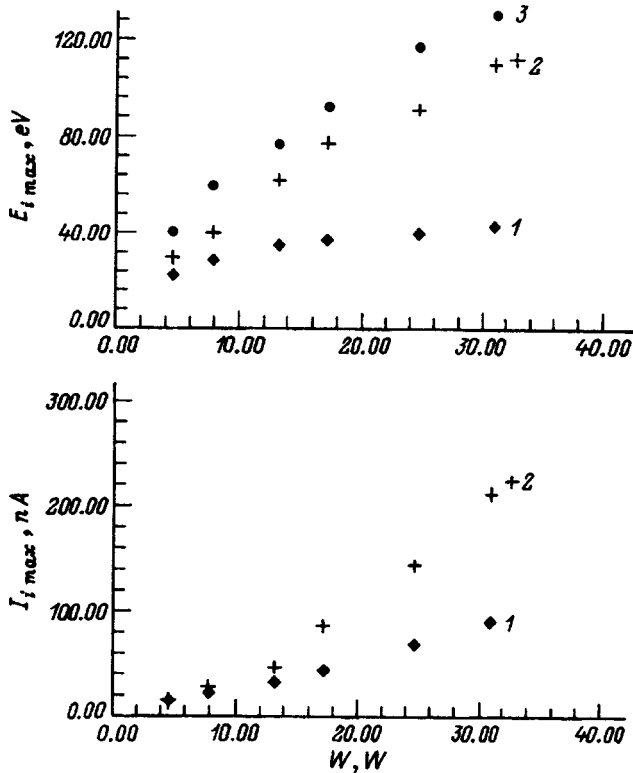


FIG. 8. Graphs of $E_{i \max}$ and $I_{i \max}$ versus rf power for a silane discharge at $f=13.56$ MHz. 1) dcSC regime; 2) dcOC regime; 3) dcOC $E_{i \max}$ plus self-bias voltage U_{sb} .

TABLE I. Parameters of the deposition process and ions.

Sample No.	f , MHz	P , torr	Q , sccm	W , mW/cm ²	U_{sb} , V	U_b , V	d , μm	V , Å/s	$E_{i\ max}$, eV	$I_{i\ max}$, arb. units
136-01	58	0.056	29.2	11	0	-	1.73	5.4	22	0.14
136-02	58	0.56	29.2	11	-	-20	1.93	4.9	13	0.14
136-03	58	0.056	29.2	11	-	+20	1.46	6.03	40	0.24
136-04	58	0.056	29.2	70	-14	-	1.64	7.0	33	1.0
136-05	58	0.056	29.2	70	-	-79	1.54	7.3	26	0.21
137-02	13.56	0.17	26.7	22	0	-	1.08	1.2	25	0.14
137-03	13.56	0.17	26.7	102	-69	-	1.39	2.4	40	1.0
137-04	13.56	0.17	26.7	32	-	+60	1.6	4.4	65	0.15
137-05	13.56	0.17	26.7	96	-	-198	1.45	5.6	32	0.51

$f=13.56$ MHz and from 5.4 \AA/s to 7 \AA/s at $f=58$ MHz. At low power the film growth rate is observed to increase when the positive bias is increased (cf. samples 136-01 and 136-03 at $f=58$ MHz and samples 137-02 and 137-04 at $f=13.56$ MHz) and to decrease when the negative bias is increased (samples 136-01 and 136-02). At high power a negative bias causes the film growth rate to increase (samples 136-04 and 136-05; 137-03 and 137-05) and leads to degradation of the electronic properties, which is discussed in the next section. An increase in the ion energy ($E_{i\ max}$) at $I_i \approx \text{const}$ causes the film growth rate to increase (samples 136-01 and 136-02; 137-02 and 137-04), whereas an increase in the ion flux without any appreciable change in the ion energy does not increase the film growth rate (samples 136-04 and 136-05; 137-03 and 137-04).

ELECTRONIC PROPERTIES OF HYDROGENATED AMORPHOUS SILICON FILMS PREPARED IN DISCHARGES WITH VARIOUS ION PARAMETERS

According to the IR spectroscopy data, assuming a constant $A = 1.6 \times 10^{19} \text{ cm}^{-2}$, the hydrogen concentration in the hydrogenated amorphous silicon films in the vicinity of 640 cm^{-1} lies in the interval 5.2–6.6 at. %. The Raman spectra of films deposited on various substrates have peaks at $\nu \approx 475\text{--}485 \text{ cm}^{-1}$ with half-widths $\Delta\nu = 60\text{--}70 \text{ cm}^{-1}$. These values are typical of hydrogenated amorphous silicon layers.

Some of the electronic properties of the films are shown in Table II. It is evident from the table that a variation of the ion parameters alters the electrical conductivity of hydrogenated amorphous silicon films prepared both at

$f=13.56$ MHz and at $f=58$ MHz. The increase in $E_{i\ max}$ due to the application of a constant bias to the powered electrode causes the activation energy E_a to increase and the room-temperature conductivity σ_{rt} to decrease (samples 136-01, 136-03, 137-02, and 137-04). The difference in the conductivities is not as significant in comparing samples prepared with close values of $E_{i\ max}$ and different ion fluxes (samples 136-03 and 136-04 at 58 MHz, 137-03 and 137-04 at 13.56 MHz). The reduction of ion bombardment by the application of a constant bias to the powered electrode at high rf power (samples 136-04 and 136-05 at 58 MHz, 137-03 and 137-05 at 13.56 MHz) decreases E_a and increases σ_{rt} .

The CPM characteristics also vary with the degree of ion bombardment. It is instructive to compare the CPM curves for samples prepared at $f=58$ MHz (series 136 samples) and at $f=13.56$ MHz (series 137 samples) under identical ion bombardment conditions. The CPM curves for ‘‘better’’ and ‘‘worse’’ samples are shown in Fig. 10. It is evident that the series 136 samples have lower absorption at phonon energies smaller than the width of the bandgap, $h\nu < E_g$, and therefore small values of E_u , E_{vt} , and N_d . Moreover, these samples are characterized by a shorter electron diffusion length L_e , but a longer hole diffusion length L_h . It is interesting to note that the reduction of ion bombardment by the application of a constant bias to the powered electrode at high rf power leads to significant degradation of the film properties (from a comparison of samples 136-04 and 136-05; 137-03 and 137-05).

The power transferred by ions to the surface of the growing film can be estimated as the product of the maximum ion

TABLE II. Electronic properties of the films.

Sample No.	$\sigma_{rt} \times 10^6$, S/cm	$\sigma_0 \times 10^{-3}$, S/cm	E_a , eV	E_F^T , eV	E_u , meV	E_{vt} , meV	W_d , eV	$N_d \times 10^{-16}$, cm ⁻³	L_e , μm	L_h , μm
136-01	1.5	6.0	0.63	0.48	59.4	54.6	0.18	0.53	0.14	0.11
136-02	0.1	3.3	0.62	0.55	63.7	54.4	0.07	1.2	0.17	0.11
136-03	0.003	16.3	0.75	0.65	53.5	50.4	0.16	0.15	0.17	0.17
136-04	0.035	4.45	0.77	0.58	56.1	53.3	0.08	0.69	0.37	0.10
136-05	1.0	3.0	0.58	0.49	65.6	57.3	0.11	1.3	0.19	0.09
137-02	0.52	0.99	0.59	0.51	67.2	59.3	0.12	1.0	0.20	0.03
137-03	0.017	4.45	0.74	0.59	77.9	73.1	0.11	0.34	0.32	0.06
137-04	0.002	4.47	0.76	0.64	61.0	55.0	0.12	0.36	0.32	0.05
137-05	0.03	9.0	0.71	0.58	71.0	62.0	0.12	1.2		

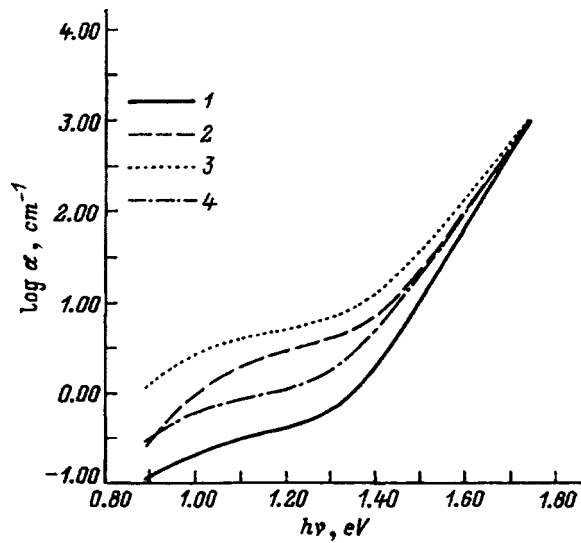


FIG. 10. Spectral dependence of the absorption coefficient $\alpha(h\nu)$, measured by the constant photocurrent method. 1) Sample 136-03; 2) 136-05; 3) 137-02; 4) 137-04.

energy and the ion current, whereupon the growth rate V and density of defects N_d as functions of W_i , i.e., $V(W_i)$ and $N_d(W_i)$, can be plotted. The corresponding curves are shown in Figs. 11 and 12. Clearly, the film growth rate increases with W_i . The behavior of $N_d(W_i)$ is more complex. It has two branches. The upper branch has N_d increasing as W_i increases. The points on this branch correspond to films prepared either at low power without a biased powered electrode or at high power with a negative bias. The lower branch of the $N_d(W_i)$ curve descends as W_i increases. The points of this branch correspond to samples prepared either at high power without a biased powered electrode or at low or high power with a positive bias on the electrode. In other words, the increase of rf power by the application of a positive bias to the powered electrode produces approximately a sixfold reduction in the density of defects in the film.

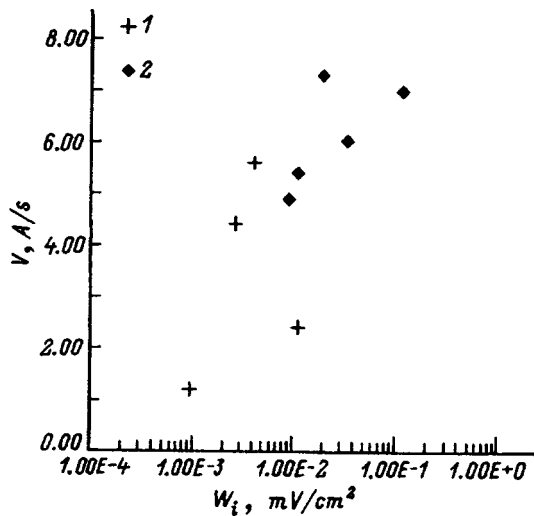


FIG. 11. Deposition rate V of a hydrogenated amorphous silicon film versus power fraction W_i . 1) $f=13.56$ MHz; 2) $f=58$ MHz.

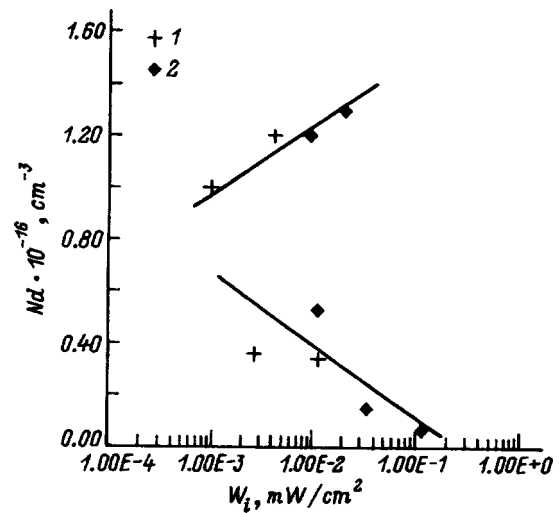


FIG. 12. Density of defects N_d versus W_i . 1) $f=13.56$ MHz; 2) $f=58$ MHz.

Consequently, within the range of discharge parameters used in the experiments discussed here we have observed an improvement in the electronic properties of hydrogenated amorphous silicon films prepared with the application of a positive bias to the powered electrode; the bias creates conditions of moderate ion bombardment of the growing film. This fact confirms previously published results for a 13.56-MHz discharge.²

CONCLUSION

In PECVD apparatus we have investigated the characteristics of ion and electron streams incident on a growing film in a discharge in silane at frequencies of 13.56 MHz and 58 MHz using various power inputs. We have grown films of hydrogenated amorphous silicon, bombarding the growing surface by ions of various energies and fluxes. We have studied the electronic properties of these films and the correlation of the properties with the characteristics of the ions.

The main results of the study are summarized below:

1) As the power input to the discharge is increased at the given frequencies, the maximum ion energy $E_{i \max}$ and the ion current I_i to the substrate have been observed to increase, the greatest variation of $E_{i \max}$ being observed in a discharge at 13.56 MHz, and the greatest variation of I_i in a discharge at 58 MHz.

2) It has been shown that the energy and flux of ions to the surface of the growing film depend on the constant bias voltage applied to the powered electrode.

3) The growth rate of a silicon film has been observed to increase (approximately fivefold) when deposited in a 58-MHz discharge in comparison with deposition in a 13.56-MHz discharge.

4) The average electron temperature T_e , determined on the assumption of a Maxwellian energy distribution function, is lower in a 58-MHz discharge ($T_e=2.5$ eV) than in a 13.56-MHz discharge ($T_e=3.25$ eV).

5) In the investigated discharges at both frequencies moderate ion bombardment of a growing silicon film has

improved the electronic properties (lowered the defect density, increased the carrier diffusion lengths, etc.) of the films; a reduction of ion bombardment, particularly at a high discharge power input, has resulted in considerable degradation of the film properties.

This work has received support from a grant of the International Association for the Promotion of Cooperation with Scientists from the Independent States of the Former Soviet Union, INTAS-93-116, along with partial support from grants of the International Science Foundation, No. ISF NUF-300, and the Russian Fund for Fundamental Research (RFFI), No. 96-02-16918.

- ¹J. C. Knights, G. Lucovsky, and R. G. Nemanich, *J. Non-Cryst. Solids* **32**, 393 (1979).
²P. Roca i Cabarrocas, P. Morin, V. Chu *et al.*, *J. Appl. Phys.* **69**, 2942 (1991).
³Y. Nakayama, K. Hitsuiishi, M. Zhang *et al.*, *J. Non-Cryst. Solids* **137–138**, 669 (1991).
⁴P. Roca i Cabarrocas, Thesis (Paris, 1988).
⁵H. Curtins, N. Wyrsh, M. Favre *et al.*, *Plasma Chem. Plasma Process.* **7**, 267 (1987).

- ⁶S. Oda, J. Noda, and M. Matsumura, *Jpn. J. Appl. Phys.* **29**, 1889 (1990).
⁷F. Finger, U. Kroll, V. Viret *et al.*, *J. Appl. Phys.* **71**, 5665 (1992).
⁸K. S. Frolov, A. I. Kosarev, A. S. Smirnov *et al.*, in *Proceedings of the 21st International Conference on Phenomena in Ionized Gases (ICPIG XXI)*, edited by G. Ecker *et al.*, Vol. 1 (Bochum, Germany, 1993), pp. 19–24.
⁹C. Bohm and J. Perrin, *Rev. Sci. Instrum.* **64**, 31 (1993).
¹⁰A. S. Smirnov, K. S. Frolov, and A. Yu. Ustavshchikov, *Zh. Tekh. Fiz.* **65**(8), 38 (1995) [*Tech. Phys.* **40**, 768 (1995)].
¹¹A. E. Dul'kin, S. A. Moshkalev, A. S. Smirnov *et al.*, *Zh. Tekh. Fiz.* **63**(7), 64 (1993) [*Tech. Phys.* **38**, 564 (1993)].
¹²M. A. Lieberman and A. J. Lichtenberg, *Principles of Plasma Discharges and Materials Processing* (Wiley, New York, 1994).
¹³Yu. P. Raizer and M. N. Shneider, *Plasma Sources Sci. Technol.* **1**, 102 (1992).
¹⁴B. Chapman, *Glow Discharge Processes* (Wiley, New York, 1980).
¹⁵G. S. Trofimov, A. I. Kosarev, P. G. Le Comber *et al.*, *J. Non-Cryst. Solids* **137–138**, 21 (1991).
¹⁶M. Vanecek, J. Koska, J. Stuchlik *et al.*, *Sol. Energy Mater.* **8**, 411 (1983).
¹⁷A. S. Smirnov and L. D. Tsendin, *IEEE Trans. Plasma Sci.* **PS-19**, 130 (1991).
¹⁸I. D. Kaganovich and L. D. Tsendin, *IEEE Trans. Plasma Sci.* **PS-20**, 66–75, 86–92 (1992).

Translated by James S. Wood

Reflection and refraction of spin waves in uniaxial magnets in the geometrical-optics approximation

Yu. I. Gorobets and S. A. Reshetnyak

Institute of Magnetism, Ukrainian National Academy of Sciences, 252142 Kiev, Ukraine

(Submitted August 8, 1996; resubmitted April 16, 1997)

Zh. Tekh. Fiz. **68**, 60–63 (February 1998)

The laws governing the propagation of magnetization waves are investigated in the geometrical-optics approximation, in which a spin wave can be treated as a ray. The refractive index for a spin wave on the interface between two magnets with different exchange coupling constants and magnetic anisotropy constants is determined. The dependences of the intensity of the reflected wave and the refractive index on the spin-wave frequency and the strength of the external uniform magnetic field are calculated. Estimates of the dimensions of inhomogeneous inclusions that perform functions analogous to the functions of lenses and mirrors in optics are presented. The possibility of using the same inhomogeneities both as lenses and as mirrors, depending on the magnetic field strength, is pointed out. © 1998 American Institute of Physics. [S1063-7842(98)01102-7]

INTRODUCTION

Recent advances in nanotechnologies and nanoelectronics¹ call for the creation of new devices utilizing the characteristic features of spin waves. Under these circumstances it is of interest to use the geometrical-optics approximation to describe the behavior of spin waves propagating in a medium with an inhomogeneous distribution of magnetic parameters.

One of the most important advantages of this approach over the electrodynamic approach is the formation of spin rays, which, first, renders the propagation of spin waves more graphic and, second, permits the use of spin-wave analogies of optical devices formed by creating artificial inhomogeneities of the magnetic parameters of a medium of assigned configuration and an external magnetic field to create inhomogeneities of the spin-wave intensity (in particular, to accomplish the focusing of spin waves). Finally, it makes it possible to create wave packets, which do not lead to significant diffraction, scattering, etc. on interfaces, for the purpose of employing these structures as filters, switches, etc. in practice.

Such a possibility is illustrated in this paper in the case of uniaxial magnetic materials.

EQUATIONS OF MAGNETIZATION DYNAMICS

Let us consider a system of two semi-infinite magnets with exchange coupling constants α_1 and α_2 and magnetic anisotropy constants β_1 and β_2 , which come into contact in the yz plane. The easy magnetization axis of each magnet is parallel to the Z axis. We direct a constant uniform magnetic field H_0 along this axis. The saturation magnetization M_0 is assumed to be constant for the entire structure.

Following Ref. 2, we represent the distribution of the magnetization in the material in the form

$$\mathbf{M}(\mathbf{r}, t) = M_0 \Psi^+(\mathbf{r}, t) \boldsymbol{\sigma} \Psi(\mathbf{r}, t), \quad (1)$$

where Ψ denotes the quasiclassical wave functions, which play the role of the order parameter of the spin density, \mathbf{r} is the radius vector in the Cartesian coordinate system, t is the time, and $\boldsymbol{\sigma}$ is a vector of Pauli matrices.

The Lagrange equations for Ψ have the form

$$i\hbar \frac{\partial \Psi(\mathbf{r}, t)}{\partial t} = -\mu_0 \mathbf{H}_e(\mathbf{r}, t) \cdot \boldsymbol{\sigma} \Psi(\mathbf{r}, t), \quad (2)$$

where μ_0 is the Bohr magneton, and \mathbf{H}_e is the effective magnetic field, which has the following form in the exchange approximation:³

$$\mathbf{H}_e(\mathbf{r}, t) = [\alpha \nabla^2 - \beta] \mathbf{M}(\mathbf{r}, t) + \mathbf{e}_z [\beta M_0 + H_0]. \quad (3)$$

Here \mathbf{e}_z is a unit vector directed along the easy magnetization axis; and ∇^2 is the Laplacian operator. Taking into account that the material is magnetized parallel to \mathbf{e}_z in the ground state and setting $\mathbf{M}^2(\mathbf{r}, t) = \text{const}$, we seek the solution of (2) in the form

$$\Psi(\mathbf{r}, t) = \exp[i\mu_0(H_0 + \beta M_0)t/\hbar] \begin{pmatrix} 1 \\ \chi(\mathbf{r}, t) \end{pmatrix}, \quad (4)$$

where $\chi(\mathbf{r}, t)$ is a small addition, which characterizes the deviation of the magnetization from the ground state.

Linearizing Eq. (2) with consideration of (3) and (4), we obtain

$$-\frac{i\hbar}{2\mu_0 M_0} \frac{\partial \chi(\mathbf{r}, t)}{\partial t} = (\alpha \nabla^2 - \beta - \tilde{H}_0) \chi(\mathbf{r}, t), \quad (5)$$

where $\tilde{H}_0 = H_0/M_0$.

Equation (5) describes the magnetization dynamics in the short-wavelength (exchange) approximation.

REFLECTION AND TRANSMISSION AMPLITUDES

Let a spin wave impinge on the interface from the homogeneous magnet with the parameters α_1 and β_1 in the positive direction of the x axis at an arbitrary angle. Here

$\chi_i = \exp(i(\mathbf{k}_1 \cdot \mathbf{r} - \omega t))$ corresponds to the incident wave, $\chi_r = R \exp(i(\mathbf{k}'_1 \cdot \mathbf{r} - \omega t))$ to the reflected wave, and $\chi_d = D \exp(i(\mathbf{k}_2 \cdot \mathbf{r} - \omega t))$ to the transmitted wave, where R is the complex amplitude describing the reflection of the spin wave from the interface, the square of whose modulus is the reflection coefficient; D is the complex transmission amplitude; \mathbf{k}_1 and \mathbf{k}'_1 are the wave vectors of the incident and reflected waves, respectively; \mathbf{k}_2 is the wave vector of the transmitted wave; and ω is the frequency. Inasmuch as⁴

$$k_1^2 = k_1'^2 = (\Omega - \beta_1 - \tilde{H}_0) / \alpha_1,$$

$$k_2^2 = (\Omega - \beta_2 - \tilde{H}_0) / \alpha_2,$$

where $\Omega = \omega \hbar / 2\mu_0 M_0$,

$$k'_{1x} = -\sqrt{k_1^2 - k_{1y}^2 - k_{1z}^2}, \quad k_{2x} = \sqrt{k_2^2 - k_{2y}^2 - k_{2z}^2}$$

(the minus sign in the expression for k'_{1x} corresponds to a wave moving away from the interface), and $k_{1i} = k'_{1i} = k_{2i}$ for $i = y, z$ on the interface, we find that the incident, reflected, and transmitted waves, as well as the normal constructed at the point of incidence, lie in one plane and that the angle of incidence equals the angle of reflection. This statement is analogous to the law of the reflection of light waves in optics.⁵

When k_{2x} is real, i.e., when the condition $k_2^2 > k_{2y}^2 + k_{2z}^2$ holds, which is equivalent to

$$\frac{\alpha_1}{\alpha_2} \cdot \frac{\Omega - \beta_2 - \tilde{H}_0}{\Omega - \beta_1 - \tilde{H}_0} > \sin^2 \theta_1,$$

we have

$$\frac{\sin \theta_1}{\sin \theta_2} = \frac{k_2}{k_1} = \sqrt{\frac{\alpha_1}{\alpha_2} \frac{\Omega - \beta_2 - \tilde{H}_0}{\Omega - \beta_1 - \tilde{H}_0}} = n, \quad (6)$$

where θ_1 is the angle of incidence, θ_2 is the angle of reflection, and n the refractive index.

If $k_2^2 < k_{2y}^2 + k_{2z}^2$ (this corresponds to the case of $k_1^2 > 0$ and $k_2^2 < 0$), then

$$k_{2x} = -i\sqrt{k_1^2 + k_{1z}^2 - k_2^2} = -i/2h,$$

$$\chi_d(\mathbf{r}, t) = D \exp(-x/2h) \exp(i(k_{2y}y + k_{2z}z - \omega t)),$$

i.e., h plays the role of the penetration depth of the spin wave in the second material and equals

$$h = \frac{1}{k_1 \sqrt{\sin^2 \theta_1 - n^2}}.$$

The limiting angle for total reflection is specified by the expression

$$\sin \theta_0 = \sqrt{\frac{\alpha_1}{\alpha_2} \frac{\Omega - \beta_2 - \tilde{H}_0}{\Omega - \beta_1 - \tilde{H}_0}}.$$

Using the following boundary conditions for $\chi(\mathbf{r}, t)$ on the interface between the layers

$$\chi(-0, y, z, t) = \chi(+0, y, z, t),$$

$$\alpha_1 \frac{\partial \chi}{\partial x}(-0, y, z, t) = \alpha_2 \frac{\partial \chi}{\partial x}(+0, y, z, t),$$

we obtain the expressions for the reflection and transmission amplitudes of a spin wave

$$R = \frac{\alpha_1 \cos \theta_1 - \alpha_2 \sqrt{n^2 - \sin^2 \theta_1}}{\alpha_1 \cos \theta_1 + \alpha_2 \sqrt{n^2 - \sin^2 \theta_1}},$$

$$D = \frac{2\alpha_1 \cos \theta_1}{\alpha_1 \cos \theta_1 + \alpha_2 \sqrt{n^2 - \sin^2 \theta_1}}. \quad (7)$$

We note that expression (6) can also be obtained on the basis of other arguments using the Wentzel–Kramers–Brillouin–Jeffreys (WKB) approximation.⁶

THE WKB APPROXIMATION

The WKB approximation allows us to go from the problem of the propagation of spin waves, which can be solved in the electrodynamic approach, to the geometrical optics of spin waves by going from the function $\chi(\mathbf{r}, t)$, which describes the behavior of a wave, to a function known as an eikonal, which characterizes the behavior of a ‘‘localized’’ wave packet like a ray. It should be noted that, as in the optics of light waves, we can refer to manifestations of wave or ray properties only when a wave interacts with an obstacle encountered along its path. A ray type of propagation is possible only if the characteristic dimension of the obstacles, which are inhomogeneities of the medium, greatly exceeds the wavelength.

Defining $\chi = \exp[i(s(\mathbf{r}) - \omega t)]$ in (5), under the condition $\lambda \ll l$,

$$\lambda \ll l, \quad (8)$$

where λ is the spin wavelength, l is the characteristic dimension of the inhomogeneities, and $s(\mathbf{r})$ is an eikonal, we obtain an analog of the classical Hamilton–Jacobi equation

$$(\nabla s)^2 + (\beta + \tilde{H}_0 - \Omega) / \alpha = 0. \quad (9)$$

In our case ∇s plays the role of \mathbf{k} , and Hamilton’s equation is equivalent to the system of equations

$$\dot{\mathbf{k}} = -\partial \omega / \partial \mathbf{r}, \quad \dot{\mathbf{r}} = \partial \omega / \partial \mathbf{k}$$

or, with consideration of the constancy of the wave frequency,

$$\mathbf{k} = \text{const}, \quad \dot{\mathbf{r}} = 4\mu_0 M_0 \alpha \mathbf{k} / \hbar. \quad (10)$$

When a wave impinges on an interface, from (9) and (10) we obtain

$$k_1 \sin \theta_1 = k_2 \sin \theta_2,$$

$$k_i^2 + (\beta_i + \tilde{H} - \Omega) / \alpha_i = 0, \quad i = 1, 2$$

whence follows Eq. (6).

The inequality (8) is the condition for going over to the geometrical optics of spin waves. In the present case the role of the inhomogeneities is played by the interface between the media, which has the form of an infinite plane and thus satisfies Eq. (8).

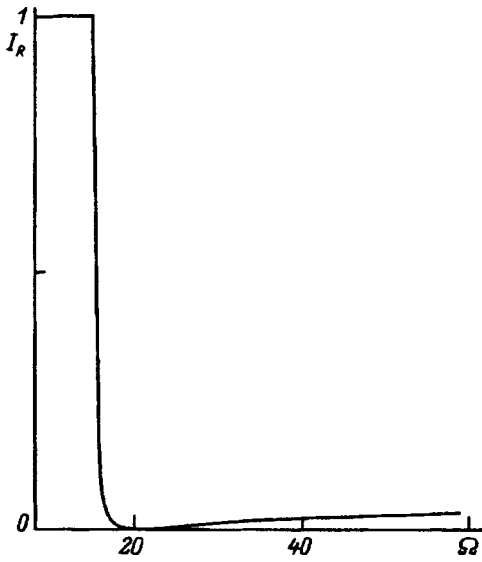


FIG. 1. Dependence of the intensity of the reflected wave on the frequency for $\alpha_2/\alpha_1=3$, $\theta=\pi/10$, $\beta_1=5$, $\beta_2=10$, and $\tilde{H}_0=3$.

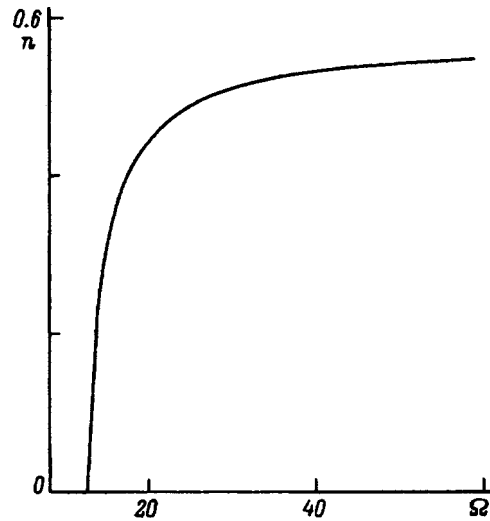


FIG. 2. Dependence of the refractive index on the frequency for $\alpha_2/\alpha_1=3$, $\theta=\pi/10$, $\beta_1=5$, $\beta_2=10$, and $\tilde{H}_0=3$.

ESTIMATES OF THE PARAMETERS

Drawing the analogy between the propagation of light and the propagation of spin waves which satisfy requirement (8), we can apply the geometrical-optics approximation to spin rays. In particular, we can devise spin-wave analogs of optical lenses and various configurations of mirrors using materials with different values of α and β . The construction of images will obey laws like those of geometrical optics; however, the refractive index on the boundary between two media will depend not only on the frequency of the incident wave and the parameters of the material, but also on the strength of the external constant uniform magnetic field.

We present estimates of the parameters of the materials in the case of a thin lens and small angles of incidence of the spin rays relative to the optical axis of the lens, which ensure the necessary transparency of the lens. Since the intensity of a reflected wave is determined by the square of the modulus of the reflection amplitude and, as follows from Eq. (7), $|R|^2 \approx [(\alpha_1 - \alpha_2 n)/(\alpha_1 + \alpha_2 n)]^2$ (for small angles of incidence), then if we require fulfillment of the condition $|R|^2 < \eta$, where η is the necessary degree of smallness of the reflection coefficient, we obtain a constraint on n and, consequently, on α , β , Ω , and \tilde{H}_0 :

$$\frac{1 - \sqrt{\eta}}{1 + \sqrt{\eta}} < \frac{\alpha_2}{\alpha_1} n < \frac{1 + \sqrt{\eta}}{1 - \sqrt{\eta}}$$

The corresponding constraints in the case of a mirror have the following form:

$$\frac{\alpha_2}{\alpha_1} n < \frac{1 - \sqrt{\eta}}{1 + \sqrt{\eta}} \quad \text{or} \quad \frac{\alpha_2}{\alpha_1} n > \frac{1 + \sqrt{\eta}}{1 - \sqrt{\eta}}$$

For fulfillment of the condition for geometrical optics (8), the thickness of the lens or mirror is restricted by the inequality

$$l \gg 2\pi \sqrt{\alpha/(\Omega - \beta - \tilde{H}_0)} \tag{11}$$

As is seen from (6) and (11), selection of the parameters for constructing a lens or a mirror does not present any difficulty for an extensive list of magnetic materials.⁷ In particular, in the case of yttrium-iron garnet, it follows from condition (11) for a thin lens that $l \gg 10^{-4} - 10^{-6}$ cm.

ANALYSIS OF RESULTS

Figures 1 and 2 show the dependence of the reflection intensity $I_R = |R|^2$ (or the reflection coefficient, which is equivalent) and the refractive index n on the spin-wave frequency for characteristic values of the parameters of the material.⁷ It is clearly seen that the required ratio between the intensities of the reflected and transmitted waves for the frequency chosen can be achieved by adjusting the parameters of the material. In addition, as follows from Fig. 3, the reflection intensity depends significantly on the strength of the

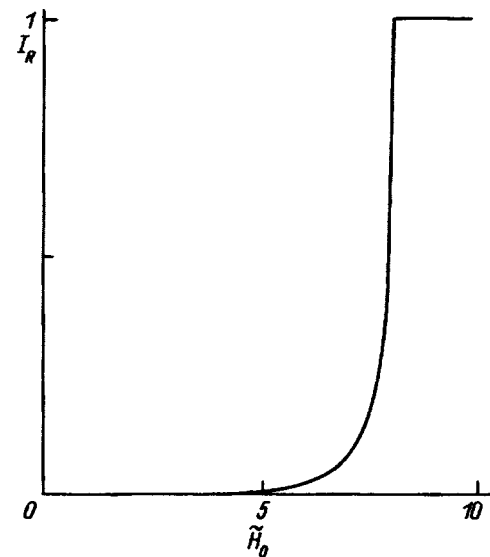


FIG. 3. Dependence of the intensity of the reflected wave on the external uniform magnetic field for $\alpha_2/\alpha_1=3$, $\theta=\pi/10$, $\beta_1=5$, $\beta_2=10$, and $\Omega=20$.

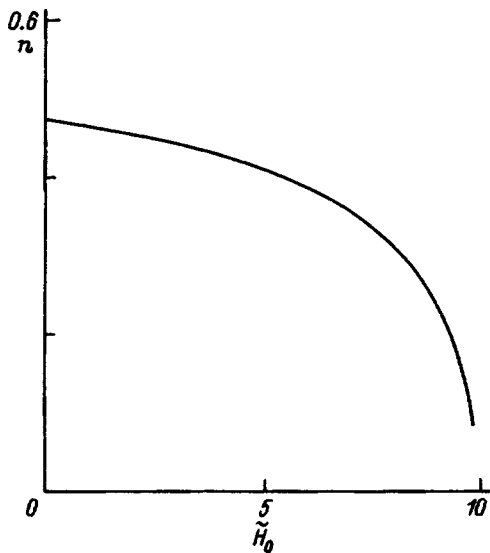


FIG. 4. Dependence of the refractive index on the external uniform magnetic field for $\alpha_2/\alpha_1=3$, $\theta=\pi/10$, $\beta_1=5$, $\beta_2=10$, and $\Omega=20$.

external uniform magnetic field, making it possible to control the intensity over a broad range by varying only the value of the external magnetic field at fixed parameters of the material. The character of the variation of the refractive index is reflected in Fig. 4.

Thus, it is possible to achieve a required reflection coef-

ficient for an inclusion that has the shape of a lens (or mirror) in a homogeneous material and values of α and β differing from the corresponding values in the homogeneous part and thus plays the role of a lens or mirror by varying the strength of the external magnetic field. The reflection coefficient can be varied practically from zero to unity (Fig. 3) without varying the parameters of the medium, making it possible to use the same inhomogeneity as a spin-wave lens and as a mirror without alteration of the parameters of the structure.

We thank B. A. Ivanov for participating in the discussion of this work.

¹*Atomic and Nanometer-Scale Modification of Materials: Fundamentals and Applications (NATO ASI Series, Ser. E)*, P. Avouris (ed.), Kluwer Academic Publishers, Dordrecht/Boston/London (1993).

²V. G. Bar'yakhtar and Yu. I. Gorobets, *Magnetic Bubble Domains and Domain Lattices* [in Russian], Naukova Dumka, Kiev (1988).

³Yu. I. Gorobets, A. E. Zyubanov, A. N. Kuchko *et al.*, *Fiz. Tverd. Tela (Leningrad)* **34**, 1486 (1992) [*Sov. Phys. Solid State* **34**, 790 (1992)].

⁴A. I. Akhiezer, V. G. Bar'yakhtar, and S. V. Peletminskii, *Spin Waves*, North-Holland, Amsterdam (1967).

⁵M. Born and E. Wolf, *Principles of Optics*, 4th ed., Pergamon Press, Oxford/New York (1970); Nauka, Moscow (1973).

⁶P. M. Morse and H. Feshbach, *Methods of Theoretical Physics, Part II*, McGraw-Hill, New York (1953); Mir, Moscow (1960).

⁷A. H. Eschenfelder, *Magnetic Bubble Technology*, Springer-Verlag, Berlin (1980); Mir, Moscow (1983).

Translated by P. Shelnitz

Cylindrical glow-discharge-pumped excimer lamps

M. I. Lomaev, A. N. Panchenko, É. A. Sosnin, and V. F. Tarasenko

*Institute of High-Current Electronics, Russian Academy of Sciences, Siberian Branch,
634055 Tomsk, Russia*

(Submitted October 24, 1996)

Zh. Tekh. Fiz. **68**, 64–68 (February 1998)

The results of investigations of the emission of glow discharges in mixtures of inert gases and halogens in cylindrical tubes of various dimensions are presented. Glow-discharge-pumped XeCl* and KrCl* excimer lamps with a homogeneous spatial distribution of the radiation and powers up to 100 W are created. It is shown that the high efficiency of excimer lamps of this type is achieved as a result of the effective formation of exciplexes in a harpoon reaction and the slow rate of their quenching in the glow-discharge plasma at low pressures of the working mixture. © 1998 American Institute of Physics. [S1063-7842(98)01202-1]

INTRODUCTION

A great deal of attention has been focused on the development of sources of incoherent (spontaneous) ultraviolet radiation (excimer lamps), which can find extensive application in photolithography, medicine, ecology, etc.¹ Excimer lamps pumped by a low-pressure glow discharge, which are distinguished by the simplicity of their design and have the highest mean radiated powers (greater than 100 W) and efficiencies (up to ~15%) known at the present time, are very promising in this context.^{2,3} It should be noted that pulsed and continuous glow discharges in mixtures of inert gases and halogen-containing molecules have been studied as sources of ultraviolet radiation to a comparatively small extent. Low-pressure Xe–Cl₂ and Xe–HCl discharges were investigated in Ref. 4, and a fluorescence conversion efficiency for XeCl* below 1% was obtained. The same efficiency was obtained in Ref. 5 for KrCl*, KrF*, XeCl*, and XeF* upon excitation by a discharge with a high current density. The low output of ultraviolet radiation was attributed to excess heating of the gas and quenching of the radiating molecules by electrons. In Refs. 6 and 7 the fluorescence conversion efficiency was raised to 12%, but great nonuniformity of the output of ultraviolet radiation along the axis of the discharge tube was noted. The work in Refs. 8 and 9 was devoted to the study of the emission of XeF*, XeCl*, and KrCl* in tubes of small diameter with pumping by a low-pressure glow discharge. In the high-power coaxial excimer lamps described in Refs. 2 and 3 there were difficulties in filling the entire working volume with the discharge, which also destroyed the uniformity of the spatial distribution of the output radiation.

This report presents the results of an investigation of the emission of a glow discharge in cylindrical discharge tubes, including tubes with a large working volume, and the parameters of cylindrical excimer lamps with a homogeneous spatial distribution of the radiation, which were developed on the basis of this research.

EXCIMER LAMP DESIGNS AND EXPERIMENTAL METHOD

Excimer lamps similar to those in Refs. 2 and 3 were fabricated from high-quality quartz tubes, at whose ends there were stainless-steel electrodes of various shape. The internal diameter of the tubes was 9, 32, 40, or 60 mm, and their length varied in the range 20–80 cm. The maximum active volume of the excimer lamps was 1 liter, and the area of the radiating surface was as large as 1000 cm². The emission of gas mixtures of Xe, Kr, and He with Cl₂ or HCl was investigated. A high-voltage source, which provided for a discharge current up to 200 mA and a pump power up to 1 kW, was used to ignite and sustain the glow discharge. The mean radiated power was recorded by an IMO-2H calorimeter or an FÉK-22SPU photodiode. The latter was additionally calibrated using the output of XeCl or KrCl lasers before the measurements. The measurements were performed in the following manner. A diaphragm with a square $d \times d$ opening, where d is the diameter of the discharge tube, was placed tightly against the excimer lamp. The radiation detector was positioned at a distance $L > 10d$ from the diaphragm. The radiating area was assumed to be a point light source that radiates uniformly into a solid angle equal to 4π sr. The fraction k of the radiation impinging on the photodetector in this case equals

$$k = \sin^{-2} \alpha/2, \quad (1)$$

where $\alpha = \arctan A/2L$ and A is the entrance aperture of the radiation detector.

Next, the mean radiated power was calculated with consideration of the length of the excimer lamps and the distribution of the radiation along its axis. The distribution of the radiation across the diameter of the excimer lamps was homogeneous in each cross section.

The spontaneous emission spectra were recorded by an ISP-30 spectrograph on RF-3 film or by an MDR-23 monochromator with 1200 lines/mm grating equipped with an FEU-100 photomultiplier, whose signal was fed into a plotter through an amplifier.

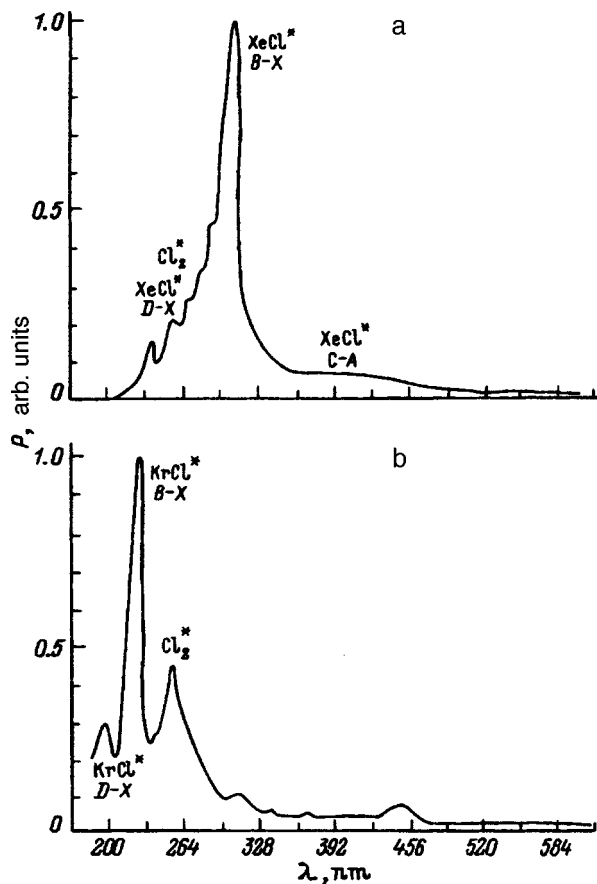


FIG. 1. Emission spectra of continuous glow discharges in Xe-Cl₂ (a) and Kr-Cl₂ (b) gas mixtures.

EXPERIMENTAL RESULTS

Figure 1 presents the emission spectra of glow-discharge-pumped XeCl* and KrCl* excimer lamps in the wavelength range from 200 to 600 nm. As in Refs. 2, 3, 6, and 7, the most intense signals in the ultraviolet region are the D-X and B-X bands of XeCl* (the maxima at 235 and 308 nm) and KrCl* (199 and 222 nm) and the broad-band emission in the CA band of XeCl*. In addition, the emission spectrum of the KrCl* excimer lamp exhibits an intense band of the Cl₂* molecules (λ_{max} ~258 nm). The radiated intensity at this wavelength was significantly smaller in the output of the XeCl* lamp. This is attributable to rapid quenching of the Cl⁺ ions and excited Cl* atoms,¹⁰ which are involved in the formation¹¹ of Cl₂⁺, in collisions with Xe atoms. The half-width of the B-X transitions of XeCl* and KrCl* usually did not exceed ~15 nm. As is seen from Fig. 1, the radiated intensity of the glow discharge in the visible region is very low, and its value does not exceed ~20% of the total radiated power of the glow discharge.

The emission of XeCl* and KrCl* in a glow discharge in tubes of small diameter was investigated in Xe(Kr)-HCl(Cl₂) mixtures. When HCl was employed as the halogen carrier, the radiated power at λ=222 and 308 nm did not exceed ~5 W, and the efficiency was no greater than 2-3%. The efficiency did not vary, but the radiated power increased proportionally to the increase in the discharge length in the range from 23 to 60 cm, attesting to mainte-

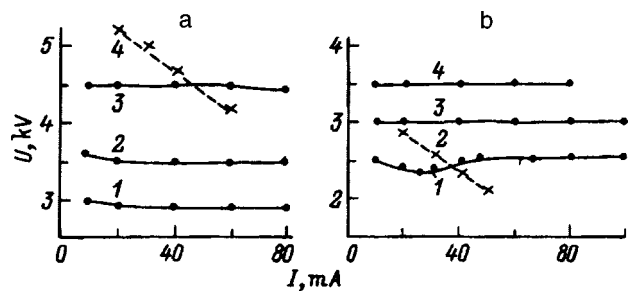


FIG. 2. Current-voltage characteristics of a glow discharge in a tube with a length of 23 cm and a diameter of 9 mm. a—Mixture with Xe:Cl₂=3:1; p, torr: 1-6; 2-9; 3-15; 4-21 (contracted discharge). b—Mixture with Kr:Cl₂=15:1; p, Torr: 1-9, 2-15 (contracted discharge) and mixture with Kr:Cl₂=3:1; Torr: 3-9, 4-12.

nance of the uniformity of the discharge. Therefore, in the subsequent experiments the discharge length was increased to 80 cm. The replacement of HCl by Cl₂, as in Refs. 6 and 7, led to significant increases in the efficiency and power of the ultraviolet radiation. However, the maximum efficiencies in the mixtures with HCl were several times greater than in Ref. 6. The increases in the efficiency and power of the ultraviolet radiation in the mixtures with Cl₂ are attributed to the small rate of formation of exciplexes through the ionic channel in a low-pressure discharge.² In addition, as we know, in mixtures with HCl the harpoon channel makes only a small contribution because of the large binding energy of HCl molecules in the ground state and the ineffective vibrational excitation of HCl molecules under the conditions of a glow discharge due to the high energy of the electrons in the plasma.¹² At the same time, in mixtures with Cl₂ the formation of exciplexes in the harpoon reaction is very efficient.^{2,6,7,10} Only mixtures with Cl₂ were used in the subsequent experiments.

Figure 2 presents the current-voltage characteristics of glow discharges in Xe-Cl₂ and Kr-Cl₂ mixtures. In contrast to Refs. 6 and 7, in our experiments the voltage needed to sustain the discharge U_{dis} depended weakly on the current and was determined by the concentration of chlorine in the gas mixture and its pressure. Descending current-voltage characteristics were observed in a contracted discharge, where the positive column narrowed to a thin bright filament or such a filament developed on a background of the bulk fluorescence. Contraction of the discharge usually occurred when the pressure of the mixture was raised or as a result of excessive heating of the tube after prolonged operation of the excimer lamp at a high pump power. Intense heating of the tube also restricted the service life of the mixture to 1-2 h because of the rapid absorption of chlorine by the hot cathode. We note that the fluorescence intensity of the exciplexes varied only slightly along the discharge tube under the experimental conditions described in Fig. 2, decreasing appreciably only in the first 3-4 cm from the cathode.

The measurements of the time dependence of the power of the ultraviolet radiation from three portions in the discharge, viz., near the anode, near the cathode, and at the middle of the discharge tube, demonstrated the following. The drop in the intensity of the ultraviolet radiation from

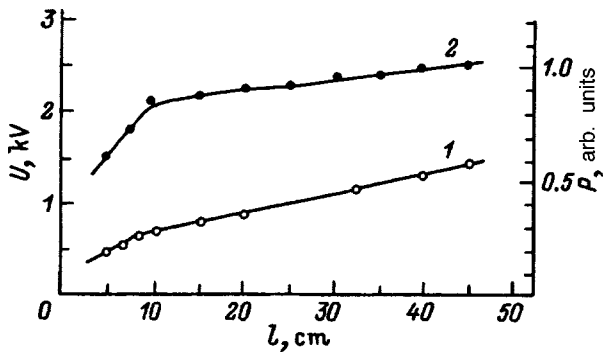


FIG. 3. Distribution of the voltage (U) and the radiation at $\lambda \approx 222$ nm (2) along the axis of an excimer lamp. Tube with a length of 45 cm and a diameter of 40 mm, a mixture with $\text{Kr}:\text{Cl}_2=6:1$ at $p=3$ torr, and a discharge current equal to 30 mA; 0 corresponds to the cathode.

these points occurs at approximately the same rate and is accompanied by a decrease in the voltage needed to sustain the discharge, which occurs because of the lowering of the chlorine concentration in the mixture. Hence it can be concluded that cathophoresis has a weak influence on the distribution of the output power along the axis of the excimer lamp. Therefore, the drop in the output of ultraviolet radiation near the cathode is not due to the depletion of chlorine from this region, as was conjectured in Refs. 6 and 7. Measurements performed using a movable electrode placed in the working volume of the excimer lamp showed that the voltage drop in the cathode region of a glow discharge in a mixture with chlorine amounts to about half of the voltage on the discharge tube (Fig. 3). Therefore, the high value of the field strength can be the cause of the low efficiency of the output of ultraviolet radiation from the near-cathode region of a glow discharge.

The dependence of the radiated power and efficiency of small-diameter KrCl^* and XeCl^* excimer lamps on the discharge current is shown in Fig. 4. The power of the ultraviolet radiation increases at discharge currents up to $I=80$ mA, but at a certain value of the current I_{cr} the rate of increase decreases appreciably, and the efficiency of the excimer lamp begins to drop simultaneously. The diameter of the discharge increases as the current is increased. At $I=I_{cr}$ the diameter of the discharge column is comparable to the internal diameter of the tube. Therefore, this break can be attributed to the increase in the rate of diffusion of charged particles to the walls of the tube at $I \geq I_{cr}$. In addition, as the discharge current increases, the temperature of the working mixture rises because of the increase in the pump power. The maximum radiated power at $\lambda \sim 222$ and 308 nm was approximately 12 W with an efficiency equal to 5–6%. When the mixture was pumped through the discharge tube, this break was not observed up to a discharge current of 100 mA, and the radiated power reached 20 W ($E_{sp}=1 \text{ W/cm}^3$) with maintenance of the efficiency at the 7–10% level, which is lower than in Refs. 2, 6, and 7. This can also be caused by the large diffusion losses in thin tubes.

As expected, the power and efficiency of the excimer lamps increased significantly after switching to discharge tubes of large diameter (30–40 mm). In these excimer lamps

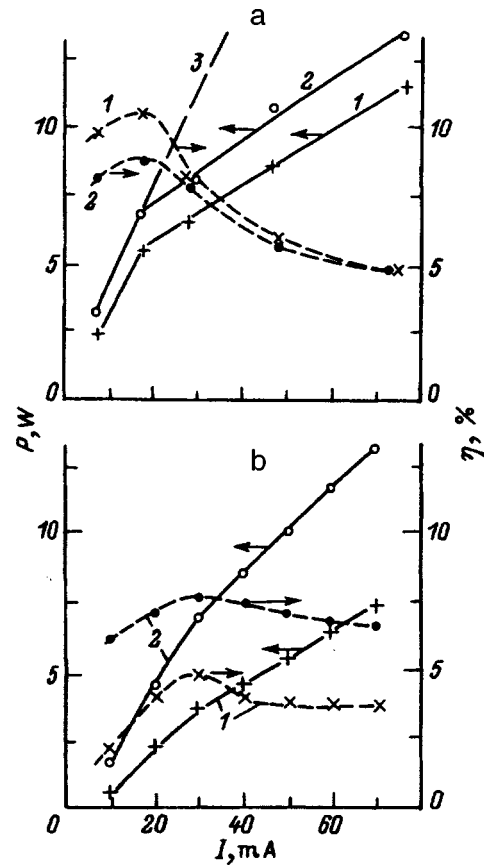


FIG. 4. Dependence of the mean power and efficiency of XeCl^* (a) and KrCl^* (b) excimer lamps on the discharge current. Tube with a length of 23 cm and a diameter of 9 mm; a—mixture with $\text{Xe}:\text{Cl}_2=3:1$ at $p=6$ (1) and 9 Torr (2). Curve 3 was obtained with pumping of the gas through the discharge tube; b—mixture with $\text{Kr}:\text{Cl}_2=15:1$ at $p=9$ Torr (1), mixture with $\text{Kr}:\text{Cl}_2=3:1$ at $p=9$ torr (2).

cathodes with a cavity, whose dimensions were selected experimentally, were used to reduce the drop in radiated power in the near-cathode region. As a result, the radiated power varied by no more than 10–15% along the axis of the excimer lamp, and the dip in power near the cathode vanished completely. The transverse power distribution of the ultraviolet radiation in an excimer lamp with a diameter of the working region equal to 60 mm was also measured (Fig. 5). The observations were made through a quartz window with a diameter of 40 mm in the endplate of the anode. When the discharge current equals 10 mA, the near-axial region of the discharge radiates more intensely. When the discharge current is increased to 30 mA, the distribution of the radiated power over a cross section of the tube, as we have already noted above, becomes more even. In addition, because of the choice of an electrode material that does not interact with chlorine and the cooling of the electrodes by flowing water, the lifetime of the mixture increased to ~ 100 h.

Figure 6 presents the dependence of the power and efficiency of XeCl^* and KrCl^* excimer lamps with a length of 80 cm and a diameter of 32 mm on the discharge current. As in the case of the small-diameter excimer lamps, the radiated power at $\lambda \sim 308$ nm increased nonlinearly. A break was observed at the point where the diameter of the discharge col-

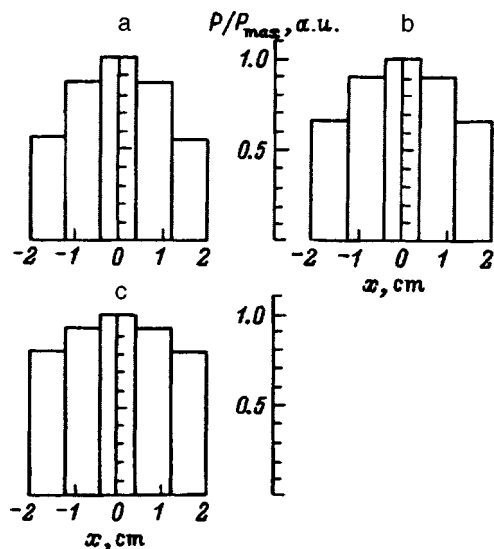


FIG. 5. Histograms of the power distribution of the ultraviolet radiation in a transverse section of an excimer lamp with a diameter of 60 mm and a length of 40 cm. Mixture with Xe:Cl₂=6:1; *p*=2 torr. Discharge current, mA: a—10, b—20, c—30.

umn became comparable to the tube diameter. The power of the KrCl* excimer lamp increased linearly, since the diameter of the discharge in the Kr-Cl₂ mixture was smaller than the diameter of the discharge tube in the range of currents investigated. A radiated power up to 100 W was obtained with an efficiency up to 15% at λ~222 and 308 nm. Similar results were obtained for the excimer lamps with diameters

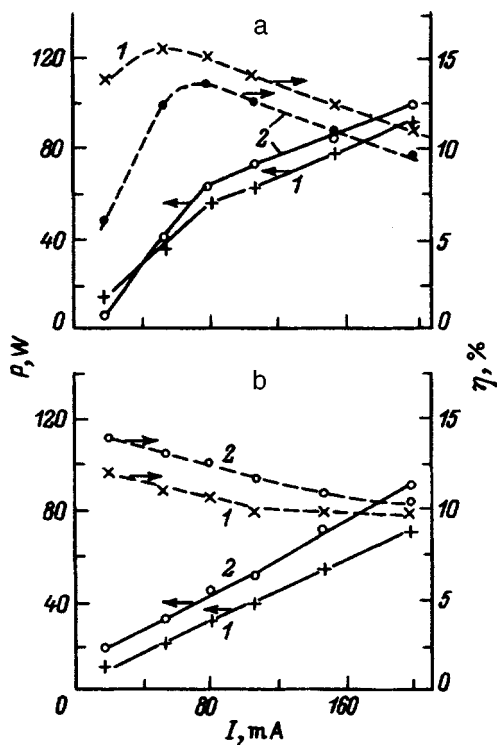


FIG. 6. Dependence of the mean power and efficiency of XeCl* (a) and KrCl* (b) excimer lamps on the discharge current. Mixtures with Xe(Kr):Cl₂=5:1; *p*, Torr: 1—1.5; 2—3.

equal to 40 and 60 mm. In addition, the emission of Cl₂* at λ~258 nm was obtained in a He-Cl₂ mixture with a power as high as 30 W and η~2%.

Since about half of the power imparted to the gas is absorbed by the cathode layer of the glow discharge in tubes with a length ~40 cm, the fluorescence conversion efficiency of the exciplexes in the positive column is close to 30%. To account for such a high efficiency, we shall evaluate the rates of formation of RX*, dN_{RX^*}/dt , in a glow-discharge plasma in the case of XeCl*.

The constants of the corresponding reactions were taken from Refs. 10 and 12. The results of the experimental and theoretical investigations of the processes in a glow-discharge plasma which we are presently conducting will be presented in our forthcoming reports. As was noted above, XeCl* molecules form in a Xe-Cl₂ mixture mainly in the harpoon reaction



The electron density in the discharge $N_e \sim 10^{11} \text{ cm}^{-3}$ can be calculated from the measured current density of the discharge and data on the drift velocity of electrons in inert gases in Ref. 13, and the concentration of metastables of the inert gas N_{Xe^*} can be estimated from the relation

$$N_{Xe^*} = K_B \cdot N_{Xe} \cdot N_e / K_h \cdot N_{Cl_2} \sim 5 \times 10^{10} \text{ cm}^{-3}, \quad (3)$$

where K_B and K_h are the constants for the excitation of xenon by electron impact and by harpoon reaction (2).

Hence, for the conditions of our experiment $dN_{XeCl^*}/dt = K_h \cdot N_{Xe^*} \cdot N_{Cl_2} \sim 10^{18} \text{ cm}^{-3} \cdot \text{s}^{-1}$. The equilibrium concentration of XeCl* in a discharge for this value of dN_{XeCl^*}/dt amounts to $N_{XeCl^*} \sim 10^{10} \text{ cm}^{-3}$, which coincides with the data from the measurements in Refs. 6 and 7.

The specific radiated power of a XeCl* excimer lamp in our experiments reached 1 W/cm^{-3} , which corresponds to the de-excitation of $1 \text{ s} \sim 10^{18}$ XeCl* molecules per cubic centimeter per second. The agreement between the rates of the creation and de-excitation of the exciplexes is an indication of the low rate of their nonradiative decay in a glow-discharge plasma. Accordingly, the high efficiency of excimer lamps pumped by a discharge of the type under consideration can be associated with the high efficiency of the formation of XeCl* and KrCl* in the harpoon reaction with Cl₂ and the slow rate of quenching of the exciplexes at low working pressures.

CONCLUSIONS

Thus, the results of an investigation of glow discharges in mixtures of inert gases and halogens in tubes of various diameters have been presented in this report. Cylindrical XeCl* (λ≈308 nm) and KrCl* (λ≈222 nm) excimer lamps with an active volume up to 1 liter, a long mixture lifetime, a radiated power up to 100 W, and an efficiency up to 15%, as well as a Cl₂* lamp (λ≈258 nm) with a power up to 30 W, have been developed. A homogeneous spatial distribution of the radiated power has been obtained by select-

ing the shape of the electrodes and the pumping conditions. The reasons for the high efficiency of excimer lamps pumped by a low-pressure continuous glow discharge have been discussed.

This work was carried out with support from the Russian Fund for Fundamental Research (Project No. 96-02-16668-a).

¹*Science and Technology of Light Sources, Proceedings of the 7th International Symposium, Kyoto, 1995.*

²A. N. Panchenko, V. S. Skakun, É. A. Sosnin *et al.*, *Pis'ma Zh. Tekh. Fiz.* **21**(20), 77 (1995) [*Tech. Phys. Lett.* **21**, 851 (1995)].

³M. I. Lomaev, A. N. Panchenko, V. S. Skakun *et al.*, *Opt. Atmos. Okeana* **9**, 199 (1996).

⁴V. T. Mikhel'son, A. B. Treshchalov, V. A. Peét *et al.*, *Kvantovaya Elektron. (Moscow)* **14**, 1404 (1987) [*Sov. J. Quantum Electron.* **17**, 890 (1987)].

⁵R. S. Taylor, K. E. Leopold, and K. O. Tan, *Appl. Phys. Lett.* **59**, 525 (1991).

⁶A. P. Golovitskiĭ, *Pis'ma Zh. Tekh. Fiz.* **18**(8), 73 (1992) [*Sov. Tech. Phys. Lett.* **18**, 269 (1992)].

⁷A. P. Golovitskiĭ and S. N. Kan, *Opt. Spektrosk.* **75**, 604 (1993) [*Opt. Spectrosc.* **75**, 357 (1993)].

⁸A. M. Boičenko, A. N. Panchenko, V. F. Tarasenko, and S. I. Yakovlenko, *Kvant. Elektron. (Moscow)* **23**, 417 (1996).

⁹A. M. Boichenko, A. N. Panchenko, V. F. Tarasenko, and S. I. Yakovlenko, *Laser Phys.* **5**, 1112 (1995).

¹⁰A. M. Boichenko, V. I. Derzhiev, A. G. Zhidkov *et al.*, *Tr. Inst. Obshch. Fiz. Akad. Nauk SSSR* **21**, 44–115 (1989).

¹¹V. A. Peét, E. V. Slivinskiĭ, and A. B. Treshchalov, *Kvantovaya Elektron. (Moscow)* **17**, 438 (1990) [*Sov. J. Quantum Electron.* **20**, 372 (1990)].

¹²H. Hokazono, K. Midorikava, M. Obara *et al.*, *J. Appl. Phys.* **56**, 680 (1984).

¹³Yu. P. Raizer, *Gas Discharge Physics*, Springer-Verlag, Berlin–New York (1991).

Translated by P. Shelnitz

Determination of the depth of formation of magneto-optical effects in CoNi films

Dong Ing Bi and V. E. Zubov

M. V. Lomonosov Moscow State University, 119899 Moscow, Russia

(Submitted March 28, 1996; resubmitted February 3, 1997)

Zh. Tekh. Fiz. **68**, 69–72 (February 1998)

The optical constants of CoNi films with magnetic properties that are nonuniform across their thickness are determined in reflected light by two methods, viz., optical and magneto-optical measurements. The values of the parameters $L = \lambda/4\pi k$ and $Z_0 = \lambda/8n$, one of which (specifically, the one which has the smaller value at a given value of λ) determines the depth of formation of reflective magneto-optical effects (l_{mo}) according to the current theories, are calculated on the basis of the values obtained for the optical constants n and k of the films (λ is the wavelength of the light used, and n and k are the refractive index and the absorption coefficient of the magnet). It is established for the CoNi films investigated that l_{mo} is determined by L and varies from about 200 to 300 Å in the range $0.33 \mu\text{m} \leq \lambda \leq 0.83 \mu\text{m}$. In CoNi films, which are inhomogeneous across their thickness and are characterized by significant variation of the magnetic properties over distances $\sim l_{mo}$, variation of the form of the magnetization curves determined by measuring the equatorial Kerr effect is observed as λ increases. © 1998 American Institute of Physics. [S1063-7842(98)01302-6]

INTRODUCTION

It was first shown in Ref. 1 that the depth of formation of reflective magneto-optical effects (l_{mo}) in transparent ferromagnets is significantly smaller than the penetration depth (L) of light into such crystals and that l_{mo} does not exceed tenths of a micron. Hubert *et al.*² established in computer experiments that in the region of weak absorption by ferromagnets l_{mo} is determined by the parameter $Z_0 = \lambda/8n$ and that in the region of strong absorption it is determined by the parameter $L = \lambda/4\pi k$, where λ is the wavelength, and n and k are the refractive index and the optical absorption coefficient of the magnet. Since Z_0 amounts to hundredths of a micron, it completely accounts for the result indicated in Ref. 1. It was established in Refs. 3 and 4 that l_{mo} is determined by L in the region of strong absorption. Since L and Z_0 , which determine l_{mo} , depend on λ , the thickness of the near-surface layer of the ferromagnet probed can be varied in a magneto-optical experiment by varying λ . This hypothesis can be tested in a magneto-optical investigation of magnets whose magnetic properties vary across their thickness. In this case significant variation of the magnetic properties should occur over distances comparable to l_{mo} .

In the present work the magnetic properties of CoNi thin films deposited at a varying angle, which are inhomogeneous across their thickness, were investigated by determining the equatorial Kerr effect at various values of λ . The optical constants and the corresponding values of L and Z_0 were obtained from the angular dependences of the equatorial Kerr effect by self-consistent determination of the optical and magneto-optical constants, as well as by an optical method from the angular dependences of the reflection coefficient.

SAMPLES AND EXPERIMENTAL METHOD

Cobalt–nickel films with a Co–30% Ni composition and a thickness (d) from 300 to 700 Å, which were vacuum-

deposited at a varying angle on polyethylene terephthalate substrates, were investigated. It was shown in Ref. 5 that the magnetic properties on opposite sides of such films differ significantly. The deposition angle α , which is measured from a normal to the plane of the film, can be varied either in the downward direction (method 1) or in the upward direction (method 2) during deposition of the films. The initial and final deposition angles for the films prepared by method 1 were equal to 90° and 57° ($d = 300$ Å) and to 90° and 70° ($d = 300$ Å). For the films prepared by method 2, the initial and final angles were 55° and 90° ($d = 500, 600, \text{ and } 800$ Å). The density of the films amounts to about 80% of the density of the CoNi ingots employed as sputtering targets, in agreement with the data of other investigators.⁶

The hysteresis loops and the coercive force on opposite sides of the CoNi films were measured by a new method for investigating the magnetic properties of near-surface layers of ferromagnets, which is based on the use of the meridional intense effect.⁷ The range of optical wavelengths used in the measurements was 0.5–0.6 μm and was stipulated by the parameters of the structural elements comprising the experimental apparatus.

The magnetization curves of the near-surface layers of the films were investigated by measuring the equatorial Kerr effect in the spectral modulation magneto-optical apparatus described in Ref. 8. The equatorial Kerr effect, which is proportional to the magnetization of the near-surface layer of the sample, was measured on both surfaces of the films in the spectral range $1.5 \leq E \leq 3.8$ eV with a frequency of the magnetizing field equal to 130 Hz. The sensitivity of the measurements of the equatorial Kerr effect was $\sim 5 \times 10^{-6}$, and the error in the determination of the magnitude of the equatorial Kerr effect was 5%. The measurement method used enabled us to obtain magnetization curves of each sample (in relative units) which pass through the corners of the dynamic

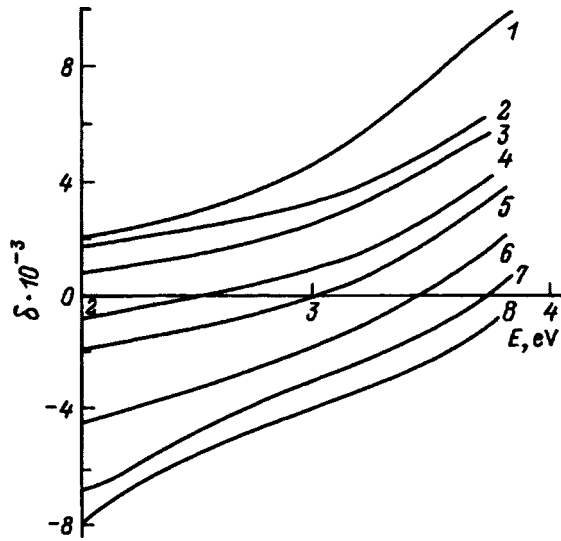


FIG. 1. Spectral curves of the equatorial Kerr effect for various values of λ . φ , deg: 1—45, 2—60, 3—63, 4—65, 5—67, 6—70, 7—73, 8—75.

hysteresis loops. Measurements on the substrate side were possible owing to transparency of the substrate material.

To determine the optical constants of the CoNi films, we measured a set of spectral curves of the equatorial Kerr effect for various values of the angle of incidence φ of the light. The values of n and k were obtained from these curves by the self-consistent method for determining the components of the dielectric tensor and the optical constants.^{9,10} The optical constants were determined on a CoNi film with a thickness of 300 Å, since the anisotropy of the physical properties is weakly expressed in it, permitting an increase in the accuracy of the determination of n and k . The influence of light reflected from the other side of the film is negligibly small, since the intensity of light which has been transmitted through the film twice is weakened by more than two orders of magnitude.

The optical constants of the CoNi films were also determined from optical measurements by finding the minimum on the dependence of the intensity of the p component of reflected light on the angle of incidence.

EXPERIMENTAL RESULTS AND DISCUSSION

Figure 1 presents spectral curves of the equatorial Kerr effect measured on the free surface of a CoNi film with a thickness of 300 Å. The optical constants determined from angular dependences of the equatorial Kerr effect are presented in Table I. The error in the determination of n and k from angular dependences of the equatorial Kerr effect in ferromagnetic metals, i.e., in our case, amounts to about 10%, according to the results in Ref. 9, when the equatorial Kerr effect is measured to within 5%. The values of n and k outside the measurement range were determined by extrapolation from the dependences on λ . It was necessary to determine the optical constants of the films, because, first, we did not find the values of n and k for alloys of the composition investigated in the literature and, second, the density of the CoNi films was lower than the density of bulk alloys of the

TABLE I. Values of the refractive index and the absorption coefficient obtained from the angular dependences of the equatorial Kerr effect for the CoNi films investigated and the corresponding values of L and Z_0 .

E , eV	λ μm	n	k	L , Å	Z_0 , Å
3.8	0.33	1.55	1.20	220	265
3.0	0.41	1.85	1.40	230	280
2.5	0.50	2.0	1.55	255	310
2.0	0.62	2.30	1.65	300	340
1.5	0.83	2.75	2.10	315	380

same composition. The spectral dependence of n and k observed in the CoNi films investigated, specifically the decrease in n and k with increasing E , is consistent with the behavior of these parameters in d transition metals and their alloys, in which the optical¹¹ and magneto-optical¹² properties in the visible and ultraviolet regions of the spectrum are determined by interband electronic transitions.

The second method used to determine the optical constants involved measuring the angular dependence of the intensity of the p component of the reflected light (J_p) and finding the angle (φ_{min}) at which the minimum of J_p is achieved for a given value of E . The minimum on the angular dependence of $J_p(\varphi)$ corresponds to the minimum on the angular dependence of the optical reflection coefficient (R_p). The angle of incidence at which the minimum of R_p is achieved is a function of the optical constants of the reflecting medium: $\varphi_{\text{min}} = \varphi_{\text{min}}(n, k)$. There is an infinite set of pairs of values of n and k that satisfy this relation. These pairs form a curve in the (n, k) plane. This curve can be determined using calculated plots of $R_p(\varphi)$ for various values of n and k . For this purpose we used the plots of $R_p(\varphi)$ presented in Fig. 5 of Ref. 13.

As an example, Fig. 2 shows the plot of $k = k(n)$ which indicates pairs of values of n and k for which a minimum of $R_p(\varphi)$ is achieved at $\varphi_{\text{min}} = 68^\circ$. Such a value of φ_{min} is observed on the plot of $R_p(\varphi)$ for a CoNi film with a thickness of 300 Å at $E = 2.5$ eV. In Fig. 2 the filled triangle (\blacktriangle) shows the point which corresponds to the values of n and k ($n = 2, k = 1.55$) determined from the magneto-optical measurements at the same value of E (Table I). It can be seen from the figure that the point on the (n, k) plane specified by the optical constants found from the angular dependence of

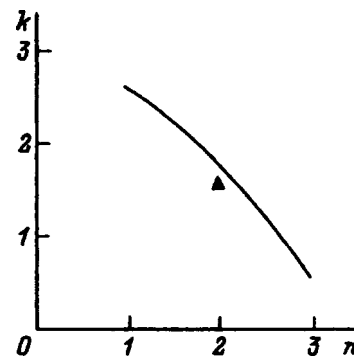


FIG. 2. Curve indicating the values of n and k which correspond to the minimum of $R_p(\varphi)$.

TABLE II. Parameters of the CoNi films investigated and values of the coercive force on the free surface (H_c^{fr}) and on the surface adjacent to the substrate (H_c^{sub}).

$d, \text{\AA}$	α, deg	$H \parallel EA$	
		H_c^{fr}, Oe	H_c^{sub}, Oe
700	90–57	186	273
800	55–90	591	130

the equatorial Kerr effect is close to the curve found from the optical measurements. Similar results were obtained for other values of E in the spectral region investigated. Thus, the results of the determination of the optical constants from the magneto-optical and optical measurements are consistent with one another. The values of L and Z_0 calculated from the values of n and k obtained are presented in Table I. The error in the determination of L and Z_0 amounts to about 10%, as in the case of n and k .

The value of l_{mo} for a magnet is determined by the smaller of the two parameters (L and Z_0) of the magnet at a given value of E (or λ). It is seen from Table I that in the CoNi films investigated the value of Z_0 greater than L at $0.33 \leq \lambda \leq 0.83 \mu\text{m}$. Therefore, in our case l_{mo} coincides with L , and its value increases by a factor of 1.5 as λ increases from 0.33 to 0.83 μm . In films with an inhomogeneous distribution of the magnetic properties across their thickness, the magnetization curves plotted from measurements of the equatorial Kerr effect should vary as λ increases, if significant changes in these properties occur at depths differing by $\sim l_{mo}$. This condition is satisfied by the CoNi films deposited at a varying angle with a thickness greater than 300 \AA . Such films have uniaxial magnetic anisotropy, which is stipulated by the shape and orientation of the crystallites.^{6,14} When the deposition angle $\alpha > 60^\circ$, the easy magnetization axis (EA) of the films lies in the deposition plane, and the strength of the effective uniaxial anisotropy field (H_a) and the coercive force (H_c for $H \parallel EA$) increase with increasing α . Therefore, the CoNi films prepared with a varying deposition angle are characterized by inhomogeneous distributions of H_a and H_c across their thickness. In the films prepared by method 1 the value of H_c on the free surface (H_c^{fr}) is smaller than the value on the surface adjacent to the substrate (H_c^{sub}). In the films prepared by method 2 the situation is reversed: $H_c^{fr} > H_c^{sub}$.

It was concluded in Ref. 15 as a result of an investigation of CoNi thin films with a thickness of $\sim 300 \text{\AA}$ prepared with variation of the deposition angle in both the downward and upward directions that the crystallites are oriented practically perpendicularly to the plane of the film in both cases. Consequently, the anisotropy of the magnetic properties in the films with $d \sim 300 \text{\AA}$ is very small. In such films the anisotropy of the optical and magneto-optical properties relative to the orientation in the plane of the films should also be insignificant.

An investigation of the hysteresis loops on both sides of the films showed that they have magnetic anisotropy with an easy axis lying in the plane of the film parallel to the depo-

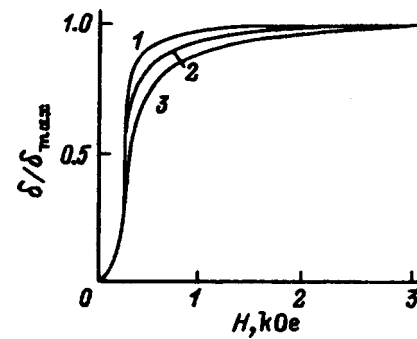


FIG. 3. Magnetization curves in a field $H \parallel EA$ on the free surface of a CoNi film (prepared by method 1). $d = 700 \text{\AA}$; $\lambda, \mu\text{m}$: 1—0.33, 2—0.50, 3—0.83.

sition plane. As an example, Table II presents the results of measurements of H_c on the two sides in a field $H \parallel EA$ for films with thicknesses of 700 and 800 \AA prepared by different methods. It is seen from Table II that the values of H_c on opposite sides of the same film differ significantly, H_c being greater on the side of the film on which the deposition angle was greater. Similar results were obtained for other films. It is natural to suppose that the magnetic properties of different layers of a film vary continuously as we go from one side of the film to the other.

Figure 3 presents magnetization curves for various values of λ on the free surface of a film with a thickness of 700 \AA , which were constructed from measurements of the equatorial Kerr effect in a field $H \parallel EA$. The analogous curves for the free surface of a film with $d = 800 \text{\AA}$ are presented in Fig. 4. It is seen from Figs. 3 and 4 that the magnetization curves depend on λ . The variations of the magnetization curves with increasing λ for the films prepared by methods 1 and 2 differ qualitatively. More specifically, as λ increases the magnetization curves for the film with $d = 700 \text{\AA}$ become less steep, i.e., magnetization of the near-surface layers investigated occurs in stronger fields. Conversely, the curves for the film with $d = 800 \text{\AA}$ become steeper, i.e., magnetization of the near-surface layers occurs in weaker fields, as λ increases.

The behavior of the magnetization curves just described can be explained under the assumption that l_{mo} increases with increasing λ . In fact, in the case of the film with $d = 700 \text{\AA}$, as l_{mo} increases, the equatorial Kerr effect is determined by magnetization averaged over a near-surface

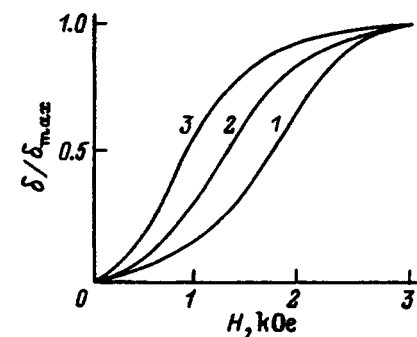


FIG. 4. Magnetization curves in a field $H \parallel EA$ on the free surface of a CoNi film (prepared by method 2). $d = 800 \text{\AA}$, $\lambda, \mu\text{m}$: 1—0.33, 2—0.50, 3—0.83.

layer of increasing thickness. Since the deeper layers relative to the free surface are characterized by larger values of H_c , the magnetization curves should become less steep as l_{mo} increases, as is observed experimentally. Similar arguments are valid for the curves presented in Fig. 4, if it is taken into account that H_c decreases as we go from the free surface to the substrate in the film with $d=800 \text{ \AA}$.

Thus, a magneto-optical investigation of CoNi films that are inhomogeneous across their thickness has shown that the shape of the magnetization curves of the films constructed from measurements of the equatorial Kerr effect depends on λ . The observed effect is attributed to the fact that the value of l_{mo} in the films and its variation with increasing λ calculated from the measured optical constants of the films coincide in order of magnitude with the characteristic distances from the surface at which significant variation of the magnetic properties of the films occurs.

This work was partially supported by the Russian Foundation for Fundamental Research (Grant No. 95-02-05601).

¹G. S. Krinchik, V. E. Zubov, and V. A. Lyskov, *Opt. Spektrosk.* **55**, 204 (1983) [*Opt. Spectrosc.* **55**, 120 (1983)].

- ²G. Traeger, L. Wenzel, and A. Hubert, *Phys. Status Solidi A* **131**, 201 (1992).
- ³A. D. Modestov, Z. A. Rotenberg, V. E. Zubov *et al.*, *Elektrokhimiya* **26**, 131 (1990).
- ⁴E. E. Chepurova, L. V. Kozlovskii, Syan'bo Du, and A. M. Liventsov, *Pis'ma Zh. Tekh. Fiz.* **20**(20), 42 (1994) [*Tech. Phys. Lett.* **20**, 829 (1994)].
- ⁵L. I. Zelenina, V. E. Zubov, S. I. Matskevich, and S. S. Subbotin, *Zh. Tekh. Fiz.* **64**(4), 51 (1994) [*Tech. Phys.* **39**, 376 (1994)].
- ⁶S. L. Zeder, J. F. Silvain, M. E. Re *et al.*, *J. Appl. Phys.* **61**, 3804 (1987).
- ⁷Inbi Dun and V. E. Zubov, *Prib. Tekh. Éksp.* (2), 121 (1996).
- ⁸V. E. Zubov, G. S. Krinchik, and V. A. Lyskov, *Zh. Éksp. Teor. Fiz.* **81**, 1489 (1981) [*Sov. Phys. JETP* **54**, 789 (1981)].
- ⁹V. E. Zubov, G. S. Krinchik, A. S. Tablin, and A. A. Kostyurin, *Phys. Status Solidi A* **119**, 297 (1990).
- ¹⁰K. G. Arkhipov and V. E. Zubov, *Opt. Spektrosk.* **73**, 952 (1992) [*Opt. Spectrosc.* **73**, 570 (1992)].
- ¹¹M. M. Kirillova, Doctoral Dissertation, Sverdlovsk (1984).
- ¹²E. A. Gan'shina, G. S. Krinchik, L. S. Mironova, and A. S. Tablin, *Zh. Éksp. Teor. Fiz.* **78**, 733 (1980) [*Sov. Phys. JETP* **51**, 369 (1980)].
- ¹³V. A. Kizel', *The Reflection of Light* [in Russian], Nauka, Moscow (1973).
- ¹⁴N. I. Vasil'eva, S. I. Kasatkin, N. V. Plotnikova *et al.*, *Zarubezhn. Elektron. Tekh.* (7–8), 3 (1992).
- ¹⁵L. I. Zelenina and S. S. Subbotin, *Technology and Properties of Materials for Recording of Information* [in Russian], NIIKhimFOTOPROEKT, Moscow (1992), pp. 110–120.

Translated by P. Shelnitz

Use of surface acoustic waves for analysis of gases and surface processes induced by them

V. I. Anisimkin and I. M. Kotelyanskii

Institute of Radio Engineering and Electronics, Russian Academy of Sciences, 103907 Moscow, Russia

E. Verona

Institute of Acoustics, CNR, Rome, Italy

(Submitted October 28, 1996)

Zh. Tekh. Fiz. **68**, 73–81 (February 1998)

An analytical expression for the magnitude of the “response” of surface acoustic waves (SAWs) to gases is obtained. It is tested experimentally. The main features of the detection of gases by means of SAWs are predicted theoretically and confirmed experimentally. The SAWs in coated and uncoated gas sensors are compared. A technique for using SAWs to determine the relative changes in the density ($\Delta\rho/\rho$) and the elastic moduli ($\Delta C_{11}/C_{11}$ and $\Delta C_{44}/C_{44}$) of films upon the adsorption (desorption) of gases is proposed. The possibility of using this technique to analyze adsorption and desorption processes is demonstrated. The adsorption properties of polycrystalline, thermally deposited palladium films before and after low-temperature vacuum annealing, as well as unannealed Pd and Pd:Ni films, are compared. The prospects of using SAWs to detect gases and to study surface processes induced by them are discussed. © 1998 American Institute of Physics. [S1063-7842(98)01402-0]

INTRODUCTION

One of the newest approaches to designing sensors for analyzing the chemical composition of the environment has led to the creation of devices (Fig. 1) whose operation is based on the utilization of surface acoustic waves (SAWs).¹ The operating principle of such sensors is based on the variation of the wave propagation rate V in response to the adsorption of atoms or molecules of the gaseous adsorbate being tested by a sorbent film. The relative change $\Delta V/V$ (the SAW “response”) is detected in the output of the device as relative phase ($\Delta\varphi/\varphi$) and frequency ($\Delta f/f$) changes. The frequency form of the “response” favorably distinguishes SAW sensors from the other already existing analogs, since it facilitates combining the sensors with digital data-processing systems, as well as increases the accuracy and sensitivity of the measurements: at typical values of the working frequency ($f \approx 100$ MHz), the linear dimensions ($L \approx l \approx 10$ mm, $\lambda \approx 20$ μ m), and the total phase ($\varphi = 360^\circ L/\lambda \approx 200\,000^\circ$) the minimum values of the SAW responses are at the $0.01 - 0.5 \times 10^{-6}$ level, and the threshold gas concentrations are at the $10^{-7} - 10^{-6}\%$ level. We note that such a high sensitivity of SAWs is achieved under the conditions of an acoustic wavelength λ that is large compared to the thickness of the sorbent film h ($h/\lambda \ll 1$), i.e., at a low concentration of wave energy in the film.

1. BASIC EQUATION

In the general case the characteristics of the propagation of SAWs in a basic structure (Fig. 1) with piezoelectric and anisotropic substrates and films are calculated using the mechanical equations of motion and Maxwell’s equations. However, in the most widely encountered case in practice of

a polycrystalline film of small thickness $h \ll \lambda$ with crystallites having a small characteristic dimension $d \ll \lambda$, the film can be considered elastically isotropic, and it can be characterized by the two second-order elastic moduli C_{11} and C_{44} and the density ρ alone. In this case the SAWs in the basic structure can be calculated by perturbation theory,² according to which we represent the SAW response in the form³

$$\frac{\Delta V}{V} = \left(\frac{\pi h}{2\lambda} \right) \left[-\frac{\Delta\rho}{\rho} A + \frac{\Delta C_{44}}{C_{44}} B + \left(\frac{\left(1 - \frac{\Delta C_{44}}{C_{44}}\right)^2}{1 - \frac{\Delta C_{11}}{C_{11}}} - 1 \right) C \right]. \quad (1)$$

Here

$$\begin{aligned} A &= \{(A_x)^2 + (A_y)^2 + (A_z)^2\} \rho V^2; \\ B &= \{4(A_z)^2 + (A_x)^2\} C_{44}; \\ C &= \{4(A_x)^2\} (C_{44})^2 / C_{11}, \end{aligned} \quad (2)$$

where A_x , A_y , and A_z are the normalized mechanical displacements of the SAWs in the substrate in the geometry in Fig. 1.

The first factor in (1) is proportional to h/λ , i.e., the normalized film thickness, and takes into account the dependence of the response on the fraction of the energy of the acoustic wave that is concentrated in the film.⁴ When $h/\lambda \ll 1$, the fraction of the energy of the waves is practically proportional to the normalized film thickness.⁵

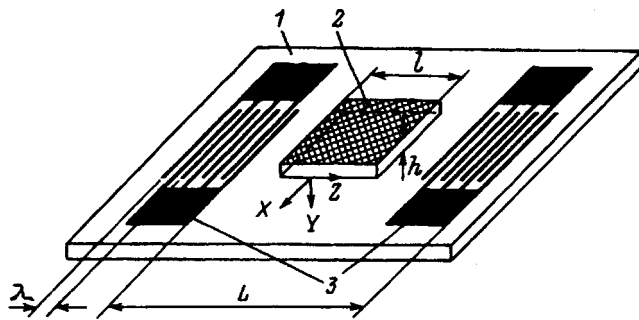


FIG. 1. Design of a typical SAW gas sensor: 1—piezoelectric substrate; 2—sorbent film; 3—interdigital transducers for exciting and receiving SAWs; L —distance between the transducers; h —film thickness; λ —wavelength of the excited SAW; l —width of the film along the wave propagation direction; x , y , z —axes of the Cartesian coordination system used in deriving Eq. (1).

The dependence of the response on the changes in the physical properties of the sorbent film is taken into account in (1) by the second factor, which contains the quantities $\Delta\rho/\rho$, $\Delta C_{11}/C_{11}$, and $\Delta C_{44}/C_{44}$. These quantities reflect the changes in the elastic properties of the film under the action of the adsorbed gas. If, not only the elastic properties, but also other properties of the film, for example, its conductivity, vary, additional terms, which take into account these changes, appear in Eq. (1).

Since the combination of the three quantities $\Delta\rho/\rho$, $\Delta C_{11}/C_{11}$, and $\Delta C_{44}/C_{44}$ is different for different films (F), gases (G), concentrations (C), and temperatures (T), this combination can be regarded as a characteristic of an FGCT system. In particular, the values of $\Delta\rho/\rho$, $\Delta C_{11}/C_{11}$, and $\Delta C_{44}/C_{44}$ for the same film and temperature are, generally speaking, different for different gases even at the same concentration and for the same gas at different concentrations.

The validity of (1) was tested experimentally on Pd films and a 1% $\text{H}_2 + \text{N}_2$ mixture⁶ in the following manner. First, the values of $\Delta\rho/\rho$, $\Delta C_{11}/C_{11}$, and $\Delta C_{44}/C_{44}$ were determined experimentally for the particular FGCT system (for further details, see Sec. 2). Then, these values were used to calculate the values of the SAW response $\Delta V/V$ for two test structures with identical films, but different substrates from Eq. (1). The calculated values differed only slightly from the experimental data (Table I).

The expression for the SAW response $\Delta V/V$ corresponding to the equilibrium state in a gas–film system is easily transformed into the expression for the time dependence of $\Delta V/V$ in the period of the absence of equilibrium. For this purpose, in a first approximation the time dependences of $\Delta\rho/\rho$, $\Delta C_{11}/C_{11}$, and $\Delta C_{44}/C_{44}$ in the period of the absence of equilibrium are approximated by linear func-

tions of the form $\Delta\rho/\rho = \alpha t$, $\Delta C_{11}/C_{11} = \beta t$, and $\Delta C_{44}/C_{44} = \gamma t$. When these functions are substituted into (1) and the expression obtained is linearized with respect to the small time parameter t , we obtain the expression for the time dependence of the nonequilibrium kinetic SAW response

$$\frac{\Delta V}{V} = t \left(\frac{\pi h}{2\lambda} \right) [-\alpha A + \beta B + (\beta - 2\gamma) C]. \quad (3)$$

It is seen from (3) that, unlike the equilibrium SAW response (1), the kinetic response depends not only on the parameters A , B , and C , i.e., on the values of V , A_x , A_y , and A_z in the substrate material and the values of ρ , C_{11} , and C_{44} in the film material, but also on the values of the coefficients α , β , and γ , which reflect the rates of variation of the density and the elastic moduli of the film during the establishment of equilibrium in the gas–film system. In the general case these rates are different for different combinations of gases being tested and films and must be determined individually for each specific case. The procedure for experimentally determining the time dependences of the parameters $\Delta\rho/\rho$, $\Delta C_{11}/C_{11}$, and $\Delta C_{44}/C_{44}$ and the coefficients α , β , and γ is described below.

We note that Eq. (3) is also valid for the time variation of the SAW response under the influence of the environment, i.e., for the “aging” of the response with time. In this case $\Delta V/V$ should be construed as the equilibrium value of the response at the respective value of t , where t is the time measured from the beginning of the preparation of the film, and α , β , and γ are the rates of variation of the density and the elastic moduli of the film under the action of the environment. Of course, α , β , and γ have different physical meanings in this case.

2. PROCEDURE FOR DETERMINING THE CHANGES IN THE DENSITY AND THE SECOND-ORDER ELASTIC MODULI OF A THIN FILM UPON THE ABSORPTION OF A GAS

The adsorption of atoms and molecules from the gaseous phase on the outer surface, as well as the penetration of adsorbed particles into the crystal lattice of a film, their diffusion along intercrystallite boundaries, capillary condensation in the space between crystallites, and trapping on crystallites and the film–substrate boundary can cause changes in the mass, volume, density, forces of interatomic interaction, and, consequently, the second-order elastic moduli of the film in the general case. The change in the mass of the film can be determined by the familiar quartz microbalance technique,⁷ which utilizes bulk acoustic modes.

To determine the relative changes in the density and the elastic moduli of a film we developed a procedure,⁸ whose essential points can be briefly described as follows. A set of test structures is prepared. It contains at least three structures with identical sorbent films and different substrates or one substrate and at least three different SAW propagation directions in the same film. The SAW response $\Delta V/V$ is measured for each of the structures after the establishment of equilibrium in the gas–film system. Substituting the measured value of $\Delta V/V$ for each of the structures and the tabulated values of the coefficients A_x , A_y , A_z , and V for the

TABLE I. Comparison of experimental values of SAW responses with values calculated from Eq. (1) (1% $\text{H}_2 + \text{N}_2$ gas mixture, 20 °C).

Test structure	$\Delta V/V, 10^{-6}$ (calculated from Eq. (1))	$\Delta V/V, 10^{-6}$ (experiment)
Pd/ZnO(001)–Si film	–110	–115
Pd/ZnO(111)–Si film	–375	–215

substrate material corresponding to the structure, as well as the parameters of the film material ρ , C_{11} , and C_{44} , into (1), we obtain a system of three equations with the three unknowns $\Delta\rho/\rho$, $\Delta C_{11}/C_{11}$, and $\Delta C_{44}/C_{44}$, whose solution is unique. The temporal variations (the kinetics) of $\Delta\rho/\rho$, $\Delta C_{11}/C_{11}$, and $\Delta C_{44}/C_{44}$ due to adsorption or “aging” are determined from the solution of the same system of equations, but with the values of $\Delta V/V$ measured at different times during the establishment of equilibrium between the film and the gas being tested or aging of the film. The data thus obtained can be used to study the equilibrium and kinetic adsorption (desorption) characteristics, the mechanisms for detecting gases using SAWs, and the variation of the respective density and elastic moduli of the film material.

Since the film thickness h was assumed to be small compared with the wavelength λ during the derivation of (1), the changes in the physical parameters of a film under the action of gases are considered to be averaged over the film thickness. The accuracy of the values of $\Delta\rho/\rho$ determined by this method was $\pm 10\%$, and the accuracy of the determination of $\Delta C_{11}/C_{11}$ and $\Delta C_{44}/C_{44}$ was $\pm 20\%$.

3. ANALYSIS OF THE SAW RESPONSE IN THE DETECTION OF GASES

The analysis of the principal components of the SAW response, as well as its kinetics and aging, yielded the following results. a) The SAW response is a sum of three terms, the first of which depends on the change in the film density (the change in the mass load), while the second and third depend on the changes in the elastic moduli (the change in the elastic load). b) The mass and elastic loads do not depend on one another and, in the general case, can make contributions of comparable magnitude to the resultant SAW response. c) The mass and elastic loads can be added or subtracted, depending on the combination of values of the elastic parameters ρ , C_{11} , and C_{44} of the film, the changes in them under the action of the gas being tested $\Delta\rho/\rho$, $\Delta C_{11}/C_{11}$, and $\Delta C_{44}/C_{44}$, and the characteristics of the SAWs in the substrate material (A_x , A_y , A_z , and V). The variation of any of these parameters permits control of the magnitude and sign of the SAW response. For a chosen film, gas, gas concentration, and temperature, i.e., for assigned values of ρ , C_{11} , C_{44} , $\Delta\rho/\rho$, $\Delta C_{11}/C_{11}$, and $\Delta C_{44}/C_{44}$, the SAW response can be increased, decreased, or “zeroed” by appropriately selecting the substrate material and/or its crystal cut (the values of A_x , A_y , A_z , and V). d) For identical substrates with different films the SAW responses can be both positive and negative. e) For assigned temporal variations of $\Delta\rho/\rho$, $\Delta C_{11}/C_{11}$, and $\Delta C_{44}/C_{44}$ during the establishment of equilibrium between the film and the gas being tested, the corresponding temporal variations of the SAW response, i.e., its kinetics, can be accelerated or slowed by appropriately selecting the substrate material and/or its orientation. f) Similarly, for assigned temporal variations of $\Delta\rho/\rho$, $\Delta C_{11}/C_{11}$, and $\Delta C_{44}/C_{44}$ in the film under the action of the environment, the corresponding temporal variations of the SAW response, i.e. its aging, can be accelerated or slowed. g) The substrate materials and crystal cuts which

TABLE II. Experimental values of the SAW responses for a single film and different substrates (1% H₂+N₂ gas mixture, 20 °C).

Test structure	$\Delta V/V, 10^{-6}$ (experiment)	Mass load, %	Elastic load, %
Pd/YZ/LiNbO ₃	-22	66	34
Pd/(001), (110)-BGO	-53	14	86
Pd/ZX-CdS	-67	17	83
Pd/ST-, X-SiO ₂	-104	27	73
Pd/ZnO/(111)-Si	-215	5	95

are optimal from the standpoint of achieving the greatest sensitivity, the greatest speed, and the slowest aging are, generally speaking, different. In view of the practical importance of these results for developing a specific SAW sensor, they were verified experimentally.

The experimental values of the SAW responses to the action of the same 1% H₂+N₂ gas mixture on different structures containing identical Pd films, but different substrates are presented in Table II. The data presented confirm that even a tenfold increase in the signal and, therefore, in the sensitivity of the sensor can be obtained by appropriately selecting the substrate.

The possibility of obtaining both positive and negative SAW responses on the same substrate with different sorbent films is demonstrated by the experimental data in Fig. 2. This figure presents the temporal variations of the kinetic responses for a YX-SiO₂ substrate and a Pd film, where one curve (a) corresponds to a structure with an unannealed Pd film, and the other curve (b) corresponds to the same structure after annealing in a vacuum with a residual pressure of 10⁻⁵ Pa at a temperature of 423 K for 15 h. This anneal clearly resulted in alteration of the adsorption properties of

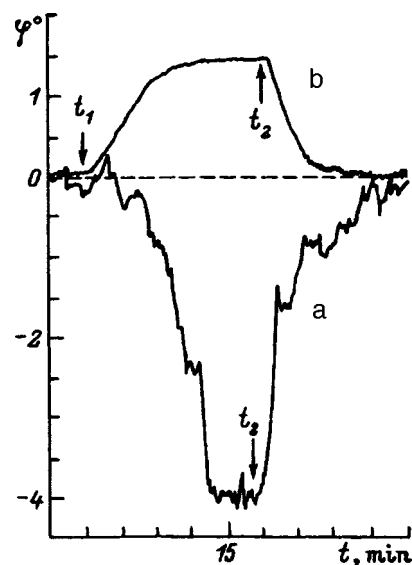


FIG. 2. Temporal variations of the SAW phase φ (the SAW response) for a single substrate (YX-SiO₂) and different films: $h(\text{Pd})=165 \text{ nm}$, $\lambda=42 \mu\text{m}$, $l/L=57\%$, $\varphi_0=171430^\circ$, 1% H₂+N₂, t_1 —time of completion of the supply of dry air and beginning of the supply of the gas mixture, t_2 —time of completion of the supply of the gas mixture and beginning of the supply of dry air.

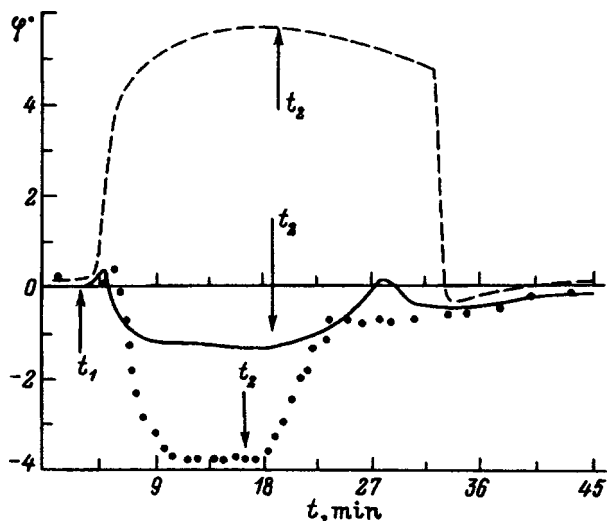


FIG. 3. Temporal variations of the SAW phase for a single film ($\text{Pd}_{0.99}\text{Ni}_{0.01}$) and different substrates. Solid curve— YX-SiO_2 substrate ($\lambda=40\ \mu\text{m}$, $l/L=48\%$, $\varphi_0=108000^\circ$), $\Delta\varphi/\varphi_0=-25.1\times 10^{-6}$; dashed curve— ST-X-SiO_2 substrate ($\lambda=32\ \mu\text{m}$, $l/L=69\%$, $\varphi_0=225000^\circ$), $\Delta\varphi/\varphi_0=+36.2\times 10^{-6}$; $\bullet\bullet\bullet$ — AT-SiO_2 substrate ($\lambda=40\ \mu\text{m}$, $l/L=48\%$, $\varphi_0=108000^\circ$), $\Delta\varphi/\varphi_0=-60.5\times 10^{-6}$. Gas mixture—1% H_2+N_2 , $h(\text{Pd}_{0.99}\text{Ni}_{0.01})=125\ \text{nm}$, t_1 —time of completion of the supply of dry air and beginning of the supply of the gas mixture, t_2 —time of completion of the supply of the gas mixture and beginning of the supply of dry air.

the Pd film and thus caused a strong change in the SAW response, even to the point of its inversion.

Figure 3 presents the temporal variations of the SAW responses of three structures containing identical $\text{Pd}_{0.99}\text{Ni}_{0.01}$ films on different substrates: YX- , ST- , X- , and AT- cut quartz. A comparison of these variations of the kinetic responses demonstrates the possibility of altering the rise time and recovery time of an SAW sensor by selecting the substrate. Figure 4 presents plots of the dependence of the relative changes in the SAW response of identical Pd films on different substrates due to aging. As is seen from these data, selection of the substrate also permits acceleration or slowing of the long-term changes in the SAW response.

It can be seen from the data presented in Figs. 2, 3, and 4 that among the structures which we investigated the sensor on the ST- cut substrate has the shortest rise time (30 s), the sensor on the AT- cut substrate has the fastest recovery after exposure to hydrogen (3 min), and the sensor on YX- cut quartz exhibits the slowest aging (19% after 6 months and 14% after another 2 months with additional vacuum and vacuum-heat treatment of the film). The sensor on the YX- cut substrate has a rise time of 40 s, a recovery time of 4.5 min, a reproducibility of the values of 10 successive measurements equal to $\pm 10\%$, and linearity of the response for hydrogen concentrations from 0.1 to 2%.

4. INVESTIGATION OF ADSORPTION AND DESORPTION PROCESSES USING SURFACE ACOUSTIC WAVES

In recent years the high sensitivity of SAWs toward external influences acting on their propagation medium has begun to be utilized not only to create sensors for various physical quantities, but also to investigate physical and

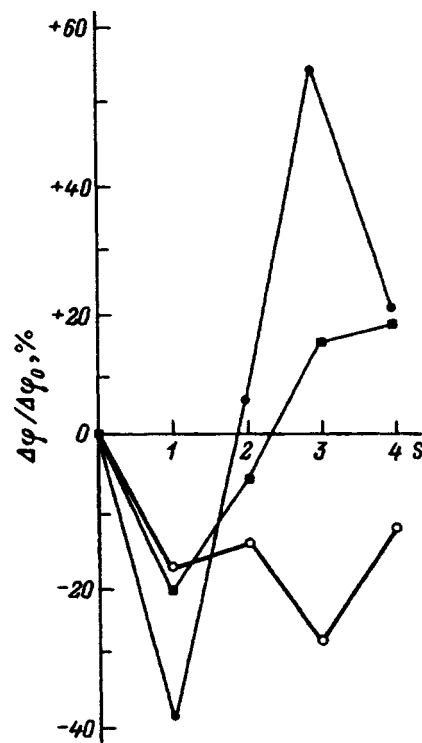


FIG. 4. Relative change in the SAW response during aging (S) of a sorbent Pd film after annealing ($423\ \text{K}$, $10^{-5}\ \text{Pa}$, 15 h): $h=165\ \text{nm}$, 0—immediately after deposition, 1—after storage in air for 6 months (20°C), 2—after holding the films in a vacuum ($10^{-5}\ \text{Pa}$) for 15 h to clean the surface, 3—after additional low-temperature annealing of the films in a vacuum ($10^{-5}\ \text{Pa}$, $683\ \text{K}$, 15 h), 4—after additional storage of the films in air for 2 months, \bullet — ST-X-SiO_2 substrate; \blacksquare — AT-SiO_2 substrate; \circ — YX-SiO_2 substrate.

chemical processes taking place on the surface of a solid. Surface acoustic waves have been used to determine the number of adsorbed particles,⁹ the specific surface area,¹⁰ adsorption isotherms,^{9,11,12} and the kinetics of thermodesorption⁹ and chemisorption¹³ processes. As in the familiar quartz microbalance technique,⁷ which utilizes bulk acoustic modes, in the research on SAW sensors and on the use of SAWs for investigating processes on the surface of a solid it has been assumed hitherto that the SAW response is determined only by the mass change Δm of the adsorbed particles. However, as follows from (1), this response, which is associated with the modification of the wave propagation rate, is determined by the changes in the density ($\Delta\rho/\rho$) and the elastic moduli ($\Delta C_{ij}/C_{ij}$) of the propagation medium.

In this section we shall attempt to demonstrate experimentally in concrete examples that consideration of both the mass and elastic loads provides new information on adsorption and desorption processes, viz., on the number of particles adsorbed (desorbed) as determined from the magnitude and sign of $\Delta\rho/\rho$, on changes in the forces of interatomic interaction in the film as determined from the values of $\Delta C_{ij}/C_{ij}$, and on the kinetics of adsorption (desorption) and the processes accompanying it as determined from the time dependences of $\Delta\rho/\rho$ and $\Delta C_{ij}/C_{ij}$.

The experiments were performed on polycrystalline Pd and Pd:Ni films that were thermally deposited in a vacuum with gas mixtures containing various concentrations of hy-

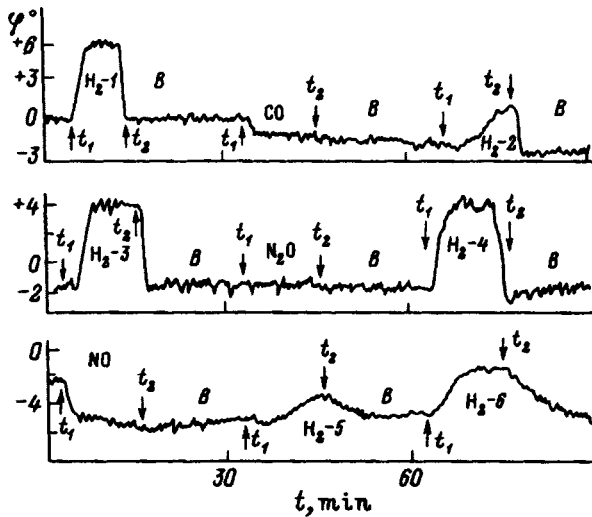


FIG. 5. Temporal variations of the SAW phase φ under the action of 1% mixtures of H_2 , CO, N_2O , and NO with nitrogen. Film—annealed Pd (423 K, 10^{-5} Pa, 15 h), $h=120$ nm. Substrate—ST-, X-SiO₂ ($\lambda=20$ μ m, $l/L=86\%$, $\varphi_0=270000^\circ$): t_1 —time of completion of the supply of dry air and beginning of the supply of the gas mixture, t_2 —time of completion of the supply of the gas mixture and beginning of the supply of dry air. H_2-1 —SAW response to hydrogen before exposure to CO, N_2O , and NO; H_2-2 , H_2-3 , H_2-4 , H_2-5 , H_2-6 —SAW response after exposure to the second gas.

drogen and nitrogen. The experimental results are presented in Tables III, IV, and V and in Figs. 5 and 6. The results were interpreted using independent experimental data,¹⁴⁻²² according to which the overall physical picture of the interaction of hydrogen with a palladium film can take the following form. A hydrogen molecule adsorbed on the film surface dissociates into atoms, which penetrate into the palladium crystal lattice and diffuse along intercrystallite boundaries. On the surface and the crystallite boundaries hydrogen interacts with impurity oxygen which was adsorbed in the film before the injection of hydrogen, i.e., during the growth of the film and its contact with air. The interaction of hydrogen with oxygen results in the formation of water, which leaves the film, and hydroxyl groups (OH), which are

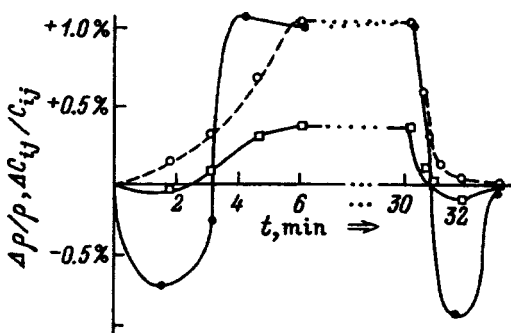


FIG. 6. Temporal variation of the relative changes in the density and the elastic moduli of an annealed Pd film during the adsorption of hydrogen. Gas mixture—0.1% H_2+N_2 ; \square — $\Delta\rho/\rho$; \bullet — $\Delta C_{11}/C_{11}$; \circ — $\Delta C_{44}/C_{44}$; $t=0$ —time of completion of the supply of dry air and beginning of the supply of the gas mixture; $t=30$ min—time of completion of the supply of the gas mixture and beginning of the supply of dry air.

TABLE III. Relative changes in the density and elastic moduli of an unannealed Pd film upon the adsorption of hydrogen (20 °C).

Gas mixture	$\Delta\rho/\rho, 10^{-2}$	$\Delta C_{11}/C_{11}, 10^{-2}$	$\Delta C_{44}/C_{44}, 10^{-2}$
0.1% H_2+N_2	+0.17	+12.7	-5
0.5% H_2+N_2	+0.33	+33.4	-30
1.0% H_2+N_2	+0.26	+35	-38

localized in the form of dipoles on crystallite surfaces and the film–substrate boundary.

The goal of our experimental investigation was to determine whether information on the processes accompanying adsorption (desorption) can be obtained from the changes in the density and elastic moduli of the propagation medium. It was assumed that the changes in the density of the film should begin to be manifested when particles are adsorbed on its outer surface and that the changes in its elastic moduli should be manifested from the onset of diffusion of the adsorbed particles into the bulk.

Estimates of the contribution of one of the mechanisms of the interaction of hydrogen with a Pd film to the penetration of hydrogen into the palladium lattice showed²³ that the attendant changes in the density and elastic moduli of the film are much smaller than the changes observed experimentally at the same hydrogen concentration. For example, the estimates for a 1% H_2+N_2 mixture give $\Delta\rho/\rho=+1.1\times 10^{-3}$, $\Delta C_{11}/C_{11}=+7.7\times 10^{-4}$, and $\Delta C_{44}/C_{44}=+3.7\times 10^{-4}$, while the experimental values are much greater (Tables II and III). Therefore, the interaction of hydrogen with oxygen impurities preadsorbed in the film, rather than its penetration into the crystal lattice, should be regarded as the dominant factor in the modification of the elastic properties of palladium films upon the adsorption of hydrogen.

Tables III and IV present the values of the relative changes in the density ($\Delta\rho/\rho$) and the elastic moduli ($\Delta C_{11}/C_{11}$ and $\Delta C_{44}/C_{44}$) under the action of hydrogen in various concentrations for identical Pd films before and after a low-temperature anneal in a vacuum (430 K, 10^{-5} Pa, 15 h). It is seen that the values of $\Delta\rho/\rho$, $\Delta C_{11}/C_{11}$, and $\Delta C_{44}/C_{44}$ for both films increase with the hydrogen concentration. It is also seen that the unannealed films are characterized by greater alteration of the elastic moduli, while the annealed films are characterized by greater alteration of the density. This finding is consistent with the data obtained by other investigative methods,¹⁴⁻²² according to which palladium films can contain at least two types of impurity oxygen: weakly and strongly bound oxygen. On the basis of these data we assume that strongly bound oxygen can predominate

TABLE IV. Relative changes in the density and elastic moduli of an annealed Pd film upon the adsorption of hydrogen (20 °C).

Gas mixture	$\Delta\rho/\rho, 10^{-2}$	$\Delta C_{11}/C_{11}, 10^{-2}$	$\Delta C_{44}/C_{44}, 10^2$
0.1% H_2+N_2	+0.33	+1.0	+1.0
0.5% H_2+N_2	+0.65	+1.75	+2.05
1.0% H_2+N_2	+0.65	+1.95	+2.05

TABLE V. Relative changes in the density and elastic moduli of an annealed Pd film upon the adsorption of nitrogen mixtures of various gases (20 °C) (*YX*-, *ST*-, and *AT*-SiO₂ substrates).

Gas mixture	$\Delta\rho/\rho, 10^{-2}$	$\Delta C_{11}/C_{11}, 10^{-2}$	$\Delta C_{44}/C_{44}, 10^2$
1.0% N ₂ O+N ₂	+0.4	-0.02	+1.6
1.0% NO+N ₂	+0.6	+0.3	+2.1
1.0% CO+N ₂	+1.05	+3.0	+2.95

in the unannealed films and that weakly bound oxygen can predominate in the annealed films. When hydrogen reacts with weakly bound oxygen, it forms water vapor, which leaves the film, its mass and density decreasing as a result. When hydrogen reacts with strongly bound oxygen, it forms charged OH hydroxyl groups, which are localized on crystallites and alter the force interaction in the space between them and, therefore, the elastic moduli of the film. Since the amount of strongly bound adsorbed oxygen in an annealed film is smaller than in an unannealed film, the values of $\Delta C_{11}/C_{11}$ and $\Delta C_{44}/C_{44}$ are also smaller. Since the amount of weakly bound adsorbed oxygen increases in the annealed film, the density change in it is greater.

The concentration of weakly bound oxygen in each of the films can be estimated from the relative density changes corresponding to the practically complete depletion of weakly bound oxygen from the films (0.5% H₂+N₂ gas mixture):²³ before annealing it was equal to 7×10^{15} , and after annealing it was equal to $16.5 \times 10^{15} \text{ cm}^{-2}$. Thus, in both cases the adsorption of weakly bound oxygen in the Pd films is polymolecular (multilayered).

The role of impurity oxygen is also manifested in experiments on the cleaning of a Pd film surface using dry air to ‘‘purge’’ adsorbed N₂O, NO and CO molecules, which have different chemical activities with respect to oxygen (Table V, Fig. 5). Since the chemical activity of N₂O toward oxygen is low, it scarcely reacts with oxygen adsorbed on the film surface. Therefore, the density and elastic moduli of the film vary to only a small extent, and the SAW response to hydrogen is restored already after a half hour of purging. The species CO and NO, which are chemically more active toward oxygen, can be retained on the surfaces of a Pd film owing to their interaction with preadsorbed oxygen. In this case the changes in the density and the elastic moduli are considerably greater. Recovery of the SAW response to hydrogen following exposure to CO requires a considerably greater purging time. After exposure to NO, the response desired cannot be achieved by prolonged purging with air, by vacuum treatment (10^{-5} Pa , 15 h), or by annealing in a vacuum (430 K, 10^{-5} Pa , 15 h), apparently because of the chemisorption of NO.

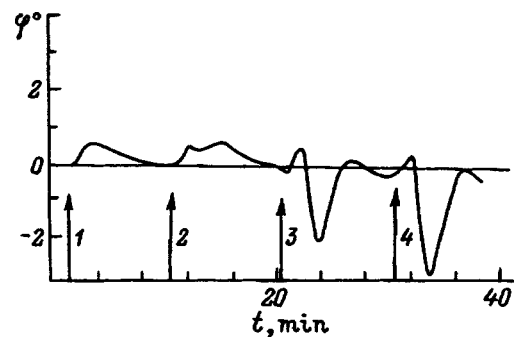
The time dependences of the relative changes in the density and each of the elastic moduli of a film during adsorption can be obtained using SAWs. These dependences can be used to experimentally determine the kinetic coefficients α , β , and γ , which appear in Eq. (3) and reflect the rates of variation of $\Delta\rho/\rho$, $\Delta C_{11}/C_{11}$, and $\Delta C_{44}/C_{44}$ during adsorption for various combinations of gases being tested and films. As an example, Fig. 6 presents the time dependences of

TABLE VI. Comparison of the relative changes in the density and the elastic moduli of as-grown Pd and Pd:Ni films upon the adsorption of hydrogen (1% H₂+N₂ gas mixture, 20 °C).

Film	$\Delta\rho/\rho, 10^{-2}$	$\Delta C_{11}/C_{11}, 10^{-2}$	$\Delta C_{44}/C_{44}, 10^{-2}$
Pd	+0.26	+35	-38
Pd _{0.97} Ni _{0.03}	-4.1	-26.1	-8.1

$\Delta\rho/\rho$, $\Delta C_{11}/C_{11}$, and $\Delta C_{44}/C_{44}$ for an annealed Pd film and a 0.1% H₂+N₂ gas mixture. It is noteworthy that the density of the film increases ($\Delta\rho/\rho < 0$) in the initial time period after the injection of hydrogen ($t=0-2 \text{ min}$) and in the final stage of complete recovery of the film ($t=31-34 \text{ min}$). In our opinion, this is because the formation of water molecules as a result of the reaction of hydrogen with oxygen is faster than the desorption of these molecules from the film. This is supported by the fact that the experimentally observed increase in the density of the film during desorption ($t=30-32 \text{ min}$) is faster than its decrease during adsorption ($t=2-6 \text{ min}$). Since the change in the density of the film is associated mainly with processes on the surface, while the changes in the elastic moduli are associated with processes in the bulk of the film, information on the processes occurring on the surface and in the bulk of the film can be obtained from these changes. For example, our measurements showed that the changes in the density and the elastic moduli of a Pd film under the action of a 1% H₂+N₂ mixture begin practically simultaneously (to within 1 s).

A different picture is observed when the same mixture is adsorbed by a Pd_{0.97}:Ni_{0.03} film. Table VI compares the relative changes in the density and elastic moduli of as-grown films of Pd and the solid solution Pd_{0.97}:Ni_{0.03} upon the adsorption of hydrogen. It is seen that even such an insignificant admixture of nickel as 3% drastically alters not only the magnitude, but also the sign of $\Delta\rho/\rho$ and $\Delta C_{11}/C_{11}$. Figure 7 presents the temporal variation of the SAW response following short injections of a 1% H₂+N₂ gas mixture. It can be seen from the figure that the shape of the response undergoes significant changes as the duration of the interaction of the film with hydrogen increases. During the shortest injection (20 s) hydrogen particles manage to be adsorbed on the outer surface of the film and increase its mass. At this point there are still practically no changes in the elastic moduli of the

FIG. 7. Changes in the SAW response after brief injections of the gas mixture being tested. Pd_{0.97}Ni_{0.03} film, 1% H₂+N₂ mixture. Injection time s: 1—20, 2—65, 3—125, 4—185.

film, and in accordance with Eq. (1) the SAW response has a positive value ($\Delta V/V > 0$, while $\Delta \rho/\rho < 0$ and $\Delta C_{11}/C_{11}$, $\Delta C_{44}/C_{44} = 0$). More prolonged injections of hydrogen (65, 125, and 185 s) are associated with diffusion of the particles adsorbed on the surface into the bulk of the film, and along with an increase in density there are increases in the elastic moduli of the film. In this case the elastic load of the surface begins to "operate" along with the mass load. As a result, in accordance with (1), both the magnitude and sign of the SAW response change, and it becomes negative in the final stage of the interaction. The negative component of the response grows as the duration of the hydrogen injection increases. The time delay between the bulk processes and the surface processes was estimated experimentally from the time difference between the negative component of the response and the positive component. For a $\text{Pd}_{0.97}\text{Ni}_{0.03}$ film and a 1% $\text{H}_2 + \text{N}_2$ mixture the delay between these two processes is about 90 s.

5. DISCUSSION OF RESULTS

The results presented above show that the use of SAWs to detect gases provides a high sensitivity and is unique in the sense of the possibility of controlling the magnitude, sign, steepness, decay, and aging of the SAW response. None of the other known types of gas sensors have this property. The prototypes of SAW hydrogen sensors with sorbent Pd films which we prepared operate in the range of hydrogen concentrations 0.1–2% with rise time equal to 30 s, a recovery time equal 3 min, reproducibility of the values of successive measurements equal to $\pm 10\%$, and aging amounting to 14% over the course of 8 months. At the same time, the high sensitivity of SAWs to any disturbances of the surface plays a negative role with respect to the reproducibility of the results and the aging of the sensor. Even trace amounts of impurities adsorbed by a film in the period between two successive exposures or as a result of prolonged contact with the environment are capable of markedly distorting the operating characteristics of a sensor.

The traditional way to overcome this deficiency is to develop thin-film coatings that are selective, sensitive, and, at the same time, stable with time. However, despite many years of efforts on the part of numerous researchers, this approach has been ineffective, except for rare exceptions. The possibility noted above of optimizing the substrate material and/or its crystal cut somewhat facilitates the solution of this problem.

Another approach is to eliminate the sorbent coating on the propagation path of the wave and, consequently, its destabilizing influence^{24,25} (Fig. 8). In this case the gas mixture under investigation is fed into a measuring chamber, in which there is an ordinary delay line heated to a temperature approximately 50 °C above the environment. If the composition of the gas mixture changes, the thermal conductivity of the medium κ , the amount of heat transferred from the heated delay line, its temperature T , and the SAW propagation rate V in the acoustic waveguide vary successively. The changes in the velocity of the SAWs are detected in the form of phase (frequency) changes. The magnitude of the thermal-

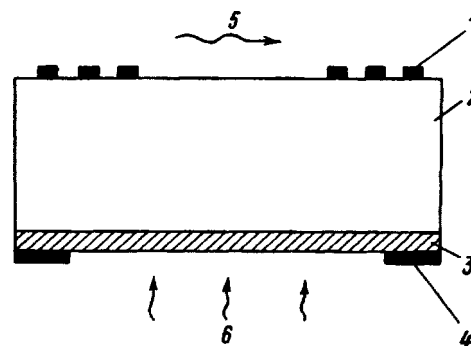


FIG. 8. Design of thermal-conductivity and calorimetric SAW sensors: 1—interdigital electromechanical transducers, 2—piezoelectric substrate, 3—thin-film heating element, 4—electrodes for applying a constant electric voltage, 5—SAW, 6—gas.

conductivity SAW response is proportional to the change in the thermal conductivity of the gas mixture $\Delta \kappa$ and the temperature coefficient of the SAW velocity in the acoustic waveguide material. Therefore, the acoustic waveguides for such sensors must be fabricated from materials with a large value for the temperature coefficient of the SAW velocity. By selecting the working temperature and the substrate material, we can increase, decrease, "zero," and invert the response. The gas being tested can also be selected on a background of another gas.²⁵

The thermal-conductivity detection of gases using SAWs is free of the deficiencies of ordinary coated SAW sensors. However, as in the case of thermal-conductivity cells of the resistive type,²⁶ it has restricted applicability. Since the thermal effect can be identical for gas mixtures consisting of different gases in different concentrations, the use of a thermal-conductivity SAW sensor is possible only for determining the concentrations of each of the *a priori* known gases comprising a binary mixture.

Gases can also be detected using SAWs on the basis of a calorimetric principle.²⁷ The design of such an SAW detector scarcely differs from the design of a thermal-conductivity SAW sensor (Fig. 8): here, too, there is no sorbent coating, and detection is based on the observation of the change in the SAW phase (frequency) because of the change in the SAW velocity in the acoustic waveguide due to the change of its temperature. However, in the design of a calorimetric SAW sensor (Fig. 8) the thin-film heating element is fabricated from a material, whose electrical resistance varies reversibly in the presence of the gas being tested in the environment. Since a voltage of constant magnitude is applied to such a heating element, the change in its resistance ΔR under the action of the gas being tested leads successively to changes in the current, the power released, and the temperature of the acoustic waveguide. A calorimetric SAW sensor has all the merits and deficiencies of ordinary resistive gas detectors. The fundamental feature distinguishing them is the form of the output signal: while the output signal of a resistive sensor represents the relative change in the resistance of the film $\Delta R/R$, the output signal of an SAW sensor represents the relative phase change $\Delta \varphi/\varphi$ or frequency change $\Delta f/f$. Therefore, a calorimetric SAW sensor not only detects a gas,

but also performs analog-to-digital conversion of the $\Delta R/R - \Delta f/f$ type with all the advantages stemming from it.

CONCLUSIONS

The advantages of using SAWs to detect gases are associated with their very high sensitivity to changes in the density and elastic moduli of the propagation medium ($\Delta\rho/\rho \approx \Delta C_{ij}/C_{ij} \approx 5 \times 10^{-5}$) and with the possibility of measuring changes in the SAW propagation rate caused by the changes $\Delta\rho/\rho$ and $\Delta C_{ij}/C_{ij}$ with a high accuracy by measuring the change in the phase (frequency) of the signal and obtaining an SAW response in frequency form.

In SAW sensors with a selected sorbent coating for the gas being tested, the magnitude, sign, and steepness (decay) of the SAW response can be controlled and the aging of the sensor with time can be reduced by selecting the substrate material and/or its crystal cut. However, the high sensitivity of SAWs to changes in the density and elastic moduli of the propagation medium, unfortunately, leads to a great problem, viz., the need to prepare sorbent coatings with a density and elastic moduli that are reproducible and stable with time.

High reproducibility and weak aging with time are exhibited by SAW gas sensors of the thermal-conductivity and calorimetric types, which do not employ sorbent coatings on the wave propagation path. However, the use of a calorimetric SAW sensor is restricted to binary and, in rare cases, ternary combinations of a priori known gases. Furthermore, the range of application of calorimetric SAW sensors is, unfortunately, restricted to a small number of known materials for the heating element, which are capable of reversibly varying their electrical resistance under the action of the gas being tested.

The high sensitivity of SAWs toward changes in the density and elastic moduli of the propagation medium creates prospects for their use in the investigation of such surface effects as the adsorption and desorption of their gaseous phase. The magnitude of the relative density change can be used to determine the number of atoms (molecules) adsorbed on the surface to within $\approx 10^{14} \text{ cm}^{-2}$ and changes in the number of particles adsorbed (desorbed) during a time $\approx 10^{-8} \text{ s}$, and the temperature dependences of these changes can be used to determine the adsorption (desorption) energy to an accuracy no poorer than 0.2 eV. The change in the temperature of the SAW propagation medium, which can be measured to within $\approx 10^{-4}$, can be used to determine the

energies of surface chemical reactions. The possibility of separately determining the temporal variations of the density and the elastic moduli permits the individual investigation of the surface processes occurring within the medium. The relative changes in the elastic moduli can be used to simulate intercrystallite interaction potentials of various kinds.

- ¹E. Verona, C. Caliendo, and A. D'Amico, *SAW Gas Sensors*, G. Sberveglieri (ed.), Kluwer, London (1992).
- ²B. A. Auld, *Acoustic Fields and Waves in Solids*, Vol. 2, Wiley Interscience, New York and other cities (1973).
- ³V. I. Anisimkin, I. M. Kotelyanskiĭ, P. Verardi, and E. Verona, *Fiz. Tverd. Tela* (St. Petersburg) **36**, 428 (1994) [*Phys. Solid State* **36**, 234 (1994)].
- ⁴V. I. Anisimkin and I. M. Kotelyanskiĭ, *Zh. Tekh. Fiz.* **55**, 2420 (1985) [*Sov. Phys. Tech. Phys.* **30**, 1440 (1985)].
- ⁵V. I. Anisimkin and I. M. Kotelyanskiĭ, *Zh. Tekh. Fiz.* **62**, 200 (1992) [*Sov. Phys. Tech. Phys.* **37**, 226 (1992)].
- ⁶V. I. Anisimkin, I. M. Kotelyanskiĭ, V. I. Fedosov *et al.*, *IEEE Ultrason. Symp.*, 515 (1995).
- ⁷V. M. Mecea, *Sens. Actuators A* **40**, 1 (1994).
- ⁸V. I. Anisimkin, I. M. Kotelyanskiĭ, P. Verardi, and E. Verona, *Sens. Actuators B* **23**, 203 (1995).
- ⁹S. J. Martin, A. J. Ricco, D. S. Ginley, and T. E. Zipperian, *IEEE Trans. Ultrason. Ferroelectr. Freq. Control* **UF34**, 143 (1987).
- ¹⁰A. J. Ricco, G. C. Frye, and S. J. Martin, *Langmuir* **5**, 273 (1989).
- ¹¹C. L. Graves, G. C. Frye, D. M. Smith *et al.*, *Langmuir* **5**, 459 (1989).
- ¹²L. J. Kepley, R. M. Crooks, and A. J. Ricco, *Anal. Chem.* **64**, 3191 (1992).
- ¹³L. Sun, R. C. Thomas, R. M. Crooks, and A. J. Ricco, *J. Am. Ceram. Soc.* **113**, 8550 (1991).
- ¹⁴R. V. Bucur, V. M. Mecea, and T. B. Flanagan, *Surf. Sci.* **54**, 477 (1976).
- ¹⁵R. V. Bucur, *J. Catal.* **70**, 92 (1981).
- ¹⁶C. Cristofides and A. Mandelis, *J. Appl. Phys.* **66**, 3986 (1989).
- ¹⁷C. Cristofides and A. Mandelis, *J. Appl. Phys.* **68**, R1 (1990).
- ¹⁸F. A. Lewis, *The Palladium Hydrogen System*, Academic Press, London—New York (1967).
- ¹⁹I. Lundstrom, *Sens. Actuators* **1**, 403 (1981).
- ²⁰I. Lundstrom, *Sens. Actuators* **2**, 105 (1981/1982).
- ²¹R. C. Hughes, P. A. Taylor, A. J. Ricco, and R. R. Rye, *J. Electrochem. Soc.* **136**, 2653 (1989).
- ²²V. G. Litovchenko, I. P. Lisovskiĭ, A. A. Efpemov *et al.*, *Poverkhnost'*, No. 10, 5 (1995).
- ²³V. I. Anisimkin, I. M. Kotelyanskiĭ, and É. Verona, *Poverkhnost'*, No. 11, 20 (1996).
- ²⁴V. I. Anisimkin, M. Penza, V. A. Osipenko, and L. Vasanelli, *IEEE Trans. Ultrason. Ferroelectr. Freq. Control* **UF34**, 978 (1995).
- ²⁵V. I. Anisimkin, M. Penza, S. A. Maksimov, and L. Vasanelli, *IEEE Ultrason. Symp.*, Seattle, Wash., USA (1995), pp. 481–484..
- ²⁶G. Wiegleb, *Sensors* [Russian transl. from German], Mir, Moscow (1989).
- ²⁷V. I. Anisimkin, I. M. Kotelyanskiĭ, S. A. Maximov, and M. Penza, in *Proceedings of the International Symposium on Acoustoelectronics, Frequency Control, and Signal Generation*, Moscow (1996), p. 70.

Translated by P. Shelnitz

Microwave pulse compression using diffraction gratings

S. N. Vlasov, N. G. Kazakova, and E. V. Koposova

Institute of Applied Physics, Russian Academy of Sciences, 603600 Nizhni Novgorod, Russia
(Submitted September 4, 1996)

Zh. Tekh. Fiz. **68**, 82–90 (February 1998)

Electromagnetic pulse compressors employing gratings of high breakdown strength in the autocollimation regime at the center frequency of the pulse for p polarization are investigated theoretically. A theory is devised on the basis of a numerical solution of the electromagnetic field equations in an integral-equation formulation. The case of the aberrationless approximation of the compression of a bell-shaped pulse with a quadratically modulated phase is considered analytically. A numerical experiment demonstrates the presence of strong distortions in the pulse after compression, which are caused by the cubic and higher terms in the expansion of the frequency dependence of the phase acquired by the wave in the compressor. The conditions for optimal pulse compression with allowance for aberrations are investigated. © 1998 American Institute of Physics. [S1063-7842(98)01502-5]

One of the ways to increase the radiated power is to compress frequency-modulated electromagnetic field pulses. This can be accomplished by using a dispersing system in the form of a set of diffraction gratings,¹⁻³ where maxima possessing dispersion are used in the radiation scattered by a grating. The simplest system employing such gratings is shown in Fig. 1. A theoretical analysis of pulse compression in these gratings without a detailed analysis of their scattering coefficients was given in Ref. 1. Such investigations are usually performed with wave beams having an electric-field vector perpendicular to the edges of the grating (s polarization). Such gratings are known to have a low breakdown strength. In this respect there is an advantage to using wave beams with an electric-field vector directed along the edges (p polarization). Such gratings have a higher breakdown strength. To obtain a high pulse compression efficiency it is clearly desirable to use gratings which would have a single maximum in the scattered radiation and for which this maximum would differ from the specular maximum. This property is exhibited by gratings in the so-called autocollimation regime,⁴ in which all the scattered radiation is concentrated in a single wave propagating toward the incident radiation and the power in the specular maximum is equal to zero. This regime was investigated in Refs. 5 and 6, where it was shown that a numerical solution of the problem of the diffraction of an electromagnetic wave in a grating is required to find the condition for realization of this regime in the case of p polarization. Electromagnetic pulse compressors employing gratings in the autocollimation regime for p polarization are investigated theoretically in the present work.

The theory is devised on the basis of a numerical solution of the electromagnetic field equations. An integral equation which describes the diffraction of a monochromatic plane wave impinging at an angle Θ onto an ideally conducting grating that is homogeneous in the z direction, as shown in Fig. 2, is written for this purpose. For p polarization, with consideration of the boundary conditions for a zero value of the tangential component of the electric field $E_z = \Psi(x, y)$ on

the grating surface $\Psi(x, y)|_{y=f(x)} = 0$, it has the form

$$\int ds' \times G(x-x', y-y') \frac{\partial}{\partial n'} \Psi(x', y')|_{y=f(x)} + \Psi_i(x, y)|_{y=f(x)} = 0. \tag{1}$$

Here $\Psi_i(x, y) = \exp(ik_{xm}x - ik_{ym}y)$ is the field of the incident wave, and $f(x)$ is the surface profile, and the total field $\Psi(x, y)$ outside the surface can be represented by virtue of the periodicity of the boundary conditions in the form of a sum of diffraction harmonics of order m :

$$\Psi(x, y) = \sum_{m=-\infty}^{\infty} R_m \exp(ik_{xm}x + ik_{ym}y) + \exp(ik_{xm}x - ik_{ym}y),$$

where

$$k_{xm} = k \sin \Theta_m = k \sin \Theta + m \frac{2\pi}{a},$$

$$k_{ym} = \sqrt{k^2 - k_{xm}^2}, \quad k = \frac{\omega}{c},$$

$$G(x-x', y-y') = \frac{1}{2ia} \sum_{m=-\infty}^{\infty} \frac{1}{k_{ym}} \times \exp(ik_{xm}(x-x') + ik_{ym}|y-y'|)$$

is the two-dimensional Green's function of an array of collinear sources which are linear in the z direction and are arranged with a period a in the x direction, ω is the wave frequency, and c is the speed of light.

The solution gave the complex scattering coefficient R into a single nonspecular minus first-order maximum. Its characteristics, the modulus $|R|$ and the phase φ_R , are presented in Fig. 3 as functions of the diffraction parameter $\kappa = a/\lambda$ ($\lambda = 2\pi c/\omega$ is the wavelength) for incidence of the wave at values of Θ from 45 to 75° near the total autocolli-

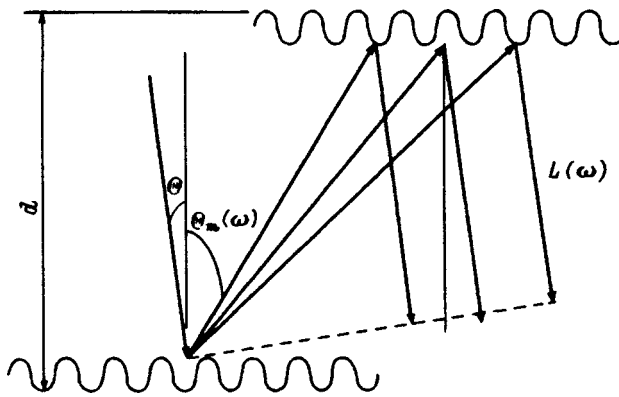


FIG. 1. Simple electromagnetic pulse compressor employing a pair of diffraction gratings.

mation reflection regimes in the case of a sinusoidal corrugated surface. The figure shows that for *p* polarization the width of the band for the existence of the nonspecular lobe rapidly narrows as the angle Θ increases, imposing an additional constraint on the degree of pulse compression in *p* polarization. The high-reflectance relative frequency bands in the minus first order at the $1/\sqrt{\epsilon}$ level near the total autocollimation reflection regimes as a function of the angle of incidence for both polarizations are compared in Fig. 4. The narrower frequency band for *p* polarization and its sharper dependence on the angle are the price for the higher breakdown strength.

We note that the amplitude of the sinusoidal surface, which is determined numerically from the conditions for the achievement of the total autocollimation reflection regimes, increases strongly at large angles (see Table I).

However, it is clear that the only working parts of such a surface are its peaks, which are cut off by the condition that

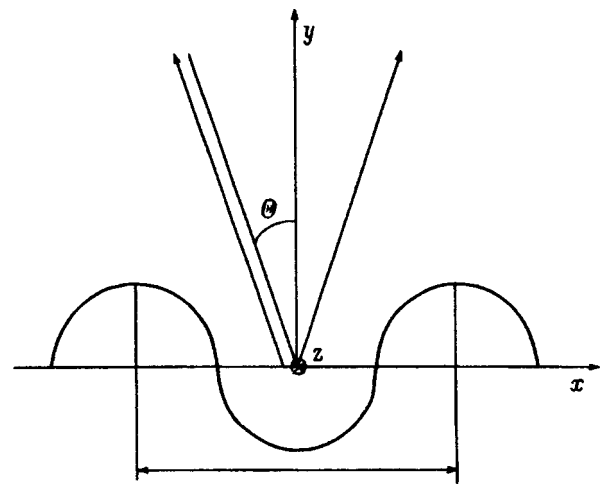


FIG. 2. Diffraction of a monochromatic plane wave on a corrugated surface.

the waveguide channels are not defined at the corresponding depth level. The numerical investigations of the scattering properties of the gratings performed for profiles having the form of sinusoids truncated at different depth levels completely confirm this. An example of one period of the “working” profile of the surface for the angle of incidence $\Theta = 60^\circ$ is illustrated on the scale of the wavelength $\lambda_0 = 1$ by the solid line in Fig. 5. The dashed line shows the corresponding period of a sinusoidal grating profile with the same scattering characteristics.

The need to avoid the overlap of the incident and reflected pulses during operation in the autocollimation regime calls for physically separating the emitter and the receiver in the plane of the edges of the grating by a certain angle α (Fig. 6). This must be taken into account in calculating the

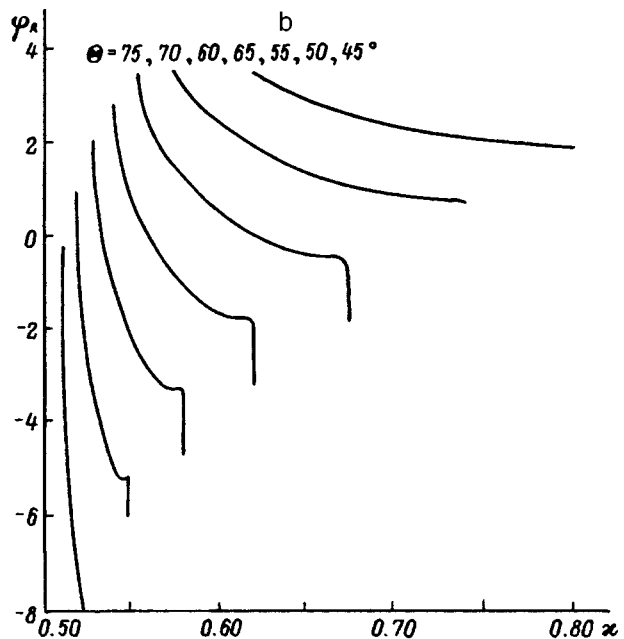
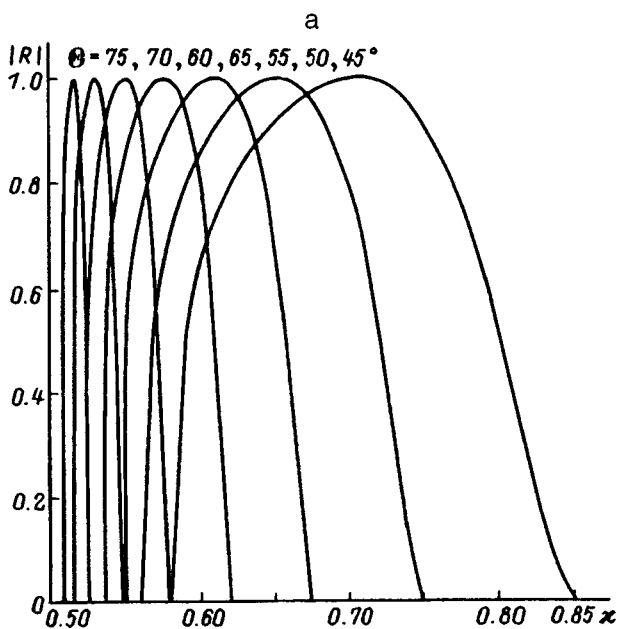


FIG. 3. a—Modulus of the scattering coefficient into a single nonspecular minus first-order maximum as a function of the diffraction parameter near the total autocollimation reflection regimes for various angles of incidence of the wave; b—phase of the scattering coefficient into a single nonspecular minus first-order maximum as a function of the diffraction parameter near the total autocollimation reflection regimes for various angles of incidence of the wave.

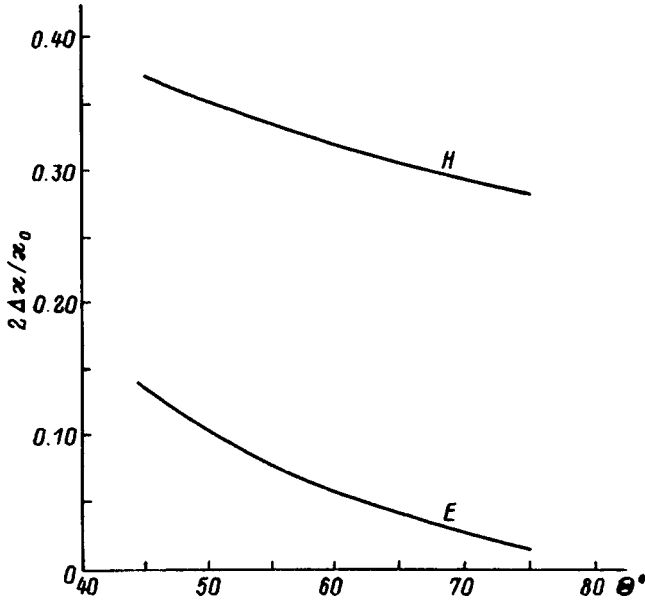


FIG. 4. Relative frequency bands of the total autocollimation reflection regimes as a function of the angle of incidence for $s(H)$ and $p(E)$ polarizations.

grating parameters for required scattering regimes ($\omega_{ekv} = \omega \cos \alpha$, $\lambda_{ekv} = \lambda / \cos \alpha$).

The structure of the output pulse of the compressor was defined in the dimensionless variables $t = t^d \omega_0$ and $\omega = \omega^d / \omega_0^d$, (t^d and ω^d are the dimensional quantities, and ω_0^d is the dimensional center frequency of the pulse) by the following expression:

$$A_{out}(t) = \int_{-\infty}^{\infty} d\omega F_{in}(\omega) R^n(\omega) \exp\{-i\omega t + i\varphi(\omega)\}, \quad (2)$$

where

$$F_{in}(\omega) = \frac{1}{2\pi} \int_{-\infty}^{\infty} dt A_{in}(t) \exp(i\omega t)$$

is the frequency spectrum of the input pulse, $A_{in}(t)$ is a function which describes the time dependence of the input pulse, $\varphi(\omega) = 2\pi\omega L(\omega)$ is a function which characterizes the phase trajectory in the compressor as a function of the frequency,

$$L(\omega) = \frac{n}{2} d \frac{1 + \cos(\Theta + \Theta_m(\omega))}{\cos \alpha \cos(\Theta_m(\omega))} = \frac{n}{2} L_0 \frac{\cos \Theta}{\cos(\Theta_m(\omega))} \times [1 + \cos(\Theta + \Theta_m(\omega))] \quad (3)$$

TABLE I. Parameters of the total autocollimation reflection regimes.

Θ^0	α_0	Amplitude ($a=2\pi$)	Amplitude/ λ_0
45	0.707	6.0	0.68
50	0.653	8.3	0.86
55	0.610	11.5	1.12
60	0.577	16.0	1.47
65	0.552	22.75	2.00
70	0.532	34.0	2.89
75	0.518	55.9	4.61

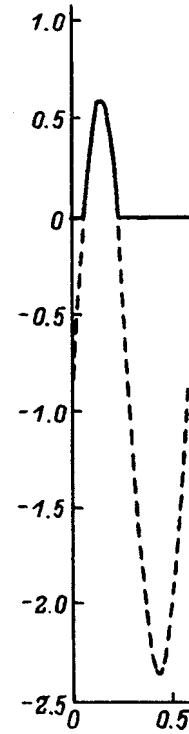


FIG. 5. Profile of a surface corrugation providing for total autocollimation reflection at $\Theta = 60^\circ$ on the wavelength scale $\lambda_0 = 1$.

is the dimensionless propagation length of the spectral component with the frequency ω in the compressor (Figs. 1 and 6) ($L = L^d / \lambda_0^d$, L^d is the dimensional quantity, $\lambda_0^d = 2\pi c / \omega_0^d$ is the center wavelength),

$$\Theta_m(\omega) = \arcsin\left(\sin \Theta + \frac{m}{\alpha_0 \omega}\right)$$

is the scattering wavelength of a wave with the frequency ω in the m th diffraction order (we are working at $m = -1$), $d = d^d / \lambda_0^d$ is the dimensionless distance between gratings along a perpendicular, $L_0 = d / (\cos \alpha \cos \Theta)$ is the dimensionless propagation length of a wave between gratings, and n is the number of repeated reflections from the gratings ($n = 2$ for the single-pass compressor scheme, and $n = 4$ for the double-pass scheme).

The characteristic form¹⁾ of the function $\varphi(\omega)$ for several characteristic values of L_0 in the example case of the angle of incidence $\Theta = 60^\circ$ is shown by the solid lines in Fig. 7. It follows from these curves that pulse compression in such a compressor has an aberrational character. The influence of only the quadratic term in the expansion of $\varphi(\omega)$ near the center frequency of the pulse is significant for the compression of pulses with a fairly smooth bell-shaped profile (in the notation adopted the dimensionless center frequency of the pulse $\omega_0 = 1$; this is taken into account in the ensuing mathematical manipulations). The approximation in which $\varphi(\omega)$ is given by the quadratic polynomial (the dashed curves in Fig. 7)

$$\varphi(\omega) = \varphi(\omega_0) + \varphi'_\omega(\omega_0)(\omega - 1) + \frac{1}{2} \varphi''_{\omega\omega}(\omega_0)(\omega - 1)^2, \quad (4)$$

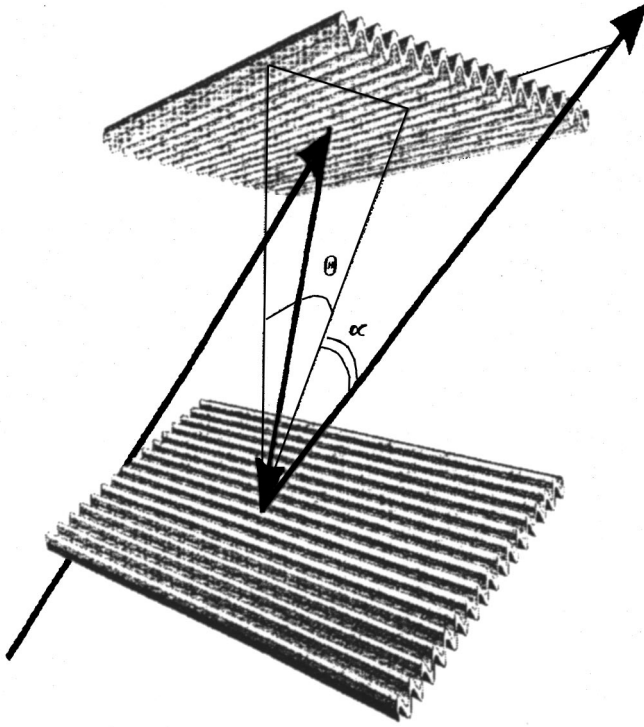


FIG. 6. Spatial autocollimation compressor.

where $\varphi(\omega_0) = 2\pi L(\omega_0)$, $\varphi'_\omega(\omega_0) = 2\pi[L(\omega_0) + L'_\omega(\omega_0)]$, $\varphi''_{\omega\omega}(\omega_0) = 2\pi[2L'_\omega(\omega_0) + L''_{\omega\omega}(\omega_0)]$, and the scattering coefficient of the Gaussian diaphragm in the frequency range

$$R(\omega) = \exp\left\{-\frac{(\omega-1)^2}{2(\Delta\omega_R)^2} + i\frac{(\omega-1)^2}{2(\Delta\omega_\varphi)^2}\right\}, \quad (5)$$

will be called the aberrationless approximation. It is valid²⁾ when the value of the next (cubic) term in the expansion of $\varphi(\omega)$ satisfies the inequality

$$\frac{1}{3!} \varphi'''_{\omega\omega\omega}(\omega_0) \Delta\omega^3 \leq \pi,$$

where

$$\varphi'''_{\omega\omega\omega} = 2\pi[3L''_{\omega\omega}(\omega_0) + L'''_{\omega\omega\omega}(\omega_0)],$$

and $\Delta\omega$ corresponds to the half-width of the pulse spectrum, i.e., to the characteristic scale $(\omega-1)$.

Let there be a frequency-modulated pulse

$$A_{in}(t) = A_0 \exp\left\{-\frac{t^2}{2T^2}(1-i\Omega T) - it\right\} \quad (6)$$

at the entrance to the compressor with the duration $2T = 2T^d \omega_0$ at the $1/e$ intensity level and with linear chirping of the frequency by $2\Omega = 2\Omega^d / \omega_0$ during its duration. Its spectrum

$$F_{in}(\omega) = \frac{A_0 T}{\sqrt{2\pi}} \frac{\exp\left\{\frac{i}{2} \arctan(\Omega T)\right\}}{\sqrt{1+(\Omega T)^2}} \times \exp\left\{-\frac{(\omega-1)^2 T^2}{2[1+(\Omega T)^2]}(1+i\Omega T)\right\}$$

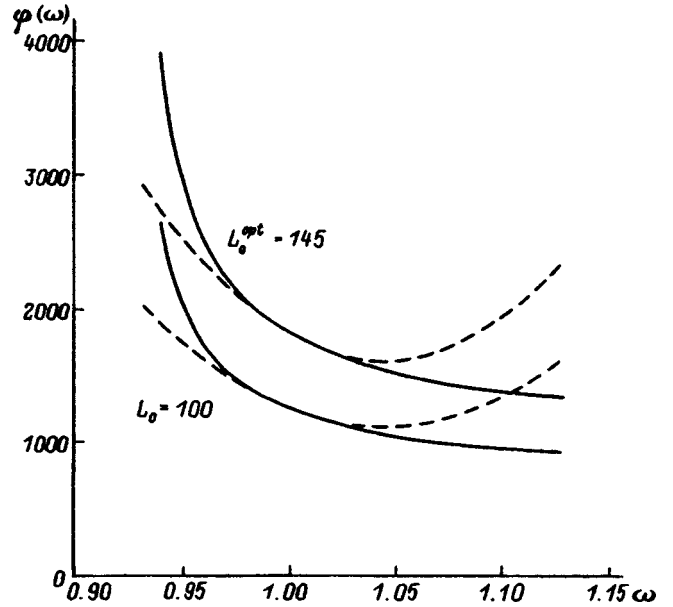


FIG. 7. Characteristic form of the frequency dependence of the phase trajectory in the compressor.

has the half-width

$$\Delta\omega = \frac{1}{T} \sqrt{1+\Omega^2 T^2} \quad (7)$$

at the same level and the quadratic phase

$$\frac{(\omega-1)^2 \Omega T^3}{2[1+(\Omega T)^2]}.$$

Because of the phase modulation the spectrum is broadened by the a factor of ΩT relative to the half-width $1/T$ of the ‘‘intrinsic’’ spectrum of the unmodulated pulse. Under strong modulation ($\Omega T \gg 1$) the half-width of the pulse spectrum is determined practically completely by the amount of frequency modulation ($\Delta\omega \approx \Omega$), and the contribution of the intrinsic spectrum can be neglected in this case. The phase of the pulse spectrum is then of the order of

$$\frac{T}{2\Omega} (\omega-1)^2.$$

Under the operating condition of a grating in the auto-collimation regime $\Theta_m = -\Theta$ [Θ is the angle of incidence; in the minus first order ($m = -1$) with the angle $\Theta = \arcsin(1/2\kappa)$ in the range of angles for the ‘‘two-wave’’ regime³⁾ the parameters of the transmitted wave at the center frequency of the complete path in the compressor are $L(\omega_0) = nL_0$, $L'_\omega(\omega_0) = -2nL_0 \tan^2 \Theta$, and $L''_{\omega\omega}(\omega_0) = 6nL_0 \tan^2 \Theta(1+2 \tan^2 \Theta)$.

The pulse duration after compression in the aberrationless approximation can be represented by the formula

$$T_{out} = \sqrt{2} \frac{|P|}{\sqrt{\text{Re}(P)}} = \sqrt{2\text{Re}(P)} \sqrt{1 + \left(\frac{\text{Im}(P)}{\text{Re}(P)}\right)^2}. \quad (8)$$

Here the complex function P has the form

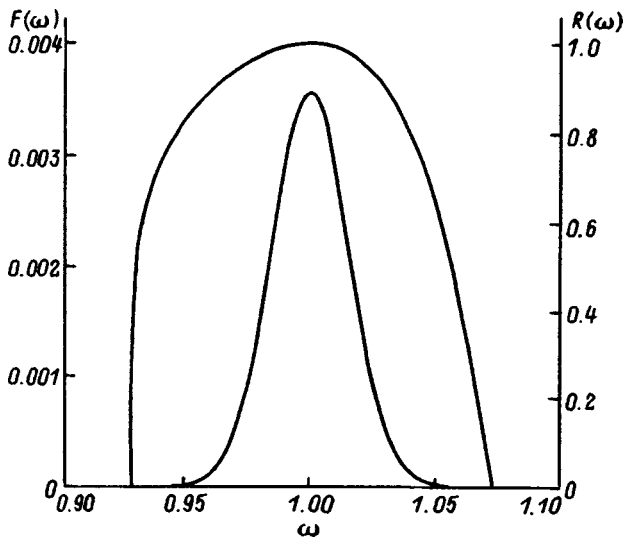


FIG. 8. Spectrum of a typical pulse and the reflectance band.

$$P = \frac{1}{2(\Delta\omega)^2} + \frac{n}{2(\Delta\omega_R)^2} + i \left\{ \frac{\Omega T}{2(\Delta\omega)^2} - \frac{n}{2} \varphi''_{R\omega\omega}(\omega_0) - \frac{1}{2} \varphi''_{\omega\omega}(\omega_0) \right\},$$

where

$$\varphi''_{\omega\omega}(\omega_0) = 4\pi n L_0 \tan^2 \Theta (1 + 6 \tan^2 \Theta) \quad (9)$$

is the curvature of the phase trajectory of the wave at the center frequency in the compressor.

The minimum of the output pulse duration

$$T_{out}^{min} = \sqrt{\frac{1}{(\Delta\omega)^2} + \frac{n}{(\Delta\omega_R)^2}} = \frac{1}{\Delta\omega\eta} \approx \frac{1}{\Delta\omega} \left\{ 1 + \frac{n}{2} \left(\frac{\Delta\omega}{\Delta\omega_R} \right)^2 \right\} \quad (10)$$

is achieved when the imaginary part vanishes: $\text{Im}(P)=0$ (upon phase compensation). Under strong modulation ($\Omega T \gg 1$) and at large angles ($\Theta > 45^\circ$), which ensure strong angular-frequency dispersion upon reflection from the grat-

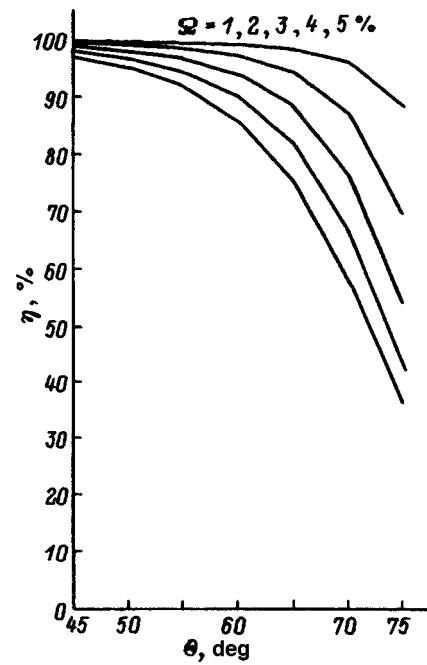


FIG. 9. Compressor efficiency in the aberrationless approximation.

ing, the pulse can be compressed by a factor of ΩT , and the optimal compressor dimension can be represented in the aberrationless approximation by a very simple expression:

$$L_0^{opt} \approx \frac{T}{24\pi n \tan^4 \Theta \Omega}.$$

Thus, the compressor dimension measured in terms of a number of wavelengths is determined in order of magnitude by the number of oscillations in the original pulse.

The efficiency of the compressor can be estimated in the approximation under consideration in the following manner:

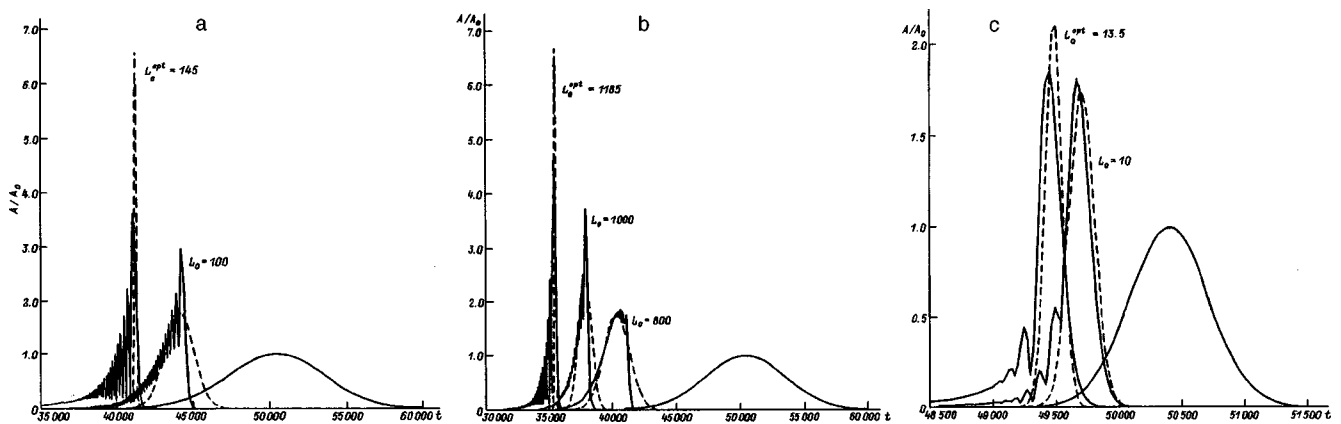


FIG. 10. a, b—Numerical simulation of pulse compression for various compressor dimensions and $\Theta = 60,45^\circ$, respectively; c—numerical simulation of the compression of a short pulse.

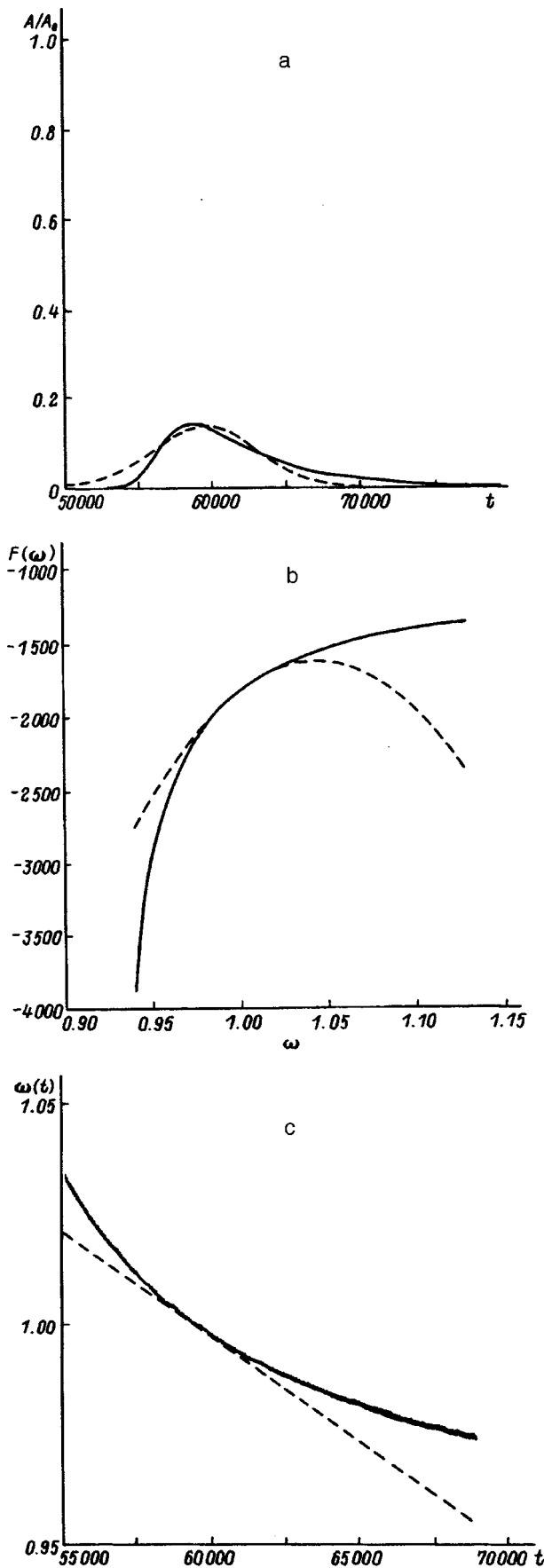


FIG. 11. a—Time dependence of the amplitude of the optimized pulse, b—frequency dependence of the phase of the optimized impulse, c—frequency modulation of the optimized pulse.

$$\eta = \frac{\int_{-\infty}^{\infty} d(\omega-1) \exp\left\{-\frac{(\omega-1)^2}{(\Delta\omega)^2} - n \frac{(\omega-1)^2}{(\Delta\omega_R)^2}\right\}}{\int_{-\infty}^{\infty} d(\omega-1) \exp\left\{-\frac{(\omega-1)^2}{(\Delta\omega)^2}\right\}}$$

$$= \sqrt{\frac{1}{1+n\left(\frac{\Delta\omega}{\Delta\omega_R}\right)^2}} \approx 1 - \frac{n}{2} \left(\frac{\Delta\omega}{\Delta\omega_R}\right)^2. \quad (11)$$

The energy losses are associated here with partial emission of waves into the specular order at frequencies which are close to the center value but differ from it because of the deviation of the reflectance from unity near the total autocollimation reflection regime in the minus first order. Figure 8 presents the typical form of the broadened spectrum of a pulse ($2\Omega = 3\%$) and the value of the reflectance for each spectral component (the outer curve) for the angle of incidence $\Theta = 60^\circ$. Although from the standpoint of increasing the dispersion it is preferable to work at angles close to glancing angles, the high-reflectance band (Fig. 3) $\Delta\omega_R$ then narrows drastically, making it impossible to obtain high efficiencies for those angles when broadening of the spectrum is needed for compression even in the aberrationless approximation. The dependence of the efficiency on the angle of incidence without consideration of the distortions is presented in Fig. 9 for the single-pass compressor ($n=2$) and various values of the modulation parameter Ω . Clearly, when $2\Omega = 3-5\%$, $\eta > 90$ is possible only at $\Theta < 60^\circ$.

A numerical experiment performed on a model of a pulse with a dimensionless duration $2T = 2\pi \cdot 1000$ (of the order of 1000 oscillations) and broadening of the spectrum $2\Omega = 3\%$ with consideration of aberrations for the single-pass scheme ($n=2$) demonstrates the presence of strong distortions after compression, which are caused by cubic and higher terms in the phase expansion.

These distortions are stronger at glancing angles ($65^\circ < \Theta < 75^\circ$) and are very significant at $\Theta = 60^\circ$ (in Fig. 10a the dashed curve corresponds to the aberrationless approximation, the solid curve corresponds to consideration of the distortions, and the solid thick curve corresponds to the original pulse), although transformation of a pulse is possible over a distance $L_0 \sim 100$, which is reasonable for the microwave range only at these angles. At smaller angles ($\Theta = 45^\circ$) the distortions decrease (Fig. 10b), but the compressor dimensions increase to $L_0 \sim 1000$.

It is noteworthy that the distortions are especially strong at the point of maximum pulse compression in the aberrationless approximation for L_0^{opt} , are significantly weaker for $L_0 < L_0^{opt}$, although the pulse achieves almost the same amplitude as at L_0^{opt} , and are practically imperceptible at a small compression factor of 2–2.5 and fairly compact compressor dimensions.

The distortions can also be diminished by diminishing the initial pulse duration, although the maximum compression factor decreases together with it. For example, when $2T = 2\pi \cdot 100$ (of the order of 100 oscillations) there are practically no distortions at the compression optimum even

for $\Theta = 60^\circ$ (Fig. 10c). However, the latter case is mainly of theoretical interest for the microwave region.

To investigate the parameters of an input pulse which is transformed into a bell-shaped (Gaussian) short unmodulated pulse at the compressor exit, we numerically simulated the inverse problem of the passage of a pulse through a compressor.

Figure 11a shows the form of the optimized pulse at the compressor entrance, which is compressed without distortions. The time dependence of its amplitude for the characteristic case of $2T_{\text{out}} = 2\pi \cdot 20$, $2\Omega = 3\%$, $n = 2$, $\Theta = 60^\circ$, and L_0^{opt} is represented by the solid line. The dashed curve is the same dependence obtained in the aberrationless approximation. The short output pulse is represented by the thick solid line. Figure 11b shows the deviation of the frequency dependence of the phase of the optimized impulse from the corresponding dependence in the aberrationless approximation. It is seen from the figure that the initial phase of such a pulse is significantly nonquadratic. Figure 11c compares the form of the frequency modulation of the optimized pulse (solid curve) with a linear chirp (dashed curve), which is needed to compress a pulse in the absence of aberrations.

We thank M. I. Petelin for the idea for this research.

This work was carried out with support from the Russian Fund for Fundamental Research (Grant No. 96-02-19620).

- ¹The function $\varphi(\omega)$ is computed in the geometric-optics approximation. The distortion of the beam structure because of ray mixing is neglected. This effect can be corrected when a two-pass compressor scheme employing a reflecting mirror after the passage of two gratings ($n = 4$) is used.¹
- ²It is not difficult to see that the variation of the phase of the reflectance of the grating $\varphi_R(\omega)$ (Fig. 3) in the characteristic frequency band $2\Delta\omega$ of the pulse can be neglected for the typical values of the compressor parameters $2\pi L_0 \gg 1$. Its magnitude and variation are three orders of magnitude smaller than the corresponding values for the phase trajectory in the compressor (Fig. 7).
- ³The "two-wave" regime is understood to be a regime in which only two waves, viz., the zeroth and minus first orders, exist as propagating waves. The condition for such a regime in the case of autocollimation is the range of angles of incidence $\arcsin(1/3) < \Theta < \pi/2$.

¹S. A. Akhmanov, V. A. Vysloukh, and A. S. Chirkin, *Optics of Femtosecond Laser Pulses*, American Institute of Physics, New York (1992).

²M. B. Vinogradova, O. V. Rudenko, and A. P. Sukhorukov, *Wave Theory* [in Russian], Nauka, Moscow (1990).

³A. Penzkofer, *Opt. Quantum Electron.* **23**, 685 (1991).

⁴V. P. Shestopalov, A. A. Kirilenko, S. A. Masalov, and Yu. K. Sirenko, *Diffraction Gratings* [in Russian], Kiev (1986), Vol. 1.

⁵R. Petit (ed.), *Electromagnetic Theory of Gratings*, Springer-Verlag, Berlin-Heidelberg-New York (1980).

⁶E. V. Sheĭnina, *Radiofizika* **31**, 885 (1988).

⁷L. A. Vainshteĭn and A. I. Sukov, *Radiotekh. Elektron. (Moscow)* **29**, 1472 (1984).

⁸L. A. Vainshteĭn, *Electromagnetic Waves* [in Russian], Radio Svyaz', Moscow (1988).

Translated by P. Shelnitz

Numerical simulation of quasisurface magnetostatic waves in a ferrite film with two magnetic channels

A. Yu. Annenkov, S. V. Gerus, and S. I. Kovalev

*Institute of Radio Engineering and Electronics, Russian Academy of Sciences, Fryazino Branch,
141120 Fryazino, Moscow District, Russia*

(Submitted September 25, 1996)

Zh. Tekh. Fiz. **68**, 91–96 (February 1998)

Quasisurface magnetostatic waves propagating in a ferrite film along two magnetized channels are simulated numerically. It is shown that the interaction between the channels is manifested differently, depending on the wavelength. In the long-wavelength region the interaction between the channels has a distributed character; in the short-wavelength region the interaction between the channels appears as if it takes place at their boundary. The magnetized region of the ferrite film between the channels behaves both as a conductor of the alternating field and as a medium with eigenmodes, so that under certain conditions the waveguide can be transformed into a three-channel structure. The dispersion curves of the magnetostatic wave modes of a two-channel waveguide lie in zones bounded by the dispersion curves of the corresponding modes of a one-channel waveguide of double width. As the gap between the channels increases, the dispersion curves of the odd modes shift toward shorter wavelengths, and those of the even modes shift toward longer wavelengths. © 1998 American Institute of Physics. [S1063-7842(98)01602-X]

INTRODUCTION

From the phenomenological standpoint, magnetostatic waves (MSWs) propagating in ferrite materials are basically combinations of oscillations of the magnetic moment density of the magnet and an alternating magnetic field. In ferrite films and wave channels created on their basis, part of the alternating field propagates outside the ferrite, decaying as the distance from it increases. In the case of a flat film, this decay has an exponential character. In channels with a two-dimensional cross section the picture of the film is more complicated and is most often not amenable to analytical calculation. When there are two or more channels, not only can they interact with one another through the boundary between them, but they can also influence one another through the long-range alternating field, even if they are separated by a fairly great distance. The investigation of the magnetic modes in ferrite waveguides has been the subject of numerous theoretical and experimental studies.

In Refs. 1–4 computer simulation was employed to study the distributions of the magnetostatic wave modes in waveguides formed by magnetizing ferromagnetic films with a nonuniform magnetic field. Both cases in which the magnetizing field has an artificial distribution of the stepwise¹ or parabolic² type and cases in which the field is induced by real magnetic systems^{3,4} were investigated. A more detailed review of the work devoted to the propagation of MSWs in wave channels of various origin was presented in Ref. 4. As far as we know, the interaction of MSW modes in waveguides arranged side by side has been studied experimentally only in Ref. 5 for backward quasivolume modes and in Ref. 6 for quasisurface MSW modes. The movement of the waves in each of the channels and their passage into

the adjacent channel were investigated. The possibility of effective coupling between the channels was demonstrated. It was concluded in Ref. 6 that this coupling has a frequency-dependent character, i.e., the coupling coefficient decreases as the frequency (wave vector) of the surface MSW increases.

This paper presents the results of a numerical simulation of quasisurface MSW modes propagating in a system of two magnetic channels arranged side by side. A stepwise configuration of a magnetization field directed tangentially to the ferromagnetic film and perpendicularly to the channel axis, i.e., the y axis (Fig. 1), was chosen as the channel-forming model. Such a field differs from a field induced by real magnetic systems^{4,6} in that, first, the H_x component is equal to zero and, second its distribution is not smooth. However, the calculations performed for the stepwise model and for a field induced by two rectangular magnetic-field sources like the ones used in Ref. 6 showed that the distribution of the wave modes in a transverse section of a channel and their dispersion characteristics differ only slightly. Therefore, the stepwise field model can apparently be used to analyze the general laws governing the interaction of fairly broad channels ($w \gg h$, where h is the thickness of the ferrite film). This model made it possible to separately study the influence of such parameters as the distance d between the channels and the barrier height G on the coupling between the channels.

CALCULATION METHOD

As we know,⁷ the propagation of magnetic moment precession waves is described fairly well by the magnetostatic approximation of the system of Maxwell's equation, which, together with the equations of motion of the magnetic mo-

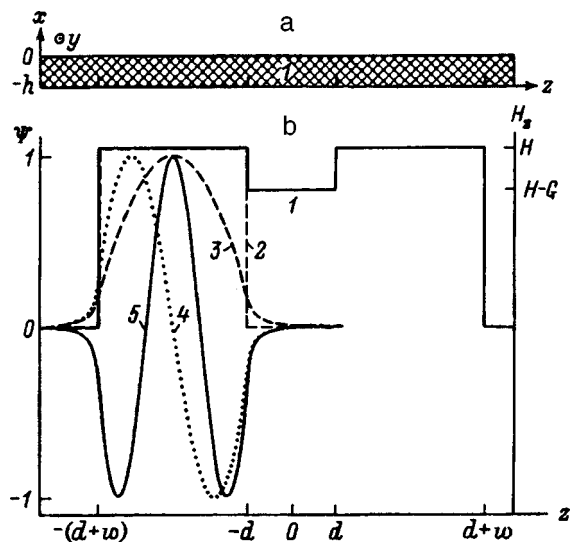


FIG. 1. Geometry of the structure investigated: a—arrangement of the ferrite film 1 relative to the coordinate axes; b—distribution of the z component of the magnetization field of two-channel (1) and one-channel (2) waveguides; 3–5—distribution of Ψ for the first, second, and third modes, respectively in the $x=0$ cross section of a one-channel waveguide ($H=450$ Oe, $d=1$ mm, $4\pi M=1857$ Gs, $f=3100$ MHz, $k_1=76$ cm $^{-1}$, $k_2=94$ cm $^{-1}$, and $k_3=115$ cm $^{-1}$).

ment, lead to an equation for the magnetic potential Ψ , which determine the distribution of the alternating magnetic field of an MSW in space:

$$\text{div}[\mu(x,z)\text{grad } \Psi]=0, \tag{1}$$

where $\mu(x,z)$ is the dynamic magnetic susceptibility tensor, in which both the jumps of the magnetic parameters of the ferromagnet on the ferrite–insulator boundary and the inhomogeneities created by the static magnetic field H_z are taken into account, while the anisotropic properties of the ferromagnetic medium and the exchange interaction are disregarded.

Despite the fact that, according to the model chosen, the static magnetic field within a channel is assumed to be uniform, with consideration of the boundary conditions the problem contained in Eq. (1) is generally essentially two-dimensional and has inseparable variables. Its solution was sought numerically by a finite-difference method. A rectangular contour, on which the potential Ψ is practically equal to zero, at a fairly large distance from a wave channel was selected. For this purpose, conditions of the “magnetic” or “electric” wall type were written. The region investigated was covered by a rectangular mesh. Then the problem (1), represented on this mesh in integral form, was reduced to the problem of a quadratic matrix operator, which was solved on a computer. This method was described in greater detail in Refs. 3 and 4.

As a result of the calculations, we obtained the wave numbers and distributions of the potential Ψ of the MSW modes for various values of the frequencies and the parameters d and G , i.e., strictly speaking, we investigated the configuration and dispersion characteristics of the modes propagating in a magnetic waveguide with the complex, two-channel configuration of the internal field shown in Fig. 1,

rather than the coupling between the two channels. However, the data obtained make it possible to interpret them as the result of the interaction of modes of single channels.

NUMERICAL SIMULATION

As was noted above, the distribution of the wave potential in a single waveguide with a static field of smooth configuration in its cross section was studied in Ref. 4. A quasisurface wave in a rectangular magnetic channel with sharp walls has a similar appearance. The distributions for the first three modes are presented in Fig. 1. On the surface of the ferrite film each mode has the form of a sinusoid, and somewhat less than a whole number of half waves fit across the width of the channel. Outside the channel Ψ decays smoothly to zero. In the long-wavelength part of the spectrum Ψ extends far beyond the channel boundary; it has a large value on the boundary and slowly decays outside the channel. In the short-wavelength frequency range Ψ is virtually cut off at the channel boundary, and all the energy of the mode is concentrated within the channel.

Let us now consider what the models of a two-channel rectangular waveguide represent. The configurations of the wave function Ψ in a transverse section of such a waveguide are presented in Figs. 2 and 3. We can see how MSWs behave as the frequency increases in the example of the first two modes shown in Fig. 2. The first and second modes of the combined waveguide appear as if they are formed from the first modes of each single waveguide, which oscillate in phase or in antiphase, respectively.

In the lower part of the spectrum the function Ψ of a single waveguide extends to a large distance, its spreading toward the neighboring channel being promoted by the magnetized state of the intermediate layer. The two channels interact very strongly, and the potential Ψ of the combined channel has the form of a single function, which barely resembles the original potentials (Figs. 2a and 2d). If the barrier G is lowered, Ψ transforms into a mode of a single channel of width $2d_2$.

As the frequency increases, the mutual penetration of the alternating magnetic fields between the channels gradually decreases, the coupling between them weakens (Figs. 2b and 2e), and we can now refer to the interaction of two separate channels.

In the short-wavelength part of the spectrum the interaction ceases, the wave functions correspond to the sum of the functions of the individual waveguides, and the wave vectors of the first and second modes become equal. In order to characterize the interaction between the channels in greater detail and to trace its evolution as the parameters of the system vary, we introduce the quantity c , which is equal to the maximum of the function Ψ of the first mode in the central cross section of the two-channel waveguide at $z=0$. Since the absolute maximum of Ψ is normalized to unity, the condition $c \leq 1$ holds. In addition, as the coupling between the channels increases, c varies from 0 to 1. We shall accordingly call c the coupling parameter.

Figure 3 shows the behavior of the coupling parameter c as a function of the wave vector and the distance between the

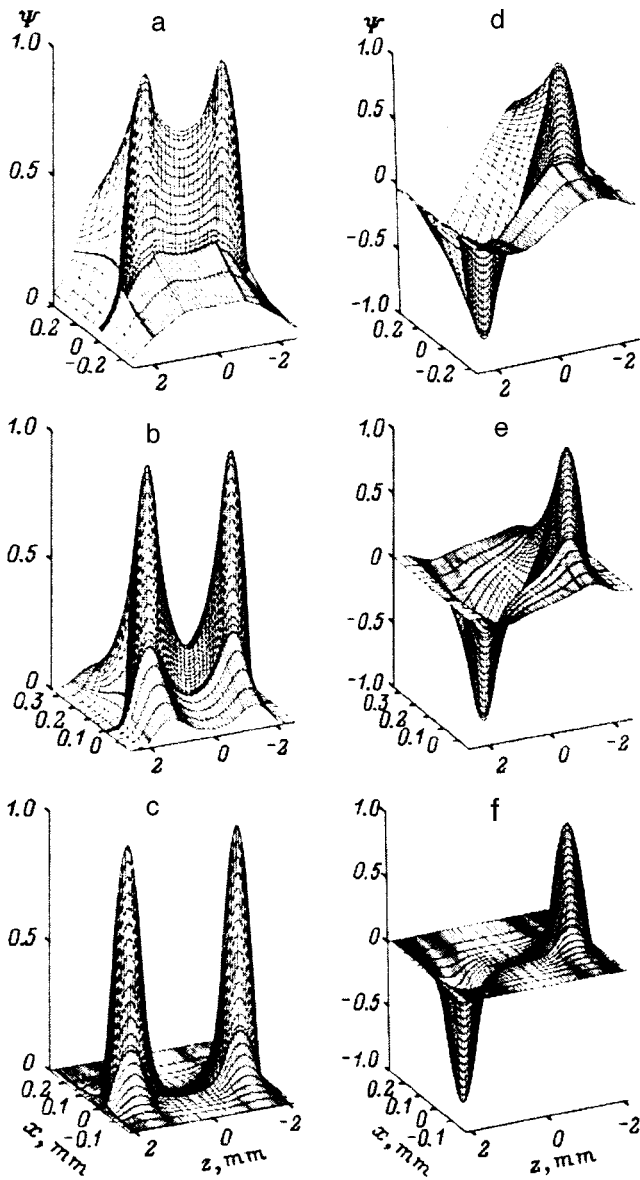


FIG. 2. Normalized distribution of the magnetic potential Ψ . First (a, b, and c) and second (d, e, and f) modes for 2900 (a and d), 3100 (b and e), and 3500 MHz (c and f). Wave numbers, cm^{-1} : a—17.3, b—72.8, c—263, d—19.1, e—73, f—263.

channels. When the distance between the channels is small, the value of c is close to unity at the beginning of the spectrum and decays to zero as the wave vector increases. As the distance d rises, c decreases, the decrease in c being more abrupt at short wavelengths than at long wavelengths. The presence of a hump on the $c(k)$ curve in the central part of the figure is noteworthy. Its existence will be explained below. In all other respects the behavior of c can be understood from the standpoint of the penetration of the long-range alternating magnetic field. This dynamic field is similar to the static field which exists, for example, in stripe domain structures. The distance to which this laterally diverging field penetrates is determined by the thickness and width of the channel, as well as by the wavelength and number of the MSW mode. As the mode number or the wave vector increases, this field is confined to an increasingly shorter dis-

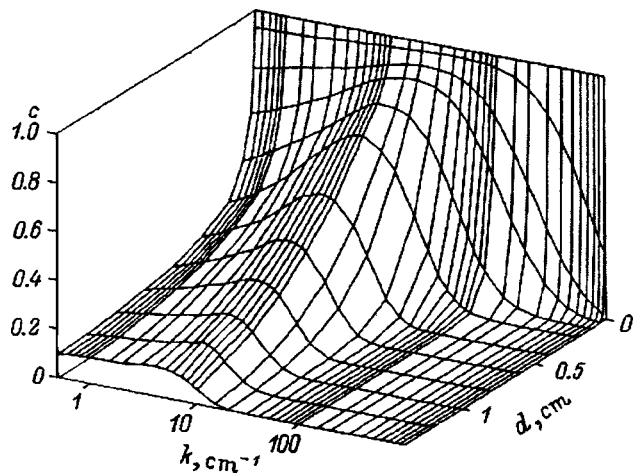


FIG. 3. Variation of the coupling parameter c as a function of the wave number k and the half distance d between the channels.

tance. The same thing occurs as the width or thickness of the waveguide is diminished.

The dependence of c on the height G of the potential barrier between the channels is presented in Fig. 4. Lowering the barrier to values less than 5 Oe causes c to achieve values equal to unity in the low-frequency region. Strictly speaking, the wave function of the two-channel system ceases to “notice” the potential barrier and appears as the function of a single channel of the form shown in Fig. 1, but of width $2(d+w)$. As the intermediate magnetic field $H-G$ between the channels decreases, the penetration of the high-frequency magnetic field through the barrier is impeded, and, as follows from Fig. 4, the coupling between the channels decreases. In addition, as in the preceding case, the decrease is more precipitous at short wavelengths than at long wavelengths. A hump is also observed on the $c(k)$ curve at small wave vectors. Its presence (for assigned values of d and G) is attributed to the fact that, as was shown in Ref. 4, the

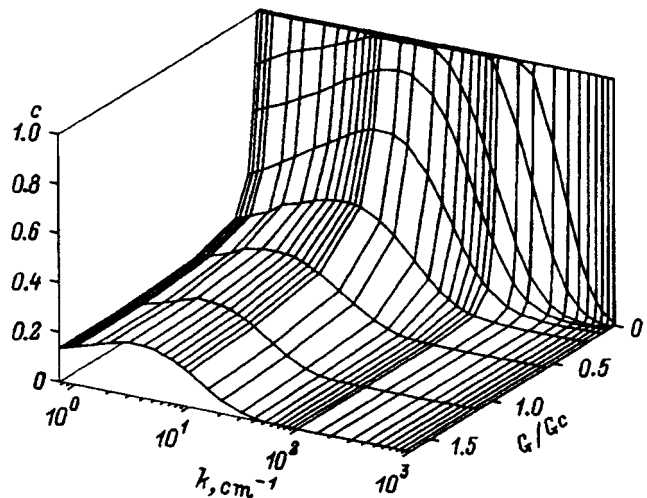


FIG. 4. Variation of the coupling parameter c as a function of the wave number k and the normalized height of the potential barrier G/G_c , where $G_c = H - 2\pi M - \sqrt{H(H + 4\pi M)}$ is the maximum height of the barrier at which MSW modes still exist in the central region.

penetration of a quasisurface wave propagating in a single channel beyond the channel boundary increases with decreasing frequency down to about the frequency at which the wavelength becomes comparable to the channel width, rather than increasing without bound. At that frequency the wave becomes a quasivolume wave in the sense that a sign reversal occurs in the dependence of the wave function on x (across the thickness of the film). The effective width occupied by the function Ψ begins to decrease. In a two-channel system this effect leads to a decrease in the coupling between channels at long wavelengths.

The parameter c for the second mode, which is determined precisely as that for the first mode, is meaningless, since Ψ is identically equal to zero in the cross section at $z=0$. The behavior of the derivative $\partial\Psi/\partial z$ in this cross section, which reflects the mutual influence of the channels to some degree, could be traced, but identification of this quantity with a characteristic of the coupling between the channels is not so obvious as the parameter chosen for the first mode. It would appear that energy characteristics like the energy flux density Π (the Poynting vector) must be used to determine the interchannel coupling; however, as we know,⁸ the integral of Π over a closed surface or over a surface intersected by the energy flux, for example, the $y=\text{const}$ plane, rather than the flux itself, has physical meaning. The integral of Π taken over the $z=0$ plane is equal to zero, since, according to the definition of a waveguide mode, there cannot be an energy flux in a direction perpendicular to its propagation. The description which was used for the first mode in terms of the coupling parameter c modes of single channels, is likewise not suitable for the higher odd modes of a two-channel waveguide.

Let us consider, as an example, the fifth mode, whose form for different frequencies is presented in Fig. 5. At small wave vectors the wave function (Fig. 5a) appears as the fifth mode of a broad waveguide. It does not "feel" the potential barrier because of the long-range action of the high-frequency magnetic field specified by the wavelength of the MSW. This "insensitivity" of the form of the function Ψ persists at higher values of the barrier height G and over a broader range of wave numbers than for the first mode. Then, as the frequency and the wave number increase, the field penetration distance decreases, and it would appear that, as in the case of the first mode, the interaction between the two channels should weaken. However, the compound waveguide under consideration effectively splits into three channels, which interact with one another virtually only at the boundaries. In this case only the modes of these channels whose wave numbers coincide at the particular frequency and whose overall form is topologically equivalent to the form of the fifth mode of a single channel are excited (Fig. 5a). To find these modes, we turn to Fig. 6. It presents dispersion curves calculated from the Damon-Eshbach formulas⁹ for such waves with a transverse component of the propagation vector $k_z = \pi n/t$, where n is the mode number and t is the channel width. According to this model, the function Ψ does not extend beyond the waveguide and, therefore, does not fully describe the modes of single waveguides. However, this model helps to qualitatively un-

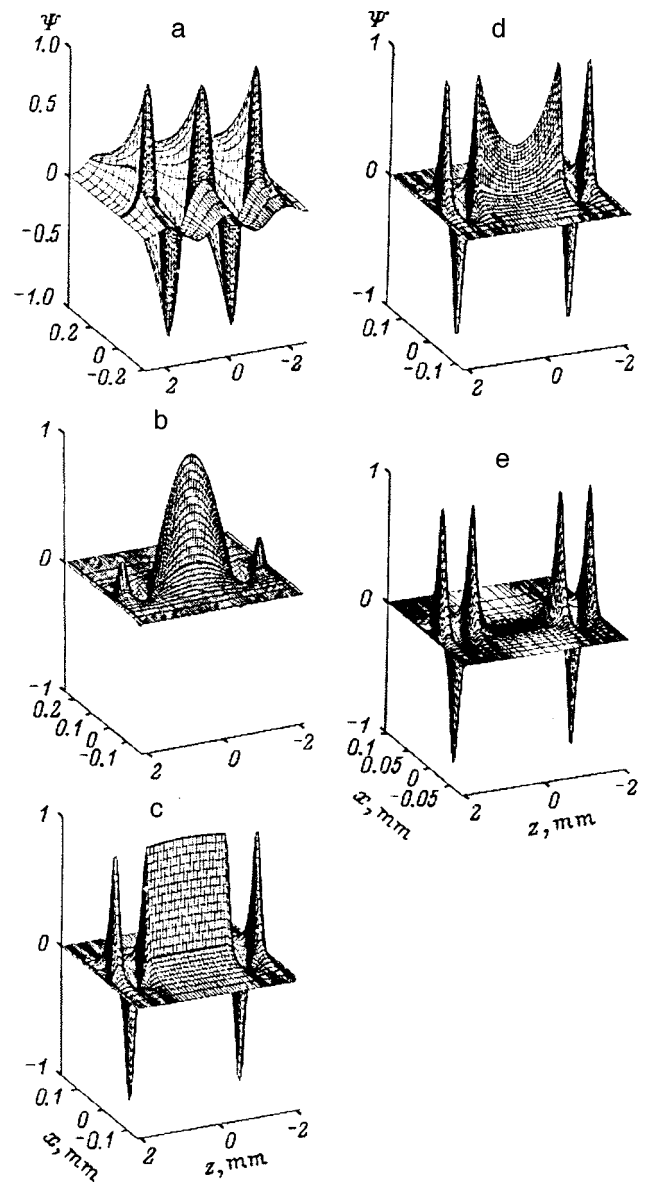


FIG. 5. Normalized distribution of the magnetic potential Ψ of the fifth mode. f , MHz: a—2900, b—3600, c—3672, d—3690, e—3800; k , cm^{-1} : a—33.7, b—374, c—472, d—503, e—839.

derstand what occurs in the channels. As follows from Fig. 6, the dispersion curves of the first mode of the central channel and the second mode of the lateral channels intersect in the range of wave numbers 300–350 cm^{-1} . A smooth transformation of the wave function from the form in Fig. 5a to the form in Fig. 5b takes place in the multichannel system under investigation. Then the third lateral mode intersects the first central mode in the vicinity of 620 cm^{-1} in Fig. 6, and the calculated function of the entire waveguide acquires the form shown in Fig. 5c. The disparity between the value of the wave vector indicated and the value for which Fig. 5c was constructed (472 cm^{-1}) is attributed to the difference between the numerically calculated mode and the mode in the model used to construct Fig. 6 (2.5 instead of 3 half waves across the width of the lateral channels and a practically homogeneous distribution instead of a half wave across the width of the central channel). Furthermore, the dashed curve

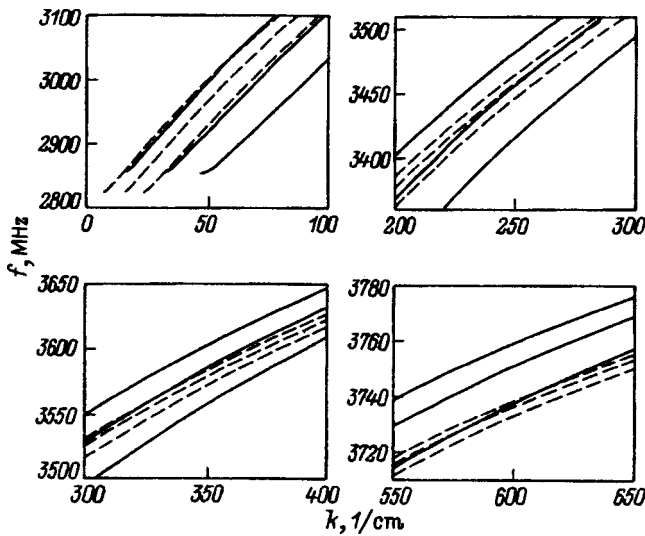


FIG. 6. Fragments of the dispersion curves of the first three modes of single waveguides with rigid walls. Solid lines—lateral channels of width $w=1$ mm, dashed lines—central channel of width $w=2$ mm. For each channel the mode numbers increase from left to right. $H=450$ Oe, $G=8$ Oe.

of the first mode of the central waveguide diverges from the third mode of the lateral channels, and restructuring of Ψ to the form in Fig. 5d and ultimately to the form in Fig. 5e takes place. As expected, two practically independent lateral channels with the third mode in each are obtained as a result. It is seen from such a simple model, for example, that the fifth mode, which is composed of the first lateral modes, and the third central mode cannot exist in this waveguide geometry. The behavior of other modes of this waveguide can be analyzed in a similar manner.

In conclusion, let us consider how the dispersion characteristics of the MSW modes of the waveguide structure appear and how they vary as a function of the distance between the channels. Figure 7 illustrates the case in which the

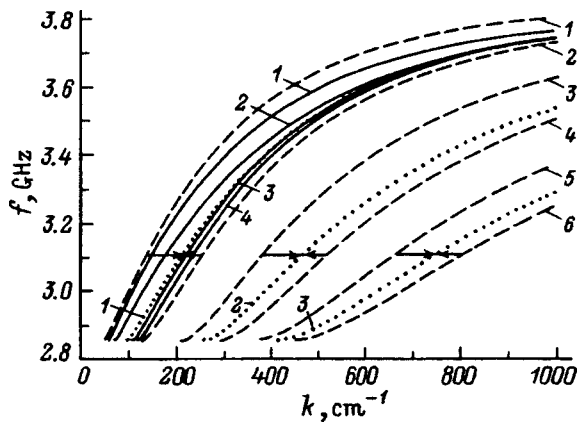


FIG. 7. Dispersion curves of the two-channel structure for various values of the interchannel distance $2d$ (computer simulation). $w=0.1$ mm; solid curves: 1,2—first mode ($d=0.002, 0.01$ mm, respectively); 3,4—second mode ($d=0.03, 0.01$ mm, respectively). The numbering of the dashed curves corresponds to the numbers of the modes of a single waveguide of width $2w$, and the numbering of the dotted curves corresponds to a waveguide of width w .

field $H-G$ in the central part is equal to zero. The figure shows how the dispersion curves vary as d varies from 0 to ∞ in the case of the first and second modes. Only the limiting cases have been left for the modes from the third to the sixth. When $d=0$, there is one waveguide of double width instead of the two-channel waveguide. The dispersion curves of the modes for this situation are indicated by the dashed lines. The other extreme configuration of dispersion curves corresponds to the case of noninteracting channels, i.e., $d=\infty$ (the dotted lines). As the distance between the channels increases, the curves move in the direction of the horizontal arrows. The area of the graph is divided into regions, within which the dispersion curves of a symmetric (odd) mode and the next antisymmetric (even) mode move toward one another, i.e., as d is increased at an assigned frequency, the wave numbers of the odd modes increase, while the wave numbers of the even modes decrease. In the limit $d=\infty$ these modes degenerate into single modes of channels that are not coupled to one another with a mode number equal to half of the number of the original even mode (curves consisting of points). The regions on the graph not marked by horizontal arrows remain “unused.” As $k \rightarrow \infty$ all the curves asymptotically tend to the upper limit for the existence of surface MSWs,⁹ but the rate of ascent of the characteristics is slower, the higher is the mode number.

CONCLUSIONS

Thus, the modes of quasisurface MSWs propagating in a system consisting of two or three interacting channels have been investigated in the present work. It has been shown that the interaction between the channels is manifested differently, depending on the wavelength. In the long-wavelength region the interaction between channels has a distributed character, since the dipolar magnetic field determining their interaction has a long-range effect in this part of the spectrum. The magnetized region of the ferrite film between the channels behaves both as a conductor of the alternating field and as a medium with eigenmodes. When the difference between the magnetization of the central region and the lateral regions is reduced to a certain threshold, a mode of a single broad waveguide, which does not “notice” the boundaries between the channels, is established. In the short-wavelength region the high-frequency field penetrates to only a short distance beyond the channel boundary, and, therefore, the interaction between the channels takes place as if it occurs at their boundary. The presence of a magnetized region in the gap between the channels can lead to the excitation of MSW eigenmodes in it, which transforms the waveguide into a three-channel structure, and, from the standpoint of the influence of the lateral wave channels on one another, increases their coupling constant. The wave functions of the MSW modes then acquire very grotesque forms. The dispersion curves of the MSW modes of a two-channel waveguide lie in zones bounded by the dispersion curves of the corresponding modes of a one-channel waveguide of double width. As the gap between the channels d increases, the dispersion curves of the odd modes shift toward shorter wavelengths, and those of the even modes shift toward longer

wavelengths; in the limit they undergo pairwise merging, signifying the degeneracy of the corresponding symmetric and antisymmetric modes.

This work was performed with support from the Russian Fund for Fundamental Research (Grant No. 96-02-17283a).

¹M. Miyazaki, Y. Yashiro, and S. Ohkawa, IEEE Trans. Microwave Theory Tech. **MTT-33**, 421 (1985).

²M. Koshiba and Y. Long, IEEE Trans. Microwave Theory Tech. **MTT-37**, 1768 (1989).

³I. V. Vasil'ev and S. I. Kovalev, Radiotekh. Elektron. **38**, 2174 (1993).

⁴A. Yu. Annenkov, I. V. Vasil'ev, S. V. Gerus, and S. I. Kovalev, Zh. Tekh. Fiz. **65**(4), 71 (1995) [Tech. Phys. **40**, 330 (1995)].

⁵E. O. Kamenetskiĭ and O. V. Solov'ev, Pis'ma Zh. Tekh. Fiz. **16**(17), 28 (1990) [Sov. Tech. Phys. Lett. **16**, 653 (1990)].

⁶A. Yu. Annenkov and S. V. Gerus, Radiotekh. Elektron. **41**, 216 (1996).

⁷A. G. Gurevich and G. A. Melkov, *Magnetization Oscillations and Waves*, CRC Press, Boca Raton, Florida (1996).

⁸W. R. Smythe, *Static and Dynamic Electricity*, 2nd ed., McGraw-Hill, New York (1950); IL, Moscow (1954).

⁹R. W. Damon and J. R. Eshbach, J. Phys. Chem. Solids **19**, 308 (1961).

Translated by P. Shelnitz

Numerical analysis and synthesis of electron-optical systems of complex structure

S. K. Demin, S. I. Safronov, and R. P. Tarasov

Scientific-Research Institute of Pulse Technique, 115304 Moscow, Russia

(Submitted June 25, 1996)

Zh. Tekh. Fiz. **68**, 97–103 (February 1998)

The problem of the numerical analysis of the electrostatic field of individual elements in complex three-dimensional electron-optical systems is considered. © 1998 American Institute of Physics. [S1063-7842(98)01702-4]

INTRODUCTION

The synthesis of electron-optical systems which adequately meet specified requirements is practically unachievable without a stage involving preliminary numerical simulation and analysis, since the latter permits the consideration of scores of variants of an electron-optical system design within a realistic time frame without resorting to the construction of experimental models, significantly expands the boundaries of the region where it is possible to search for the optimum design of an electron-optical system, permits evaluation of the parameters of electron-optical systems whose measurement is either tedious or impossible with the required accuracy, etc.

The mathematical simulation of an electron-optical system can be regarded as a set of several problems, whose numerical solution represents a computational model of an initial electron-optical system. The most difficult problem to solve numerically is the calculation of the electromagnetic field created by the electrodes of an electron-optical system. The field of an electron-optical system (or, more precisely, of the physical model of an electron-optical system) satisfies a certain linear boundary-value problem with a set of boundary points that form a surface S . It is known¹ that this boundary-value problem can be represented in the form of a boundary integral equation on the surface S , the numerical solution of which ultimately permits the determination of approximate values of the field in the working region of the electron-optical system. The employment of such boundary integral equations has turned out to be one of the most effective methods for the numerical simulation of electron-optical systems.

At the same time, if the surface S has a complicated configuration and large relative dimensions and is multiply connected, discretization of the corresponding boundary equation leads to a mesh problem with a densely filled matrix of large order (several thousand or higher). The numerical solution of such a mesh problem by direct or iterative methods is associated with numerical instability and requires great machine resources. Therefore, the list of boundary-value problems that are subject to numerical analysis is confined mainly to problems with cylindrical or axial symmetry, under which the boundary integral equation is written for a certain contour, or problems with a singly connected boundary surface S of canonical form and small relative dimen-

sions. The latter is responsible for the short list of types of electron-optical systems which can be numerically simulated on the basis of known numerical methods.

One of the methods for expanding the region of application of boundary integral equations to the numerical solution of boundary-value problems is to utilize the finite symmetry groups of the boundary surface. This method is implemented most simply for finite Abelian groups,^{2–5} since character theory can be employed directly in this case. In the case of boundary-value problems with a non-Abelian symmetry group,^{6,7} the basis for constructing computation schemes is a noncommutative harmonic analysis in finite groups. In addition, a definite class of boundary-value problems can be represented in the form of two problems, one of which has a boundary surface with a finite symmetry group, while the other allows an effective numerical solution.^{4,8,9} The symmetry of the individual components of the boundary surface S can also be taken into account in developing economical computational algorithms on the basis of the combined employment of the methods of Refs. 2–9 and the iterative methods of Ref. 10. As the numerical experiments in Refs. 2–10 show, the utilization of finite groups permits the numerical analysis of essentially three-dimensional problems, and the corresponding computational algorithms are tens to hundreds of times more economical and significantly more stable to implement than the algorithms ordinarily used. The approach described in Refs. 2–10 is also effective for the numerical analysis and synthesis of electron-optical systems of complex structure¹¹ consisting of tens of electrodes of different configuration.

MATHEMATICAL SIMULATION OF ELECTRON-OPTICAL SYSTEMS

Let us assume that the initial electron-optical system corresponds to the following physical model. The electrostatic field of the electron-optical system is determined only by a system of N infinitely thin, ideally conducting electrodes $\{S_i\}$, which form a multiply connected surface:

$$S = \bigcup_{i=1}^N S_i, \quad S_i \cap S_j = 0 \quad (i \neq j). \quad (1)$$

Each electrode $S_i \in \{S_i\}$ is supplied with either a known potential φ_i^0 or a known charge σ_i^0 , or a given electrode is immersed in the external field of the remaining electrodes.

Then, if $E = \{E_i\}$ ($i = 1, 2, 3$) is the electric-field vector, $E(x) = -\nabla\varphi(x) \rightarrow E_i(x) = -\partial\varphi(x)/\partial x_i$, where $x = \{x_i\}$ is the set of Cartesian coordinates in the three-dimensional Euclidean space V_3 , and $\varphi(x)$ is the potential of the field E which satisfies the Poisson equation

$$\Delta_3\varphi(x) = -4\pi\mu(x),$$

$$\Delta_3 \equiv \partial^2/\partial x_1^2 + \partial^2/\partial x_2^2 + \partial^2/\partial x_3^2. \quad (2)$$

Here $\mu(x)$ is the bulk charge density, which can be a singular generalized function in the general case. The solution of Eq. (1) with known conditions on $\mu(x)$ has the form

$$\varphi(x) = \varphi_0(x) + [\Delta_3^{-1}]\mu(x),$$

$$[\Delta_3^{-1}]\mu(x) = \int \frac{\mu(x^{(1)})}{|x-x^{(1)}|} d^3x^{(1)}, \quad (3)$$

where $\varphi_0(x)$ is a certain solution of the equation $\Delta_3\varphi(x) = 0$, d^3x is a Euclidean volume element of the space, and $|x-x^{(1)}|$ is the Euclidean distance between the points x and $x^{(1)}$.

In the case of the problem of the scattering of a potential field on the screen S , the function $\varphi_0(x)$ is interpreted as the potential of the initial field, and $\varphi_1(x) = [\Delta_3^{-1}]\mu(x)$ is interpreted as the potential of the scattered field. Here $\mu(x) = \rho(x)\delta(S)$, where $\delta(S)$ is a Dirac delta function with a carrier on the surface S , and $\rho(x)$ is the surface charge density induced by the external field on the screen S . Since S is the multiply connected surface (1), i.e., the screen sought is formed by a system of N electrodes, we have

$$\varphi(x) = \varphi_0(x) + \sum_{i=1}^N \{[\Delta_3^{-1}]\mu_i(x)\},$$

$$\mu_i(x) = \rho_i(x)\delta(S_i) \quad (i = 1, \dots, N). \quad (4)$$

The function $\varphi_1(x)$ can be calculated, if the $\rho_i(x)$ are defined. For their part, the $\rho_i(x)$ can be determined by utilizing relations (3) and (4) and the conditions¹²

$$\varphi(x) = C_i, \quad x \in S_i,$$

$$\int \rho_i(x)\delta(S_i)d^3x = \sigma_i^{(0)} \quad (i = 1, \dots, N), \quad (5)$$

where C_i is, in the general case, an unknown constant which determines the value of the potential at the point S_i on the screen, and $\sigma_i^{(0)}$ is the assigned value of the surface charge at the same point.

In fact, introducing the function $\varphi_i(x) = \chi_{S_i}(x)\varphi(x)$ and $\varphi_i^{(0)} = \chi_{S_i}(x)\varphi_0(x)$, where $\chi_{S_i}(x)$ is the characteristic function of the set of the surface points S_i , relation (3) can be represented in the form

$$\varphi_i(x) = \varphi_i^{(0)}(x) + \chi_{S_i}(x) \sum_{j=1}^N \{[\Delta_3^{-1}]\mu_j(x)\},$$

and to determine $\rho_i(x)$ we write the system of integral equations

$$\sum_{j=1}^N A_{ij}\rho_j = C_i - \varphi_i^{(0)},$$

$$A_{ij}\Psi(x) = \int \frac{\delta(S_j)\Psi(x^{(1)})}{|x-x^{(1)}|} d^3x^{(1)}, \quad x \in S_i. \quad (6)$$

The system of equations (6), supplemented by conditions (5), is closed. The numerical methods for solving Eqs. (6) for a smooth boundary surface S of simple structure are well known. At the same time, in the case of a multiply connected surface S of complicated configuration, which arises in the analysis and synthesis of electron-optical systems, the use of even the simplest type of approximation, viz., the piecewise constant approximation followed by employment of a highly economical collocation method, leads to the need to numerically solve systems of linear algebraic equations of high order with densely filled matrices. Because of the incorrectness of the initial equation, the latter leads to numerical instability, whose suppression requires additional regularizing procedures. As extensive practical experience in the numerical solution of mesh problems which approximate (6) has shown, when the discretization order is high, the known regularizing procedures are ineffective and require large expenditures of machine resources. Stable algorithms for the numerical solution of these mesh problems, which are based on the methods in Refs. 2–11, are presented below.

Thus, the solution of equations (6) with the additional conditions (5), according to (2), permits the determination of approximate values of $\varphi(x)$ and $E(x)$ at any point in the Euclidean space, including points in the working region of an electron-optical system. The latter, in turn, enables us to move on to consideration of the properties of the image created by the instrument. The properties of this image will be studied under the assumption of the absence of noise in the signal, the instrument, and the receiver.

The most complete information on the properties of the image created by an instrument is provided by the instrumental function $S(x, y)$, which describes the distribution of the illuminance in the image of a point source.¹³ For example, in emission systems $S(x, y)$ describes the scattering of electrons emitted by a point emitter on a screen. Various physical characteristics of electron-optical systems, including the one-dimensional instrumental function, the frequency-contrast characteristic, etc., can easily be calculated from $S(x, y)$. In addition, if $\varphi(s, p)$ is the input signal, and $f(x, y)$ is the output signal (the signal actually detected), then

$$\int_{-\infty}^{\infty} S(x-s, y-p)\varphi(s, p)dsdp = f(x, y).$$

The relation enables us to study fairly general properties of an image, for example, to consider the question of reconstructing the input signal $\varphi(s, p)$ in accordance with the experimental possibility of measuring the output signal $f(x, y)$ etc.

The problem of determining the instrumental function $S(x, y)$ in emission instruments reduces to a calculation of the electron trajectories. The motion of a particle with a mass m and a charge e in an electrostatic field is specified by the equation

$$\frac{d}{dt} \left(m \frac{dr}{dt}(x, t) \right) = -e\nabla\varphi(x), \quad (7)$$

where r is the radius vector of the particle and t is the time of flight.

The initial conditions for the escape of a particle are known, if the distribution functions of the initial velocities of the electrons emitted from a point with respect to their magnitude and direction are assigned. These distribution functions, in turn, are individual characteristics of the cathode and are usually determined experimentally.

The Cauchy problem for the ordinary differential equation (7) with known right-hand sides is solved numerically by standard procedures, such as the Runge–Kutta method, the Adams method, etc. On the other hand, if the solution of the boundary integral equation (6) with the additional conditions (5) has been obtained, the calculation of the right-hand side of (7) at an assigned point in the Euclidean space $x \in V_3/S$ reduces to ordinary numerical integration:

$$\nabla \varphi(x) = \nabla \varphi_0(x) + \int \rho(x_1) \nabla \left(\frac{1}{|x-x_1|} \right) d^3x^{(1)},$$

$$x_1 \in S, \quad x \in V_3/S. \tag{8}$$

At the same time, the algorithm described here for finding the trajectories of charged particles in the electrostatic field of an instrument of complex configuration is effective only for a small number of trajectories (several hundred) and is generally used in preliminary calculations to estimate the efficacy of the initial model. The analysis and synthesis of electron-optical systems calls for the determination of such characteristics as the instrumental function, the optimal focusing surface, the resolution and magnification factor on the screen, the time of flight of electrons, the sensitivity to divergence, etc. to sufficient accuracy, which requires the calculation of about several thousand charged-particle trajectories. In this case the calculation of the right-hand sides of (7) on the basis of (8) leads to unjustifiably large expenditures of machine resources.

One of the possible ways to reduce the expenditures of machine resources for calculating the charged-particle trajectories is as follows. An auxiliary three-dimensional mesh is introduced in the region of flight of the charged particles determined during the preliminary calculations of (7) and (8). The points of the cells of this mesh are located at the vertices of hexahedrons, whose bases are rectangles that are parallel to an assigned plane. The potential $\varphi(x)$ is calculated on the basis of the numerical integration of relations (2) only at the mesh points. Within the cells of the mesh, the potential $\varphi(x)$ at the point $x(x_1, x_2, x_3)$ is approximated in the form

$$\varphi(x) = a + bx_1 + cx_2 + dx_3 + ex_1x_2 + fx_2x_3 + gx_1x_3 + hx_1x_2x_3,$$

and the field strength $E(x) = -\nabla \varphi(x)$ is, accordingly,

$$E_{x_1}(x) = -b - ex_2 - hx_2x_3,$$

$$E_{x_2}(x) = -c - ex_1 - hx_1x_3,$$

$$E_{x_3}(x) = -d - fx_2 - hx_1x_2.$$

Since the cells of the three-dimensional mesh have relatively large dimensions, the reduction of the expenditures of machine resources for calculating the charged-particle trajectories by the method described can reach a factor of several tens without a significant loss of accuracy in the calculations.

Thus, the methods of mathematical simulation and the algorithms described in this section permit the analysis and synthesis of electron-optical systems of complex structure provided a numerical solution of Eqs. (6) with the additional conditions (5) is obtained to sufficient accuracy.

FINITE GROUPS IN THE NUMERICAL ANALYSIS OF BOUNDARY INTEGRAL EQUATIONS

To simplify the further presentation, we shall assume that the surface S formed by the system of electrodes in the initial model of an electron-optical system is the set of boundary points of the first, second, or third boundary-value problem for the Laplace equation

$$\Delta u(x) = 0, \quad x \in V_3/S, \quad lu(x) = f(x), \quad x \in S, \tag{9}$$

where l is the boundary operator defined by one of the relations of the form

$$lu(x) = u(x), \quad lu(x) = \frac{\partial u(x)}{\partial n},$$

$$lu(x) = \frac{\partial u(x)}{\partial n} + \alpha u(x), \quad \alpha = \text{const}, \quad x \in S.$$

Also, let

$$A\rho = \varphi, \quad [Au](x) = \int A(x, x_1)u(x_1)d\mu(x_1),$$

$$x, x_1 \in S, \tag{10}$$

where $d\mu(x)$ is the narrowing of the Euclidean volume element on the surface S , be the boundary integral equation of the boundary-value problem (9). In this case the symmetry of the boundary-value problem (9) and the integral equation (10) follows directly from the symmetry of the boundary surface. More specifically, if $\{\tau_k\}$ ($k = 1, 2, \dots, N$) is a finite group of symmetry transformations of the surface S , i.e., if the surface S allows a division of the form

$$S = \bigcup_{i=1}^N S_i, \quad S_i \cap S_j = 0, \quad i \neq j,$$

$$\tau_i S_i = S_1, \quad i = 1, 2, \dots, N, \rightarrow S = \bigcup_{i=1}^N \tau_i^{-1} S_1 \tag{11}$$

into the congruent components $\{S_i\}$ ($i = 1, 2, \dots, N$) relative to the group $\{\tau_i\}$ ($i = 1, 2, \dots, N$), then the operators Δ_3 and l of the boundary-value problem (9) and, therefore, the boundary integral equation (10) are invariant with respect to the transformations of the group $\{T_i\}$ ($i = 1, 2, \dots, N$),

$$T_k^{-1} \Delta_3 T_k = \Delta_3, \quad T_k^{-1} l T_k = l \rightarrow T_k^{-1} A T_k = A,$$

$$T_k u(x) = u(\tau_k^{-1} x) \nu \tau_k \in \{\tau_k\} \quad (k = 1, 2, \dots, N), \tag{12}$$

which constitute a representation of the group $\{\tau_k\}$ in terms of the unitary shift operators acting in a space of functions

defined in the entire Euclidian space or in a space of functions defined on the surface S . Furthermore, if we introduce the space of vector functions $\{\chi_{S_i}\Psi(x)\}$ ($i=1,2,\dots,N$), where $x \in S$ [χ_{S_i} is the characteristic function of the set of surface points S_i corresponding to the division of S into congruent components (11)], on the surface S , the representation of the group $\{\tau_i\}$ will be assigned by the operator matrices T'_i ($i=1,2,\dots,N$):

$$T'_k \Psi_i(x) = \sum_{i=1}^N P_{ji}^{(k)} T_k \Psi_i(x) = \sum_{i=1}^N P_{ji}^{(k)} \Psi_i(\tau_k^{-1}x), \quad (13)$$

where $\{P^{(k)}\}$ is a regular representation of the group $\{\tau_k\}$ in terms of permutation matrices.

The integral equation (10) of the boundary-value problem (9) in the space of vector functions, in turn, has the form

$$\sum_{j=1}^N A_{ij} \rho_j(x) = \varphi_i(x), \quad x \in S_i \quad (i=1,2,\dots,N). \quad (14)$$

By virtue of (12)–(14) we can write

$$(T'_i)^{-1} \|A_{ij}\|_{i,j=1}^N (T'_i) = \|A_{ij}\|_{i,j=1}^N.$$

The latter, in turn, means that system of integral equations (14) can be brought into a diagonal form in the case of an Abelian symmetry group of finite order. In fact, let $\{\tau_i\}$ ($i=1,2,\dots,N$) be an Abelian group with the symmetry $\tau_k \tau_j = \tau_j \tau_k$ ($k,j=1,2,\dots,N$). We go from the basis $\{\rho_i(x)\}$, $x \in S$ to the basis $\{\rho'_i(x)\}$, $x \in S_1$, $\rho'_i(x) = \rho_i(\tau_i^{-1}x)$ ($i=1,2,\dots,N$), in which the representation $\{T'_k\}$ of $\{\tau_k\}$ transforms by virtue of (13) into a regular representation in terms of the permutation matrices $\{P^{(k)}\}$ ($k=1,2,\dots,N$), and the matrix $\|A_{ij}\|$ of the system of integral equations (14) transforms into the matrix $\|A'_{ij}\|$ of the form

$$\begin{aligned} \|A_{ij}\| &\rightarrow \|A'_{ij}\|_{i,j=1}^N = \sum_{k=1}^N A_{1k} T_k^{-1} \|P_{ij}^{(k)}\|_{i,j=1}^N \\ &= \sum_{k=1}^N T_k A_{1k} [\|P_{ij}^{(k)}\|_{i,j=1}^N]^{-1}. \end{aligned}$$

Now, if $\|F_{ij}\|_{i,j=1}^N$ is the Fourier transformation matrix corresponding to the character table of the irreducible representations of the group $\{\tau_k\}$ ($k=1,2,\dots,N$), then in the basis

$$\bar{\rho}'_i(x) = \sum_{j=1}^N F_{ij} \rho'_j(x) \quad (i=1,2,\dots,N)$$

the matrix $\|A'_{ij}\|$ acquires a diagonal form. The system of equations (14) then transforms into uncoupled equations on one of the congruent components of S

$$A_i \bar{\rho}'_i(x) = \bar{\Psi}'_i(x), \quad x \in S_1 \quad (i=1,2,\dots,N), \quad (15)$$

where

$A_i = \bar{A}'_{ii} = \sum_{k,m}^N F_{ik} A'_{km} \hat{F}_{mi} = \sum_{j=1}^N A_{1j} \bar{F}_{ij} = \sum_{j=1}^N A_{j1} F_{ij}$, $\|\hat{F}_{ij}\|_{i,j=1}^N$ is the inverse Fourier transformation matrix, and the bar denotes complex conjugation.

For its part, the diagonalization of the system of equations (14), on the one hand, renders the process of finding an approximate solution of the boundary integral equation (10)

on the computational level more stable and, on the other hand, permits a reduction of the amount of required random access memory by a factor of N and a reduction of the expenditure of processor time by a factor of N^2 in comparison to the direct numerical solution of (10). The case of non-Abelian symmetry groups was described in Refs. 6 and 7.

Nevertheless, the surface S does not always have a certain symmetry. In that case a reduction method can be utilized.

Let us consider the boundary-value problem (9), whose set of boundary points form the surface \bar{S} , which does not have a symmetry group or has a symmetry group of low order. We assume the existence of a surface S with a symmetry group $\{\tau_k\}$ ($k=1,2,\dots,N$) of a finite order N and which is such that $\bar{S} \in S$. Next, let the boundary operator $l(\bar{S})$: $lu(x) = f(x)$, $x \in \bar{S}$ of the initial boundary-value problem of type (9) with the boundary \bar{S} be capable of being continued onto the surface S : $l(\bar{S}) \rightarrow l(S)$ in such a manner that $T_k^{-1} l(S) T_k = l(S)$. We note that these two conditions can easily be satisfied in most cases. For example, the surface \bar{S} with the boundary operator $l(\bar{S})$ appropriately assigned on it can undergo mirror reflection relative to a certain plane, etc. At the same time, under these two conditions the reduction method considered here, which is confined to representing the initial boundary-value problem in the form of two problems, one of which is a problem with a finite symmetry group, while the other allows a fairly simple solution, will be effective in a numerical procedure only when the area of \bar{S} is greater than that of S/\bar{S} . In fact, if the assumptions indicated above hold, then we can pass from the initial boundary-value problem (9) with the boundary surface \bar{S} to a treatment of (9) with S , provided that the values of $f(x)$: $lu(x) = f(x)$, $x \in S$ for $x \in S/\bar{S}$ are unknown. This problem corresponds to the integral equation (10) with the additional condition $\rho(x) = 0$, $x \in S/\bar{S}$. In this case Eq. (10) can be represented in the form of a system of integral equations (14), which can be reduced, in turn, to the uncoupled form (15). At the same time, in this case the right hand sides $\{\bar{\varphi}'_i\}$ ($i=1,2,\dots,N$) in the expressions (15) are not defined for all $x \in S_1$, since the values of $f(x)$ for $x \in S/\bar{S}$ are unknown. To determine the unknown values of the $\{\bar{\varphi}'_i\}$, we use the condition $\rho(x) = 0$, $x \in S/\bar{S}$. As a result, we have

$$\begin{aligned} - \sum_{i=1}^N \hat{F}_{ki} \bar{\rho}'_i(x) &= \sum_{n \in K} \sum_{i=1}^N \hat{F}_{ki} F_{in} A_i^{-1} \varphi'_n(x), \\ x \in S_1 \cap \tau_k(S/\bar{S}), \quad n, k \in K, \end{aligned} \quad (16)$$

where K is a subset of the set of integers $k=1,2,\dots,N$ which is such that $S_1 \cap \tau_k(S/\bar{S}) \neq \emptyset$, and $\{\rho'_i(x)\}$ is the solution of Eqs. (15) with the condition that $f(x) = 0$ for $x \in S/\bar{S}$. Therefore, the initial boundary-value problem with the boundary surface \bar{S} is reduced to N independent integral equations (15) and system of equations (16). The latter, in turn, means that the reduction method considered here will have the same

advantages in a numerical procedure as the approach described above for problems with symmetry provided the area of S/\bar{S} is smaller than that of \bar{S} .

SIMULATION OF INDIVIDUAL CASCADES OF ELECTRON-OPTICAL SYSTEMS

Let us examine the possibilities of the method described in the preceding section in greater detail in the case of the simulation of concrete electron-optical systems or individual cascades of electron-optical systems. Let the surface S formed either by all or by some of the electrodes of an electron-optical system be described by the fourth Klein symmetry group $\{\tau_i\}$ ($i=1,2,3,4$): $S=S_1+\tau_2^{-1}S_1+\tau_3^{-1}S_1+\tau_4^{-1}S_1$, where S_1 is one of the four congruent components of the surface S . It is known that there are three symmetry point groups that are isomorphic to the fourth Klein group: the C_{2h} group with the elements e (the identity transformation), C_2 (rotation by π), σ_h (mirror reflection in the plane orthogonal to the rotation axis), and I (inversion); the C_{2v} group with the elements e , C_2 , σ_v , and σ_v' , where σ_v and σ_v' denote mirror reflection relative to planes passing through the rotation axis; and the D_2 group with the elements e , C_z , C_y , and C_x , where C_z , C_y , and C_x are rotations by π relative to the orthogonal axes. These symmetry groups are often used to describe cascades of divergent systems, diaphragms, etc. In this case the system of four boundary integral equations (14) can be brought into the form¹⁴

$$\begin{aligned} [A_1+A_2+A_3+A_4]\bar{\rho}_1 &= \bar{\varphi}_1, \\ [A_1+A_2-A_3-A_4]\bar{\rho}_3 &= \bar{\varphi}_3, \\ [A_1-A_2-A_3+A_4]\bar{\rho}_2 &= \bar{\varphi}_2, \\ [A_1-A_2+A_3-A_4]\bar{\rho}_4 &= \bar{\varphi}_4, \end{aligned}$$

where

$$\begin{aligned} A_1 &= A_{11}, \quad A_2 = A_{12}T_2, \quad A_3 = A_{13}T_3, \quad A_4 = A_{14}T_4, \\ \bar{\rho}_1 &= \rho_1 + T_2\rho_2 + T_3\rho_3 + T_4\rho_4, \\ \bar{\rho}_2 &= \rho_1 - T_2\rho_2 - T_3\rho_3 + T_4\rho_4, \\ \bar{\rho}_3 &= \rho_1 + T_2\rho_2 - T_3\rho_3 - T_4\rho_4, \\ \bar{\rho}_4 &= \rho_1 - T_2\rho_2 + T_3\rho_3 - T_4\rho_4, \\ \bar{\varphi}_1 &= \varphi_1 + T_2\varphi_2 + T_3\varphi_3 + T_4\varphi_4, \\ \bar{\varphi}_2 &= \varphi_1 - T_2\varphi_2 - T_3\varphi_3 + T_4\varphi_4, \\ \bar{\varphi}_3 &= \varphi_1 + T_2\varphi_2 - T_3\varphi_3 - T_4\varphi_4, \\ \bar{\varphi}_4 &= \varphi_1 - T_2\varphi_2 + T_3\varphi_3 - T_4\varphi_4. \end{aligned}$$

For example, in the case of the C_{2h} group, the corresponding shift operators have the form $T_i u(x) = u(\tau_i^{-1}x)$, where $\tau_1 = e$, $\tau_2 = C_2$, $\tau_3 = \sigma_h$, and $\tau_4 = I$. Thus, when we go over to the mesh problem, consideration of the symmetry of the boundary operator in this case permits fourfold reduction of the size of the matrices being inverted with maintenance of the order of the approximation. The latter, in turn,

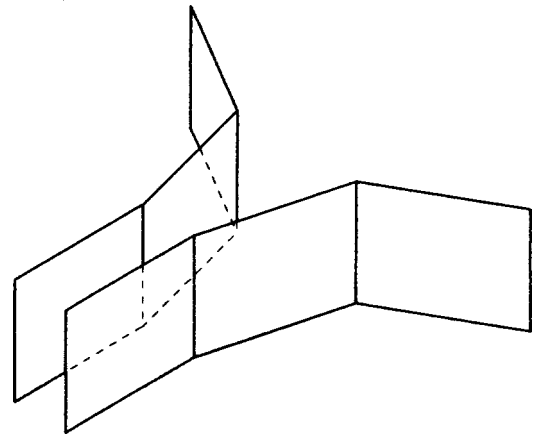


FIG. 1.

renders the algorithms for finding the approximate solution more stable and reduces the expenditures of machine resources by a factor of ~ 16 .

Figure 1 presents a pair of diverging plates, each of which consists of three rectangular sections oriented at assigned angles relative to one another. Such systems are often encountered in electron-optical systems of various types. Figure 2 presents plots of the distribution of the density of electrostatic charge for the case where the potential (in volts) $\varphi_1=2$ is supplied to one plate, while $\varphi_2=1$ is supplied to the other. The order of the mesh problem is then equal to 800, i.e., regardless of the symmetry of the initial problem, a densely filled matrix of dimension 800×800 must be inverted.

Now let the surface S be described by the cyclic symmetry group $C_n\{e, \tau, \dots, \tau^{n-1}\}$ of order N : $S=S_1+\tau^{n-1}S_1+\dots+\tau S_1$, where S_1 is one of the N congruent components of S , and τ denotes rotation by $2\pi/N$. If N is

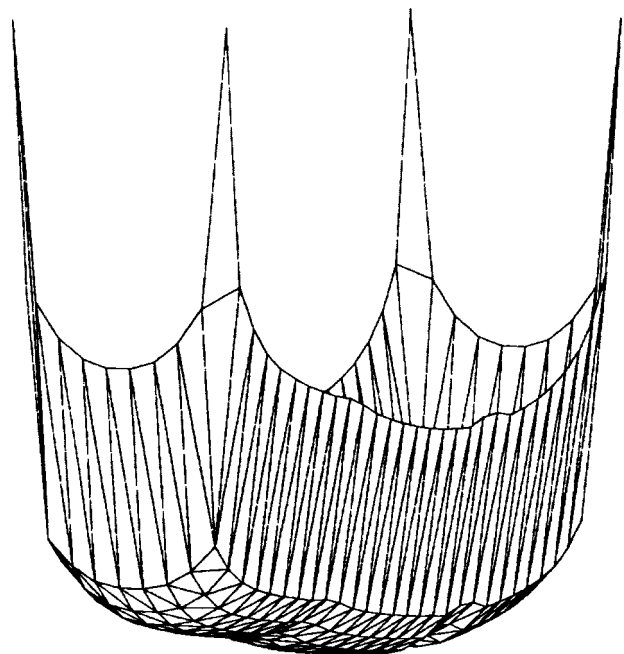


FIG. 2.

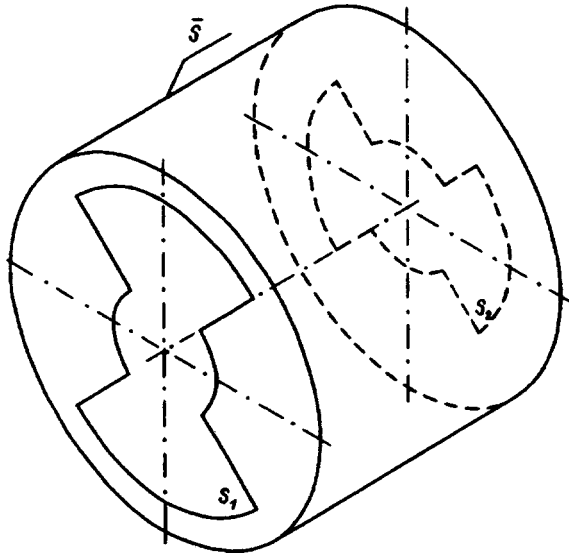


FIG. 3.

even, this group is isomorphous to $S_n\{e, \sigma, \dots, \sigma^{n-1}\}$, where σ is a symmetry transformation of a Euclidean space corresponding to rotation by $2\pi/N$ and reflection in a plane that is orthogonal to the rotation axis. Surfaces of revolution are described, for example, by the C_∞ symmetry group and, therefore, by the C_n group for any n . Regular n -hedrons and the like are also described by the C_n symmetry group. In this case a system of N boundary integral equations (14) is brought into form (15), where, accordingly,

$$A_i = \sum_{j=1}^N A'_{1j} \varepsilon^{N-(j-1)(i-1)} \quad (i=1, 2, \dots, N).$$

Here $\varepsilon = \exp(2\pi i/N)$, i is the unit imaginary number, and $i^2 = -1$. For the operators A'_{1j} we have $A'_{1j} = A_{1j} T^{N-j+1}$

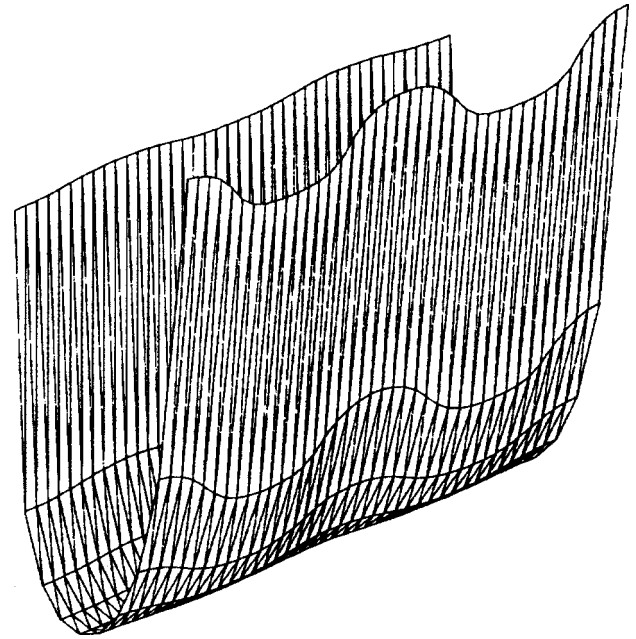


FIG. 5.

($j=1, 2, \dots, N$), where T is a shift operator [$Tu(x) = u(\tau^{-1}x)$ and, accordingly, $T^{N-1}u(x) = u(\tau^{j-1}x)$ ($j=1, 2, \dots, N$)], and $\|A_{ij}\|_{i,j=1}^N$ is the operator matrix of the initial system of integral equations on the surface S .

Furthermore, if the initial surface does not have a symmetry group, but admits supplementation to a surface S with a Klein symmetry group or with the cyclic symmetry group C_n within the reduction method, the solution of the initial problem reduces to the solution of the independent equations presented above and to Eqs. (16), where the set K is specified

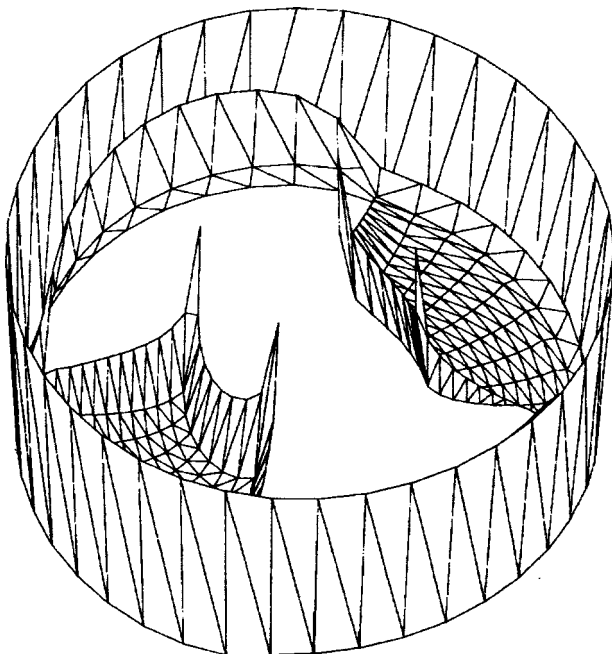


FIG. 4.

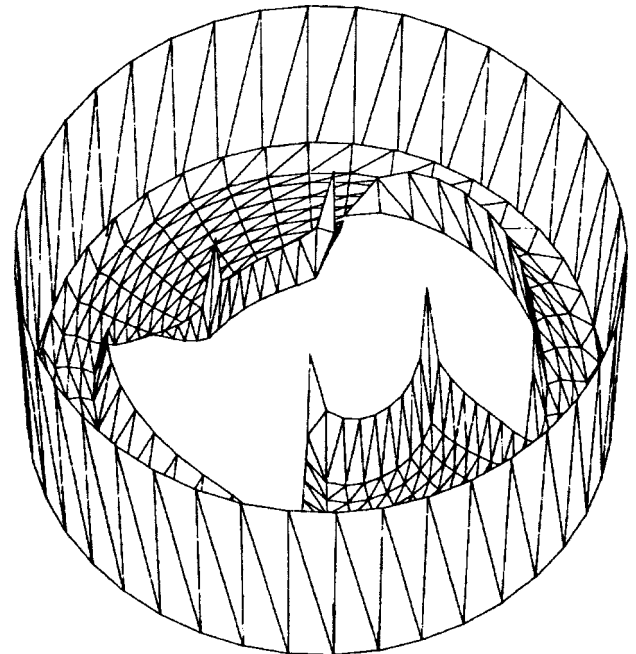


FIG. 6.

by the form of the initial surface \bar{S} and the surface S with a symmetry group.

Figure 3 presents the form of a diaphragm \bar{S} having a Klein symmetry group. At the same time, at the computational level it is significantly more economical to treat it as a surface \bar{S} which admits supplementation to a surface of revolution $S = \bar{S} \cup S_1 \cup S_2$ with the C_∞ symmetry group. Figures 4, 5, and 6 present the distribution of the charge density on the diaphragm (more precisely, of S , since the density equals zero on S_1 and S_2) obtained on the basis of the reduction method. More specifically, Fig. 4 presents the distribution of the charge density on the nearby bottom of the diaphragm, Fig. 6 presents the distribution on the distant bottom, and Fig. 5 presents the distribution of the charge density on the cylindrical surface. An approximate solution was obtained for an order of discretization of the initial boundary equation $M = 3000$.

Fairly simple electron-optical systems, which can be simulated on the basis of the methods in the preceding section, usually have a finite symmetry group or admit supplementation to a surface with symmetry within the reduction method. In the case of electron-optical systems of complex configuration it is usually only individual structural units that have such symmetry.

- ¹D. L. Colton and R. Kress, *Integral Equation Methods in Scattering Theory* [Wiley, New York (1983); Moscow (1987)].
- ²S. K. Demin and R. P. Tarasov, *Zh. Vychisl. Mat. Mat. Fiz.* **29**, 1308 (1989).
- ³E. V. Zakharov, S. I. Safronov, and R. P. Tarasov, *Dokl. Akad. Nauk SSSR* **314**, 589 (1990) [*Sov. Phys. Dokl.* **35**, 799 (1990)].
- ⁴E. V. Zakharov, S. I. Safronov, and R. P. Tarasov, *Zh. Vychisl. Mat. Mat. Fiz.* **30**, 1661 (1990).
- ⁵E. V. Zakharov, S. I. Safronov, and R. P. Tarasov, *Differ. Uravn.* **29**, 1620 (1993).
- ⁶R. P. Tarasov, *Zh. Vychisl. Mat. Mat. Fiz.* **31**, 1515 (1992).
- ⁷R. P. Tarasov, *Zh. Vychisl. Mat. Mat. Fiz.* **33**, 1815 (1993).
- ⁸E. V. Zakharov, S. I. Safronov, and R. P. Tarasov, *Zh. Vychisl. Mat. Mat. Fiz.* **31**, 40 (1992).
- ⁹E. V. Zakharov, S. I. Safronov, and R. P. Tarasov, *Zh. Vychisl. Mat. Mat. Fiz.* **35**, 1582 (1995).
- ¹⁰E. V. Zakharov, S. I. Safronov, and R. P. Tarasov, *Zh. Vychisl. Mat. Mat. Fiz.* **33**, 1030 (1993).
- ¹¹R. P. Tarasov, S. I. Safronov, and S. K. Dyomin, in *Twentieth International Congress on High Speed Photography and Photonics*, Victoria, Canada (1992).
- ¹²J. A. Stratton, *Electromagnetic Theory* [McGraw-Hill, New York (1941); Gostekhizdat, Moscow (1948)].
- ¹³A. G. Vlasov and Yu. A. Shapiro, [in Russian], *Mashinostroenie*, Leningrad (1974).
- ¹⁴S. K. Demin and R. P. Tarasov, *Mat. Model.* **5**(7), 113 (1993).

Translated by P. Shelnitz

Dynamics of the tunneling contact in a tunneling microscope during a pulsed increase in the voltage between the tip and sample

I. A. Dorofeev, V. Ya. Kosyev, and A. A. Petrukhin

Institute of Physics of Microstructures, Russian Academy of Sciences, 603600 Nizhniĭ Novgorod, Russia

(Submitted August 8, 1996)

Zh. Tekh. Fiz. **68**, 104–109 (February 1998)

The current flow regime between the tip and the sample during the supply of voltage pulses of various duration, amplitude, shape, and polarity is investigated experimentally. Solid silver and films of other materials of nanometer thickness are employed as samples. It is shown that the tunneling gap decreases as the voltage across the tunneling contact increases due to deformation of the tip and the sample until they come into mechanical contact. The resistance of the contact is measured for various samples. Various mechanisms of deformation of the tip and the sample are considered. It is concluded on the basis of estimates that solid metals are deformed mainly as a result of thermal expansion. Experimental current–voltage characteristics are compared with theoretical plots for the case of field emission. © 1998 American Institute of Physics. [S1063-7842(98)01802-9]

INTRODUCTION

The investigation of a solid surface by means of a scanning tunneling microscope (STM) calls not only for obtaining the image of the surface in various scanning regimes, but also for analyzing it by tunneling-spectroscopic methods. In this case abundant information is provided by the current–voltage characteristics of the tunneling contact of the microscope. The sweep of the voltage across the contact should clearly be limited to values which do not lead to catastrophic changes in the properties of the surface, unless such changes are the investigator's goal. The value of the limiting voltage corresponding to the appearance of local changes on an STM image depends mainly on the properties of the sample material and the distance between the tip and the surface, which is assigned by the tunneling current I_t and the tunneling voltage U_t . It should be expected that under the condition $eU \geq \phi$, where e , U , and ϕ are, respectively, the electron charge, the voltage applied to the tunneling contact, and the work function, the dependence of the current on the voltage between the STM electrodes should acquire a field-emission form. This is possible, because the electric field between the microscope electrodes reaches values of up to $E = 10^8$ V/cm at such voltages. The high density of the field-emission current corresponding to such fields can be a cause of heating and destruction of both the tunneling microscope tip and the surface being investigated. The electric field produced upon the increase in the voltage across the gap and also the fluctuational electromagnetic field of the heated substance give rise to a ponderomotive interaction in the tunneling contact, which can lead to deformation of the electrode surfaces and induce diffusion processes both on the surface and in the bulk of the material. This set of diverse factors ultimately leads to local alteration of the properties of the sample surface under the STM tip, as has been reported in numerous publications, which were reviewed in Refs. 1–3. Various physical mechanisms have been proposed to account for the

local modification of the surface of a solid, generally on the basis of calculations of the electric field strength and the surface temperature of the tip and the sample.^{4,6} Knowledge of the current flowing in the regime selected is needed in this case. The current flow regime clearly depends on the design features of the electrical circuit of the microscope, the relative arrangement of the tip and the sample, the specific properties of the tip and sample materials, and the shape, amplitude, and duration of the voltage supplied to the tunneling gap. Local influences can be applied to the sample surface when the microscope feedback loop is closed or open; therefore, the character of the current flow is also determined by the dynamics of the changes in the geometric relief and physical properties of the surface. This paper presents the results of an experimental investigation of the dependence of the current flowing between an STM tip and a sample on applied voltages of various amplitude, duration, shape, and polarity.

EXPERIMENTAL CONDITIONS

The experimental setup is presented in Fig. 1. Pulse shaper 1 included a square pulse generator, which permitted variation of the pulse duration in the range 10^{-5} –1 s and of the amplitude up to 10 V with high accuracy, and an integrating circuit with a time constant equal to 10^{-5} s for smoothing the steep edges of the pulses from the generator. The experiments with large loads were carried out using an additional power amplifier, whose output pulse was supplied to tunneling gap 2 of the STM. A special scheme based on a sliding temporal integrator, which produces a linearly increasing voltage from 0 to 10 V on the tunneling gap, was used to create pulses of triangular shape, the sweep time being regulable in the range from 10^{-4} to 10 s. The current flowing was determined using an oscillograph from the signal from the load resistance R_{load} . The measurements were performed in the following manner. The STM tip was posi-

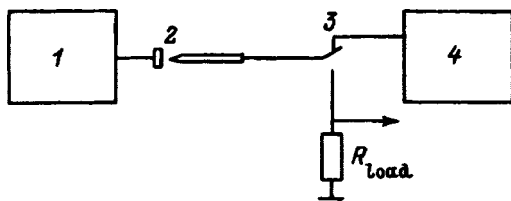


FIG. 1. Experimental setup.

tioned at a definite distance from the sample surface with assigned U_t and I_t , whereupon the feedback circuit was broken with simultaneous recording of the voltage on the Z motor of the microscope and switching of relay 3 from the input of STM preamplifier 4 to the load resistance. Depending on its level, the signal from R_{load} was fed either directly to the input of the storage oscillograph or through an amplifier with a 60 kHz transmission band.

The samples used were solid silver, a chromium film of thickness 500 Å deposited on a polished silicon substrate, and a three-layer carbon-nickel-carbon structure with layer thicknesses equal to 25, 30, and 25 Å, respectively, which was also on a silicon substrate. The films were deposited by laser sputtering in a vacuum, as was done in Ref. 7. Tungsten wire tips, which were fabricated by the standard method of electrochemical etching in a potassium hydroxide solution, were used in the work. The experiments were carried out in air at atmospheric pressure under ordinary laboratory conditions.

EXPERIMENTAL RESULTS

The current flowing depends on the voltage supplied, the resistance of the tunneling gap, and the load resistance. The conductance of the tunneling gap increases with increasing voltage at a fixed distance between the microscope electrodes, i.e., is a variable. For the values selected $U_t=0.1$ V and $I_t=1$ nA, the initial resistance of the tunneling contact R_t is of the order of $10^8 \Omega$. Figure 2 presents the dependence of the amplitude of the signal U_{load} from the load resistance R_{load} during a voltage pulse with a duration of 10^{-3} s and an amplitude of 10 V on the load resistance.

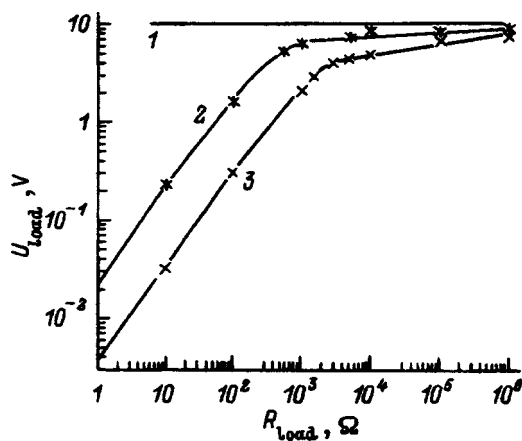


FIG. 2. Dependence of the amplitude of the signal from the load resistance on the value of the latter.

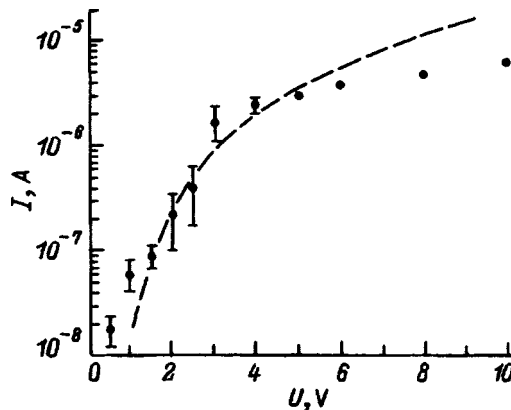


FIG. 3. Dependence of the maximum current I flowing through the tunneling gap on the amplitude of the voltage pulse U . Points—experimental values, dashed line—calculation based on the Fowler-Nordheim formula.

Curve 1 in this figure corresponds to a short-circuited contact between the electrodes, curve 2 was obtained for the chromium film, and curve 3 was obtained for the three-layer carbon-nickel structure with an initial distance between the electrodes corresponding to $U_t=0.1$ V and $I_t=1$ nA. As we see, there is a certain characteristic resistance R^* , which specifies the discontinuity on the curves. All of the voltage clearly falls on the tunneling contact when $R_{load} < R^*$, and the converse is true when $R_{load} > R^*$. Apparently, R^* is the resistance of the tip-sample contact at the end of the pulse. For the chromium film we have $R^* \approx 420 \Omega$, and for the three-layer structure $R^* \approx 2000 \Omega$. Thus, the resistance of the gap varies by 5–6 orders of magnitude during a pulse. We note that the character of the curves and the value of R^* did not vary when pulses of any duration in the range $10^{-5} - 1$ s were used.

The real electrical circuit of the preamplifier of the tunneling microscope used to perform the experiments on the modification of multilayer structures in Refs. 7 and 8 is such that the equivalent resistance $R_{load} = 10^6 \Omega$. The current-voltage characteristic of the tunneling contact formed by the tungsten tip and the three-layer structure for $U_t=0.1$ V and $I_t=1$ nA was recorded with such a value for the load resistance. Figure 3 presents the dependence of the current on the amplitude of the voltage pulse with a duration of 10^{-3} s supplied to the tunneling contact. Each time the measurement was performed after the microscope tip was positioned over a new portion of the surface of the multilayer structure. The statistical spread of the values indicated in the figure corresponds to falling in this range with a 96% probability. As follows from our measurements, at typical voltage pulse amplitudes, at which local modification of the multilayer metal-carbon structure occurs, the maximum current does not exceed 10^{-5} A with the load indicated. Of course, the value of the maximum current increases with decreasing R_{load} as long as $R_{load} > R^*$. In the experiments with solid silver and $R_{load} < 10 \Omega$ spot welding was presumably observed in some cases, since a mechanical contact between the tip and the sample, which could be broken with difficulty by the piezoelectric micropositioners, could be detected after a voltage pulse was supplied and the feedback loop was restored.

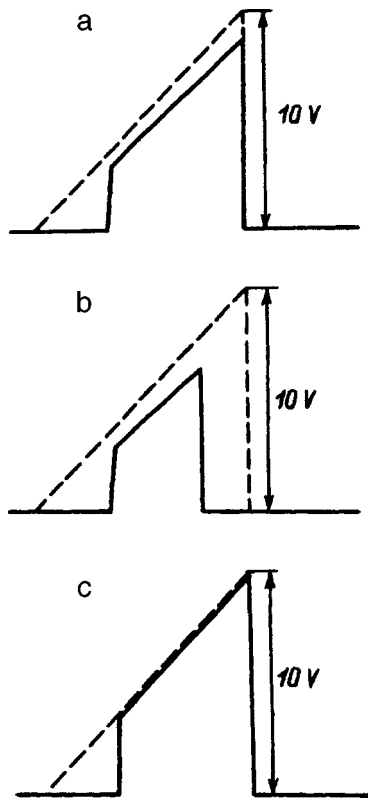


FIG. 4. Oscillograms of the signal from the load resistance.

A similar dependence was recorded during the supply of a triangular pulse to the tunneling gap or a linear sweep of the voltage from 0 to 10 V of various duration. Figure 4 presents oscillograms of the signal from the load resistance (solid line) and the shape of a voltage pulse of duration 10^{-3} s at the output of the pulse shaper (dashed lines) for a relative arrangement of the tip and the sample which corresponds to $U_t = 0.1$ V and $I_t = 1$ nA. The oscillogram in Fig. 4a was obtained in an experiment with the three-layer structure and clearly corresponds completely to the current-voltage characteristic in Fig. 3. In the case of a voltage sweep, there is an abrupt, exponential increase in the current followed by a change in the character of its flow at the end of the sweep. In some cases oscillograms similar to the one in Fig. 4b with a sharp drop in the amplitude of the signal from the load at the end of the sweep were observed and are probably attributable to accidental rebound of the tip from the sample surface. Figure 4c shows the oscillogram of the signal obtained in an experiment with a solid silver sample. We note that the form of the signal from the load resistance did not depend on the duration of the sweep, but the reproducibility was better for short durations. This should be attributed to the smaller probability of random variation of the gap between the tip and the sample during a voltage sweep.

As we have already noted, with consideration of the assigned values of U_t and I_t , the electronic system of the microscope should keep the tip at a definite distance above the sample surface. In a real situation, especially in an experiment in air, there are fluctuations of the current between the microscope electrodes, because of which the scanning tunneling microscope, attempting to maintain the assigned

tunneling current, displaces the tip in a certain range near the mean value of the distance between the tip and the sample. These current fluctuations and the corresponding changes in the voltage on the piezoelectric micropositioner are easily recorded. The causes of such current fluctuations can be associated both with physicochemical processes on the surfaces of the microscope electrodes in the electric field between them and with random modulation of the width of the tunneling gap due to acoustic and temperature noise. At an arbitrary moment in time the operator disrupts the feedback loop of the microscope, recording the random value of the voltage on the piezoelectric micropositioner and, therefore, the random value of the distance of the tip from the surface. Even if the tip is positioned above the same point on the surface with assigned parameters, the measured values will have a certain statistical spread. Contributions to this spread are made by the dynamic changes in the contact associated with heating and deformation of the tip and the sample, as well as with the increase in the rates of diffusive processes due to the increase in the current and the field during the sweep of the voltage across the tunneling gap. The statistical curves described below were obtained in an experiment with the three-layer structure and a square voltage pulse with a duration of 10^{-3} s and a rise time of 10^{-5} s. The maximum signal from the load resistance had the same shape and duration as the voltage pulse. At the same time, as the amplitude of the voltage pulse was diminished, the frequency of the appearance of a signal from the load resistance with a totally different shape and a significantly smaller amplitude increased, the maximum of such a signal on the oscillogram being capable of occupying any position within the duration of the voltage pulse. Figure 5a presents a plot of the appearance of the maximum signal from the load resistance as a function of the amplitude of the voltage pulse on the tunneling gap for $U_t = 0.1$ V and $I_t = 1$ nA. The dependence was obtained by computing the frequency of the appearance of the maximum signal in 100 experiments, the microscope tip being displaced to a new position each time. Figure 5b shows the dependence of the probability of the appearance of the maximum signal from the load on the tunneling voltage U_t for $I_t = 1$ nA and an amplitude of the voltage pulse equal to 10 V.

We specially note that within the statistical spread obtained the results of our experiments with the concrete samples described under the experimental conditions described did not depend on the sign of the voltage pulse supplied to the tunneling gap.

DISCUSSION OF RESULTS

It can be concluded on the basis of the data obtained that closing of the gap between the tip and the sample occurs in the regime characteristic of surface modification, probably because of their thermal expansion and a ponderomotive interaction. Corresponding estimates of the temperature, the thermal strain, and the field-induced strain will be performed, but now we shall estimate the width of the contact on the basis of a measurement of its resistance at the end of a voltage pulse. For the chromium film we have $R^* = 420 \Omega$.

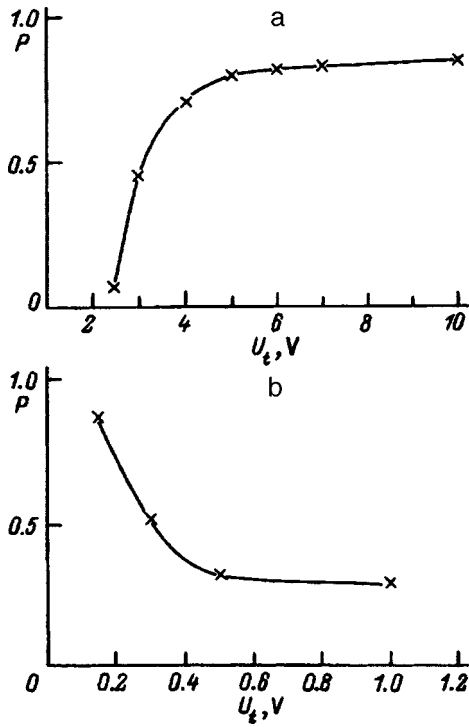


FIG. 5. Dependence of the probability of achieving the maximum value of the signal from the load resistance on the amplitude of the voltage pulse U (a) and on the value of the tunneling voltage for a fixed amplitude of the voltage pulse (b).

The resistance of this film measured by the contact method is equal to $300 \Omega/\text{cm}$. With consideration of the geometric features of the sample holder we find that the resistance of the contact is approximately equal to 270Ω . Assuming that the electron mean free path λ^* in the tip and sample materials is much greater than the width of the contact d , we shall use the expression for the resistance of such a contact obtained by Sharvin and Wexler:^{9,10} $R = 16\rho\lambda^*/\pi d^2$, where $\rho \sim 10^{-6} \Omega \cdot \text{cm}$ is the typical value of the resistivity for metals. Setting $\lambda^* \approx 10^2$, we have $d \approx 14 \text{ \AA}$. We note that closing of the contact occurs after a very short time, apparently on the leading edge of the square pulse.

As the experiments show, the local modification of an extensive list of samples does not depend on the sign of the voltage pulse; therefore, we shall confine ourselves to the case in which the flow of electrons is directed from the tip to the sample. The corresponding estimates of the temperature of the tip apex and the time of the achievement of an assigned value are obtained most simply on the basis of the known solution of the one-dimensional problem.¹¹ As follows from Fig. 3, the maximum current I flowing between the tip and the sample equals $5 \times 10^{-6} \text{ A}$. Since the effective area of current flow $S \approx 10^{-13} - 10^{-14} \text{ cm}^2$, the current density $j \approx 5 \times 10^7 - 5 \times 10^8 \text{ A/cm}^2$. In the initial stage of the heating of a material with the electrical conductivity and thermal conductivity of tungsten, the Joule heating can be neglected. Heating as a result of the Nottingham effect is most efficient for a cold emitter.¹² Assuming that it is a surface effect, we can estimate the corresponding power density $q \approx \pi^2 k T^2 \cot(\pi T/2T_i) I/2eT_i \sin(\pi T/2T_i) S$, where k is

Boltzmann's constant, and T and T_i are the temperature of the emitter and the temperature at which reversal of the sign of the Nottingham effect occurs. For $T = 300 \text{ K}$ and the experimental value $T_i \approx 700 \text{ K}$ we have $q \approx 5.5 \times 10^6 - 5.5 \times 10^7 \text{ W/cm}^2$. The temperature increment is given by $T(t) \approx q(4\kappa t/\pi)^{1/2}/\lambda$, where λ and κ are the thermal conductivity and the thermal diffusivity. For $\lambda = 1.7 \times 10^7 \text{ erg/cm} \cdot \text{s} \cdot \text{deg}$ and $\kappa = 0.65 \text{ cm}^2/\text{s}$ we find that the tip is heated to a temperature of 10^3 K after $t \approx 10^{-9} - 10^{-7} \text{ s}$. We note that the contribution of the Nottingham effect decreases until its sign changes during the heating and that the role of the Joule losses increases; therefore, the exact heating dynamics can be given only by a numerical calculation. However, even a very simple estimate provides evidence that it is possible to heat the material to high temperatures and that if a steady-state temperature is possible at all, it is achieved on the leading edge of the voltages pulses that we used in the experiments. Solving the nonstationary thermal problem for the field of a space with a thermally insulated boundary and a heat source that is constant with time, for example, like the one in Ref. 6, we can find the asymptotic law ($t \rightarrow \infty$) for the achievement of a steady-state temperature on the sample surface under the microscope tip, if it is possible under the specific conditions assigned:

$$T(0,0,t) \approx T_0 + T_s \left(1 - \frac{L_a}{4\sqrt{\pi\kappa t}} \right),$$

where T_0 is the initial temperature, T_s is the steady-state temperature at the same point (for a Joule heat source $T_s \approx j^2 L_a^2 / \lambda \sigma$, and $L_a \approx 10^{-5} \text{ cm}$ is the characteristic dimension of the bulk heat source).

Hence it is seen that the characteristic time for the establishment of a steady-state distribution of the temperature on the sample surface under the microscope tip is of the order of $10^{-7} - 10^{-8} \text{ s}$. The temperature also drops rapidly after the heat source is switched off. The corresponding solution has the form

$$T(0,0,t) = T_s \left[1 - \exp\left(-\frac{L_a^2}{4\kappa t}\right) \right] \Phi\left(\frac{L_a}{\sqrt{4\kappa t}}\right),$$

where Φ is an error function.

We estimate the thermal strain of the tip, assuming that it is a cylinder, which is uniformly heated to the temperature T . For the characteristic value of the coefficient of thermal expansion $\alpha = 10^{-5}$ and $T = 10^3 \text{ K}$, the relative elongation of the tip equals 10^{-2} , which amounts to about 10 \AA of absolute elongation and, accordingly, shortening of the tunneling gap for a tip with a length of 10^3 \AA . The thermal strain of a flat sample surface was estimated in Ref. 6. It is equal in order of magnitude to $(10^{-2} - 10^{-3})L$, where $L \approx 10^3 \text{ \AA}$ is the scale of thermal inhomogeneity. Hence it is seen that the bending of the surface under the tip is of the order of $1 - 10 \text{ \AA}$. Thus, very simple estimates show that thermal heating of the tip and the sample surface to $T \approx 10^2 - 10^3 \text{ K}$ can lead to shortening of the tunneling gap by a few or tens of angstroms to mechanical contact between the microscope electrodes. Shortening of the tunneling gap obviously leads to an in-

crease in current and a further rise in temperature. As a result, the form of the current–voltage characteristic in such a regime will be determined by the thermal-strain instability of the tip and sample surfaces.

Along with thermal strain, ponderomotive forces can also act on the surfaces. These forces are associated with the presence of electromagnetic fields between the electrodes. First, an electric field is induced by a pulsed increase in voltage. Second, at short distances between bodies the effect of the fluctuational electromagnetic field, whose density increases sharply as the surfaces of the bodies are approached, must be taken into account. The strain of a surface can be calculated as the voltage across the tunneling gap increases by determining the Maxwell stress tensor. Strictly speaking, finding the ponderomotive forces acting on the surface of a body requires finding the distribution of field in the space between the electrodes. This calls for solving the self-consistent problem of the distribution of the field in the tip, the sample, and the space between them under the conditions of strong emission in the three-dimensional case. This problem has not yet been solved. Therefore, we shall utilize the results of the solution of the boundary-value problem formulated in Ref. 6. In this case the strain can be estimated using the formula $u_z \approx L_1 j^2 / 10E\sigma^2$, where L_1 is the characteristic dimension of the region where current flows, j is the current density, σ is the conductance of the material, and E is Young's modulus. For $E \approx 10^{12}$ dyn/cm² and $\sigma \approx 10^{16}$ s⁻¹, which are characteristic of solid tungsten, the magnitude of the strain of the surface is negligibly small even under conditions that are typical of the modification of the surface of a solid, where $j \approx 3 \times 10^{17}$ esu and $L_1 \approx 10^{-5} - 10^{-6}$ cm. We note that films of other materials, for example, graphite films, have significantly smaller values for Young's modulus and the conductivity; therefore, their deformation under the action of the field can influence the dynamics of the flow of current between the microscope tip and the sample. We shall estimate the magnitude of the strain under the action of a fluctuational electromagnetic field using the results of the theory of molecular forces of attraction between solids separated by a gap l which is small compared with the wavelengths specifying the absorption spectrum of those solids.¹³ In this approximation we obtain an expression for the attractive force per unit of surface for two identical bodies at the same temperature

$$F(l) = \frac{\hbar}{8\pi^2 l^3} \int_0^\infty \left[\frac{\varepsilon(i\xi) + 1}{\varepsilon(i\xi) - 1} \right]^2 d\xi,$$

where $\varepsilon(i\xi)$ is the dielectric constant, and the variable ξ is related to the frequency ω by the expression $\omega = i\xi$.

Thus, the form of the function $\varepsilon(i\xi)$ must be known in order to calculate the force. For an estimate we set $\varepsilon(\omega) = \varepsilon'(\omega) + i4\pi\sigma/\omega$. Using the Kramers–Kronig formula, we can find $\varepsilon(i\xi)$ and obtain the expression for the force $F(l) \approx \hbar\omega_m/8\pi^2 l^3$, where $\omega_m \approx 10^{13} - 10^{14}$ s⁻¹, in the limit $\sigma \gg \omega$. Knowing the expression for the Green's tensor and the characteristic dimension $L_2 \approx 10^{-5} - 10^{-6}$ of the region where the force F_l is applied, we can easily estimate the magnitude of the strain of the surface $u_z \approx 2F(l)L_2/E$ (Ref.

6). Hence it can be seen that the strain of a surface, for example, of tungsten will be negligibly small when the microscope electrodes are separated by a distance of the order of $l \sim 10^{-7}$ cm.

The experimental data and the estimates obtained show that in a typical surface modification regime the form of the current–voltage characteristics depends on the heating dynamics and the sample; therefore, the current through the tunneling contact rises not only because of an increase in voltage, but also as a result of a decrease in the thickness of the barrier down to mechanical contact between the tip and the sample. This is why a direct comparison of experimental current–voltage characteristics and the theoretical dependences for field emission must be made with consideration of the dynamic changes described. In Fig. 3 the dashed curve corresponds to the Fowler–Nordheim formula for $\phi = 0.2$ eV, $l = 5 \times 10^{-7}$ cm, and an area for current flow S equal to 10^{-14} cm². Clearly, the agreement can be considered satisfactory only in the small range of voltages where the thermal strain can apparently be neglected. The small value of the work function obtained from a comparison of the experimental results with the theoretical dependences, which has been noted frequently in the literature, should be stressed here. A qualitative explanation for its small value can be given on the basis of the phenomenon of the resonant tunneling of electrons through the complex potential relief between the tip and the sample, which includes both potential wells and barriers. As we know,¹⁴ resonance of the barrier transparency to electrons appears in certain regions of their energy spectrum in this case. Such a barrier can be formed by adsorbed atoms, molecules, films, etc. Because the radius of curvature of the microscope tip is nonzero, the barrier between the tip and the sample is nonuniform, and the transparency regions for different groups of electrons can overlap in forming the total current. A comparison of an experimental current–voltage characteristic obtained under such conditions with a theoretical dependence which is valid for one potential barrier in the one-dimensional case gives a low value for the effective work function. The proposed explanation is fully permissible both in the range of small applied voltages, i.e., at $eU_t \ll \phi$, and for $eU_t \gg \phi$.

The statistical character of the flow of current, which is reflected in Fig. 5, can be attributed not only to the factors already indicated, but also to the inhomogeneous distribution of the value of the work function over the sample surface. In fact, between a tip and a sample joined by a conductor to a source U_t there is a contact potential difference, which is determined by the difference between the local work functions of the sample and the tip. The magnitude of the contact potential difference can be of the order of U_t (Ref. 15). Therefore the real potential difference applied to a tunneling gap is equal to the algebraic sum of U_t and the contact potential difference. The values of U_t and the applied voltage assign the distance between the microscope electrodes. This distance can vary over a locally inhomogeneous surface, as is reflected in the form of the current–voltage characteristic and the statistical dependences.

CONCLUSIONS

This paper has presented the results of an experimental investigation of the current flow regime between the sample and the tip of a tunneling microscope when voltage pulses of different duration, amplitude, and polarity are supplied between them. The data obtained and the estimates performed have shown that deformation of the tip and the sample surface can result in mechanical contact between them, whose resistance has been measured experimentally for various objects. The geometric width of the contact has been evaluated in the Sharvin approximation. Various mechanisms for deforming the tip and sample materials have been considered, and it has been shown that the heating of the tip and sample material by the flowing current makes the main contribution in the case of solid metals. A comparison of the experimental current–voltage characteristics with simple theoretical dependences allows us to conclude that satisfactory agreement is possible in a small range of applied voltages for small values of the effective work function. This is apparently attributable to the fact that because of an adsorbate, the potential relief between the microscope electrodes has the form of a set of potential wells and barriers, and resonant transparency of the gap between the microscope electrodes to the electrons emitted is possible as a result. It should be noted that the difference between the experimental and theoretical characteristics is clearly due to dynamic changes in the tunneling contact, which result in a decrease in the distance between the STM electrodes until they come into contact.

We thank D. G. Volgunov and N. N. Salashchenko for their assistance in performing the experiments and discussing the results obtained.

This work was supported by the Russian Fund for Fundamental Research (Grant No. 95-02-03595).

- ¹V. S. Edel'man, *Prib. Tekh. Éksp.* **1**, 24 (1991).
- ²*Scanning Tunneling Microscopy I, II, and III*, H.-J. Güntherodt and R. Wiesendanger (Eds.), Springer-Verlag, Berlin–Heidelberg (1992–1993).
- ³V. V. Vladimirov and A. A. Gryazev, *Vestn. S.-Petersb. Univ.* (1), 24 (1993).
- ⁴V. Khi, K. Lager, R. Moller *et al.*, *Appl. Phys. A: Solids Surf.* **59**, 155 (1994).
- ⁵U. Gratzke and G. Simon, *Phys. Rev. B* **52**, 8535 (1995).
- ⁶I. A. Dorofeev, *Zh. Tekh. Fiz.* **65**(10), 99 (1995) [*Tech. Phys.* **40**, 1031 (1995)].
- ⁷A. D. Akhsakhalyan, S. V. Gaponov, and I. A. Dorofeev *et al.*, *Zh. Tekh. Fiz.* **64**, 144 (1994) [*Tech. Phys.* **39**, 427 (1994)].
- ⁸D. G. Volgunov, I. A. Dorofeev, N. N. Salashchenko, and M. I. Tokman, *Pis'ma Zh. Tekh. Fiz.* **21**(8), 39 (1995) [*Tech. Phys. Lett.* **21**, 601 (1995)].
- ⁹Yu. V. Sharvin, *Zh. Éksp. Teor. Fiz.* **48**, 984 (1965) [*Sov. Phys. JETP* **21**, 655 (1965)].
- ¹⁰G. Wexler, *Proc. Phys. Soc. London* **89**, 927 (1966).
- ¹¹H. S. Carslaw and J. C. Jaeger, *Conduction of Heat in Solids*, Oxford University Press, New York (1959).
- ¹²W. B. Nottingham, *Phys. Rev.* **59**, 907 (1941).
- ¹³M. L. Levin and S. M. Rytov, *Theory of Equilibrium Thermal Fluctuations in Electrodynamics* [in Russian], Nauka, Moscow (1967).
- ¹⁴D. Bohm, *Quantum Theory*, Prentice-Hall, New York (1951); Nauka, Moscow (1965).
- ¹⁵L. N. Dobretsov and M. V. Gomoyunova, *Emission Electronics*, Israel Program for Scientific Translations, Jerusalem (1971).

Translated by P. Shelnitz

Control of the metal–semiconductor phase transition in a vanadium dioxide film with the aid of a fast-acting thermoelectric cooler. III

V. L. Gal'perin, I. A. Khakhaev, F. A. Chudnovskii, and E. B. Shadrin

A. F. Ioffe Physicotechnical Institute, Russian Academy of Sciences, 194021 St. Petersburg, Russia

(Submitted July 17, 1996; resubmitted July 11, 1997)

Zh. Tekh. Fiz. **68**, 110–115 (February 1998)

The pulsed-cooling dynamics of fast-acting thermoelectric coolers is analyzed. Good agreement is obtained between the theory and the experimental results on information erasure with an interference vanadium dioxide structure in the single-pulse and repetitive-pulse modes. It is shown that the actually achievable overwrite frequency with thermoelectric erasure of information is about 30 Hz, and a fast-acting thermoelectric cooler is capable of providing a temperature difference of at least 10 °C between the cold and hot junctions under such conditions.

© 1998 American Institute of Physics. [S1063-7842(98)01902-3]

INTRODUCTION

The optical parameters of thin-film materials with a metal–semiconductor phase transition taken together leave no doubt that such materials hold promise for applications in working optical memory systems. The problem of erasing recorded information is solved by using the thermoelectric cooling effect.¹

Analysis of published data² shows that the speed of operation of such systems still does not exceed 2–3 Hz (with complete erasure of recorded information). However, in “robot eye” type recognition systems employing an on-line optical memory system it is necessary to work in real-time, i.e., with a frequency of 25 Hz, since otherwise the system loses its recognition capability for spatial evolutions of the object of recognition.³

In an earlier work^{4,5} we were able to increase the working frequency of the system from 3 to 10 Hz by producing a fast-acting thermoelectric cooler (FTEC). The present paper is a direct continuation of these investigations. In the present paper, theoretical methods are given for analyzing a fast-acting thermoelectric cooler that controls the process of erasing information from an vanadium dioxide interference structure (VDIS) in single- and repetitive-pulse modes, the theory is compared with experiment and it is shown that the two are in good agreement with each other, and ways are indicated for further increasing the speed of operation of systems of this kind.

PRINCIPLE OF OPERATION OF A FTEC–VDIS SYSTEM

If the VDIS is stabilized at the temperature of the maximum reflectivity difference ΔR_{\max} , then when its surface is locally heated in the process of recording an image the principal branch of the temperature hysteresis loop is traversed up to either complete or partial metallization (depending on the intensity of the heating pulse); after heating stops the principal (or secondary in the case of partial metallization) cooling branch is traversed in the reverse direction down to the stabilization temperature T_{stab} (Fig. 1).

The recorded information is erased by applying a cooling pulse 1–3 (Fig. 1). If the intensity (I) of the pulse is sufficient for complete restoration of the semiconductor state of VDIS (i.e., reaching the value R_s), then the value ΔR_{\max} is obtained once again after the cooling pulse is removed and T_{stab} is reached. However, if the cooling intensity (2,3) is inadequate to reach R_s , then there arises at $T = T_{\text{stab}}$ a low reflectivity difference $\Delta R'$ or $\Delta R''$, i.e., incomplete erasure of the information recorded in the VDIS occurs.

To estimate the quality of erasure we introduce the criterion Q of the quality of erasure of recorded information

$$Q = \frac{R(T_{\text{stab}}) - R_c(T_{\text{stab}})}{R_s(T_{\text{stab}}) - R_c(T_{\text{stab}})},$$

where $0 < Q < 1$, and the functions $R(T)$ have the form presented in Ref. 6.

MEASUREMENT PROCEDURE AND EXPERIMENTAL RESULTS

The experimental arrangement was described in our earlier work.^{4,5} The investigations were performed on two VDIS samples with identical optical characteristics. The samples were deposited on substrates consisting of 40 μm thick mica and 200 μm thick single-crystalline silicon. These samples were secured to the cooled surface of the FTEC, which made it possible to investigate the dependence of the information erasure quality Q on the duration and amplitude of the cooling pulse in the single-pulse mode in the time interval 0.04–1 s and in the repetitive-pulse mode with frequency 0–10 Hz and a off-duty factor of up to 1.2. The temperature of the VDIS was stabilized with an external thermostating system, which was in thermal contact with the hot junctions of the FTEC.

For both samples the measurements were performed in the both the single- and repetitive-pulse modes (the single-pulse mode is the mode in which the interval between the erase pulses is longer than the time constant for establishing thermal equilibrium between the memory cell and the thermostat). In the first case, a test image was recorded in the

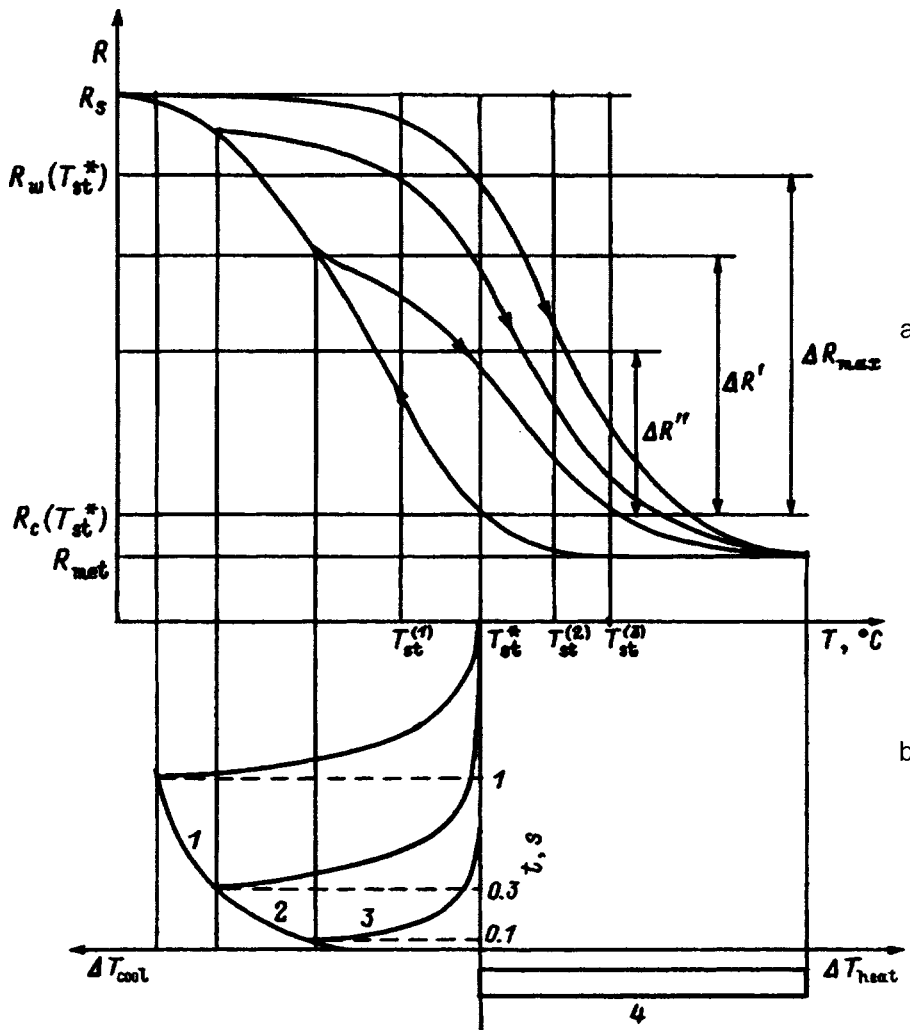


FIG. 1. Reflectivity hysteresis loop of a vanadium dioxide interference structure (a) and the heat pulses controlling it (b). 1-3—Information erasing cooling pulses; 4—information recording heating pulse.

experimental optical memory cell. Next, a cooling pulse was applied and the optical response was registered, after which the system was allowed to come to thermodynamic equilibrium on its own, i.e., it was left undisturbed until the optical response of the cell assumed the value that it had before the information was recorded. In the second case the following operations were performed within each time interval equal to one period of operation of the system: The image was recorded with a 40 ns pulse from a neodymium laser; the recorded image was erased by applying a 0.08 s cooling pulse to the FTEC element; the system was allowed to stand undisturbed for about 0.02 s; and, the cycle was repeated.

The results of the measurements of Q versus the cooling pulse duration in the single-pulse mode for mica (a) and silicon (b) substrates are presented in Fig. 2. We note that the erasure quality for the thicker silicon substrate is less than 1 for all experimental cooling pulse durations, while for a thin mica substrate virtually complete erasure was observed for durations longer than 0.1 s.

Without doubt, this difference is due to the high specific heat of the thick silicon substrate, in contrast to the thin microsubstrate whose temperature evolves identically to that of the cold junction of the FTEC. To a high degree of certainty, it can be asserted that when the erase pulse ends in the

single-pulse mode the temperature of both the "hot" and "cold" junctions of the FTEC with the sample secured on it equals the thermostat temperature. This requires a definite, though short, time interval determined by the thermal conductivity of the material of the thermocouple branches, the presence of a nonzero thermal resistance between the "hot" junction and the thermostat, as well as a lag of heat propagation into the thermostat.

Figure 3 shows curves of the intensity of the optical signal probing the memory cell for different duration but constant amplitude of the cooling pulse current in the case of the thin mica sample. As is obvious from this figure, shortening the cooling duration decreases the maximum achievable reflectivity difference of the VDIS, and the quality of erasure of the information recorded on the VDIS decreases.

The problem of reaching, over short time intervals determined by the duration of the cooling pulse in the single- and repetitive-pulse modes, the temperature differences required for high-quality information erasure and the problem of finding the corresponding optimal current characteristics required a theoretical analysis of the nonstationary thermal processes occurring in the thermocouples. The next section is devoted to a discussion of the results.

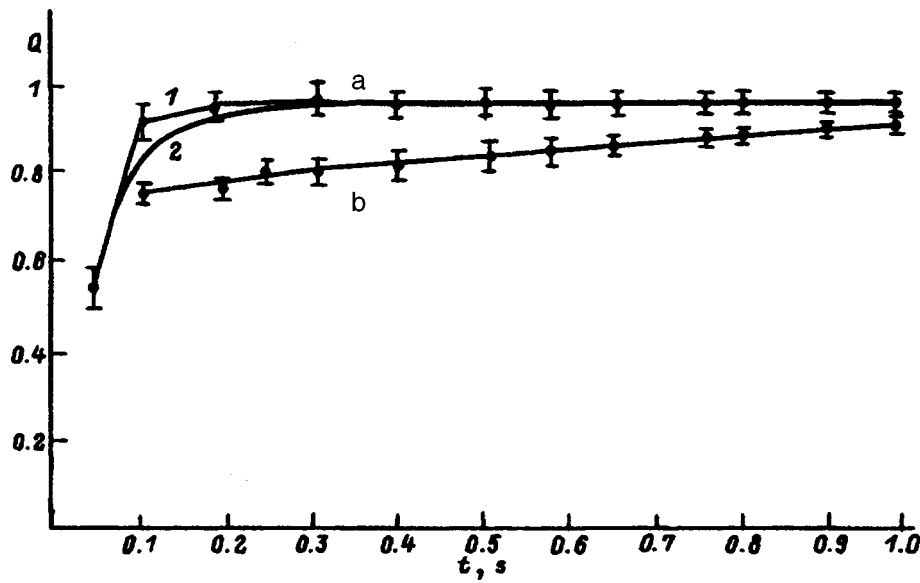


FIG. 2. Information erasure quality versus cooling pulse duration in the single-pulse mode. 1—Experiment, 2—theory; a—40 μm thick mica substrate, b—200 μm thick silicon substrate.

COMPUTATIONAL RESULTS

1. *Single-pulse mode.* In Ref. 7 analytical expressions were obtained for calculating the maximum temperature differences ΔT_{\max} between the ‘‘cold’’ and ‘‘hot’’ junctions of a thermocouple as well as the currents I_{p0} required for this for different supply pulse durations τ_p

$$\Delta T_{\max} = \Delta T_{\max} \sqrt{\frac{\tau_p}{\tau_0}}, \tag{1}$$

$$I_{u0} = I_0 \sqrt{\frac{\tau_0}{\tau_p}}, \tag{2}$$

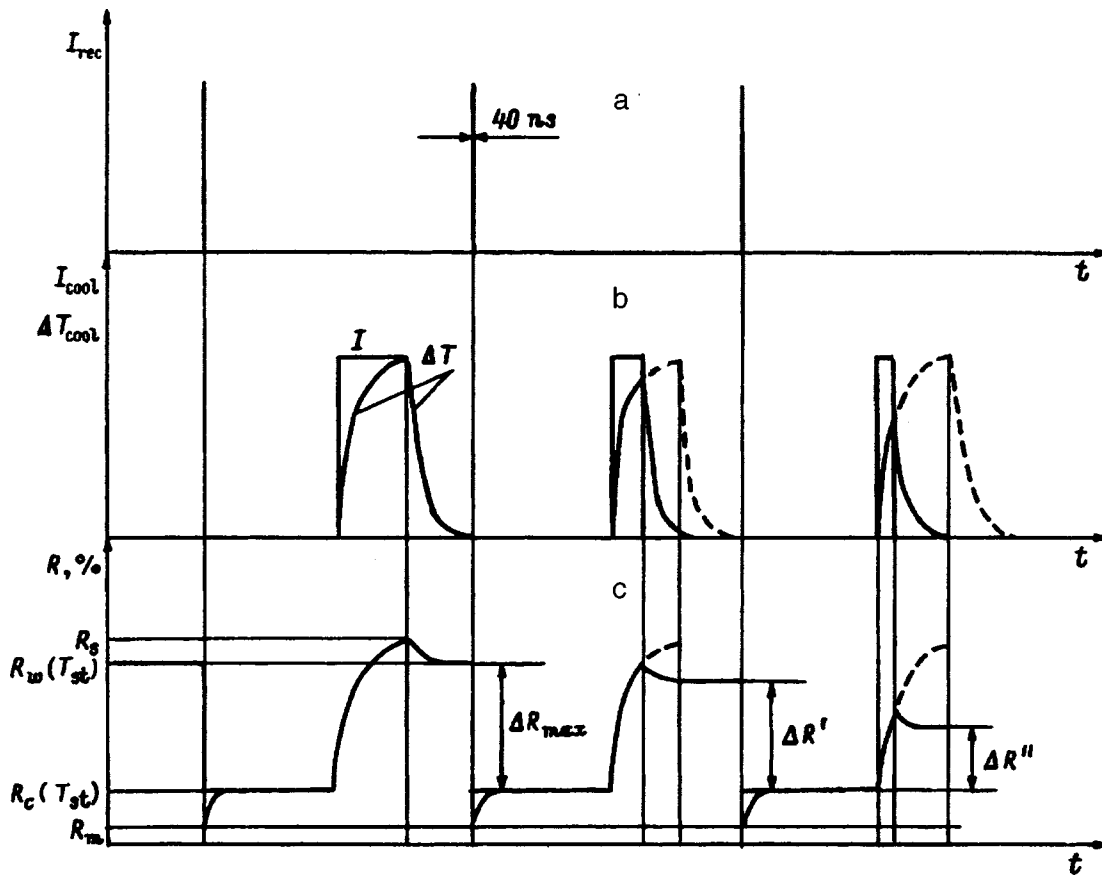


FIG. 3. Relative position of the pulses on the time scale. a—Recording pulses; b—FTEC supply current pulses and cooling pulses; c—VDIS reflectivity changes corresponding to the cooling pulses.

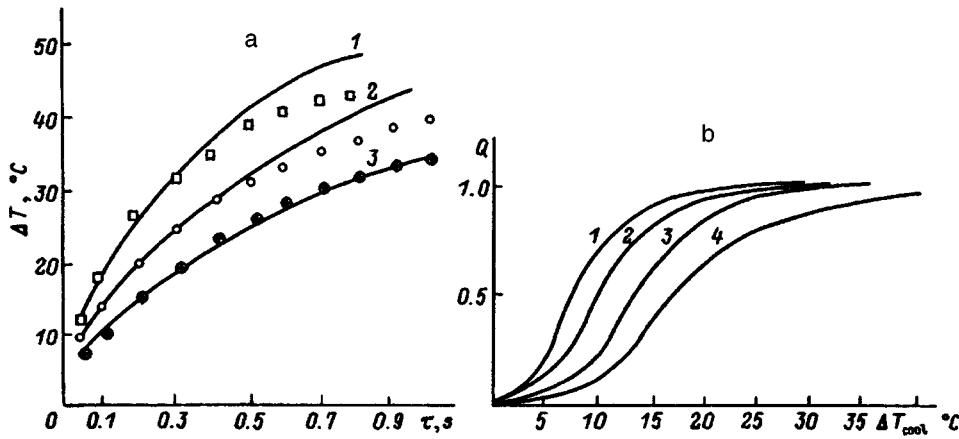


FIG. 4. Temperature difference on the cold junction of FTEC versus the duration of the supply current pulses for different heights of the thermocouple branches (a) and theoretical erasure quality versus cooling degree ΔT for different VDIS stabilization temperatures (b). a: Symbols—experiment, curves—theory; h , mm: 1—1, 2—2, 3—3; b: 1— $T_{st}^{(1)}$, 2— $T_{st}^{(*)}$, 3— $T_{st}^{(2)}$, 4— $T_{st}^{(3)}$.

where ΔT_{max} is the maximum difference of the temperatures on the thermocouple in the stationary state, τ_0 time constant of the thermocouple, and I_0 is the optimal current of the thermocouple in the stationary state.

The maximum temperature difference ΔT_{max} and the optimal current I_0 are universal characteristics of a thermocouple in the stationary state and, as a rule, are known. The time constant τ_0 determines the rate of establishment of the stationary state and depends on the characteristic specific heat of the thermocouple, the specific heat of the object being cooled, and the conditions of heat exchange with the surrounding medium. The quantity τ_0 can be found by a computational method.⁸ In the cases when this is difficult to do, τ_0 can be found experimentally. Given the amplitude ΔT_{max} and duration τ_p of the erase pulse, the required thermocouple parameters and optimal current can be determined. Conversely, for a specific thermocouple the maximum achievable temperature difference can be determined for a prescribed supply pulse duration τ_p . For example, for $\Delta T_{max}=70$ °C and $\tau_0=1$ s the value $\Delta T_{max}=10$ °C can be attained with $\tau_p=20$ ms and current $I_0=30$ A.

The pulsed cooling dynamics for one of the junctions of a thermocouple as a function of the amplitude I_0 of the cooling pulse of the supply current is described by the formula

$$\Delta T_p(\tau) = \Delta T_{max}(2I\tau_p/I_0\tau_0I^2\tau_{p3/2}/I_0\tau_0). \quad (3)$$

2. Repetitive-pulse mode. The repetitive-pulse operating mode differs substantially from the single-pulse mode, since there is not enough time in the intervals between the cooling pulses for the system to return to the initial thermal state. Two opposite cases are possible: a) Heat removal from the hot junctions of the FTEC is ideal, i.e., the temperature of these junctions is constant for any admissible currents flowing through the thermocouple; in this case, since the transition to the repetitive-pulse mode (with no changes in the parameters of the erase pulses) is inevitably accompanied by the appearance of a constant component of the cooling current, the average temperature of the working surface of the FTEC decreases and the VDIS is driven out of the temperature-hysteresis loop in the direction of low temperatures, i.e., it becomes incapable of storing information. b) Heat removal is limited. In this case there is not enough time for the heat released each second, $I_0^2R\tau_p f$ (f is the number of

pulses per second), to be dissipated over the total time of the intervals between the pulses. This results in substantial overheating of the system and a corresponding change in the stabilization temperature of the VDIS, which once again becomes incapable of recording information, since it is driven out of the temperature hysteresis loop, but this time in the direction of high temperatures.

In summary, to ensure a high information erasure quality it is necessary to choose an optimal (for each frequency) amplitude of the current of the cooling pulses and optimal conditions of heat removal that give the maximum possible temperature differences between the cold and hot junctions of the FTEC while preserving the stabilization temperature of the VDIS.

The equations (2) and (3) make it possible to solve this problem and obtain an expression for the optimal current I_f and the maximum temperature difference ΔT_f in the repetitive-pulse mode

$$I_f = I_0 \sqrt{\frac{\tau_0}{\tau_p f}}, \quad (4)$$

$$\Delta T_f = \Delta T_{max}^{single} (2/\sqrt{f} - 1/f). \quad (5)$$

Specifically, using the same conditions of heat removal into the surrounding medium when switching to the repetitive-pulse mode as in the single-pulse mode and only optimizing the amplitude of the cooling pulse, it is possible to attain with a frequency of 25 Hz a temperature difference $\Delta T_f=4.5$ °C with a current $I_f=5$ A with no change in the stabilization temperature of the VDIS. However, if the heat-exchanger temperature is lowered, then $\Delta T_{max}=13$ °C can be obtained by increasing the amplitude of the erasing current pulse. This temperature difference is sufficient for achieving information erasure quality Q the order of 0.92–0.94 operating with a VDIS with a small slope of the cooling branch of the temperature-hysteresis loop. At the modern level of technological development synthesis of such VDISs does not present any difficulties.²

COMPARISON OF THEORY WITH EXPERIMENT

To compare the proposed theory with experiment, we performed measurements of the temperature difference be-

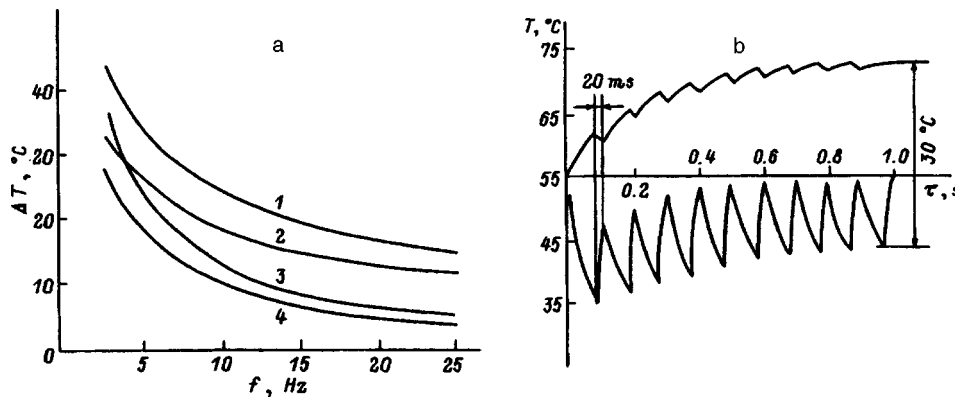


FIG. 5. Theoretical curves of the temperature difference on the cooled surface of the FTEC versus the supply pulse repetition frequency (a) and diagram of the temporal variation of the temperatures of the cold and hot junctions of FTEC in the repetitive-pulse mode (b). 1,2—Optimal currents; 3,4—nonoptimal current; h, m : 1,3—1; 2,4—2.

tween the cold and thermostatted surfaces of the FTEC as a function of the supply pulse duration [i.e., the function $\Delta T(\tau_p)$] with 1 and 2 mm high thermocouple branches for the optimal (for each pulse duration) amplitude of the supply current pulse and the temperature of the heat releasing surface of the FTEC equal to 60 °C (Fig. 4a). In these experiments the temperature of the cold surface of the FTEC was measured with a quick-response thermocouple. Figure 4b demonstrates good agreement between the computational results and the experimental data.

We note that in studying the operation of the system FTEC+VDIS we used a thermocouple with a working area of $12 \times 14 \text{ mm}^2$ and a branch height $h = 2 \text{ mm}$. Figure 2 shows both the experimental and computed curves of the information erasure quality Q versus the duration of the supply pulse of the FTEC in the single-pulse mode. The calculations were performed on the basis of the results presented in Fig. 4b, which in turn were obtained by analyzing the shape of the temperature-hysteresis loop of the reflectivity of the VDIS. Figure 2 shows that the experimentally obtained values of the information erasure quality agree, to within the limits of error, with the computed values for the hysteresis loop of the experimental sample (Fig. 1). The experiment was performed with a VDIS stabilization temperature of 52 °C. It should be noted that the stabilization temperature has a large effect on the dependence of the erasure quality factor on the magnitude of the cooling pulse (Fig. 4b).

The data obtained make it possible to predict the expected information erasure quality as a function of the erase pulse duration and to determine the minimum possible working duration of the erase pulse.

Figure 5a shows the temperature differences versus the repetition frequency of the erase pulses ($\tau_p = 0.8/f$) when operating in the repetitive-pulse mode. The curves 3 and 4 in Fig. 5a were calculated according to Eq. (5). It is evident from these curves that it is impossible to obtain the temperature differences required for high-quality information erasure with working frequencies of 20–25 Hz by preventing heating of the system solely by lowering the amplitude of the supply pulses. However, as one can see from curves 1 and 2 in Fig. 5a, if the amplitude of the supply pulses in the repetitive-pulse mode is close to a value corresponding to the optimal value in the single-pulse mode and at the same time over-

heating of the system is prevented by lowering the thermostat temperature, then high erasure quality can be obtained at these frequencies for samples with a 10–12 °C wide hysteresis loop. This is especially easy to do for 1 mm high thermocouples.

We obtained the experimental value $Q = 0.7$ when working at a frequency of 10 Hz (and with erase pulse duration 80 ms). The computed value, calculated by the method described above, was equal to $Q = 0.66$.

Figure 5b shows the character of the variation of the temperatures of the cold and hot junctions of the FTEC in the repetitive-pulse mode with $f = 10 \text{ Hz}$ (erase pulse duration 80 ms). The exponential drift of the midpoint of the full amplitude of the temperature oscillations and the maximum value of the temperature of the cold junction (i.e., the stabilization temperature of VDIS) as well as its asymptotic approach to a new stationary value are clearly seen in this figure.

CONCLUSIONS

1. The dynamics of pulsed cooling processes in fast-acting thermoelectric coolers was analyzed.
2. It was shown that the theoretical expressions obtained are in good agreement with the experimental results on information erasure from a vanadium dioxide interference structure in the single- and repetitive-pulse modes.
3. It was determined that the 10 Hz overwrite frequency obtained is not the maximum possible value and an overwrite frequency of 25–30 Hz can actually be attained with the current level of development of the technology for synthesizing VDISs. In addition, the FTEC gives in this mode a temperature difference of at least 10 °C.

¹F. A. Chudnovskii, *Sov. Phys. Tech. Phys.* **20**, 999 (1978).

²A. A. Bugaev, B. P. Zakharchenya, and F. A. Chudnovskii, *Metal-Semiconductor Phase Transition and Its Applications* [in Russian], Nauka, Leningrad.

³E. A. Antonov, *Optical Holography: Practical Applications* [in Russian], Sov. Radio, Moscow, 1978.

⁴V. L. Gal'perin, I. A. Khakhaev, F. A. Chudnovskii, and E. B. Shadrin, *Zh. Tekh. Fiz.* **61**(10), 194 (1991) [*Sov. Phys. Tech. Phys.* **36**, 1190 (1991)].

⁵V. L. Gal'perin, I. A. Khakhaev, F. A. Chudnovskii, and E. B. Shadrin,

Pis'ma Zh. Tekh. Fiz. **18**(10), 74 (1992) [Sov. Tech. Phys. Lett. **18**, 329 (1992)].
⁶I. A. Khakhaev, F. A. Chudnovskii, and E. B. Shadrin, Fiz. Tverd. Tela (St. Petersburg) **36**, 1643 (1994) [Phys. Solid State **36**, 898 (1994)].
⁷V. L. Galperin, in *Fourteenth International Conference on Thermoelec-*

trics, St. Petersburg, 1995, pp. 446–448.
⁸M. A. Kaganov and M. R. Privin, *Thermoelectric Heat Pumps* [in Russian], Energiya, Leningrad, 1970.

Translated by M. E. Alferieff

On the character of the destruction of a copper foil by intense x-ray irradiation

V. K. Golubev, K. G. Rabinovich, and A. K. Chernyshev

*Russian Federal Nuclear Center, All-Russia Scientific-Research Institute of Experimental Physics,
607190 Sarov, Nizhegorod District, Russia*

(Submitted September 25, 1996; resubmitted February 10, 1997)

Zh. Tekh. Fiz. **68**, 116–117 (February 1998)

The character of the destruction of copper foil by x-rays produced by a nuclear explosion is investigated. Results on the removal of material from the front surface and on spallation fracture are obtained. The latter results are compared with those obtained under different loading conditions. © 1998 American Institute of Physics. [S1063-7842(98)02002-9]

The critical conditions of macroscopic spallation fracture of copper foil were determined under conditions of nearly uniform¹ volume absorption and surface^{2,3} absorption of electromagnetic radiation. The range of mechanical load durations realized in these cases (10^{-8} – 10^{-7} s) was investigated for copper under purely mechanical shock loading.⁴ Different conditions of loading of copper foil obtain when foil is irradiated with an intense flux of x-rays from a nuclear explosion.⁵ Volume heating of the sample in this case is strongly nonuniform. Some material on the front surface vaporizes and melts, whereas on the back surface the heating temperature remains far below the melting point. In the present paper we studied the problem of determining the character of the destruction of copper foil under such unique loading conditions.

Samples in the form of disks 14 mm in diameter were cut from a 0.56 mm thick foil sheet and placed in appropriate holders–casings in a manner so that the front surface faced the nuclear explosion and the back surface was supported by a layer of low-density foam plastic. The casings with the samples were positioned at two distances from the source of radiation, two casings for each marker. In the first case the surface density of the total energy flux in the x-ray pulse was chosen from the conditions of possible complete destruction of the sample and was equal to 9.0 MJ/m^2 . In the second case the surface energy flux density was equal to 2.9 MJ/m^2 . The absorbed-energy profiles over the thickness of the samples were determined by a computational method. The cross sections of the interaction of the radiation with the sample material which are required for the calculations were taken from Ref. 6.

After irradiation, the casings containing the tested samples were examined visually. The samples located at the first marker were strongly fractured and dispersed. Individual sections of the copper layer, not more than 0.05 mm thick, remained on the foam-plastic substrate. The samples located at the second marker remained largely undamaged, making a more detailed analysis possible. In performing a metallographic analysis of the samples the characteristic features of their were examined with magnification up to $\times 500$. The measurements showed that material was removed from the front surface to a depth of about 0.11 mm and the macroscopic spallation fracture occurred at a distance of about 0.03

mm from the back surface. The nonuniformity of energy release at these coordinates was characterized by the values 4.80 and 0.14 MJ/(kg·mm), whereas on the front surface it had the value 1.64 J/(kg·mm).

The duration of the x-ray pulse was much shorter than the transit time of an acoustic wave over the thickness of the sample so that the x-ray pulse duration could be neglected in an initial analysis of the physicomechanical phenomena occurring under a load. The properties of copper which are required for such an analysis were taken from Ref. 7. According to the estimates made, the absorbed energy 450 kJ/kg required for the copper to start melting was realized at a depth of 0.10 mm in the undamaged sample at the second marker and the energy 660 kJ/kg required for complete melting was realized at a depth of 0.07 mm. The estimates made also showed that at the location of the macroscopic spallation fracture the maximum negative pressure could reach a value of 6.5 GPa over a time of 1.5×10^{-8} s and the copper temperature at this location was equal to 170 °C.

The result obtained on the removal of material from the front surface of the samples indicates that in the case at hand the removal depth is characterized mainly by the absorbed energy corresponding to the solidus point for copper. The conditions required for spallation of the removed layer are produced by a quite intense wave of fracture arriving from the front surface. The results on spallation fracture of copper agree well with the results obtained under different loading conditions. Thus, under conditions close to uniform heating¹ the characteristic loading time of 1.5×10^{-6} s corresponds to a critical negative pressure of 5.5 GPa and the estimated temperature of the sample equals 670 °C. In the case of surface absorption of the pulsed laser radiation^{2,3} a copper foil thickness of 0.56 mm corresponds to a 0.04 mm thick spalled layer. The maximum negative pressure at the location of spallation reaches 6.0 GPa here. Under shock loading⁴ a critical negative pressure 6.7 GPa corresponds to a characteristic loading time of 1.5×10^{-8} s. It can be concluded from an analysis of all results taken together that for the indicated characteristic load time heating copper up to a temperature of the order of 700 °C decreases the critical fracture load by 8–18%. This decrease reaches 45% when the characteristic load time increases by two orders of magnitude,⁸

i.e., the loading time and the temperature have a combined effect on the spallation fracture process.

In closing, we thank N. A. Yukina for performing the metallographic analysis of the samples.

¹I. P. Borin, V. I. Lagutin, E. K. Bonyushkin *et al.*, *Vopr. At. Nauki Tekh. Ser. Impul's. Reaktory Prost. Krit. Sborniki*, No. 1, 40 (1985).

²S. Eliezer, I. Gilath, and T. Bar-Noy, *J. Appl. Phys.* **67**, 715 (1990).

³M. Boustie and F. Cottet, *J. Appl. Phys.* **69**, 7533 (1991).

⁴S. A. Novikov, A. P. Pogorelov, and V. A. Sinitsyn, *Prikl. Mekh. Tekh. Fiz.*, No. 3, 136 (1983).

⁵V. K. Golubev, K. G. Rabinovich, A. K. Chernyshev, and N. A. Yukina, in *Abstracts of Reports at the International Conference "4th Zababakhinskii Lectures"* [in Russian], Russian Federal Nuclear Center, All-Russian Scientific-Research Institute of Theoretical Physics, 1995, pp. 199-200.

⁶E. Strom and Kh. Israël', *Gamma-Ray Interaction Cross Sections (For Energies from 0.001 to 1000 MeV and Elements from 1 to 100)* [in Russian], Atomizdat, Moscow, 1973.

⁷I. K. Kikoin (Ed.), *Tables of Physical Quantities* [in Russian], Atomizdat, Moscow, 1976.

⁸V. K. Golubev, S. A. Novikov, Yu. S. Sobolev, and N. A. Yukina, *Problemy Prochnosti*, No. 1, 63 (1985).

Translated by M. E. Alferieff

Adsorption sensitivity of Si–electrolyte and Si–porous-Si–electrolyte systems

V. M. Demidovich, G. B. Demidovich, V. R. Karib'yants, and S. N. Kozlov

M. V. Lomonosov Moscow State University, 119899 Moscow, Russia

(Submitted June 8, 1996; resubmitted February 3, 1997)

Zh. Tekh. Fiz. **68**, 118–121 (February 1998)

The adsorption sensitivities of silicon–electrolyte and silicon–porous-silicon–electrolyte systems with respect to organic molecules of different types are compared. It is shown that an additional nanoporous layer on the silicon surface does not improve appreciably the adsorption sensitivity of the silicon–electrolyte system, but it does make it possible in principle to increase the selectivity of this system. © 1998 American Institute of Physics.
[S1063-7842(98)02102-3]

1. INTRODUCTION

Chemical sensors (CSs) based on semiconductor–electrolyte systems are very promising for monitoring pH and detecting different ionic and molecular impurities in liquid media. However, up to now investigations directed toward the development of CSs based on the semiconductor–electrolyte systems have been mainly limited to the detection of different ions or very complicated biological macromolecules.^{1,2} In systems intended for detection in liquid media the “intermediate link” between simple ions and biomacromolecules are organic molecules, such as, for example, different phenols, quinones, amines, and so on. The sensor possibilities of a new semiconductor material with an enormous specific surface area (hundreds m²/g)—porous silicon (PS)—likewise have not been adequately ascertained.

Earlier, we showed that information about the simultaneous presence of donor and acceptor impurities in an electrolytic solution can be obtained from the electrophysical characteristics of the Ge–alcohol electrolyte interface, and we proposed methods for controlling the adsorption sensitivity of this system.^{3,4} In the present paper, we examine and compare the sensor possibilities of Si–electrolyte and Si–porous-Si–electrolyte systems.

2. EXPERIMENTAL PROCEDURE

The measurements were performed on *p*-silicon single crystals with resistivity $\sim 1 \Omega \cdot \text{cm}$. The crystals were pretreated in a HF-based etchant and also on *p*-Si–PS structures. Porous silicon layers of the order of 1 μm thick were produced on a *p*-Si surface by anodization in a 24% HF solution (the anodic current density was varied in the range 1–40 mA/cm²). The layers obtained under these anodization conditions possess a porosity of 60–70% and are characterized by a narrow pore-diameter distribution (from 2 to 5 nm) with a maximum in the region 3–4 nm.⁵

The potential φ_e of the semiconductor electrode was measured relative to a large-surface platinum reference electrode, which also served as a field electrode. The voltage on the electrode was varied with frequency 0.005 Hz and the differential capacitance C_s of the semiconductor–electrolyte interface was recorded. The measurements of the differential

capacitance were performed by a pulse method. The duration of the charging pulse was equal to 40 μs , the current density in the pulse did not exceed 50 $\mu\text{A}/\text{cm}^2$, and the repetition frequency of the charging pulses was equal to 10 Hz. The current–voltage characteristics (IVCs) of the semiconductor–electrolyte interface were also measured.

The electrolyte consisted of centinormal solutions of KBr in distilled water and ethanol. The adsorbates consisted of parabenzoquinone (BQ), diphenylamine (DPA), alizarin, polyethylene glycol (PEG-400), and the commercially produced nonionogenic surfactant (SUR)—tremoctyl polyethylene glycol monoester (Triton-X-100). All measurements were performed at room temperature.

3. RESULTS AND DISCUSSION

Figure 1 displays the IVCs of Si–electrolyte and Si–porous-Si–electrolyte systems for alcohol and water electrolytes.¹⁾ One can see that in the experimental range of electrode potentials the density of the current flowing through the semiconductor–water electrolyte interface is appreciably higher than in the case of the alcohol electrolyte. This is due to the more intense electrochemical oxidation (and, correspondingly, reduction) of the silicon in the water electrolyte.⁶ It is interesting to note that the IVCs of the semiconductor–electrolyte systems for single-crystalline and porous silicon are virtually identical, despite the fact that the true surface area of the interface between the phases is much larger in the second case. Apparently, because of the low free charge-carrier density in the walls of the porous framework, the current through the Si–PS–electrolyte interface flowed mainly near the “bottoms” of the pores, whose total surface area, taking account of the roughness of the interface between the silicon and PS, does not differ much from the surface area of the initial silicon. The data on the differential capacitance also attest to this: The lowest measured values of C_s for Si–electrolyte and Si–PS–electrolyte systems were, as a rule, virtually identical and differed by a factor of 2–3 only in separate cases (Figs. 2–5).

The curves $C_s(\varphi_e)$ for Si–alcohol electrolyte and Si–PS–alcohol electrolyte systems in the initial state and after the addition of BQ, whose molecules exhibit electron-

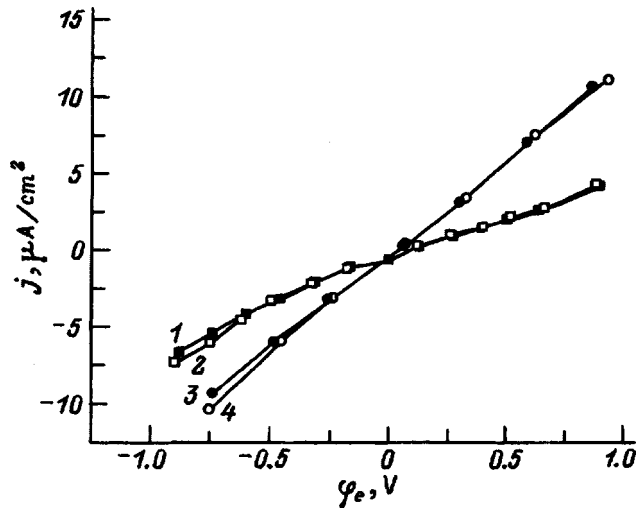


FIG. 1. Current-voltage characteristics of the systems Si-electrolyte (1,3) and Si-PS-electrolyte (2,4) in ethanol-based (1,2) and water-based (3,4) electrolytes.

acceptor properties,^{3,4} are displayed in Fig. 2. One can see that in the case of single-crystalline Si adding a small quantity of BQ (10 μ mole/liter) to the electrolytic solution decreases the slope of the curve $C_s(\varphi_e)$; this decrease is due to the appearance of the electronic states at the silicon surface. These surface states do not contribute to the capacitance measured by the pulse method (i.e., they are “slow”), but they do lead to partial pinning of the Fermi level. The accep-

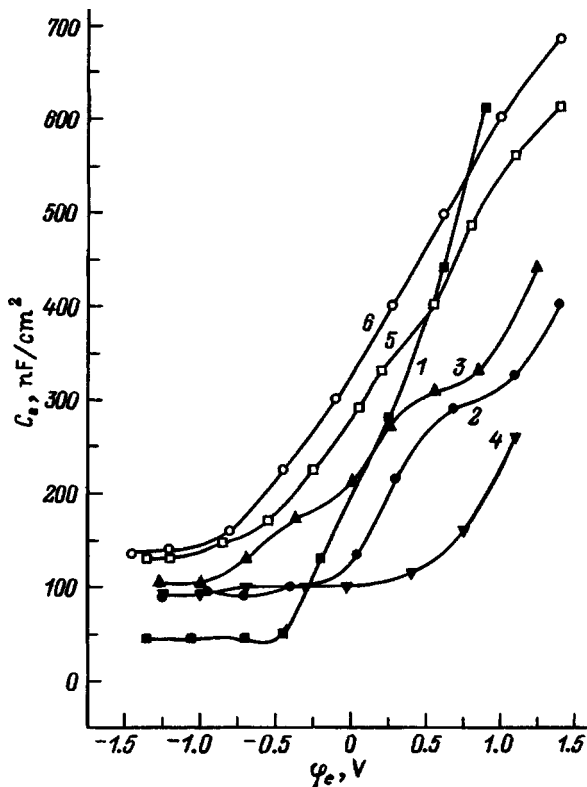


FIG. 2. Curves of the differential capacitance of the systems Si-alcohol electrolyte (1-4) and Si-PS-alcohol electrolyte (5,6) versus the electrode potential. 1,5—Initial state; 2—after addition of 10 m mole/liter of BQ into the electrolyte; 3,6—0.2 m mole/liter; 4—0.2 m mole/liter DPA.

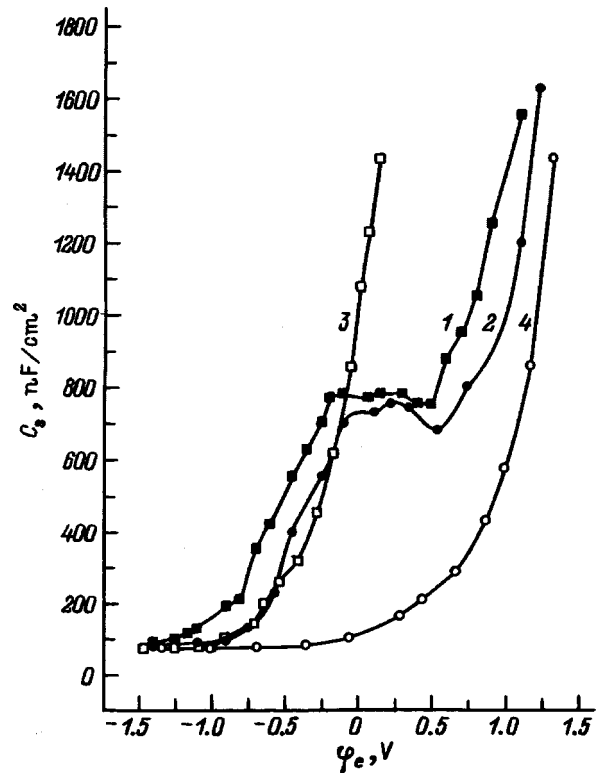


FIG. 3. Curves of the differential capacitance versus electrode potential for the systems Si-water electrolyte (1,2) and Si-PS-water electrolyte (3,4). 1,3—Initial state; 2,4—after addition of alizarin to the electrolyte. The alizarin concentration equals 0.2 mmole/liter.

tor character of these states is clearly manifested as an increase in the concentration of the BQ in solution up to 0.2 m mole/liter; the entire curve $C_s(\varphi_e)$ shifts into the cathode region by $\Delta\varphi_e \approx 0.3-0.4$ eV (compare curves 2 and 3 in Fig. 2). The density of the electronic states that arise with the adsorption of BQ can be estimated if it is assumed that a charge equal to the electron charge is transferred to a BQ molecule which is a constituent of the donor-acceptor complex and it is also assumed that the specific capacitance of the Helmholtz layer $C_H = 20 \mu\text{F}/\text{cm}^2$ (Ref. 7): $N_{ss} \approx C_H \Delta\varphi_e / q \approx 5 \times 10^{13} \text{ cm}^{-2}$.

The adsorption of BQ molecules from an alcohol electrolyte onto the Si-PS structure causes the curve $C_s(\varphi_e)$ to shift into the region of negative electrode potentials; for the same BQ concentration in solution (0.2 μ mole/liter) the magnitude of the shift ($\Delta\varphi_e \approx 0.2-0.25$ V) is approximately the same as for silicon without a porous layer. The absence of a change in the form of the function $C_s(\varphi_e)$ as a result of the adsorption of BQ apparently shows that the rate of the electronic exchange between the adsorption states and the volume of the semiconductor is slower in a silicon-PS-electrolyte system than in the silicon-electrolyte system (there is not enough time for the surface states to be recharged during the measurements of the voltage on the field electrode). This is also indicated by the fact that the equilibrium charge is established more slowly on the surface of the semiconductor with a porous layer than for single-crystalline Si. For the silicon-PS-electrolyte system a stationary dependence $C_g(\varphi_e)$ was established in 15-20 h after adsorbate

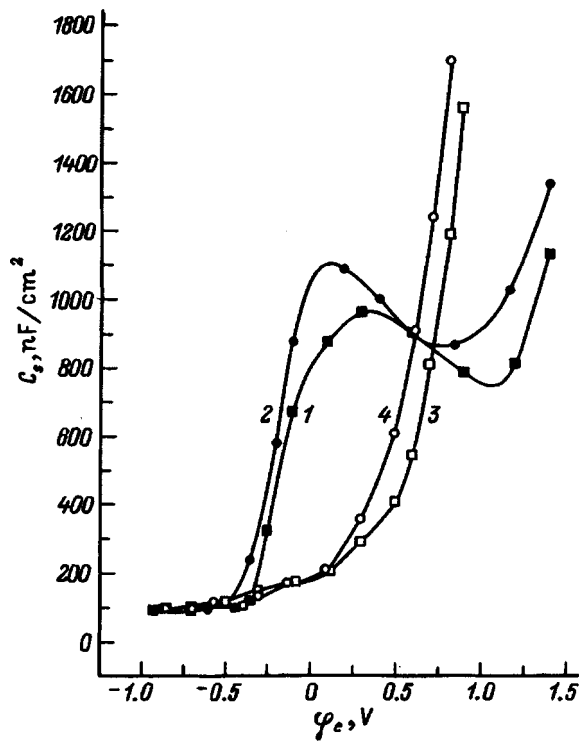


FIG. 4. Differential capacitance versus electrode potential for the systems Si-water electrolyte (1,2) and Si-PS-water electrolyte (3,4). 1,3—Initial state; 2,4—after addition of the surfactant Triton to the solution. Surfactant concentration, mmole/liter: 2—2, 4—0.2.

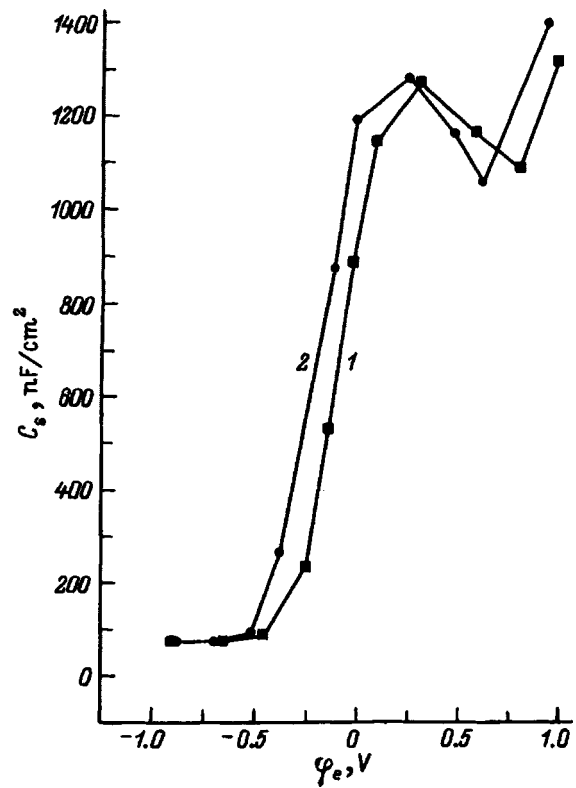


FIG. 5. Curves of the differential capacitance of the system Si-water electrolyte versus electrode potential before (1) and after (2) the addition of 2 mmole/liter PEG to the electrolytic solution.

was added to the solution, and for the silicon-electrolyte system it was established within 20–30 min. Apparently, diffusion of adsorbate molecules through nanopores plays a definite role in limiting the rate of recharging of the silicon-PS interface. The threshold concentration for detecting BQ in solution was of the order of 10 μmole/liter for both systems investigated.

An important practical problem is detection of organic impurities in water solutions. Figure 3 illustrates how adding 1.2-dihydroxyanthraquinone (alizarin), which on account of its structure can be both a donor and acceptor, to the electrolyte solution affects the dependence $C_s(\varphi_e)$ for Si-water electrolyte and Si-PS-water electrolyte systems. For both systems the adsorption of alizarin caused the curves $C_s(\varphi_e)$ to shift into the region of positive electrode potentials, which attests to the appearance of slow donor surface states. The magnitude of this shift with an alizarin concentration in solution of 0.2 mmole/liter was equal to ~0.25 V for single-crystalline silicon and in some cases reached 1.2 V for the Si-PS structure. An especially high sensitivity to donor impurity molecules in solution was observed for silicon-PS systems obtained with quite high anode current densities (~40 mA/cm²; Fig. 3, curves 3 and 4). Such systems in the initial state were characterized by a high negative charge on the silicon surface. Earlier, we observed for germanium-electrolyte systems a similar sensitization of the semiconductor surface to molecules of a definite type.³

The fact that the adsorption of alizarin molecules leads to the appearance of donor surface states attests to the fact that the formation of surface states of this type is energeti-

cally more favorable. This is also confirmed by the character of the effect of the adsorption of DPA on a silicon surface on which acceptor BQ molecules have already been adsorbed (Fig. 2, curve 4). The donor DPA molecules completely compensate the cathodic shift of the dependence $C_s(\varphi_e)$ and, moreover, give rise to an additional shift into the region of positive electrode potentials by approximately 0.5 V compared with the initial dependence. Apparently, DPA and BQ molecules are adsorbed on the same active surface centers and in the process the DPA molecules displace from these centers the acceptor molecules which were adsorbed on them.

The Si-electrolyte and Si-PS-electrolyte systems can be used to detect the presence of large molecules (including polymers) in a water electrolyte. Figure 4 shows the curves $C_s(\varphi_e)$ in the initial state and after the addition of the surfactant Triton to the electrolyte. The addition of this adsorbate to the solution causes the curve $C_s(\varphi_e)$ to shift into the region of negative electrode potentials. It is interesting to note that for the same concentration of adsorbates in solution these shifts for Si and Si-PS structure differ very little and at a concentration of 2 mmole/liter $\Delta\varphi_e \sim 0.1-0.12$ V. In the case of single-crystalline silicon, an appreciable shift of the curve $C_s(\varphi_e)$ (by $\Delta\varphi_e \sim 0.04-0.05$ V) was observed at a surfactant concentration in solution of the order of 20 μmole/liter. A stationary curve $C_s(\varphi_e)$ was established 20–30 min after the adsorbate was introduced. In the case of the Si-PS structure a stationary curve $C_s(\varphi_e)$ was established 15–20 h after the adsorbate was added to the electro-

lytic solution. Comparing the kinetics of the variation of the differential capacitance in time attests to the fact that the recharging of the semiconductor surface with the adsorption of BQ occurs more quickly than with the adsorption of Triton: A shift of approximately by 1/3 of the steady-state value is reached in 30 min in the first case and by about 1/4 of the steady-state value in 90 min in the second case. This is apparently explained by the much larger size of the Triton molecules and also by the micelle-formation properties of Triton, which impedes transport of BQ through nanopores.

The structure of Triton molecules suggests that the sign of the shift of the curve $C_s(\varphi_e)$ under the influence of this adsorbate is apparently due to not the appearance of new slow acceptor-type surface states but rather a restructuring of the Helmholtz layer (specifically, the displacement of positive ions away from the semiconductor–electrolyte interface). This is also confirmed by the fact that the adsorption of polyethylene glycol, being a hydrophilic component of Triton, also produces a cathodic shift of the curve $C_s(\varphi_e)$ by a virtually identical amount for the same concentration of Triton and PEG in solution (Fig. 5).

4. CONCLUSIONS

1. The silicon–electrolyte and silicon–porous-silicon–electrolyte systems are characterized by a quite high sensitivity with respect to the presence of impurity organic molecules in the liquid phase. The threshold concentration for

detecting impurity molecules in solution by electrophysical methods is $\sim 10\text{--}20\ \mu\text{mole/liter}$ in both systems.

2. The development of an additional nanoporous layer on the silicon surface does not give any appreciable gain in the adsorption sensitivity of the silicon–electrolyte system, but it does make it possible in principle to increase the selectivity of the system with respect to different molecules, since the recharging kinetics of the semiconductor surface with the addition of impurity molecules to the solution depends on the type of molecules.

¹⁾The current density in all cases was calculated per unit geometric (apparent) surface area of the sample.

¹T. Seiyama, in *Chemical Sensor Technology*, Vol. 1, Elsevier, Amsterdam, 1988, pp. 1–13.

²W. Gopel, T. A. Jones, T. Seiyama, and N. J. Zemel, *Sensors: A Comprehensive Survey*, Vol. 2, VCH, Weinheim, 1991, pp. 29–61.

³V. M. Demidovich, G. B. Demidovich, V. R. Karib'yants, and S. N. Kozlov, *Poverkhnost'*, No. 5, 37 (1994).

⁴G. B. Demidovich, V. M. Demidovich, V. R. Karibyants, and S. N. Kozlov, *Solid State Commun.* **98**, 189 (1996).

⁵A. Halimaoui, in *Porous Silicon Science and Technology*, Springer, Berlin, 1995, pp. 34–52.

⁶V. A. Myamlin and Yu. V. Pleskov, *Semiconductor Electrochemistry* [in Russian], Nauka, Moscow, 1965.

⁷H. Kobayashi, N. Takeda, H. Sugahara, and H. Taubomura, *J. Phys. C* **95**, 813 (1991).

Translated by M. E. Alferieff

On microwave transition radiation

I. I. Kalikinskiĭ

Astrakhan State Pedagogical University, 414050 Astrakhan, Russia

(Submitted October 23, 1996; resubmitted June 2, 1997)

Zh. Tekh. Fiz. **68**, 122–123 (February 1998)

The energy of the radiation emitted by an ultrarelativistic (1 GeV) electron at a transition from vacuum into yttrium iron garnet $I_3Fe_5O_{12}$ at the ferromagnetic resonance frequency (vacuum wavelength 3 cm) is estimated. The energy at this frequency was found to be 10^{-13} eV·s. If modern electron accelerators are used (particle current 10 mA), then for 1 s the energy at the ferromagnetic resonance frequency will be of the order of 1 J·s, so that the effect could have practical applications. © 1998 American Institute of Physics. [S1063-7842(98)02202-8]

Transition radiation was discovered theoretically in 1946.¹ Subsequently, many works concerning this question have appeared.² Charged-particle counters utilizing transition radiation have been constructed, mainly by the Erevan school of physicists. X-ray transition radiation was discovered by G. M. Garibyan³ (the work of K. A. Barsukov⁴ also played a large role in this question). These investigations are summarized in Refs. 5 and 6. However, it is too early to make a final summary. There are still problems of the theory of transition radiation which have not been studied. For example, the question of the generation of electromagnetic waves by means of transition radiation in the SHF and UHF ranges remains open. This question is the subject of two papers by the present author.^{7,8} These papers are concerned with transition radiation arising with a transition of a charge⁷ and a current filament⁸ from the vacuum into a medium characterized by an anisotropic impedance. The boundary conditions in this case at $z=0$ have the form

$$\begin{aligned} E_x &= -\rho_0(a_{11}H_x - a_{12}H_y), \\ E_y &= -\rho_0(a_{21}H_x - a_{22}H_y), \end{aligned} \quad (1)$$

where $\rho_0=377 \Omega$ is the characteristic impedance of the vacuum.

The charge moves along the z axis, producing a current with density $\mathbf{j}=(0,0,-j)$, where

$$j = qv \delta(x) \delta(y) \delta(z+vt). \quad (2)$$

The boundary conditions (1) and the condition

$$\text{div } \mathbf{\Pi}_\omega^{(1)} = 0 \quad (3)$$

make it possible to find the field and its energy at frequency ω . The Hertz electric vector $\mathbf{\Pi}$ was used as the potential:

$$\mathbf{\Pi}_\omega = \mathbf{\Pi}_\omega^{(0)} + \mathbf{\Pi}_\omega^{(1)}, \quad (4)$$

where $\mathbf{\Pi}_\omega^{(0)}=(0,0,\Pi_{\omega z}^{(0)})$ is the Hertz electric vector of the field generated by the charge, and $\mathbf{\Pi}_\omega^{(1)}=(\Pi_{\omega x}^{(1)}, \Pi_{\omega y}^{(1)}, \Pi_{\omega z}^{(1)})$ is the same for the radiation field.

The vacuum occupies the space $z>0$ and the magnetized ferrite occupies the space $z<0$. The components of the im-

pedance tensor can be expressed in terms of the components of the magnetic permeability tensor (for a ferrite magnetized in the direction of the z axis)⁹

$$\hat{\mu} = \begin{pmatrix} \mu & -i\mu_a & 0 \\ i\mu_a & \mu & 0 \\ 0 & 0 & 1 \end{pmatrix} \quad (5)$$

according to the equations

$$a_{11}=a_{22}=\frac{i}{2\varepsilon}(n_1-n_2), \quad a_{12}=a_{21}=\frac{1}{2\varepsilon}(n_1+n_2), \quad (6)$$

where

$$n_1^2 = \varepsilon(\mu + \mu_a), \quad n_2^2 = \varepsilon(\mu - \mu_a). \quad (7)$$

Here

$$\mu = \mu' + i\mu'', \quad \mu_a = \mu'_a + i\mu''_a, \quad (8)$$

where

$$\begin{aligned} \mu' &= 1 - \frac{(1-\zeta^2)\sqrt{1+\alpha^2} - 2\alpha^2/\sqrt{1+\alpha^2}}{(1-\zeta^2)^2 + 4\zeta^2\alpha^2/(1+\alpha^2)} \zeta A, \\ \mu'' &= (1+\zeta^2) \frac{\alpha A}{(1-\zeta^2)^2 + 4\zeta^2\alpha^2/(1+\alpha^2)}, \\ \mu'_a &= \frac{1-\zeta^2}{(1-\zeta^2)^2 + 4\zeta^2\alpha^2/(1+\alpha^2)}, \\ \mu''_a &= \frac{2\zeta\alpha A}{\sqrt{1+\alpha^2}[(1-\zeta^2)^2 + 4\zeta^2\alpha^2/(1+\alpha^2)]}. \end{aligned} \quad (9)$$

The parameter A is related with the magnetization of the ferrite

$$A = \frac{4\pi M_s}{\omega} \gamma,$$

where $\gamma=1.76 \cdot 10^7 \text{ Oe}^{-1} \cdot \text{s}^{-1}$ is the gyromagnetic ratio.

The parameter α characterizes losses in ferrite and is related with the width $2\Delta H$ of the ferromagnetic resonance line; $\alpha=\Delta H/H_0$, where $H_0=\omega_0/\gamma$ is the resonance value of the constant magnetic field inside the ferrite medium; $\zeta=\omega_0/\omega$ is a parameter characterizing the relative detuning

from resonance; ω_0 is the ferromagnetic resonance frequency; and, ω is the frequency of the radiation field. It is evident from Eqs. (9) that for small α and $\zeta=1$ the magnetic permeability of the ferrite is large and the ferrite medium differs sharply from vacuum. The case of ideal ferrite, for which $\alpha=0$ and ζ was assumed to be equal to 0.9999, was studied in Refs. 7 and 8. However, if we take $\zeta=1$ and $\alpha=0$ (ideal ferrite at the ferromagnetic resonance frequency), then the radiation energy is infinite.

As I later learned, nearly ideal ferrites are grown commercially. These are yttrium iron garnets. For example, for the garnet $Y_3Fe_5O_{12}$ the resonance frequency $\omega_0=2\pi c/\lambda$, where $\lambda=3$ cm. The width of the ferromagnetic line is $2\Delta H=0.6$ Oe, the resonance value of the constant magnetic field is $H_0=3000$ Oe and $\alpha=\Delta H/H_0=0.0001$; $4\pi M_s=1750$ J·s, so that $A=0.5$ and $\varepsilon=10$.¹⁰ A quite complicated formula for the energy at frequency α is presented in Ref. 7. In the present work computer calculations of the radiation energy were performed using this formula for a 1 GeV electron and $\omega=\omega_0$. In this case the radiation is sharply directed and is virtually independent of φ . This makes it possible to estimate the energy of the radiation at the frequency $\omega=\omega_0$ ($\zeta=1$).

Let us now examine the results of these calculations. The radiation is concentrated in the interval of angles $0<\theta<0.0025$. Integrating over angles, we find that the energy at the frequency $\omega=\omega_0$ equals 10^{-13} eV·s per ultrarelativistic electron. Therefore the radiation energy of one electron is low, but it can be 7 orders of magnitude higher than at other frequencies. An appreciable energy output can be obtained by using modern synchrotrons (particle current $J=10$ mA). Let us fix the time, setting $t=1$ s. Then $N=10^{16}$ electrons will pass through the interface. It is known that the radiation energy of N particles is N^2 times higher than the radiation energy of one particle. For this

reason, the radiation energy of $N=10^{16}$ particles at the ferromagnetic resonance frequency is ~ 1 J·s for this case.

It is known⁷ that radiation accompanying the transition of an electron into a metal ($\varepsilon'=\infty$) occurs at the point where the trajectory of the charge crosses the boundary of the medium, since the length of the radiation formation zone equals zero. This will also happen in our case, since the magnetic permeability is high and the radiation formation zone can be neglected.

In closing, I thank B. M. Boltovskiĭ for a discussion and Yu. Yu. Tarasevich for assisting in the computer calculations, and I thank the reviewer for comments leading to improvements in this paper.

¹V. L. Ginzburg and I. M. Frank, Zh. Éksp. Teor. Fiz. **16**, 15 (1946).

²L. A. Vardanyan and I. G. Melkumova, *Bibliography of Works on the Transition Radiation of Charged Particles (1945–1982)* [in Russian], Erevan Physical Institute, Erevan, 1983.

³N. M. Garibyan, Zh. Éksp. Teor. Fiz. **37**, 527 (1959) [Sov. Phys. JETP **10**, 372 (1960)].

⁴K. A. Barsukov, Zh. Éksp. Teor. Fiz. **37**, 1106 (1959) [Sov. Phys. JETP **10**, 787 (1960)].

⁵V. L. Ginzburg and V. N. Tsytovich, *Transition Radiation and Transition Scattering* [in Russian], Nauka, Moscow, 1984.

⁶G. M. Garibyan and Yan Shi, *X-Ray Transition Radiation* [in Russian], Erevan, 1983.

⁷I. I. Kalikinskiĭ, "On SHF and UHF transition radiation" [in Russian], Deposited in VINITI, May 15, 1995, No. 1361-V95.

⁸I. I. Kalikinskiĭ, "Radiation from a current filament accompanying a transition from vacuum into magnetized ferrite," Deposited in VINITI, February 2, 1995, No. 290-V95.

⁹E. P. Kurushin, E. I. Nefedov, and A. T. Fialkovskii, *Diffraction of Electromagnetic Waves by Anisotropic Structures* [in Russian], Nauka, Moscow, 1975.

¹⁰N. D. Gorbunov and G. A. Matveev (Eds.), *Reference Data on Ferrites and Magnetodielectrics* [in Russian], Sov. Radio, Moscow, 1968.

Translated by M. E. Alferieff

Optical nonlinearity of azodye-doped polymer waveguides

A. V. Tomov, A. I. Voïtenkov, and A. V. Khomchenko

Institute of Applied Optics, Academy of Sciences of Belarus, 212793 Mogilev, Belarus
(Submitted October 16, 1996)

Zh. Tekh. Fiz. **68**, 124–126 (February 1998)

Results of investigations of the optical and photochromic properties of waveguides prepared by chemical diffusion of the azodyes methyl red and Sudan G into polycarbonate are reported.

High optical nonlinearity of the layers is observed under conditions of self-action of $\lambda = 633$ nm laser radiation, and the mechanism of this effect is established. © 1998 American

Institute of Physics. [S1063-7842(98)02302-2]

The potential applications of purely optical signal-processing devices in information transmission systems have stimulated in recent years broad investigations in nonlinear optics, the main focus being on the nonlinear optics of waveguides.¹ In this connection investigators are once again showing interest in structures based on organic and polymer materials, specifically, polymers doped with azodyes.^{2,3} One method for producing nonlinear optical waveguides is to diffuse a dye into a polymer matrix.⁴

We report below the results of our investigations of the linear and nonlinear optical properties of waveguides obtained by diffusing dyes in polycarbonate.

The waveguides were produced by chemical diffusion⁵ from saturated solutions of the azodyes methyl red (MR) and Sudan G in a multicomponent xylool-based solvent. Propagation losses ($\lambda = 633$ nm) were measured by the method of Ref. 6 and amounted to less than 1.5 dB/cm in single-mode and 3–4 dB/cm in multimode waveguides.

The index profiles of waveguide layers calculated by the WKB method were found to be nearly step-shaped. The increment Δn to the refractive index at the surface of waveguides obtained in the same solvent does not depend on the diffusion time t , while their thickness increases as $t^{1/2}$. Increasing the xylool fraction in the solution from 20 to 40% approximately doubles Δn , but in the process the losses due to degradation of the optical quality of the waveguide surface increase substantially. Similar trends are also observed with increasing solution temperature. The maximum attainable values of Δn with acceptable losses were equal to 0.012 for methyl red and 0.007 for Sudan. The dye concentration was estimated from the light absorption coefficient as 0.04 and 0.1 M, respectively.

It is known that the strong nonlinear optical properties of polymer films containing methyl red are due to photoinduced *trans-cis* isomerization of the dye.^{7,8} The most informative methods for studying this process are photomodulation of the absorption coefficient⁹ and different waveguide methods.¹⁰ The investigations showed that the absorption spectra of methyl red in the diffused layers obtained are identical to those of the monomeric *trans* isomer of methyl red in other polymer matrices.^{9,11} The induced absorption spectra under the action of linearly polarized $\lambda = 515$ nm light (Fig. 1, curve 1), which were obtained with photomodulation at 4 Hz, are

also similar to those studied earlier.⁹ The samples are intensively bleached in the range 415–565 nm and they darken slightly in the yellow–red region of the spectrum. Only the short-wavelength band is strongly dichroic.

It was found that the layers studied are also sensitive to $\lambda = 633$ nm light. The changes induced in the absorption spectrum of methyl red (curve 3) by such light are opposite to the changes observed to occur with short-wavelength radiation. Only the “red” band is dichroic. In both cases the sample becomes clear in the range of the spectrum bordering on the wavelength of the irradiating light. Additional illumination of the sample with unmodulated $\lambda = 515$ nm radiation with comparable intensity greatly intensifies the effect (curve 4). The photosensitivity of the sample to green light can be increased by irradiating the sample simultaneously with red light (curve 2). The magnitude of the additional response in both variants is virtually independent of the state of polarization of the third beam. We note that the average position of the isobestic point near $\lambda \sim 565$ nm, which, as one can see by analyzing Fig. 1, is only approximately such, agrees with the position indicated in Ref. 11 for the S^1 level of the *trans* isomer of methyl red.

The method described in Ref. 12 was used to estimate

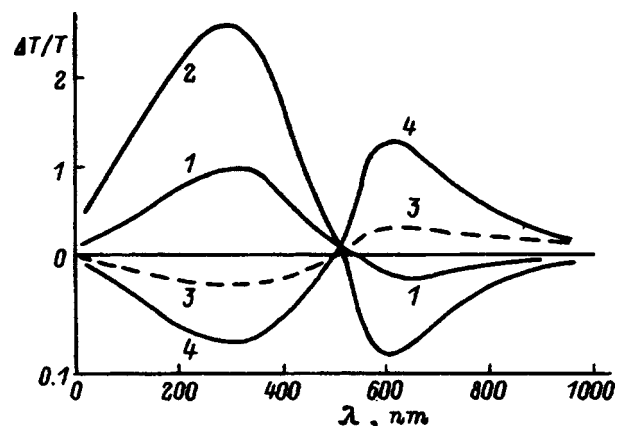


FIG. 1. Spectra of the photoinduced change in the transmittance of a sample with methyl red under the action of light with $\lambda = 515$ (1,2) and 633 nm (3,4) and 2,4—with additional illumination with $\lambda = 633$ and 515 nm light, respectively. The intensity of the green light equals in all cases 5 mW/cm^2 and the intensity of the red light equals 100 mW/cm^2 .

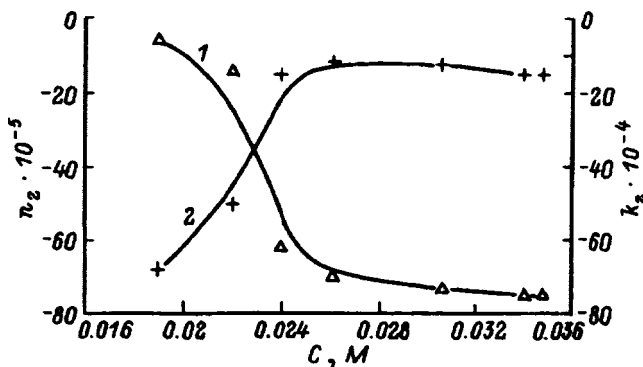


FIG. 2. Nonlinear optical constants n_2 (1) and k_2 (2) of diffused waveguides versus the concentration of methyl red dye added.

the nonlinear optical characteristics of waveguide layers at $\lambda = 633$ nm under the conditions of self-excitation (stationary case). The method is based on analyzing the changes occurring in the intensity distribution in the light beam, reflected from the prismatic element exciting directed TE modes, as its intensity varies. The intensity P of the light introduced into the waveguide ranged from 0.01 to 1 W/cm². A photoinduced decrease in the refractive index and induced bleaching of the layers under the action of the light propagating in them were recorded. The dependences of the nonlinear optical constants $n_2 = \Delta n/P$ and $k_2 = \Delta k/P$ on the methyl red concentration are presented in Fig. 2, where Δn and $\Delta k = \lambda \Delta \alpha / 4\pi$ are the changes induced in the refractive index and in the absorption coefficient, respectively. Close values of the nonlinear coefficients were also obtained for waveguides with Sudan ($C = 0.1$ M, $n_2 = 4 \times 10^{-5}$ cm²/W, $k_2 = 5 \times 10^{-6}$ cm²/W). We note that in determining n_2 the refractive index in the range of variation of P was a linear function of the probe beam power.

In our opinion, the observed saturation of n_2 (Fig. 2) is due to the long-wavelength shift of the absorption band with a maximum at 610 nm accompanying an increase in the dye concentration.⁹ The stabilization of k_2 with increasing C is in all probability due to the operation of a number of factors influencing the kinetics of the photochromic process and depending on the dye concentration.

The observed behavior can be explained by assuming that the inverse *cis-trans* isomerization process can be induced not only by thermal activation but also by the action of red light, i.e., by assuming that the *cis* isomer of the dye possesses photochromic properties. According to the Ref. 11, the *trans* isomer intensively absorbs $\lambda = 565$ nm light and the

cis isomer absorbs light only with λ shorter than 400 nm. The long-wavelength induced absorption band in the modulation spectra 1 and 2 in Fig. 1 evidently corresponds to a $n - \pi^*$ transition in the *cis* isomer. When red light is absorbed, the equilibrium density of the *cis* isomer decreases and the sample becomes clear in this band. As a result of an increase in the relative fraction of the *trans* isomer, absorption in the band with a maximum at 495 nm increases ($\pi - \pi^*$ transition). The fact that these induced absorption bands are not simultaneously dichroic likewise indicates that they belong to different isomers of the dye. Thus, the role of additional illumination in the spectra 2 and 4 (Fig. 1) is to shift the dynamic equilibrium in the system in the direction of the *cis* or *trans* isomer, respectively. The sensitivity of the experimental objects only to red light signifies that a definite fraction of methyl red is initially in the *cis* form.

The green light induced change in the absorption coefficient $\Delta \alpha \approx (1/d)\Delta T/T$ at $\lambda = 633$ nm equals tens of inverse centimeters with radiation intensity 10 mW/cm², which is sufficient for effective external modulation of the intensity of the light propagating in the waveguide. The contributed losses in this case should reach 100 dB/cm.

To summarize, in the present work the optical properties of diffused polymer waveguides were studied. Curves making it possible to predict the nonlinear optical parameters of waveguides as a function of the dye concentration in the polymer were obtained. It was shown that on the basis of their properties these structures can be used for optical information processing, specifically, for obtaining completely optical modulation of light.

¹G. I. Stegeman, *J. Lightwave Technol.* **6**, 953 (1988).

²G. J. Bjorklund, *Appl. Opt.* **26**, 227 (1987).

³K. K. Sharma, Rao K. Divahara, and G. R. Kumar, *Opt. Quantum Electron.* **26**, 1 (1994).

⁴C. Poda, M. G. Kuzyk, and C. W. Dirk, *J. Opt. Soc. Am.* **11**, 80 (1994).

⁵A. V. Tomov, *Pis'ma Zh. Tekh. Fiz.* **21**(10), 25 (1995) [*Tech. Phys. Lett.* **21**, 362 (1995)].

⁶V. P. Red'ko *et al.*, *Pis'ma Zh. Tekh. Fiz.* **18**(4), 14 (1992) [*Sov. Tech. Phys. Lett.* **18**, 100 (1992)].

⁷C. Egami, K. Nakagawa, and H. Fujiwara, *Jpn. J. Appl. Phys.* **29**, 1544 (1990).

⁸I. V. Tomov, *J. Opt. Soc. Am.* **8**, 1477 (1991).

⁹A. I. Voimenkov, V. A. Ereshchenko, and A. S. Borbitskiĭ, *Zh. Prikl. Spektrosk.* **63**, 305 (1996).

¹⁰T. Luckemeyer and H. Franke, *Appl. Phys. Lett.* **53**, 2017 (1988).

¹¹G. J. Lee, D. Kim, and M. Lee, *Appl. Opt.* **34**, 138 (1995).

¹²A. B. Sotskiĭ, A. V. Khomchenko, and L. I. Sotskaya, *Pis'ma Zh. Tekh. Fiz.* **20**, 49 (1994) [*Tech. Phys. Lett.* **20**, 667 (1994)].

Multiple recording of rainbow holograms on the same section of a photosensitive material

S. Ya. Gorelik

St. Petersburg Institute of Precision Mechanics and Optics (Technical University), St. Petersburg, Russia

(Submitted November 14, 1996)

Zh. Tekh. Fiz. **68**, 127–129 (February 1998)

A technology is proposed for multiple recording of holograms on the same section of thin recording media using the technique for obtaining rainbow holograms. It is shown that in this case the individual holograms can be reconstructed and read independently of one another.

Experimental results are presented. © 1998 American Institute of Physics.

[S1063-7842(98)02402-7]

A method for recording and reconstructing images by means of pseudodeep holograms was proposed earlier.^{1,2} It was shown that such holograms, which are recorded on obliquely arranged thin photosensitive layers, admit multiple recording on the same section of such photosensitive materials. Individual holograms in this case can be reconstructed and read independently of one another.³ In the present paper it is shown that multiple recording of holograms followed by independent reconstruction of the holograms can also be

achieved in conventionally (i.e., vertically) arranged thin photosensitive layers by using the method for obtaining rainbow holograms.⁴

The principle of recording such multiple holograms is as follows (Fig. 1a). A linear object AB is recorded with a reference wave R on a photosensitive plate H . Next, a reference wave R_1 , whose direction of propagation differs from that of the wave R by an angle $\Delta\varphi$, records the object A_1B_1 placed at the location of the object AB . If the hologram recorded in this manner is illuminated with one of the waves, which is a reference wave during the recording process, for example, the wave R , then images of both recorded objects will be reconstructed. The image of the object AB , corresponding to the wave R , can be picked out by the output slit D (Fig. 1b), in the manner as when reconstructing a multiple pseudodeep hologram, and the image of the object A_1B_1 is cut off by the slit. It is easy to see that if the wave R_1 were used at the reconstruction stage, then for the same position of the output slit the image of the object A_1B_1 would be picked out. It can be easily shown that the angular width $\Delta\Psi$ of the output slit will be determined (neglecting diffraction diver-

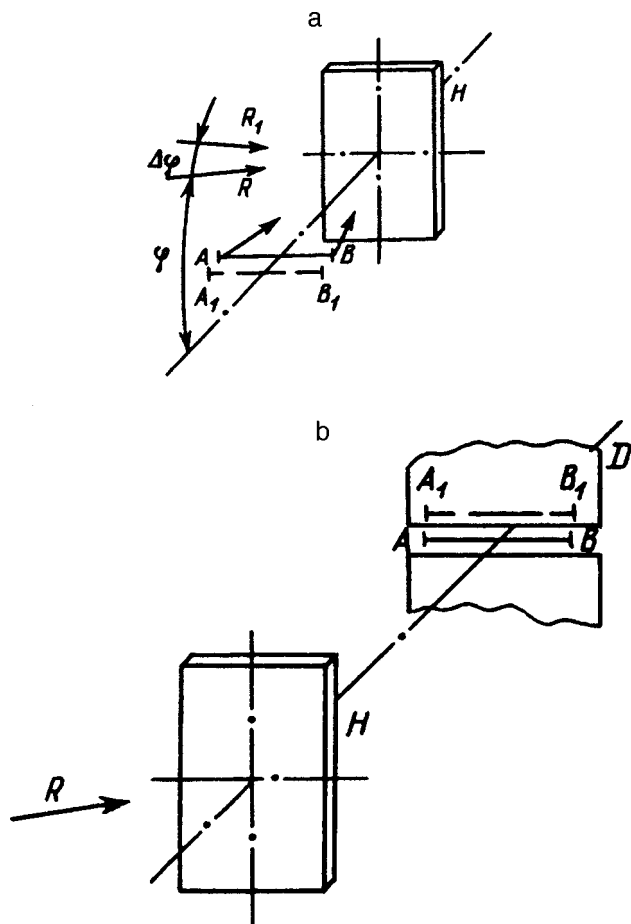


FIG. 1. Principle of recording (a) and reconstructing (b) of a multiple rainbow hologram.

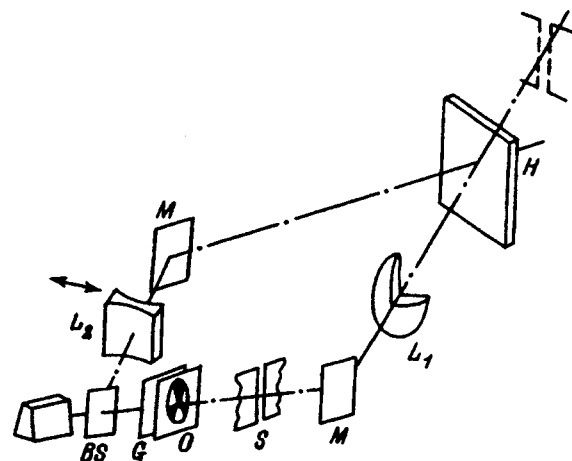


FIG. 2. Experimental arrangement for recording/reading multiple rainbow holograms. M —mirror; BS —beam splitter; G —ground glass; O —object recorded; S —filtering slit; L_1, L_2 —lenses; H —photosensitive material. The dot-dash line shows the position of the output slit D .

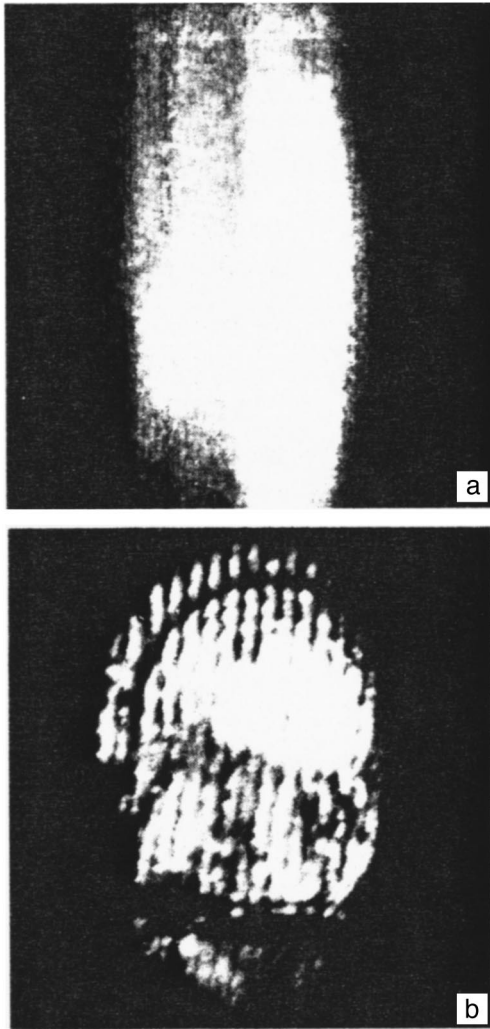


FIG. 3. Image reconstructed by a double hologram and observed in planes which are conjugate to the plane of the filtering slit (a) and to the object plane (b).

gence) by the change $\Delta\varphi$ in the angle of incidence of the reference wave during the recording/reconstruction and should not exceed the value

$$\Delta\psi \approx \Delta\varphi \cos \varphi. \quad (1)$$

To confirm that the proposals made above are well founded, a series of experiments on obtaining multiple rainbow holograms was performed in which the image of different sections of a transparency, consisting of a photographic test object (focusing aid), was recorded. The recording procedure was done in a two-beam scheme (with angle of incidence of reference beam $\varphi \approx 40^\circ$) by a one-step method⁵ (Fig. 2). The radiation scattered by the ground glass G and passing through the transparency O was filtered out by the slit S , which had an angular width of about 1° . The lens L_1 , located at twice the focal distance from the slit S , formed an image of the object and the filtering slit in a manner so that they were located behind the plane of the recording medium. The angle of incidence of the reference beam was changed (by the amount $\Delta\varphi \approx 1^\circ$) by moving a diverging cylindrical lens L_2 . A He-Cd laser with working wavelength



FIG. 4. Image of one of the recorded objects. The image was reconstructed by a double hologram and picked out by the output slit.

$\lambda = 0.4416 \mu\text{m}$ served as the source of radiation. Du Pont photopolymer films were used as the recording medium.

The experimental results on recording and reconstructing a double rainbow hologram are presented in the subsequent figures. As expected, in accordance with what has been said above, an image of two slits lying next to one another (Fig. 3a) was observed in the plane conjugate to the plane of the slit S , and an image consisting of a mixture of the two recorded images was observed in a plane conjugate to the plane of the volume O (Fig. 3b). When an output slit D was placed in the plane conjugate to the plane S , each recorded image could be read (according to the scheme described in, for example, Ref. 2) independently (Fig. 4).

In summary, the method for preparing rainbow holograms makes possible multiple recording on thin recording media with independent readout of the images recorded. However, it should be noted that although multiple pseudodeep and rainbow holograms operate in a similar manner in separating the reconstructed images, the mechanism of this phenomenon for them is very different: In the first case information about the spatial distribution of the intensity of the recorded interference pattern is preserved (because of the inclination of the recording medium), while in the second case there is a change in the spatial frequency of the pattern in the plane of the recording medium.

In closing, I wish to thank Yu. N. Denisyuk and the staff at his laboratory for their interest in this work and for kindly providing the opportunity for performing the experiments.

¹ Yu. N. Denisyuk and N. M. Ganzherli, Zh. Tekh. Fiz. 60(11), 154 (1990) [Sov. Phys. Tech. Phys. 35, 1321 (1990)].

² Yu. N. Denisyuk, Pis'ma Zh. Tekh. Fiz. 18(2), 15 (1992) [Sov. Tech. Phys. Lett. 18, 31 (1992)].

³ Yu. N. Denisyuk and N. M. Ganzherli, Pis'ma Zh. Tekh. Fiz. 15, 14 (1989) [Sov. Tech. Phys. Lett. 15(15), 585 (1989)].

⁴ S. A. Benton, J. Opt. Soc. Am. 59, 1545A (1969).

⁵ Poohsan N. Tamura, Appl. Opt. 17, 3343 (1978).

Calculation of the noise factor of a traveling-wave gyrotron

M. V. Oleĭnik and D. I. Trubetskov

Kolledzh State Educational-Scientific Center, Saratov State University, 410071 Saratov, Russia
(Submitted November 16, 1996)

Zh. Tekh. Fiz. **68**, 130–132 (February 1998)

The problem of calculating the noise factor of a traveling-wave gyrotron is solved for a model of a thin annular multistart-helical electron flux taking into account the effect of the quasistatic space-charge field. Plots of the gain and the noise factor of the traveling-wave gyrotron versus the electrical parameters of the amplifier are obtained. © 1998 American Institute of Physics. [S1063-7842(98)02502-1]

The interaction of electrons and microwave electromagnetic fields has been investigated many times in the theory of gyrodevices. However, thus far the problem of calculating the noise factor of a traveling-wave gyrotron (TWG) has not been studied. In the present paper this problem is solved for the model of a thin annular multistart-helical electron flux taking into account the effect of the quasistatic space-charge field. The noise properties of a TWG in the linear regime must be determined, for example, when building networks of gyrodevices in which a wide-band TWG with a high gain in the weak-signal regime must be incorporated. Moreover, it is known from theory and experiment with *O*-type traveling-wave tubes (TWTO) that, even in the strong-signal regime, only the weak noise signal is amplified during the pauses, and it can happen that even that must be reduced.¹

The calculation of the quasistatic space-charge fields is based on a model described in detail in Ref. 2. We shall use the Green’s function method (see, for example, Ref. 2) to solve the Poisson equation together with the boundary conditions on the waveguide wall ($r=b$). We shall employ the expressions obtained in Ref. 2 which relate the projections of the volume current density j_r , j_ϕ , and j_z at a point with radial coordinate r and the microwave displacements of the electrons z_1 and Θ_1 . Then, according to Ref. 2, we have for the projections of the first harmonic of the space-charge field along an electron trajectory

$$E_{\Theta 1} = -\frac{2\omega_p^2 \Gamma \beta_{\parallel}}{\eta k \xi \pi^2} \left(\xi z_1 + \frac{a \Theta_1}{q} \right) E_{\Theta}^* ; E_{z 1} = 0 ;$$

where

$$\begin{aligned} E_{\Theta}^* = & -q \psi_2 \int_0^\pi \cos(y) \cos(\Theta) d\Theta - (\psi_5 \\ & + q \psi_6) \int_0^\pi \sin(y) \sin(\Theta) d\Theta \\ & + iq \int_0^\pi \frac{R}{r} \sin(\Theta) \sin(y) \cos(\Theta) d\Theta ; \\ \psi_2 = & T \int_0^{\Gamma b} \frac{\Gamma R \cos(\Theta) \cot(\Theta)}{(\Gamma r)^2} d\Gamma r ; \end{aligned}$$

$$\psi_5 = T \int_0^{\Gamma b} -\cot(\Theta) d\Gamma r ;$$

$$\psi_6 = T \int_0^{\Gamma b} \Gamma R \sin(\Theta) d\Gamma r ;$$

$$T = \frac{I_0(\Gamma R)}{I_0(\Gamma b)} [I_0(\Gamma R) K_0(\Gamma b) - I_0(\Gamma b) K_0(\Gamma R)] ;$$

$$A = \frac{-i I_0}{2 \pi^2 a R} ; \quad \xi = \frac{h_e - h_c}{h_c} ; \quad h_c = \frac{\omega_c}{v_{\parallel}} ; \quad h_e = \frac{\omega}{v_{\parallel}} ;$$

$$q = \frac{\beta_{\perp}}{\beta_{\parallel}} ; \quad \beta_{\perp} = \frac{v_{\perp}}{c} ; \quad \beta_{\parallel} = \frac{v_{\parallel}}{c} ;$$

I_0 is the constant beam current; R is the average beam radius; a is the Larmor radius; ω_c is the cyclotron frequency; v_{\parallel} and v_{\perp} are the longitudinal and transverse components of the unperturbed electron velocity; $I_0(\Gamma R)$ and $K_0(\Gamma R)$ are modified Bessel functions of the first and second kinds, respectively; y is the angle between the radii of the elementary current tube and the waveguide which are drawn from the point where the current density is calculated;

$$\omega_p = \sqrt{\frac{\eta I_0}{4 \pi R a v_{\parallel} \epsilon_0}}$$

is the plasma frequency; and, η is the specific charge of an electron.

Let us consider a TWG with a cylindrical waveguide where an electron beam with the described configuration interacts with the microwave field of the working TE_{01} mode of the waveguide. We shall neglect the effect of the microwave magnetic field on the interaction processes.

To describe the electrodynamic part of the problem we employ the equation describing the excitation of a transmission line by a curvilinear electron flux.³ In dimensionless units this equation is

$$\frac{dE}{d\zeta} + \frac{i}{D} E = -ika \Theta_1, \tag{1}$$

where $\zeta = \Gamma_s D z$ is the dimensionless length of the interaction space

$$D = \sqrt{\frac{I_0 R_v}{4U_0}} (1 + q^2)$$

is the interaction parameter, and

$$E = \frac{C_s E_s \Theta_1 \eta}{D \Gamma_s v_{\parallel} c}$$

is the normalized amplitude of the wave.

In the equations of motion of electrons in an microwave field, which are presented in Ref. 4, we shall study the terms determined solely by *O*-type bunching. Then the equations of motion of electrons in a field which is the sum of the field of a synchronous wave and the quasistatic space-charge field, taking account of the one-to-one correspondence between $i\Delta\omega_1$ and the differential operator $v_{\parallel}(d/dz) + i(\omega - \omega_c)$, in the dimensionless variables are

$$\begin{aligned} & \frac{d^2\Theta_1}{d\xi^2} + 2i\left(b + \frac{1}{D}\right) \frac{d\Theta_1}{d\xi} - \left[\left(b + \frac{1}{D}\right)^2 - \bar{h}_p^2 C_{\Theta\Theta}\right] \Theta_1 \\ & = -\bar{h}_p^2 C_{\Theta z} \bar{z}_1 + \frac{E}{D\Gamma_s a} \beta_{\perp} q, \\ & \frac{d^2\bar{z}_1}{d\xi^2} + 2i\left(b + \frac{1}{D}\right) \frac{d\bar{z}_1}{d\xi} - \left[\left(b + \frac{1}{D}\right)^2 - \bar{h}_p^2 C_{zz}\right] \bar{z}_1 \\ & = -\bar{h}_p^2 C_{z\Theta} \Theta_1 + \frac{E}{D\Gamma_s a} \beta_{\perp}, \end{aligned} \quad (2)$$

where $b = \omega - \omega_c - \Gamma_s v_{\parallel} / \Gamma_s D v_{\parallel}$ is the desynchronization parameter, $\bar{z}_1 = z_1/a$, $\bar{h}_p = h_p(\Gamma_s D)$ is the normalized plasma propagation constant, and

$$\begin{aligned} C_{\Theta\Theta} &= \frac{2\beta_{\parallel}\beta_{\perp}\omega_c}{\pi^2\omega} E_{\Theta}^*, & C_{\Theta z} &= \frac{2\omega_c}{\pi^2\omega} \beta_{\perp}^2 \xi E_{\Theta}^*, \\ C_{zz} &= \frac{2\omega_c}{\pi^2\omega} \beta_{\parallel}\beta_{\perp} \xi E_{\Theta}^*, & C_{z\Theta} &= \frac{2\omega_c\beta_{\parallel}^2}{\pi^2\omega} E_{\Theta}^*. \end{aligned}$$

The equations (2) together with the excitation equation (1) comprise the working system of equations of the linear theory of a TWG in the model adopted for the flux.

Let us now analyze noise phenomena in a TWG. This problem reduces to analysis of a gyroamplifier with premodulation of the microwave displacements and beam velocity at the entrance into the interaction space, the modulation being of a random, noise character. In determining the initial conditions for solving the problem of calculating the noise factor, the fluctuations of the azimuthal displacements at the entrance into the interaction space were calculated according to the formula presented in Ref. 5. The fluctuations of the longitudinal displacements were assumed to be of the same order of magnitude as the fluctuations of the azimuthal displacements. The fluctuations of the velocities were assumed to be approximately equal to the corresponding fluctuations at the cathode of a *M*-type beam device.⁶ Thus, values characteristics for magnetron guns employed in gyrodevices were used in the calculations.

The gain *G* and the noise factor *F* of a TWG were calculated by solving the system of equations (1) and (2) nu-

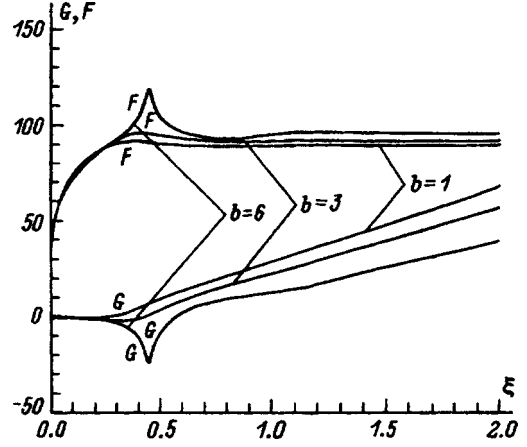


FIG. 1. Noise factor *F* and gain *G* versus the dimensionless length ξ of the interaction space for different values of the desynchronization parameter *b*.

merically by a fourth-order Runge–Kutta method. The noise factor was calculated according to the formula

$$F = 1 + \frac{|C_s E_s \Theta_1|^2}{kT_0 \Delta f \Gamma_s^2 R_v C},$$

where $T_0 = 290$ K is the noise temperature of the source matched with the amplifier input.

The dependence of the noise factor *F* and the gain *G* on the dimensionless length ξ of the interaction space with different values of the desynchronization parameter *b* and the interaction parameter *D* is presented in Figs. 1 and 2. One can see from the figures that for certain values of the interaction parameter *D* and the desynchronization parameter *b* a weakening of the signal and a sharp increase in the noise factor occur on the initial section of the interaction space. This happens because the values of the parameters are close to the conditions for a suppression effect, similar to the well-known Kompfner suppression. Unfortunately, in the literature there is no information on the noise factor of TWGs, so that at present it is impossible to compare with experiments.

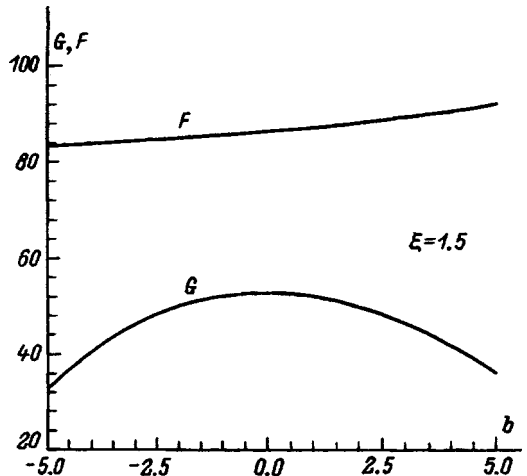


FIG. 2. Noise ratio *F* and gain *G* versus the desynchronization parameter *b*.

¹A. G. Lzerson and M. Z. Shlyakhter, Radiotekh. Elektron. **38**, 2010 (1993).

²S. I. Vyrovoř, Izv. Vyssh. Uchebn. Zaved. Radiofiz. **17**, 1378 (1974).

³L. A. Vařnshteřn and V. A. Solntsev, *Lectures on Microwave Electronics* [in Russian], Sov. radio, Moscow, 1973.

⁴A. V. Gaponov, Izv. Vyssh. Uchebn. Zaved. Radiofiz. **4**, 547 (1961).

⁵D. I. Trubetskov and E. Ya. Shepeleva, Izv. Vyssh. Uchebn. Zaved. Radiofiz. **34**, 426 (1991).

⁶D. I. Trubetskov, in *Lectures on Microwave Electronics. 2nd Winter School-Seminar of Engineers* [in Russian], Saratov, 1972, Vol. 5, p. 130.

Translated by M. E. Alferieff

Expansion of spark channels in air and possibilities of plasma crowbar in high pulsed current and magnetic field technique

A. K. Sořka and I. M. Vashkevich

Institute of Solid-State and Semiconductor Physics, Academy of Sciences of Belarus, 220072 Minsk, Belarus

(Submitted December 23, 1996)

Zh. Tekh. Fiz. **68**, 133–136 (February 1998)

The radial expansion velocities and diameters of spark channels in air are measured by the plasma–metal contact method. An LC discharge circuit with energy up to 50 kJ and with current frequencies ranging from $\sim 10^2$ to $\sim 10^4$ Hz served as the source of the channels. It is concluded on the basis of the results obtained that the previously proposed automatic plasma crowbar based on the expansion of spark channels in gases is a universal switch for an inductive load in LC discharge circuits that could find very wide applications in high pulsed current and magnetic field technology. © 1998 American Institute of Physics. [S1063-7842(98)02602-6]

In Refs. 1 and 2 a new method is described for obtaining strong unipolar magnetic field pulses with different shapes and inductions of up to 100 T in oscillatory LC discharge circuits by means of the so-called automatic plasma crowbar, which operates on the basis of the phenomenon of radial expansion of the spark discharge channels in gases.^{3,4} However, the range of application of the proposed crowbar was limited to the frequencies of LC circuits $\sim 10^4$ Hz.

Our objective in the present work was to investigate experimentally the expansion of spark channels in air by the method of contact of gas-discharge plasma with a metal for discharge-current frequencies ranging from $\sim 10^2$ to $\sim 10^4$ Hz and to determine the possibilities of wide applications of the plasma crowbar in high pulsed current and magnetic field technology.

It should be noted that the existing works on the expansion of spark channels in gases (see, for example, Refs. 3–6 and the references cited there) employ essentially the same method of investigation. This method is based on studying the temporal evolutions, obtained by one or another method, of the photographic image of a spark discharge. A criterion for the boundary of a channel was a definite photographic blackening density, depending on an entire series of factors not associated with the phenomenon under study. Apparently, this explains in part the very large variance of data obtained by different authors on the expansion velocities and diameters of plasma columns of spark discharges for the same gaseous media and with identical or close parameters of the discharge circuits.

In the present work we have performed the first measurements of the expansion velocities and diameters of spark channels in air under conditions when the degree of ionization of gas perturbed by the discharge served as the criterion of their boundary, i.e., a definite magnitude of the electrical conductivity of the gas-discharge plasma, whose value in our experiments was close to the conductivity of a metal.

The experimental arrangement is shown in Fig. 1. The capacitor C with stored energy $W=52\times 10^3$ J and voltage

up to 5.5×10^3 V was discharged through a controllable three-electrode air spark gap (trigatron) on a coil with inductance L . The value of L ranged from 1.2×10^{-3} up to 1.2×10^{-7} H, which corresponded to a change in the frequency of the LC circuit from 80 Hz up to 9 kHz, calculated according to the formula $f=1/T$, where T is the duration of the first period of the discharge current obtained from its oscillogram. The damping decrements $\delta=RT/2L$ of the discharge currents varied from 0.3 ($f=80$ Hz) to 1.2 ($f=9$ kHz) and the current amplitudes varied from several kiloamperes up to $\sim 4\times 10^5$ A, respectively.

A fundamentally new element of the scheme shown in Fig. 1 is the fourth (crowbar) electrode of the trigatron. In the case at hand it consists of a short (approximately 2–3 cm with an up to 7 mm long discharge gap) brass or steel tube with 3–5 mm thick walls, which is arranged symmetrically (Fig. 1) and coaxially with respect to the trigatron electrodes and is connected with one of the outputs of the coil by the conductor ab .

The main parameter of the crowbar electrode is its inner radius. As soon as the expanding gas-discharge plasma reaches the crowbar electrode, its contact with the metal short-circuits the outputs of the coil (Fig. 1), as a result of which the further temporal evolution of the discharge current in the circuit changes, and this change is uniquely recorded in its oscillogram (the character of this change depends on the moment (phase) of the discharge process in which the crowbar is actuated). The distribution and sizes of the contact spots on the inner surface of the crowbar electrode make it possible to judge the electrical conductivity of the part of the plasma column that touches it, i.e., its form at the moment the coil is shorted.

In summary, a crowbar electrode makes it possible not only to change radically the properties of an LC discharge circuit as a source of current (magnetic field) pulses of a definite shape but also to investigate in detail the spatiotemporal picture of the expansion of the spark-discharge channel.

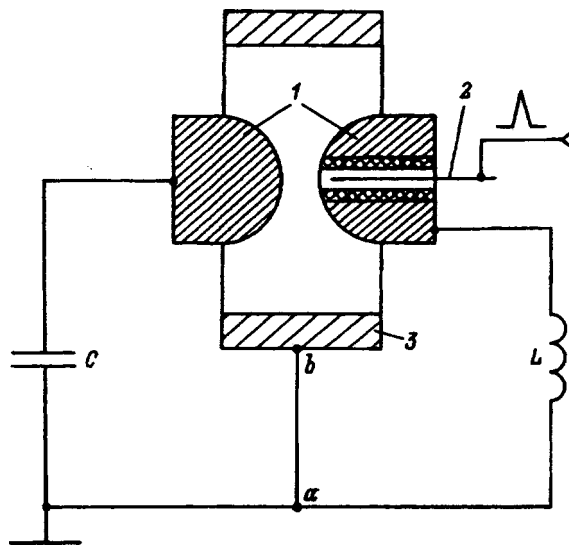


FIG. 1. Schematic diagram of the experiment (LC discharge circuit with plasma crowbar). 1,2—Trigatron electrodes; 3—crowbar electrode.

From the standpoint of practical applications of the plasma crowbar, the expansion of a discharge column is best characterized by its radius, equal to the radius r_c of the crowbar electrode that shorts the coil at the moment of the first maximum of the current, and its average radial expansion velocity $V_{mid} = r_c / \tau_m$ over the time $\tau_m \approx T/4$ during which the current reaches its maximum value. The usefulness of this characterization is due to the fact that it is of greatest interest (and most difficult) to short-circuit the inductive load in an LC discharge circuit or to supply additional energy to it at the moment of the first maximum of the current.⁷

The main results that we obtained by the method described above are as follows. Under conditions of an oscillatory discharge with weak damping, the column continues to expand for at least two periods of the current, the expansion velocity decreasing, according to our estimates, monotonically. The highest expansion velocity, several times and more higher than V_{mid} , is observed at the initial stage of the discharge. For example, for $f \approx 10^2$ Hz and $W = 16$ kJ the average (over the time $\tau_m/3$ from the start of the discharge) expansion velocity of the column is four times higher than $V_{mid} \approx 0.02$ mm/ μ s. By the first maximum of the current the expansion of the column slows down substantially, but further expansion of the column is even slower.

In the case of discharges with strong damping, when the oscillogram clearly records not more than one or two periods of the current, the plasma crowbar is actuated (for any radius of the crowbar electrode) only during the first period, i.e., the plasma column already reaches its maximum transverse size during this period.

For all of our discharges the column remained symmetric (cylindrical) for not longer than 2×10^{-4} s from the start of the discharge. We note that for $\tau_m < 2 \times 10^{-4}$ s the crowbar electrode need not be cylindrical. It is only necessary that the initial streamer around which a discharge channel later forms arose near the longitudinal axis of the trigatron electrode. This conditions is satisfied automatically if the work-

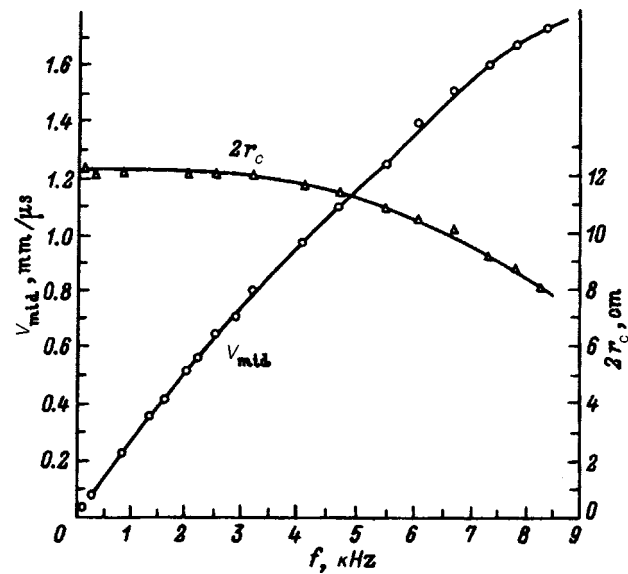


FIG. 2. Diameter $2r_c$ of the crowbar electrode and the average (over the first fourth of the first period of the discharge current) expansion velocity V_{mid} of the plasma column of the trigatron discharge versus LC-circuit frequency for discharge energy $W = 16$ kJ.

ing surfaces of the electrodes are spherical with a radius not exceeding 2–3 cm.

It must be underscored, however, that the radius of the plasma column that corresponds to some moment in time of the discharge process and for which the coil is short-circuited at this moment is stable and is reproduced from discharge to discharge, though the direction of the discharge can be different. This is indicated by the exceedingly high actuation stability of a plasma crowbar for fixed r_c and the fact that the parameters of the discharge circuit, including the shape and state of the working surfaces of the trigatron electrodes, as well as the length of the discharge gap remain unchanged.

It should be noted that the spherical shape and state of the surfaces (cleanliness, absence of irregularities, locations of melting, and so on) of the spark gap electrodes are especially important at low (< 3 kHz) discharge current frequencies. For discharges with $\tau_m < 8 \times 10^{-5}$ s the crowbar remains highly stable even with highly deformed and dirty (as a result of charring and fusing) electrode surfaces.

Figure 2 shows for discharge energy $W = 16$ kJ plots of V_{mid} and r_c versus the LC-circuit frequency, which, as indicated above, was found from oscillograms of the discharge current which were obtained using a Rogowski loop with an RC integrator.

Up to $f \approx 3$ kHz V_{mid} grows almost linearly with frequency, as a result of which the diameter $2r_c$ of the crowbar electrode remains unchanged. It is interesting that the first appreciable deviation from linearity is observed when V_{mid} reaches the speed of sound in air (0.33 mm/ μ s). This could be due to a decrease in the compressibility of air, which depends on the ratio of the speed of the shock wave to the speed of sound (the Mach number).

The curves in Fig. 2 essentially show V_{mid} and r_c as a function of the discharge power, determined as the ratio W/τ_m , which varies from $\sim 6 \times 10^6$ ($f \approx 10^2$ Hz, $\tau_m = 2.4$

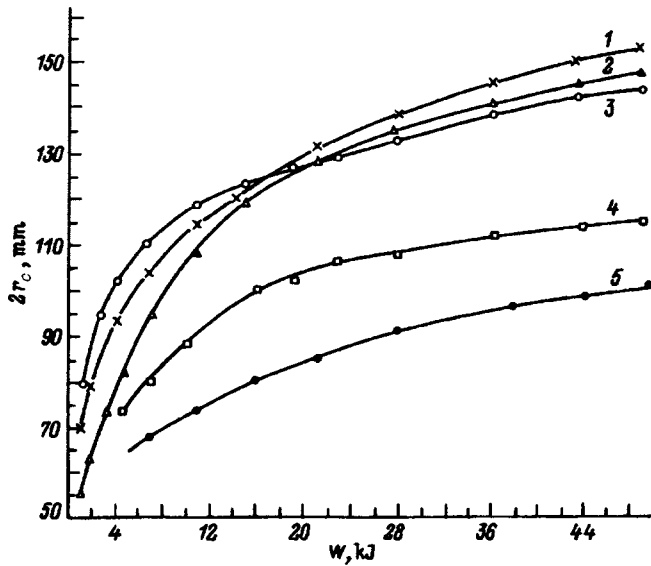


FIG. 3. Diameter $2r_c$ of the crowbar electrode short-circuiting a coil at the first maximum of the current versus the discharge energy for different LC -circuit frequencies. $f=100$ Hz (1), 1.1 kHz (2), 2.1 kHz (3), 5.5 kHz (4), 9 kHz (5); $\tau_m=2400$ (1); 110 (2,3); 40 (4); and $23 \mu\text{s}$ (5).

$\times 10^{-3}$ s) to $\sim 7 \times 10^8$ W ($f \approx 9$ kHz, $\tau_m = 2.3 \times 10^{-5}$ s). It is obvious that the growth of V_{mid} with increasing power tends to saturate, at which point r_c would not depend (or depend very weakly) on the discharge energy. The possibility that the column expands in this manner during τ_m is also supported by the curves of r_c versus energy for different frequencies of the LC circuit (Fig. 3). It is also evident from these curves that saturation, if it exists, is reached at discharge powers much higher than $\sim 2 \times 10^9$ W, for which the Mach number for V_{mid} already equals 7 (Fig. 3, curve 5).

The dependence of r_c on frequency and energy of the discharge circuit as seen in the plots can be represented by the following empirical formula

$$r_c = \frac{60}{17+f} W^{0.2},$$

where W is in kJ, f in kHz, and r in cm.

The error of this formula in the ranges of f and W indicated in Figs. 2 and 3 does not exceed 30% for $f < 3$ kHz and 15% for $f > 3$ kHz, making this dependence useful for practical applications of the circuit shown in Fig. 1.^{2,8} The following experimentally established inequalities should also be helpful: $r_c < r_1 < 1.5r_c$, where r_1 is the radius of the crowbar electrode for short-circuiting the coil in the first minimum of the discharge current.

Two conclusions can be drawn from the results presented above. First, the plasma-metal contact method is completely workable and applicable for studying gas discharges. Second, and much more important from the standpoint of the objective of the present work, an automatic plasma crowbar is a universal switch for an inductive load; this could have wide applications in high pulsed current and magnetic field technology. It has the following advantages over other switches described in the well-known literature:^{2,7,9} a) It is technically extremely simple and easily

accessible to a wide circle of experimenters; b) there are no limits on the current amplitude (trigatrons can be connected in parallel, and it is not at all necessary that each one be equipped with a crowbar electrode); c) the range of τ_m from $\sim 10^{-3}$ to $\sim 10^{-5}$ s includes the high pulsed current and magnetic field durations most often used in practice (apparently, a plasma crowbar is also applicable in the widest range of τ_m , but here additional investigations are required).

The drawbacks of the plasma crowbar as an apparatus are the same as for air-filled spark gaps⁷ (noise during operation (especially with high discharge powers), charring and fusing of crowbar electrodes, and so on). Here it should be noted that there is no doubt that the plasma crowbar can be used in combination with vacuum or high-pressure spark gaps, which have a number of advantages over air-filled spark gaps. However, in this case, the main advantages of the ‘‘air’’ crowbar—simplicity of operation and universality, i.e., applicability (with replacement of crowbar electrodes) in LC circuits with different parameters—will be inevitably partially or completely lost.

It should also be noted that the technical possibilities of plasma crowbars are by no means exhausted by the scheme shown in Fig. 1. Many other variants of a plasma crowbar are possible on both a fundamental level and in regard to constructional details. For example, one variant is to use several crowbar electrodes or one trigatron and several uncontrolled spark gaps placed at certain distances from one another so that when the trigatron is ignited, the other spark gaps automatically kick in simultaneously or in series as the plasma expands (programmable discharge^{10,11}).

The even the simplest variants of the scheme in Fig. 1 make it possible to obtain in an inductive load of an LC circuit the following current pulses (magnetic field pulses): 1) in the form of a half wave or whole wave of a sinusoid—short-circuiting of the load in the first or second minimum of the current;^{12,13} 2) asymmetric pulses with sinusoidal front and exponential cutoff—short-circuiting at the first maximum of the current (passive crowbar);^{14–16} 3) pulses in the form of a decaying sinusoid, whose half waves have flat tops—short-circuiting of a coil at the first maximum of the current with a capacitor bank and a small inductance connected in series in the crowbar section ab of the discharge circuit (active crowbar) (Fig. 1); 4) nearly square pulses—active crowbar, as in crowbar 3, plus a second crowbar electrode, short-circuiting the outputs of the coil at the end of the first half wave^{17,18} (in this case the first crowbar electrode can be ‘‘half-transmitting’’ for the plasma, i.e., for example, it can be made in the form of a grid or it can have ‘‘through’’ radial openings over the entire surface).

In closing, we note several points which should be taken into account in any practical implementation of the scheme shown in Fig. 1. A crowbar electrode must possess adequate mechanical strength, depending on the power of the discharge, and it must be strongly secured. Special attention should be devoted to the dynamic strength of the contacts at the points a and b of the discharge circuit (Fig. 1) as well as the strength of the conductor ab itself.¹⁵

This work was supported by the Fund for Fundamental Research of the Republic of Belarus.

- ¹A. K. Soïka, Pis'ma Zh. Tekh. Fiz. **14**, 1238 (1988) [Sov. Tech. Phys. Lett. **14**, 542 (1988)].
- ²B. B. Boïko, A. K. Soïka, and L. P. Mit'kovskaya, Prib. Tekh. Éksp., No. 5, 13 (1993).
- ³J. M. Meek and J. D. Craggs, *Electrical Breakdown of Gases* [Clarendon Press, Oxford, 1953; Inostr. Lit., Moscow, 1960].
- ⁴I. S. Marshak, Usp. Fiz. Nauk **77**, 249 (1962) [Sov. Phys. Usp. **5**, 478 (1962)].
- ⁵B. P. Giterman, D. I. Zenkov, A. I. Pavlovskii *et al.*, Zh. Tekh. Fiz. **52**, 1983 (1982) [Sov. Phys. Tech. Phys. **27**, 1218 (1982)].
- ⁶S. I. Andreev and B. I. Orlov, Zh. Tekh. Fiz. **35**, 1411 (1965) [Sov. Phys. Tech. Phys. **10**, 1097 (1965)].
- ⁷P. N. Dashuk, S. L. Zaïents, V. S. Komel'kov *et al.*, *High Pulsed Current and Magnetic Field Technology* [in Russian], Atomizdat, Moscow, 1970.
- ⁸B. B. Boïko, A. K. Soïka, and L. P. Mit'kovskaya, Prib. Tekh. Éksp. No. 2, 184 (1990).
- ⁹H. E. Knopfel, *Pulsed High Magnetic Fields* [North-Holland, Amsterdam, 1970; Mir, Moscow, 1972].
- ¹⁰B. É. Fridman, Elektrichestvo, No. 12, 36 (1989).
- ¹¹B. B. Boïko, A. K. Soïka, and L. P. Mit'kovskaya, Inventor's Certificate (USSR) No. 1723900 [in Russian]; Byull. Izobret., No. 12, 226 (1992).
- ¹²A. K. Soïka and I. M. Vashkevich, Dokl. Akad. Nauk Belarusi, **40**(3), 117 (1996).
- ¹³B. B. Boïko, A. K. Soïka, and L. P. Mit'kovskaya, Inventor's Certificate (USSR) No. 1701091 [in Russian]; Byull. Izobret., No. 47, 241 (1991).
- ¹⁴B. B. Boïko, A. K. Soïka, and A. I. Kachan, Inventor's Certificate (USSR) No. 1250057 [in Russian]; Byull. Izobret., No. 29, 265 (1986).
- ¹⁵A. K. Soïka and I. M. Vashkevich, Prib. Tekh. Éksp., No. 5 (1996).
- ¹⁶A. K. Soïka, B. B. Boïko, and I. M. Vashkevich, Dokl. Akad. Nauk Belarusi **40**, 46 (1996).
- ¹⁷B. B. Boïko, A. K. Soïka, and L. P. Mit'kovskaya, Inventor's Certificate (USSR) No. 1701032 [in Russian]; Byull. Izobret., No. 47, 241 (1991).
- ¹⁸B. B. Boïko, A. K. Soïka, and L. P. Mit'kovskaya, Dokl. Akad. Nauk BSSR **34**, 1073 (1990).

Translated by M. E. Alferieff

Optical control of photopolymerization during stereolithographic synthesis

S. N. Mensov and A. V. Semenov

N. I. Lobachevski Nizhegorod State University, 603600 Nizhniĭ Novgorod, Russia
(Submitted February 3, 1997)

Zh. Tekh. Fiz. **68**, 137–139 (February 1998)

The possibility of using the multiple-scattering spectrum of incident radiation to make a real-time determination of the degree of conversion of compositions undergoing photopolymerization in optical stereolithography is investigated. It is shown that the fluctuations arising in the refractive index grow in amplitude in the course of photopolymerization. The extremal dependences of the scattered radiation intensity on the degree of conversion are analyzed theoretically and experimentally. © 1998 American Institute of Physics. [S1063-7842(98)02702-0]

Real-time determination of the degree of conversion of two-phase media is required in order to solve the problem of stabilizing a number of physical and chemical processes. Specifically, this is important in layer-by-layer optical synthesis of three-dimensional objects from a photopolymer—the most promising form of stereolithography.¹ In this case, the preparation of a model requires a completely determined mechanical stiffness and uniformity. The monitoring of the degree of polymerization must be invasive, it must be performed for each point of the object being formed, and it should not affect the synthesis process. Since the photopolymer hardens under the action of the light incident on it, it is convenient to use the method of optical diagnostics. In the present work the possibility of obtaining information about the degree of polymerization from the form of the scattering spectrum of the laser light passed through the polymer layer is investigated.

A typical curve of the degree of conversion P (fraction of the polymer in the composition) versus the polymerization time with constant intensity of the incident radiation is presented in Fig. 1. The nonlinearity of the section AB introduces a positive feedback into the two-phase system that can intensify polymer concentration fluctuations, which are characterized by the nonuniformity of the refractive index with some correlation radii l_n , up to a macroscopic level.² As a result of the diffraction of the incident radiation by this “phase screen,” there arises in the layer undergoing polymerization a randomly-nonuniform distribution of light intensity with the same correlation radius l_n ,³ and this in turn results in additional intensification of the nonuniformities of the polymer concentration.

Let us examine the scattering of a laser beam (characteristic transverse size of the order of several millimeters¹) by nonuniformities of the photopolymer (l_n of the order of several tens of microns²). For simplicity, we shall assume that there is no absorption and that the nonuniformities arising are described by a Gaussian correlation function³

$$\Psi_n(\mathbf{r}) \equiv \langle \tilde{n}(\mathbf{r}) \tilde{n}(\mathbf{r}') \rangle = a_n^2 \exp\left(-\frac{r^2}{2l_n^2}\right), \quad (1)$$

where $n(\mathbf{r}) = \bar{n}(\mathbf{r}) + \tilde{n}(\mathbf{r})$ is the index of refraction at the

point \mathbf{r} of the layer undergoing polymerization, $\bar{n}(\mathbf{r})$ is the average value over the volume undergoing polymerization, $\tilde{n}(\mathbf{r})$ are the fluctuations of the index of refraction, and a_n is the amplitude of the fluctuations (intensity of the nonuniformities).

Since the average refractive index of the composition in the liquid phase $\bar{n}_m \approx 1.5$ (monomer) increases at a transition to the solid phase (polymer) by 2–3%,⁴ the amplitude of the nonuniformities will lie in the range $0 \leq a_m \leq 0.04$. Since layers of thickness h ranging from 250 to 750 μm are ordinarily used in stereolithography,¹ it must be assumed that the radiation which has passed through the photopolymer layer has undergone multiple scattering^{3,5}

$$h \cdot \sigma_{\max} \gg 1, \quad (2)$$

where σ_{\max} is the maximum possible effective scattering cross section σ per unit volume, determined according to the relation³

$$\sigma = \frac{\sqrt{2\pi} a_n^2 k_0^2 l_n}{4\bar{n}}, \quad (3)$$

and the wave number $k_0 \approx 10^7 \text{ m}^{-1}$.

To analyze the information characteristics of the multiple-scattering spectrum under our conditions we employ the solution

$$I_s = \frac{I_0}{4\sigma z \theta_{\max}^2} \exp\left(-\frac{\sin^2(\theta)}{\sigma z \theta_{\max}^2}\right), \quad (4)$$

of the transport equation in the small-angle approximation⁵

$$\frac{\partial I(z, \boldsymbol{\rho}, \mathbf{s})}{\partial z} + (\mathbf{s} \nabla_s I(z, \boldsymbol{\rho}, \mathbf{s})) = -\sigma I(z, \boldsymbol{\rho}, \mathbf{s}) + \frac{\sigma}{4\pi} \times \int \int p(\mathbf{s}, \mathbf{s}') I(z, \boldsymbol{\rho}, \mathbf{s}) ds', \quad (5)$$

where $I(z, \boldsymbol{\rho}, \mathbf{s})$ is the radiation intensity; $\mathbf{k} = (\mathbf{s} + \gamma \mathbf{z}_0) k_0$ is the wave vector of the scattered radiation, $\gamma \approx 1$; $\mathbf{r} = \boldsymbol{\rho} + z \mathbf{z}_0$ is the radius vector of a point in space; $p(\mathbf{s}, \mathbf{s}')$ is the scattering phase function of a unit volume; θ_{\max} is the width of

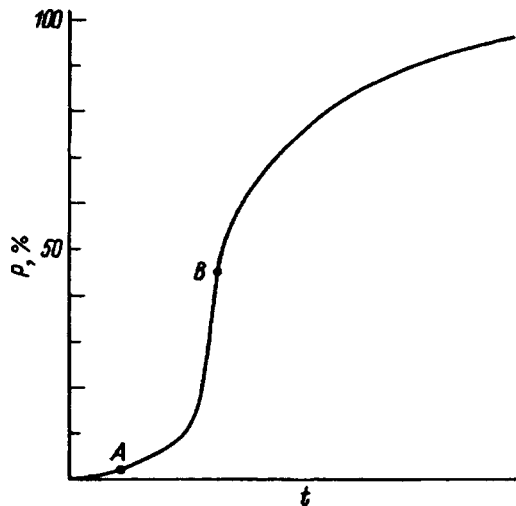


FIG. 1. Degree of conversion of a photopolymer versus polymerization time.

the scattering phase function for one particle at the half-power level; θ is the angle between the direction of the incident (\mathbf{z}_0) and scattered radiations; and, I_0 is the intensity of the incident beam, which can be assumed to be a plane wave within the nonuniformity.

From Eqs. (3) and (4) it is evident that for constant thicknesses h of the layer undergoing polymerization and size l_n of the Gaussian nonuniformities the scattering spectrum I_s depends nonmonotonically on the amplitude a_n of the refractive index fluctuations. The position

$$\tilde{a}_n^2 = \frac{4\bar{n} \sin^2(\theta)}{\sqrt{2\pi h \theta_{\max}^2 k_0^2 l_n}} \quad (6)$$

of the maximum $I_{s \max}$ of the scattering spectrum is virtually proportional to θ .

Since the polymerization process evolves in time, and the degree of polymerization of the composition corresponds to a definite intensity a_n of the nonuniformities, the degree of conversion can be controlled according to the multiple-scattering spectrum on the basis of the extremal dependences of the functions $I_s(a_n(t), \theta)$ (4) as follows: Measuring $I_s(t, \theta)$ continuously during polymerization, we determine the time at which the function reaches an extremum as a function of θ . Using Eq. (6), it is easy to find the dependence of the amplitude of the refractive index fluctuations arising in the photopolymer and therefore also the degree of conversion as a function of time.

We investigated experimentally the scattering spectrum of the polymerizing radiation, which passed through a layer of a photopolymerizing composite material based on oligoester acrylates with carbanil-containing photoinitiators. The maximum value of the scattering cross section of random nonuniformities of the photopolymer was found experimentally to be $\sigma = 70000 \text{ m}^{-1}$.

On this basis, when a layer of thickness $h = 0.01 \text{ mm}$ undergoes polymerization, the angular spectrum can be analyzed using the single-scattering approximation^{3,5}

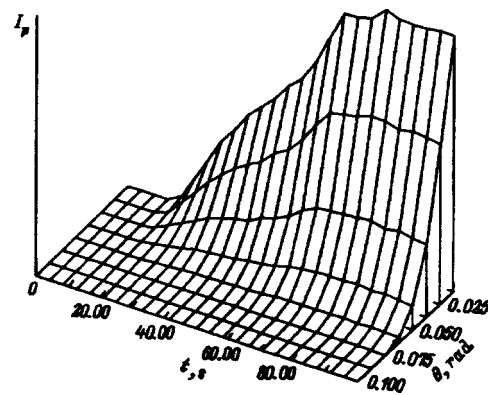


FIG. 2. Time dependence of the angular scattering spectrum in the process of polymerization of a 0.01 mm thick layer.

$$I_p = \frac{\sigma z}{\pi \theta_{\max}^2} \exp\left(\frac{\sin^2(\theta)}{\theta_{\max}^2}\right) \exp(-\sigma z). \quad (7)$$

Measuring the density of the scattered field propagating at angles $\theta = 0.0125, 0.025, 0.0375, 0.05, 0.0625, 0.075, 0.0875,$ and 0.1 rad with respect to the direction of the incident wave, we obtained the time dependences presented in Fig. 2. It is evident from these dependences that the angular spectrum obtained is a Gaussian function with constant width $\theta_{\max} \approx 0.03$ rad with the harmonics amplitude increasing monotonically with time. Correspondingly, the nonuniformities arising in the photopolymer have a Gaussian shape and a constant size $l_n \approx 20 \mu\text{m}$, and their intensity (amplitude of the refractive index fluctuations) grows monotonically with the degree of polymerization.

The time dependences of the intensity of the scattered radiation (Fig. 3), recorded at the same angles as in the case of single scattering, were obtained for a layer of thickness $h = 0.5 \text{ mm}$ (which corresponds to multiple scattering (2))

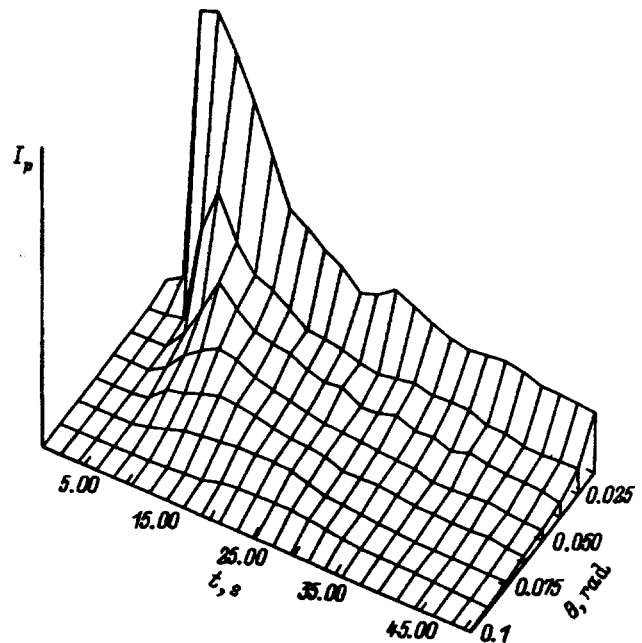


FIG. 3. Time dependence of the angular scattering spectrum in the process of polymerization of a 0.5 mm thick layer.

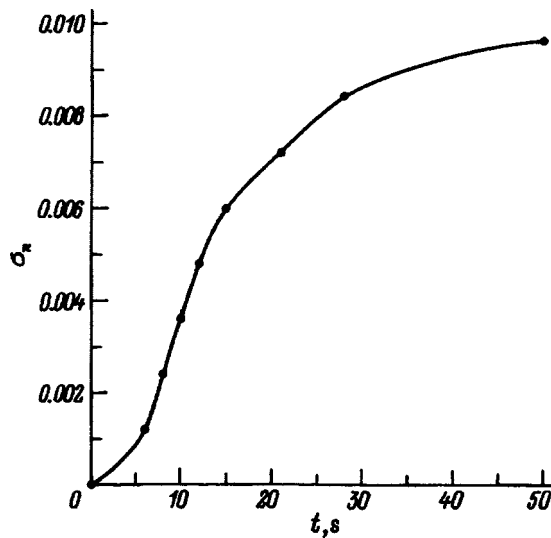


FIG. 4. Refractive-index fluctuation amplitudes versus polymerization time. ●—Experimental values.

undergoing polymerization. The results (Fig. 4) obtained by analyzing these diagrams by the method proposed above showed a monotonically increasing function $a_n(t)$ for the photopolymer employed. Therefore if we wish to obtain a photopolymer with a definite degree of conversion, corresponding to one value of the amplitude of the refractive index fluctuations, then it is necessary to measure in the pro-

cess of polymerization the intensity of the scattered light propagating at angle θ corresponding to the condition (6). Then the polymerization time will be determined by the time at which the maximum is reached.

The method which we have proposed above can be used to determine the degree of polymerization not only of photopolymers but also transparent polymers with chemical initiators (for example, methyl methacrylate). However, it is necessary to take into account the fact that in this case the concentration nonuniformities arising in the course of the reaction are much smaller in amplitude and partially relax.² In other words, two degrees of polymerization will correspond to one value of the refractive index fluctuations. For this reason, for purposes of diagnostics the dynamics of the variation of the scattered intensity must be followed not at one angular frequency but rather over the entire angular spectrum simultaneously.

¹J. P. Kruth, *Ann. CIRP* **40/2**, 69 (1991).

²A. I. D'yachkov, A. I. Levinskii, and S. N. Mensov, *Vysokomol. Soedin.* **29**, 1917 (1987).

³S. M. Rytov, Yu. A. Kravtsov, and V. I. Tatarskii, *Introduction to Statistical Radio Physics. Part 2. Random Fields* [in Russian], Nauka, Moscow, 1978.

⁴A. A. Berlin, *Acrylic Oligomers and Materials Based on Them* [in Russian], Khimiya, Moscow, 1983.

⁵A. Akira, *Propagation and Scattering of Waves in Randomly Inhomogeneous Media* [Russian translation], Mir, Moscow, 1981.

Translated by M. E. Alferieff

Theory of heat and moisture transfer in a capillary-porous body

O. L. Reshetin and S. Yu. Orlov

*Agrophysical Scientific-Research Institute of the Russian Academy of Agricultural Sciences,
195220 St. Petersburg, Russia*

(Submitted February 11, 1997)

Zh. Tekh. Fiz. **68**, 140–142 (February 1998)

New differential equations describing the dynamics of the formation of temperature and moisture fields in capillary-porous media are derived on the basis of a complete analysis of the physical processes occurring in a capillary-porous body. The derivation of the equations is based on the well-known diffusion laws and functional relations between the temperature, moisture content, and vapor content, which are physical characteristics of the body. The equations obtained contain experimentally measurable physical quantities and dependences which characterize a specific capillary-porous body. © 1997 American Institute of Physics. [S1063-7842(97)03110-3]

The theory of mass and energy transfer in capillary-porous bodies is important in power engineering, technological processes in the food, construction, chemical, and light industries, and in agrophysics. At the present time, the system of differential equations obtained by Academician A. V. Lykov is used for the theoretical description of heat and moisture transfer processes in capillary-porous media.^{1,2}

A. V. Lykov proposed the following simplified physical model for the mathematical description of heat and moisture transfer processes in a capillary-porous body. The mass of the matter present in pores equals, to a high degree of accuracy, the mass of the liquid phase (the gas-phase mass is negligibly small). Transfer of only the part of the vapor that participates directly in a phase transition is important. Therefore in studying mass transfer processes the transfer law for only one phase, for example, the liquid phase, need be posited and the entire effect of vapor transfer and phase transitions can be taken into account by means of only one parameter — the phase-transformation $\varepsilon = dW_\phi/dw$. The phase transformation criterion ε is determined as the ratio of the change in the moisture content by evaporation and condensation to the change in the moisture content due to transfer of liquid. This approach led to the following equations describing these processes in the capillary-porous body:¹⁾

$$C_\Sigma \frac{\partial}{\partial t} T - \varepsilon r \frac{\partial}{\partial t} W_l = \nabla \cdot (\lambda \nabla T) - (C_l D_l \nabla W_l + C_l D_{Tl} \nabla T) \nabla T, \\ (1 - \varepsilon) \frac{\partial}{\partial t} W_l = \nabla \cdot (D_l \nabla W_l) + \nabla \cdot (D_{Tl} \nabla T). \quad (1)$$

This approach greatly simplifies the system of differential equations describing the heat and moisture transfer in capillary-porous media, but it creates certain difficulties in the practical application of these equations since the phase-transformation criterion ε is a fictitious physical parameter.

The equations (1) have been used in many theoretical works to investigate heat and mass transfer in capillary-porous media. However, a large number of attempts to measure correctly all coefficients appearing in the equations pre-

sented above for a specific capillary-porous body yielded very contradictory results. This is due primarily to the fundamental impossibility of measuring the parameter ε . For this reason, the present work is devoted to the rigorous derivation of differential equations which describe transfer processes in a capillary-porous body and are free of this shortcoming.

A capillary-porous body contains two interacting phases: moist air and liquid. The framework of a porous body is a rigid solid which does not swell, absorb water, or dissolve in water and does not enter into chemical interactions with water. We write the equation of conservation of energy and mass as

$$\frac{\partial}{\partial t} H = -\nabla \cdot \mathbf{q}, \quad (1a)$$

$$\frac{\partial}{\partial t} (W_v + W_l) = -\nabla \cdot (\mathbf{J}_v + \mathbf{J}_l), \quad (2)$$

where H is the enthalpy of the system per unit volume of the capillary-porous body (enthalpy density); \mathbf{q} is the heat flux vector; W_v and W_l are the mass of the vapor (vapor content) and liquid (moisture content), respectively, per unit volume of the capillary-porous body; \mathbf{J}_v and \mathbf{J}_l are the vapor and liquid flux vectors, respectively; ∇ is the del or nabla operator; and, t is the time.

The enthalpy density for the system under study is

$$H = H_s + h_v W_v + h_l W_l, \quad (3)$$

where H_s is the enthalpy of the solid phase per unit volume of the porous body and h_v and h_l are, respectively, the enthalpy of the vapor and liquid per unit mass (specific enthalpies).

Let us differentiate (3) with respect to time and take account of the fact that the derivative of the specific enthalpy with respect to temperature at constant pressure is the specific heat. This gives the expression

$$\frac{\partial}{\partial t} H = C_\Sigma \frac{\partial}{\partial t} T + h_v \frac{\partial}{\partial t} W_v + h_l \frac{\partial}{\partial t} W_l, \quad (4)$$

where $C_\Sigma = C_s + W_v C_v + W_l C_l$; T is the temperature of the system at a given point; C_s is the specific heat per unit volume of the dry porous body; and, C_v and C_l are the specific heats of the vapor and liquid.

The first term on the right-hand side of expression (4) describes the change in enthalpy due to a temperature change and the two other terms take account of the change in enthalpy due to a change in the amount of matter.

In the system under study, heat propagates by conduction and also by transfer of vapor and liquid. Therefore the heat flux is

$$\mathbf{q} = -\lambda \nabla T + h_v \mathbf{J}_v + h_l \mathbf{J}_l, \tag{5}$$

where λ is the effective thermal conductivity of the system.

The divergence of the heat flux vector can be written as

$$\begin{aligned} \nabla \cdot \mathbf{q} = & -\lambda \Delta T + h_v \nabla \cdot \mathbf{J}_v + h_l \nabla \cdot \mathbf{J}_l \\ & + (-\nabla \lambda + C_v \mathbf{J}_v + C_l \mathbf{J}_l) \cdot \nabla T, \end{aligned} \tag{6}$$

where $\Delta = \nabla^2$ is the Laplace operator.

Using expression (2) it can be shown that

$$\begin{aligned} h_v \frac{\partial}{\partial t} W_v + h_l \frac{\partial}{\partial t} W_l + h_v \nabla \cdot \mathbf{J}_v + h_l \nabla \cdot \mathbf{J}_l \\ = -r \left(\frac{\partial}{\partial t} W + \nabla \cdot \mathbf{J}_l \right), \end{aligned} \tag{7}$$

where $r = h_v - h_l$ is the heat of the phase transition.

Substituting expressions (4) and (6) into Eq. (1) and using Eq. (7) the energy equation assumes the form

$$\begin{aligned} C_\Sigma \frac{\partial}{\partial t} T - r \left(\frac{\partial}{\partial t} W + \nabla \cdot \mathbf{J}_l \right) \\ = \lambda \Delta T + (\nabla \lambda - C_v \mathbf{J}_v - C_l \mathbf{J}_l) \cdot \nabla T. \end{aligned} \tag{8}$$

The thermal conductivity of the system depends on the moisture content and temperature. This gives a basis for representing $\nabla \lambda$ in the form

$$\nabla \lambda = \frac{\partial \lambda}{\partial W_l} \nabla W_l + \frac{\partial \lambda}{\partial T} \nabla T. \tag{9}$$

In the general case the vapor partial pressure p_v and vapor density ρ_v in capillary-porous bodies depend on temperature and moisture content $p_v = p_v(T, W_l)$ and $\rho_v = \rho_v(T, W_l)$.

Then the time derivative of the vapor density is

$$\frac{\partial \rho_v}{\partial t} = \frac{\partial \rho_v}{\partial T} \frac{\partial T}{\partial t} + \frac{\partial \rho_v}{\partial W_l} \frac{\partial W_l}{\partial t}. \tag{10}$$

The porosity (Π) of the capillary-porous body is the ratio of the free volume, containing water and moist air, to the total volume of the porous body calculated for an elementary volume. Then we can write

$$W_v = \rho_v \left(\Pi - \frac{W_l}{\rho_l} \right), \tag{11}$$

where ρ_l is the density of the liquid phase.

Let us differentiate the equation (11) with respect to time and take account of Eq. (10). Then

$$\begin{aligned} \frac{\partial}{\partial t} W_v = & \frac{\partial \rho_v}{\partial T} \left(\Pi - \frac{W_l}{\rho_l} \right) \frac{\partial T}{\partial t} \\ & + \left(\frac{\partial \rho_v}{\partial W_l} \left(\Pi - \frac{W_l}{\rho_l} \right) - \frac{\rho_v}{\rho_l} \right) \frac{\partial}{\partial t} W_l. \end{aligned} \tag{12}$$

As shown in Refs. 1 and 2, the main laws governing the transfer of vapor and liquid can be represented in the form

$$\mathbf{J}_l = -D_l \nabla W_l - D_{Tl} \nabla T, \tag{13}$$

$$\mathbf{J}_v = -D_v \nabla W_v - D_{Tv} \nabla T, \tag{14}$$

where the coefficients D_l , D_v , D_{Tl} , and D_{Tv} characterize the specific capillary-porous body. These coefficients can be expressed in terms of experimentally determined physical quantities.

We substitute expressions (9), (13), and (14) into Eq. (8) and perform some elementary transformations. Then the energy equation can be written in the final form as

$$\begin{aligned} C_\Sigma \frac{\partial}{\partial t} T - r \frac{\partial}{\partial t} W_l = & \lambda \Delta T + (k \nabla W_l + m \nabla T) \cdot \nabla T \\ & - r \nabla \cdot (D_l \nabla W_l) - r \nabla \cdot (D_{Tl} \nabla T), \end{aligned} \tag{15}$$

where $k = \frac{\partial \lambda}{\partial W_l} + C_v D_v + C_l D_l$,

and $m = \frac{\partial \lambda}{\partial T} + C_v D_{Tv} + C_l D_{Tl}$.

Substituting expressions (12)–(14) into Eq. (2), we obtain a final expression for the mass transfer equation

$$\begin{aligned} R \frac{\partial}{\partial t} T + Q \frac{\partial}{\partial t} W_l = & \nabla \cdot ((D_l + D_v) \nabla W_l) \\ & + \nabla \cdot ((D_{Tv} + D_{Tl}) \nabla T), \end{aligned} \tag{16}$$

where

$$R = \frac{\partial \rho_v}{\partial T} \left(\Pi - \frac{W_l}{\rho_l} \right), \quad Q = 1 + \frac{\partial \rho_v}{\partial W_l} \left(\Pi - \frac{W_l}{\rho_l} \right) - \frac{\rho_v}{\rho_l}.$$

The equations (15) and (16) comprise a system of equations which describe heat and mass transfer in capillary-porous bodies.

The theory presented above makes it possible to establish the required set of specific, experimentally observable physical quantities of the system under study (C_Σ , λ , D_l , D_{Tl} , D_v , D_{Tv} , Π , $p_v(T, W_l)$) and it makes it possible to investigate transfer processes in capillary-porous media theoretically in diverse situations.

The idea for this work arose at the Agrophysical Institute in discussions between one of us and A. F. Chudnovskii and B. M. Mogilevskii, to whom we are deeply grateful.

¹All notations for physical quantities in Ref. 1 are reduced to the notations employed in the present paper.

¹A. V. Lykov, *Heat and Mass Transfer in Drying Processes* [in Russian], GÉI, Moscow, 1956.

²A. V. Lykov, *Transport Phenomena in Capillary-Porous Bodies* [in Russian], GITTL, Moscow, 1954.